Modelling Subduction Zone Magmatism

Rebekah Lawton

School of Earth and Ocean Sciences

Cardiff University

Submitted in partial fulfilment of the requirements for the degree of

Doctor of Philosophy

February 2016

DECLARATION

This work has not been submitted in substance for any other degree or award at this or any other university or place of learning, nor is being submitted concurrently in candidature for any degree or other award.

This thesis is being submitted in partial fulfillment of the requirements for the degree of PhD.

This thesis is the result of my own independent work/investigation, except where otherwise stated. Other sources are acknowledged by explicit references. The views expressed are my own.

I hereby give consent for my thesis, if accepted, to be available online in the University's Open Access repository and for inter-library loan, and for the title and summary to be made available to outside organisations.

Rebekah Lawton

February 2016

ACKNOWLEDGEMENTS

First of all I would like to thank my fantastic supervisor Huw Davies for all your help and guidance throughout my PhD. Thank you to Matthew Price for being a great office mate for three years and helping to assemble my PhD. Thanks also go to the team Geodynamics; Peter Webb, Hein van Heck, Fanny Garel and Cian Wilson for your comments and discussions and to Ian Merrick for Matlab assistance.

A big thanks to team PhD; Emily Deaney, Sarah Lee, Miriam Olivier, Chris Kirkham and Henry Coombs for your friendship and moral support, we are all square of the week! Thank you as well to the rest of the PhD students and staff in the school of Earth and Ocean sciences for making the last four years a great experience. I am grateful to the Friday night crew; Matthew Bond, Kim Williams, Alan Dowell and Matthew and Emma Whitby for providing a welcome distraction away from my PhD.

Thank you to my parents, Stephen and Gail and my siblings, Harriet and David for your love and support over the years and also for your unofficial proofreading services. Last of all thank you to my boyfriend Graham Carr for being there for me during my PhD, I couldn't have done it without you.

ABSTRACT

Subduction zone magmatism is a well studied area due to dangerous consequences of volcanic activity at subduction zones. Whilst it is widely accepted that water leaving the slab causes the magmatism, the method in which the water leaves the slab and causes magmatism is unclear. In this thesis we will examine the hypothesis that water leaving the slab via a large hydraulic fracture will cause instantaneous 'flash' melting in the mantle wedge. We will test whether this flash melting occurs and whether it produces sufficient melting. We will also look at hydrous flux melting and hydrous decompression melting occuring after the initial flash melting to see if they increase the melting.

A thermal model for a subduction zone is built, with the wedge flow solved analytically, to provide the temperature input for the melting models. Four melting models were tested; flash melting, flash melting followed by hydrous flux melting, flash melting followed by hydrous decompression melting and flash melting, then hydrous flux melting followed by hydrous decompression melting. Another thermal model was also made with the wedge flow solved numerically, this allowed buoyancy to be added into the model to allow investigation into the magma migrating buoyantly.

We show that the flash melting model does produce flash melting from large hydraulic fractures but the melting produced is not sufficient compared to observations from volcanic arcs. The flash melting followed by hydrous flux melting model also did not produce sufficient melting however the two decompression melting cases did when compared to observations from volcanic arcs. The addition of buoyancy in to the melting model allows

migration of the partial melt towards the wedge corner providing a melt focussing mechanism which is required to get a sharp volcanic front.

TABLE OF CONTENTS

LIST OF FIGURES

LIST OF TABLES

CHAPTER 1

INTRODUCTION

1.1 Plate Tectonics

The theory of plate tectonics describes the outer shell of the Earth as divided into tectonic plates that move relative to one another. It had been noted for a long time that there were correlations across oceans in palaeontological records and stratigraphy; the most noticeable sign was the coasts of West Africa and East South America were very similar in shape. This led Alfred Wegener to develop the hypothesis of continental drift in 1912. In 1962 Harry Hess hypothesised that at the axis of a ridge sea floor was created and moved away from the ridge; this is now known as sea floor spreading. This process helped explain the similarity in the coasts of West Africa and East South America. They were once joined together but as the continent broke apart an ocean ridge formed with ocean floor being created symmetrically either side of the ridge: this ocean is now the Atlantic Ocean. Concerns about the driving mechanism and the rigidity of the mantle led to plate tectonics only being widely accepted in the late 1960s.

The distribution of the tectonic plates is shown in Figure 1.1. The majority of earthquakes, volcanoes and mountain building occur at plate boundaries. There are three main types of plate boundary: divergent, convergent and conservative. At the divergent boundaries,

adjacent plates pull apart from one another and hot mantle rock rises to fill the gap between the diverging plates, creating new oceanic crust. This is most commonly seen at Mid Ocean Ridges (MOR) such as the Mid-Atlantic Ridge. At convergent boundaries plates move towards one another. There are are either of two types; collision and subduction. At collision margins the plates converge and deform creating mountain regions. At subduction margins the plates also converge but one plate will descend under the other. Convergent boundaries consume crust whereas divergent boundaries create it, thus keeping the surface area of the Earth constant. An example of a convergent margin is the Nazca plate subducting under the South America plate. Conservative margins are where the plates move alongside one another also known as transform faults and at this margin no crust is created or destroyed. Large earthquakes occur at conservative margins but there is little to no volcanism, an example of a conservative margin is the San Andreas Fault in California. There are two types of plate: oceanic and continental, both being made up of an overlying crust and mantle lithosphere. The oceanic crust is thin and is created at divergent boundaries; the continental crust is thicker, but less dense, than the oceanic crust which is important for the process of subduction. The main region of interest for this thesis is the subduction type of convergent plate boundaries, in particular subduction zones that form as a consequence. Many important natural resources such as diamonds, uranium and gold are found at subduction zones. However, subduction zones are associated with some of the most explosive volcanism and the largest earthquakes; indeed both cause great destruction. Greater understanding of the complex processes involved at subduction zones will hopefully help to predict and minimize the dangers posed.

1.1.1 Subduction Zones

There are two types of subduction zone: oceanic versus oceanic, and continental versus oceanic. At the continental vs oceanic subduction zones, the denser oceanic crust is forced under the less dense continental crust. At oceanic vs oceanic subduction zones, the older,

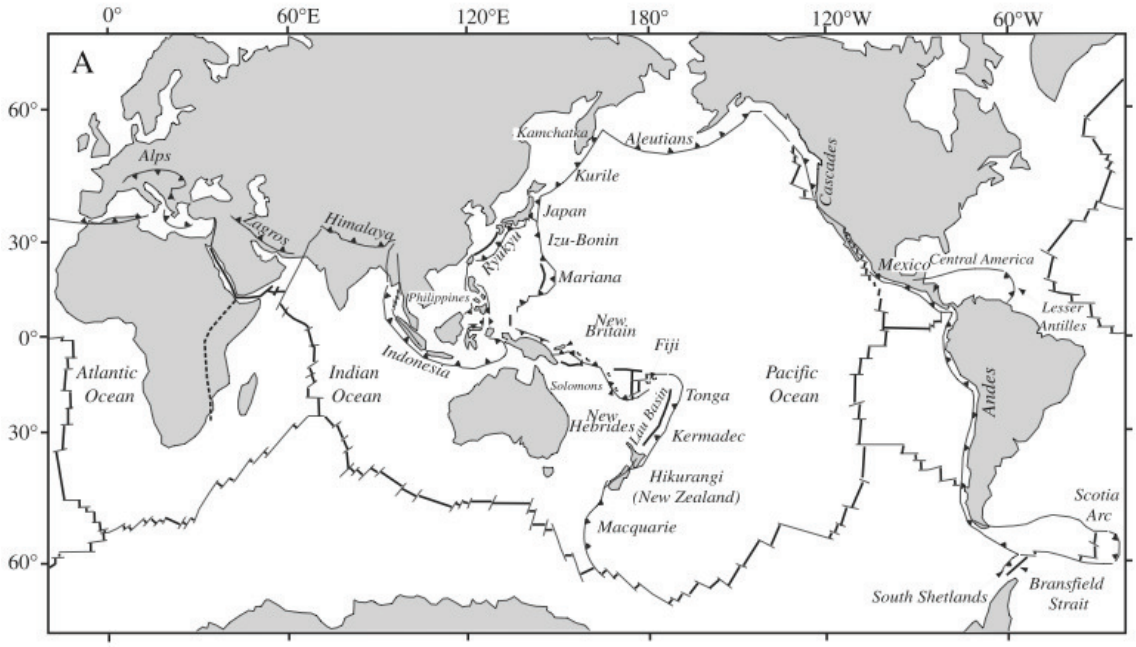

Fig. 1.1 Map of plate boundaries on Earth. The convergent margins are marked with triangles. The solid lines are divergent boundaries and transform faults. Taken from Stern (2002).

colder, oceanic plate will be denser and will be subducted under the younger plate. Where the two plates meet a deep oceanic trench forms. Subduction zones are the location of major arc volcanism and are the only sites of deep earthquakes, subduction being the major driving force of plate tectonics as old dense lithosphere is pulled into the mantle. Earthquakes occur within the subducting slab in a region called the Wadati-Benioff zone, where the seismicity gives an insight into the depth and shape of subducting slabs. Syracuse and Abers (2006) contoured the top of the Wadati Benioff zone based on the earthquake catalogue by Engdahl et al. (1998); they showed that subduction zones have a wide range of geometries ranging from deeply dipping to shallowly dipping slabs. The location of volcanoes at subduction zones indicates melting occurs. The accepted theory for magmatism at subduction zones is that release of water from the subducting slab into the mantle wedge causes melting by lowering the peridotite melting temperature (Van Keken, 2003). How the water gets in the slab, leaves the slab and the melting processes will be explored further.

1.2 How Water Enters the Subducting Slab

It is generally accepted that water released from the subducting slab is responsible for subduction zone magmatism, but what process hydrates the slab? It has been suggested that the subducting slab is hydrated at three levels: sediments, altered oceanic crust and serpentinized mantle. van Keken et al. (2011) estimated that for a case with 2 wt% water hydration of the upper mantle, 7% of the water input is in the sediment, 35 % is contained in the upper crust, 28 % is in the lower crust and 31 % is in the mantle.

In order for the mantle to become hydrated the fluid must be able to pass through the sediments and crust to reach the mantle. It is proposed that normal faulting between the outer rise and trench axis would occur during plate bending and provide possible pathways for water to the mantle (Ranero et al., 2003). Multibeam bathymetry off the coast of Nicaragua, along the Middle America Trench (MAT), showed that bending related extensional faults (bend faults) were prevalent across most of the ocean trench slope (Ranero et al., 2003). Deep imaging, high resolution seismic reflection profiles show that bend faults cut at least 20 km deep into the lithospheric mantle. Ranero et al. (2003) proposed that the reflectivity in the seismic data could be best explained by mineral alteration and water percolation along the fault planes. Key et al. (2012) mapped the electrical resistivity of the MAT using controlled source electromagnetic imaging; observing anisotropy and resistivity decreases, which they hypothesised was caused by a porosity increase along the fault planes. This was interpreted as evidence that the necessary permeable fluid pathways are provided by bend faults, which are required for serpentinization of the mantle. Low heat flow values observed at the trench off Costa Rica is another support for bend faults and their associated hydrothermal circulation (Langseth and Silver, 1996). The serpentinization around the bend faults would occur at the trench and the extent of upper mantle alteration is dependent on the 'spacing' of the bend faults in the faulting region (Key et al., 2012; Rüpke et al., 2004).

1.3 How Water Leaves the Subducting Slab

As the slab subducts and pressure and temperature increase, dehydration reactions occur and release water from the slab into the mantle wedge (Peacock, 1990). The dehydration will be continuous over a range of depths rather than a single phase dehydration at specific depths (Schmidt and Poli, 1998). It was found that at a given depth several hydrous phases will decompose through either continuous or discontinuous reactions, by phase relationships in mafic and ultramafic lithogies. Most dehydration reactions will not take place at a distinct depth, but will be smeared out over a depth range, due to a high temperature gradient near the slab surface. (Schmidt and Poli, 1998). van Keken et al. (2011) used the global subduction zone thermal models by Syracuse et al. (2010) to predict the water content in the slab and the metamorphic facies. Figure 1.2 is their 'Tokyo Subway Map' of the water content loss as a function of depth for each subduction zone. Figure 1.2 shows there is a large variation in the depth and magnitude of water release from the subducting slabs. The thermal models van Keken et al. (2011) used assumed the mantle wedge coupled to the slab at 80 km depth and in Figure 1.2 a large release of water occurs at this depth. In Figure 1.2 some slabs have distinct pulses of water release, whereas other show a more continuous water loss with depth. It must be noted that the results of van Keken et al. (2011) were sensitive to the assumed hydration amounts of the slab and the thermal structure. Even so the results from van Keken et al. (2011) demonstrate water release varies between subduction zones and over a range of depths.

1.3.1 Porous Flow

Movement of hydrous fluid by porous flow along solid grain boundaries is relatively slow, but maximises interaction of the fluid with the mantle. Fluids can move through solids near the surface as they are porous, but porosity in the mantle can only exist if there is a fluid present

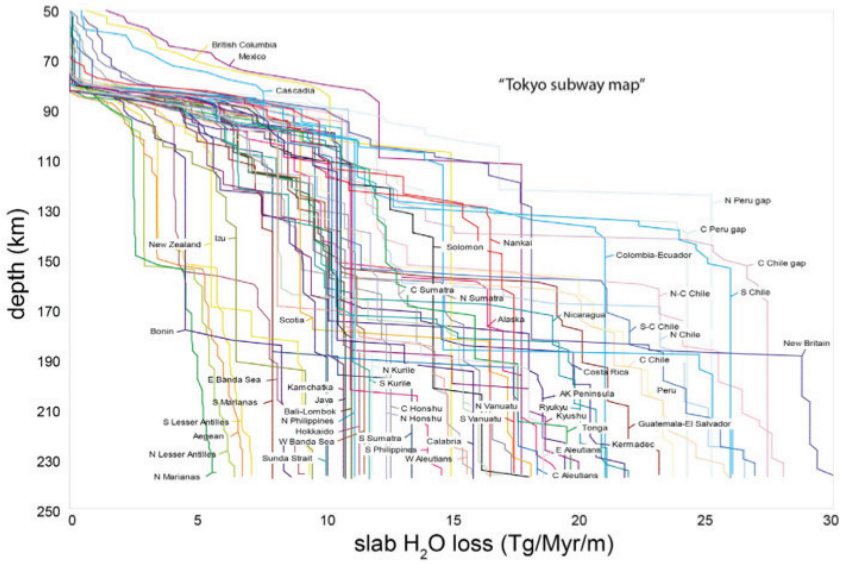

Fig. 1.2 H_2O loss as a function of depth for each subduction zone. Most subduction zones have significant H_2O loss at 80 km depth. Taken from van Keken et al. (2011).

to hold it open. The factor that determines whether a fluid can be transported by porous flow is the dihedral angle. This angle θ is formed between two mineral/fluid interfaces at a grain boundary. If $\theta > 60^\circ$ then the fluid can not move as it will be in isolated pores. If $\theta < 60^\circ$ then the fluid can move by porous flow as the fluid is interconnected along grain edges (Stern, 2002).

Various studies have discussed and modelled porous flow of fluid in subduction zones (Cagnioncle et al., 2007; Davies and Stevenson, 1992; Iwamori, 1998; Wilson et al., 2014). Davies and Stevenson (1992) discussed the lateral movement of fluid due to porous flow, this proposed transport mechanism is shown in Figure 1.3, taken from Stern (2002). From Figure 1.3 there are several stages of the lateral transport shown by the letters (A) to (M). Firstly water is carried downwards by the slab (A), and aqueous fluid is continuously released by dehydration from the subducted sediment, crust and serpentinites (B). The fluid rises into the overlying mantle and forms hydrous minerals (C). In Figure 1.3 and in Davies and Stevenson (1992) amphibole is chosen as the representative mineral but it is stated in Davies and Stevenson (1992) that in a reality a wide range of hydrous minerals will form. The

mantle with amphiboles located by the slab moves downwards with the slab until $\sim$ 100 km, the maximum stability of amphibole peridotite. There it breaks down to aqueous fluid and anhydrous peridotite (D). The fluid released from the amphibole breakdown rises vertically towards the hotter region of the mantle and at some point it forms amphibole again, by reacting with anhydrous peridotite (E). The amphibole descends until it breaks down again (F). Fluid rises and forms amphibole (G), then descends until it breaks down (H). The mantle above (H) is hot enough that the addition of water leads to melting (I). (K)-(M) are the migration of the melt, which in this case is via a diapir. Schmidt and Poli (1998) concluded that the additional time that would be required for lateral transport would take too long, compared to the time interval between dehydration and eruption. Recent work by Cagnioncle et al. (2007) and Wilson et al. (2014) have the fluid moving vertically with porous flow due to the buoyancy of the fluid; horizontal migration still occurs but due to the interaction of the buoyant fluid with the solid flow of the mantle wedge.

1.3.2 Channelized Flow

Another mechanism by which water may leave the slab is by channelized flow. Faulting at intermediate depths would cause the fluids trapped in isolated pores to interconnect, causing a hydraulic fracture out into the mantle wedge (Davies, 1999). Channelized flow would be much more rapid than porous flow. Experimental data by Keppler (1996) showed that U is highly mobile in oxidising aqueous fluids, whereas Th is immobile. Redox conditions have reducing oxidising in the mantle wedge but in the altered oceanic crust are strongly oxidising. Fluids released by dehydration of the slab are taken to be shown by U excesses (Elliott et al., 1997; Hawkesworth et al., 1997). U will become less mobile as the fluids become more reducing in the wedge causing the fractionation of U/Th to diminish. Initial fluid addition to the wedge will have the highest U/Th results. Over time Th ingrowth will cause the U/Th disequilibria to decrease, therefore this data is used to constrain the time between dehydration

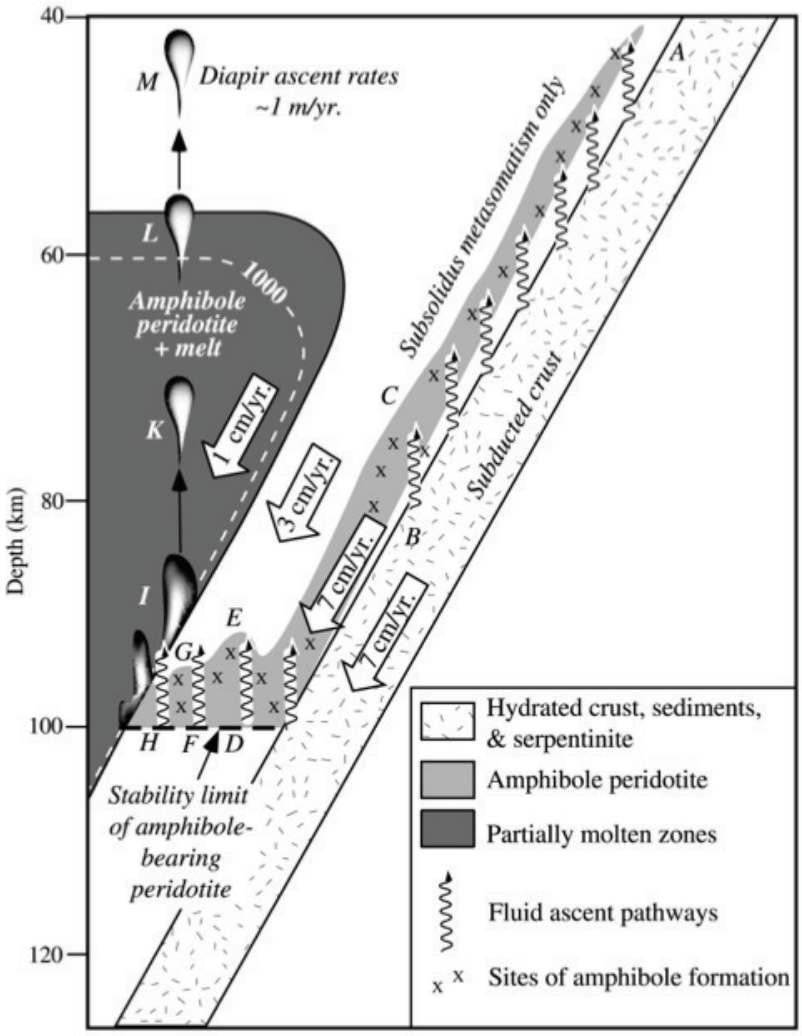

Fig. 1.3 Cartoon of how water might be transported from the slab to the region of melting based on the lateral transport theory by Davies and Stevenson (1992). Taken from Stern (2002)

of the slab and eruption (Turner and Hawkesworth, 1997). The time between fluid release and eruption was found to be $\sim$ 30,000 to 50,000 yr for the Tonga-Kermadec system (Turner and Hawkesworth, 1997). It was found that integrated fluid and melt transport was $\sim$ 1 - 4 m yr^{-1} (Hawkesworth et al., 1997). John et al. (2012) used Lithium diffusion modelling to show fluids released by dehydration travelled along major conduits through the slab in pulses of duration $\sim$ 200 yr. They concluded that although dehydration is continuous over a long time scale, fluids produced by dehydration of the slab were mobilised in channelized

flow, short lived events. Channelized flow would also explain a characteristic feature of subduction zone magmas; that they contain a high ratio of large ion lithophile elements to high field strength elements. This is thought to be caused by the fluid released from the slab carrying the large-ion lithophile elements (Pearce and Peate, 1995). As a hydrofracture would transport water rapidly to the source region then the water and the large ion lithophile elements contents will not have time to interact with the mantle wedge (Davies, 1999).

I am going to focus on channelized flow as the water transport mechanism from the slab; in particular I will use the hydraulic fracture hypothesis by Davies (1999). This hypothesis is that high pore pressure provided by non percolating water causes faulting and that this faulting will interconnect the pores. A hydraulic fracture occurs when a sufficient amount of water is interconnected, transporting water out into the mantle wedge.

For intermediate earthquakes to be produced in dry faults at depths, rock would need to overcome high frictional stresses so would need to be unreasonably strong. Due to the presence of non-percolating water in subducting slabs, the pore pressure is increased and the effective normal stress and frictional stress are reduced. This can facilitate intermediate depth earthquakes (Green and Houston, 1995). Davies (1999) suggested that in the slab, water would be subjected to high pressure by ductile creep of the rock. The isolated pockets of water will nucleate micro-cracks which are held open by the water. Thus when an earthquake occurs the micro-cracks filled with water will interconnect. He then suggests that if a large intermediate depth earthquake occurs, enough water would be able to interconnect to cause a hydraulic fracture. It should be noted that hydraulic fractures cannot explain intermediate depth earthquakes themselves as the earthquakes show no isotropic component (Frohlich, 1989). Davies (1999) hypothesises that the initial volume of water will affect the distance the fracture propagates. The smallest hydraulic fractures may not leave the subducted slab or the sediments. Intermediate and large hydraulic fractures will reach the mantle wedge with the large fractures reaching the source region of the mantle wedge.

1.3.2.1 Direction of Propagation of Fractures

In Davies (1999) and Davies and Stevenson (1992), the fracture propagation direction is controlled by the principal stresses. The hydraulic fracture will widen in the direction of the least compressive stress and will propagate perpendicular to the least compressive stress. The hydraulic fractures near the subducting slab will propagate out away from the wedge corner.

Dahm (2000) modelled the growth and propagation of fluid filled fractures. He concluded that the propagation direction is controlled by other factors as well as the principal stresses. He discovered that tectonic stress gradients, apparent buoyancy forces and the length of the fracture all have an effect on the fracture growth and propagation. He also found for a water filled fracture, the fracture path would be away from the wedge corner, similar to Davies and Stevenson (1992). Dahm (2000) discovered that the water filled fractures would often not propagate a large distance in the wedge, and showed the lower part of the mantle wedge had the potential to halt the fracture propagation.

1.3.3 Global Water Flux to and from the Subducting Slab

Estimating the water flux from a subduction zone is difficult and there have been many different estimates of the input and output flux of water from a subduction zone. Some of these values have been summarised in Table 3.2.

An early estimate was by Peacock (1990) for water bound in the subducting sediment of 0.7×10^8 Tg Myr^{-1} and in igneous crust of 8×10^8 Tg Myr^{-1}. Bebout (1995) calculated a bound water flux of $0.3 \times 10^8 - 1.4 \times 10^8$ Tg Myr^{-1} for sediment and $9 \times 10^8 - 18 \times 10^8$ Tg Myr^{-1} for igneous crust, by bulk rock analysis of high pressure meta-sedimentary rocks. Jarrard (2003) improved the estimate of water bound in the igneous crust by using an age based alteration model. This gave an estimate of 1.2×10^8 Tg Myr^{-1} of water bound in the sediment and 6×10^8 Tg Myr^{-1} in the igneous crust. Schmidt and Poli (2003) updated their earlier model (Schmidt and Poli, 1998). They assumed that subducted slabs consisted of

2 km water saturated basalt, 5 km of partially hydrated gabbro and 5 km of serpentinized mantle. This led to an estimate of $4.9 \times 10^8 - 8.6 \times 10^8$ Tg Myr^{-1} of water bound in the mantle. Rüpke et al. (2004) assumed subduction of sediment with 1.6×10^8 Tg Myr^{-1} bound water, igneous rock with 4.6×10^8 Tg Myr^{-1} water and serpentinized mantle with $2.4 \times 10^8 - 12 \times 10^8$ Tg Myr^{-1}. This led to an estimate of $9 \times 10^8 - 18 \times 10^8$ Tg Myr^{-1} of total water bound during subduction. Hacker (2008) calculated phase diagrams for a range of bulk compositions and merged these calculations with global subduction zone rock fluxes. They estimated 1.5×10^8 Tg Myr^{-1} water bound in the sediment, 6.1×10^8 Tg Myr^{-1} was in the igneous crust and 5.7×10^8 Tg Myr^{-1} was in the mantle. van Keken et al. (2011) used the global compilation of thermal structure of subduction zone by Syracuse et al. (2010) to predict the global water flux. They predicted that water of 0.7×10^8 Tg Myr^{-1} was bound in the sediment and 6.3×10^8 Tg Myr^{-1} was in the igneous crust. If they assumed serpentinization of the upper mantle then that contained 3×10^8 Tg Myr^{-1} of water.

Schmidt and Poli (2003) and van Keken et al. (2011) also predicted the global flux of water output from subduction zones. Schmidt and Poli (2003) estimated water loss of $4.8 \times 10^8 - 7.5 \times 10^8$ Tg Myr^{-1} down to 100 km depth, $1.8 \times 10^8 - 8 \times 10^8$ Tg Myr^{-1} water loss between 100 - 150 km depth, $1.6 \times 10^8 - 3.6 \times 10^8$ Tg Myr^{-1} loss between 150 - 230 km and that $0 - 10 \times 10^8$ Tg Myr^{-1} would be released past 230 km. van Keken et al. (2011) estimates were within the range set by Schmidt and Poli (2003) of water loss measuring 3.2×10^8 Tg Myr^{-1} down to 100 km, 1.4×10^8 Tg Myr^{-1} between 100 and 150 km, 2×10^8 Tg Myr^{-1} between 150 and 230 km and 3.4×10^8 Tg Myr^{-1} past 230 km for the case with serpentinized mantle.

1.4 Melting Processes Within Subduction Zones

It is commonly assumed that fluid fluxed melting occurs in subduction zones. The high U/Th ratios commonly found in subduction zone regions that indicate fluid addition, support

	P90	B95	J03	SP03	R04	H08	VK11 ws	VK11 w/os
Subduction zone H_2O input								
Sediment	0.7	0.3-1.4	1.2		1.6	1.5	0.7	0.7
Igneous crust	8	9-18	6		4.6	6.1	6.3	6.3
Mantle				4.9-8.6	2.4-12	5.7	3.0	0
Total input	8.7	9-19		9-12	9-18	13	10.0	7
Slab H_2O output to wedge								
$<$100 km depth				4.8-7.5			3.2	3.2
100-150 km				1.8-8.0			1.4	3.2
150-230 km				1.6-3.6			2.0	0.6
$>$230 km				0-10			3.4	2.2

Table 1.1 Estimates of global subduction zone water flux in 10^8 Tg/Myr. P90, Peacock (1990); B95, Bebout (1995); J03, Jarrard (2003); SP03, Schmidt and Poli (2003); R04, Rüpke et al. (2004); H08, Hacker (2008); VK11, van Keken et al. (2011); w s, with 2 km serpentinized upper mantle (2 wt %); w/o s, without serpentinized upper mantle. Table reproduced from van Keken et al. (2011).

this theory. Another melting process that is thought to occur in subduction zone regions is decompression melting. Many studies have linked decompression melting to back arc spreading regimes as they provide a similar environment to mid ocean ridges where decompression melting occurs (Kelley et al., 2006; Langmuir et al., 2006), whereas others suggest it can occur after fluid fluxed melting (Pearce et al., 1995). A common theory is that a combination of fluid fluxed melting and decompression melting occurs in subduction zone regions (Caulfield et al., 2012; Jagoutz et al., 2011; Kelley et al., 2006). From lava samples from arc regions plotting Ba against Yb is used as a way of discriminating between the fluid flux melting and the decompression melting regimes (Caulfield et al., 2012; Peate et al., 2001). During decompression melting, as the melting increases, the concentration of highly incompatible Ba and mildly incompatible element Yb decreases. On the other hand, during fluid fluxed melting the addition of fluid increases Ba. The increase in melting due to fluid addition also dilutes the concentration of fluid immobile elements like Yb. Therefore fluid fluxed melting should show a negative Ba-Yb trend and decompression melting will result in a positive Ba-Yb trend (Caulfield et al., 2012). In the Tonga arc, lavas from the

Valu Fa Ridge and the Fonualei Spreading Centre plot a negative Ba-Yb trend indicating a fluid fluxed melting. Further west from the trench lavas sampled from the Central and Eastern Spreading Centres plot a positive Ba-Yb trend which suggest decompression melting (Caulfield et al., 2012; Peate et al., 2001). For the Tonga arc there appears to be a progression from fluid fluxed melting to decompression melting as distance progresses from the trench.

Bourdon et al. (2003) had several possible melting scenarios for a subduction zone region. The first would be instantaneous addition of fluid causing a 'flash melting' scenario. This could be modelled with a batch melting model such as Katz et al. (2003). The second scenario was flux melting over a range of depths, followed by fast melt migration to the surface. Another melting scenario was flux melting, followed by decompression melting. There are other melt scenarios such as decompression melting of hydrated sediments as suggested by Behn et al. (2011) or plumes developing from the slab (Gerya and Yuen, 2003; Hall and Kincaid, 2001).

1.4.1 General Wet Melting Parameterisation

Katz et al. (2003) developed a hydrous melting parameterisation of the form $F = f(P,T,X_{H_2O},M_{cpx})$, where F is the melt fraction, P is the pressure in GPa, T is the temperature in °C, X_{H_2O} is the water content of the melt in wt% and M_{cpx} is the modal clinopyroxene of the residual (unmelted) peridotite. They start by parameterising a dry melting scenario, then expanded it to include wet melting. This is done by calculating the temperature decrease in the solidus due to a water content in the melt $\Delta T(X_{H_2O})$. Katz et al. (2003) treat water as a trace element, this allows the equilibrium partitioning between solid and silicate melt to be modelled with a bulk distribution coefficient D_{H_2O}. They chose to use a constant D_{H_2O} value for their parameterisation in order to preserve its simplicity. However they recognise that D_{H_2O} would possibly vary with pressure. Katz et al. (2003) calibrated both the anhydrous and hydrous melting parametrisations from experimental data. When calibrating the hydrous melting

there was no experimental data for pressures above 2 GPa. This meant Katz et al. (2003) had to extrapolate the water saturation curve from low pressures, this leads to ambiguity in water saturation values at high pressures. However Katz et al. (2003) concluded that to account for greater variability would require a more complex model. They concluded that their parameterisation contained the appropriate level of detail to strike a balance between accuracy and efficiency.

1.4.2 Flux Melting parameterisation

There has been two main hydrous flux melting parameterisations; Grove et al. (2006) and Davies and Bickle (1991).

Grove et al. (2006) developed a simple flux melting parameterisation, using the vapour saturated phase relations for peridotite as a starting point. Their model assumes the first melt is vapour saturated and will occur everywhere above the slab where the temperature exceeds the vapour saturated solidus. After the initial melt occurs and starts to ascend, melting will continue but now at water under-saturated conditions. They approximate a relationship between melt water content X_{H_2O}, temperature T and pressure P based on the thermodynamic models by Silver and Stolper (1985) for simple silicate -water binary systems. For the initial melting a high water content of the vapour saturated solidus is assumed of $\sim$ 30 wt% water and a low initial melt fraction is assumed. Grove et al. (2006) in their calculations chose an initial melt fraction of 2.5 wt% as that yielded final melt fractions comparable to observations by Grove et al. (2002). Grove et al. (2006) assume the melt ascends by reactive porous flow and also a closed system for the water, so that no water is lost to the surrounding mantle. Heat can be exchanged between the melt and the surrounding mantle.

Grove et al. (2006) intended for this model to explore the general melting trend due to flux melting and state it is a simplified model. There are several assumptions they made about the model that would need to be resolved, in order for the model to be used for less

generalised results. Firstly they assume initial melting can only occur at the vapour saturated solidus whereas Katz et al. (2003) suggests this not the case. Katz et al. (2003) state that requiring water saturation at the solidus is equivalent to insisting on the saturation of a rare earth element phase at the solidus. That can only take place if the amount that can be taken into the solution by solid phases is exceeded by the concentration in the element phase. They also state that partition coefficients can be used instead. This way the initial X_{H_2O} will be calculated using a bulk partitioning coefficient so does not have to be saturated. Grove et al. (2006) also chose an initial melt fraction based on the reasoning it would give final melt fractions that matched previous observations. It would be better to calculate the initial melt fraction using a melting parameterisation such as Katz et al. (2003). Grove et al. (2006) make no attempt to quantify the bulk water content that is released by the slab which is another reason why they have to assume the initial melt fraction, as the bulk water content is required in most melting parameterisation to calculate the initial melt i.e (Katz et al., 2003; Kelley et al., 2010).

Davies and Bickle (1991) also developed a model for flux melting in a subduction zone. Similar to Katz et al. (2003), Davies and Bickle (1991) started with a dry melting parameterisation, in this case by McKenzie and Bickle (1988), and expanded it to include hydrous melting. They stated the main controls on the amount of melting was the relationship between the temperature of the melt, water content and melt fraction. They approximated this relationship by modelling a 1D column of partial melt rising into hotter mantle. Into the side of the column flows unmelted dry mantle . This dry mantle melts by reacting with any excess water flowing up the column and the wet magma. A temperature drop will occur due to the latent heat of melting. This cooler residual (partially melted) mantle will then leave the melt region. From the conservation of energy Davies and Bickle (1991) calculated the degree of melting. They did this by balancing the heat advected into the melt region with the

latent heat of melting. In order for Davies and Bickle (1991) to do this they calculated the weight fraction of peridotite that melts as a function of water content and temperature.

Davies and Bickle (1991) make the same assumptions as Grove et al. (2006) that there will be a closed system for water and they also assume the melt is in thermal equilibrium with the surrounding mantle. Davies and Bickle (1991) also make assumptions specific to their 1D melting column such as assuming steady state with a constant water flux up the column. They also chose to ignore the conduction of heat up the column and the advection of heat by the melt, which they state can be shown a posteriori to be reasonable. Even though Davies and Bickle (1991) say their parameterisation is a simple model it is more complex than the model by Grove et al. (2006). They also do not make the assumption that the initial melt has to be water saturated. The model by Davies and Bickle (1991) allows for the calculation of the initial melt due to the initial water flux into the source region, unlike Grove et al. (2006) who assumed the initial melt water content and initial melt fraction.

1.4.3 Adiabatic Decompression Melting Parameterisation

McKenzie (1984) parameterised dry adiabatic decompression melting. He assumed there would be no movement between the melt and the solid matrix and the partial melt would rise towards the surface with constant entropy. When the solid material rises and reaches the solidus it will start to melt, as it continues to rise to decreasing pressures the melting increases. Katz et al. (2003) took the McKenzie (1984) dry melting parameterisation and extended it to include wet adiabatic decompression melting. The addition of water causes the melting to start at lower depths compared to dry adiabatic melting.

The parameterisation by McKenzie (1984) does not account for variation in partial specific entropies as a function of F (Asimow et al., 1997). It was demonstrated by Hirschmann et al. (1999) that the effect of partial specific entropy variations may be significant just above the

solidus. However Katz et al. (2003) had no way of estimating partial specific entropies so they chose to use the simplified parameterisation by McKenzie (1984).

1.5 Observations from Arcs

1.5.1 Water content in the melt

Quantifying the water content in the melt has been an ongoing challenge, as near complete degassing of magmas occurs during ascent, eruption and cooling. Magmas trapped inside crystals do not degas and retain their water contents. Examining these melt inclusions and experimental phase equilibria are the main methods used to determine the pre-eruption volatile contents of magma (Plank et al., 2013). In the mid 90s these analytical methods were used on melt inclusions and submarine glasses from subduction zones magmas, by a series of studies (Roggensack et al., 1997; Sisson and Layne, 1993; Stolper and Newman, 1994). These studies demonstrated that magmas originating from subduction zones are wet, with water contents being at least 2 wt% and up to 6 wt % in more evolved basalts. In some parental arc magmas complementary phase equilibria studies supported very high water contents of 6-16 wt% Carmichael (2002); Grove et al. (2003). As magmas lose water to degassing as they ascend, only melt inclusions trapped within crystals that are cooled rapidly at the surface have a chance of retaining their original water concentration. Olivine is the preferred choice to trap the melt inclusion, as in arc basaltic magmas it is one of the first minerals to crystallise. Also olivine only contains minor concentrations of incompatible elements that could exchange with the melt inclusion. Some minimal degassing may still occur, so the maximum water content is generally taken as the minimum for the primary water content in the magma (Plank et al., 2013).

Various approaches have been implemented to infer primary water contents in magmas. Some studies such as Kelley et al. (2010) screen melt inclusions based on S or CO_2 thresholds.

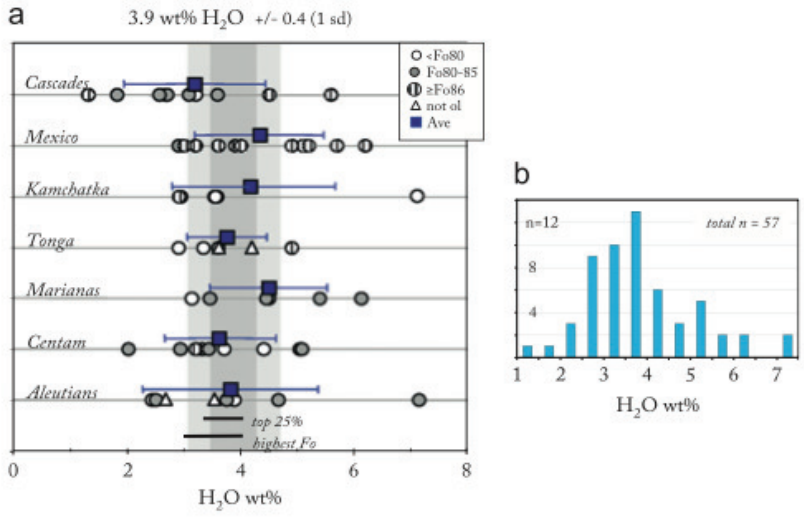

Fig. 1.4 (a) water content in melt inclusions from 7 volcanic arcs. Blue boxes are the average water content for each arc. The grey vertical bar is the average of all the arcs (dark grey is 1 sd, light grey is 2 sd). (b) Histogram of maximum water contents in each volcano. Taken from Plank et al. (2013).

The simplest method is to select the maximum H_2O/K_2O ratio or H_2O concentration recorded in the melt inclusion as representative of the parental magma (Johnson et al., 2010; Zimmer et al., 2010). Using this method Plank et al. (2013) gathered results from nearly 60 volcanoes for melt inclusions mainly hosted in olivine. They found that the water content values from the volcanoes plotted at each arc, resulted in similar averages and a narrow range as shown in Figure 1.4a. Most of the results were between 2-6 wt% H_2O. Nearly all of the arc volcanoes had a higher water content than MORB, BABB or OIB which are typically ≤ 2 wt% (Zimmer et al., 2010). Comparing the averages of each arc shows an even narrower range from 3.2 for the Cascades to 4.5 for the Marianas, this gives a global average of 3.9 ± 0.4 wt% H_2O. This average was calculated from the maximum water concentration at each volcano which was then averaged for each arc. The histogram in Figure 1.4b reflects a strong peak at $\sim 3-4$ wt% showing the ~ 4 wt% average is not an artefact of averaging end members between 2-6% (Plank et al., 2013).

Even though the global average is ~ 4 wt% and the overall range is narrow, individual volcanoes could register higher water contents. Carmichael (2002) proposed a water content of 10 wt% for the Mexican volcanic belt and water contents of 10-14 wt% were proposed for the Mt Shasta volcano (Grove et al., 2003; Krawczynski et al., 2012).

1.5.2 Melt Fraction

The melt fraction F is determined from the elements that are assumed to be conservative and are not added to the source with the water. High-field-strength-elements (HFSE), Hf,Nb,Ti,Y and Zr are thought to be insoluble in fluids and therefore reflect the melt fraction and initial source composition (Pearce and Parkinson, 1993). If the source concentration and partition coefficients are known for the elements, then F can be determined using the batch melting equation (Langmuir et al., 2006). Kelley et al. (2006) used TiO_2 as their incompatible element as its overall low abundance in arc lavas suggests it was not added with the fluid. They solved for F using the batch melting equation (1.1):

$$F = \frac{\left(\frac{C^o_{Ti}}{C^l_{Ti}}\right) - D_{Ti}}{(1 - D_{Ti})} \tag{1.1}$$

where C^o_{Ti} is the concentration of TiO_2 in the mantle source, C^l_{Ti} is the concentration of TiO_2 in the melt and D_{Ti} is the bulk distribution coefficient for Ti during mantle melting. Melt fractions vary in and between subduction zones and have a positive correlation with the initial water content (Kelley et al., 2006). Some estimates of melt fractions from subduction zones are 0.05-0.14 for the Kamchatka and Northern Kurile Arc (Portnyagin et al., 2007) and 0.05-0.25 for the Mariana Arc (Kelley et al., 2010, 2006; Langmuir et al., 2006).

1.5.3 Magma Productivity Rate

Magma production is highly variable between subduction zones. The magma production rate can be estimated based on the hypothesis that arc crust is formed due to magmatism, then the growth rates of the arc crust can be inferred from gravity and seismic studies (Dimalanta et al., 2002; Hochstein, 1995; Taira et al., 1998). The estimated magma production rate is dependent on the inferred width and thickness of the crust across the arc. Another method to estimate magma productivity rate is to consider the long term volumetric output rate from a volcano or length of volcanic arc (Wada and Wang, 2009; White et al., 2006). For the 17 subduction zone regions Wada and Wang (2009) chose to study the volcanic output rate varied from 24 km^3Myr^{-1} to 11000 ± 1000 km^3Myr^{-1}.

1.5.4 Melt Temperature and Pressure

The temperature and pressure of primary melts in the mantle wedge can be quantified using thermobarometric information, which is recorded by mineral-melt equilibria and melt composition (Kelley et al., 2010). Lee et al. (2009) quantified in a thermobarometer the effects of temperature on MgO content, and the pressure on SiO_2 content, of the mantle melts that were olivine and orthopyroxene saturated. This model was used by Kelley et al. (2010) to examine the P-T melting conditions of the Mariana Arc and Trough. The wet Mariana Trough melts record temperature T($\sim 1250 \pm \sim 40^\circ$C) at $\sim$1 GPa. The Mariana Arc had a wider range of pressure and temperatures, P($1.0 - 2.4 \pm 0.2$ GPa) and T($\sim 1200 - 1400 \pm \sim 40^\circ$C) indicating hotter deeper melting occurs beneath the Mariana arc than the back arc at the Mariana Trough. Kohut et al. (2006) used several geothermometers to estimate the average magmatic temperature at the Mariana Arc as $\sim 1367^\circ$ at 1-1.5 GPa, which falls in the range suggested by Kelley et al. (2010). Other studies such as Portnyagin et al. (2007) calculate the water content in the source and the melt fraction from the melt compositions, then use a

hydrous melting parameterisation such as Katz et al. (2003) to estimate the P-T conditions of the melt.

1.5.5 Location of the Volcanic Arc

The long held view of the location of volcanic arcs is that they occur where the depth to the top of the slab is $\sim 120 \pm 40$ km (Gill, 1981; Tatsumi and Eggins, 1995). As this range is quite narrow this implies that a process in either the generation or transport of the magma has a similar range. Several processes have been suggested to explain this focussing. Schmidt and Poli (1998) suggested volcanic arcs are located above places where the melt fraction in the wedge becomes high enough for segregation of the melt to occur. Others suggest strongly pressure dependent reactions that release fluid from the slab control the location (Gill, 1981; Tatsumi and Eggins, 1995), whilst others suggest the reactions are temperature dependent (Grove et al., 2009; Ulmer and Trommsdorff, 1995). A recent theory by England and Katz (2010a) is that volcanic arcs are located above the place where the anhydrous solidus makes it closest approach to the trench.

The global earthquake hypocentral locations by Engdahl et al. (1998) shows that along individual sections of arc, the depths to the top of the slab is constant to a few kilometres. However between different sections of volcanic arc the depth varies from 80 to 160 km (England et al., 2004; Syracuse and Abers, 2006). This variation in depth rules out the hypothesis of the depth to the slab corresponding to a single pressure dependent reaction (Gill, 1981; Tatsumi and Eggins, 1995). Another hypothesis that England and Katz (2010a) state can be discounted is the location of the arc is determined by a temperature dependent reaction (Grove et al., 2009; Ulmer and Trommsdorff, 1995). This is due to the isotherms near the slab being almost parallel, therefore a temperature will be found over a large range of pressures. This means temperature dependent reactions must occur over a range of down dip distances and will not be sharply localised (England and Katz, 2010b). In the core of the

mantle wedge the steep lateral thermal gradients provide a setting for the localisation of a temperature dependent process. In the theory by England and Katz (2010a), magma formed at temperatures above the anhydrous solidus are focussed towards the trench, to the 'nose' of the region which is bound by the solidus. Thermal erosion by the rising magma above the 'nose' makes a pathway to the arc volcanoes for the magma. This hypothesis by England and Katz (2010a) provides the best theory currently for the location of arc volcanoes as other hypotheses have been discounted.

1.6 Modelling Subduction Zones

Modelling subduction zones spans over four decades, starting with the first geodynamic modelling paper by Minear and Toksöz (1970). Subduction models cover a range of themes such as; the thermal structure of a subduction zone, subduction initiation, crustal growth and magmatic arc development, slab break off and fluid and melt transport etc. (Gerya, 2011). Due to the wide range and extensive subduction modelling literature, I will briefly describe some of the major papers particularly associated with thermal modelling and transport of fluid and melt in subduction zones.

Davies and Stevenson (1992) was one of the first to clarify the significance of water propagation in the mantle wedge. In their subduction zone model the plates were prescribed by a kinematic boundary condition inducing a cornerflow in the mantle wedge, allowing a steady state thermal field to be evaluated. They proposed a lateral transport of water across the mantle wedge by a vertical motion of water in a free phase, followed by the transport of a hydrous phase, such as amphibole by the mantle wedge flow. This lateral movement would occur until water reached the amphibole solidus triggering melting.

Iwamori (1998) was the first to create a numerical subduction model that included dehydration, mantle hydration, water transport and melting. He assumed the aqueous fluid would migrate by porous flow and have chemical interaction with the mantle wedge, which

included melting reactions. There was two main suggestions from the model. The first was a serpentinite-chlorite layer forming just above the slab due to aqueous fluid release, the second is that most of the water is subducted in the serpentinite layer until a depth where the serpentine and chlorite in the layer start to break down. He found similarly to Davies and Stevenson (1992) that the melt and aqueous fluid generally do not have vertical migration to the volcanic front.

Gerya and Yuen (2003) took into account mantle hydration and melting due to fluid release from the slab and developed a 2D model of thermal-chemical convection. They demonstrated that Rayleigh-Taylor instabilities can develop at the cold surface of the slab due to hydration and partial melting. This led to 'cold plumes' where diapirs colder than the surrounding mantle by 300-400 °C were driven upwards due to compositional buoyancy. The 'cold plumes' had a velocity in excess of 10 cm yr^{-1} and were able to ascend into the hotter region of the mantle wedge, cooling the surrounding mantle, within a couple million years.

Cagnioncle et al. (2007) used a 2D model that included solid mantle flow, buoyant migration of fluid and melting to investigate the distribution of fluid and melt in the wedge. They found that hydrous fluid is deflected from its vertical migration by solid flow in the wedge. This causes the melting not to occur vertically above the region of fluid release, which matches the conclusion from Iwamori (1998). They discovered a melting front occurs where the mantle is hot enough to melt due to the addition of hydrous fluid. The melt fraction and production rate increase with increased convergence rate and grain size. This is due to increased melting front temperatures and water contents reaching the melting region.

Van Keken et al. (2008) developed a suite of benchmarks for the dynamics and thermal structure of subduction zones. They proposed several cases to investigate the influence of rheology and boundary conditions on the wedge flow and subsequent thermal field. They used a thermomechanic approach where the slab is prescribed kinematically and the wedge flow is computed dynamically. They explore consequences of an isoviscous wedge with the

first case having a analytic cornerflow solution (Batchelor, 1967; McKenzie, 1969). The next two cases solve for the wedge flow numerically and investigate the boundary conditions for the wedge inflow and outflow. The last set of cases examine the effect of a stress dependent rheology and more realistic temperature in the wedge.

1.6.1 Types of Subduction Model

There are two common types of subduction model; simple and complex. Simple models use simplified numerical setups in an attempt to isolate the influence of a small number of parameters on subduction processes. Some of these simplifications are; models with uniformly dipping slabs that are kinematically prescribed and steady state, a constant subduction velocity and an assumption of a free slip or no slip upper surface etc. The mantle properties are also simplified to include; no compositional buoyancy, no phase transitions, constant thermal conductivity, simple viscous rheology etc. These models are easier to investigate systematically as they have a limited parameter space. The downside to simple models is the results obtained may not be comparable with nature as over simplification may cause some essential subduction zone physics to be lost (Gerya, 2011).

Complex models take into account the widest range of possibilities relevant to subduction zones so the models can be more realistic. More complex models will consider and include; spontaneous subduction rather than kinematically driven, free erosion and sedimentation, use experimentally based flow laws to use complex viscoplastic rheologies, phase transformations and transport of fluid and melt etc. Complex models will produce more realistic subduction models, however it is difficult to isolate the influence of individual parameters as the parameter space is so large. Minimal complexity models also exist that are between simple and complex models. They try to be simple enough to be investigated systematically but are also realistic enough to be applicable to nature (Gerya, 2011).

1.7 Aim and Overview

The hypothesis by Davies (1999) is that hydraulic fractures can transport water from the slab to the mantle wedge. The theory is that the largest hydraulic fractures would transport water to the source region and cause melting. This thesis is going to examine the hypothesis that large hydraulic fractures can transport sufficient water to cause melting in the mantle wedge. This instantaneous addition of water will cause instant melting or 'flash melting'. After the initial flash melting four scenarios will be examined. The first, covered in Chapter 3 is the flash melting followed by rapid melt transport to the surface. The second is the melt will rise to the point of maximum temperature in the wedge whilst undergoing hydrous flux melting, then it will be transported rapidly to the surface. The third will examine the theory by Pearce et al. (1995) that hydrous decompression melting can occur after initial wet melting. The final scenario will combine the three melting processes so there will be flash melting followed by hydrous flux melting and then decompression melting. These four cases will all have rapid migration, so a final case will examine melting on a slower time scale, by having the partial melt rise due to the addition of buoyancy whilst undergoing decompression melting.

The first step is to create a thermal model of a subduction zone. The model will have the same boundary conditions and set up as the thermal subduction zone benchmark by Van Keken et al. (2008), to allow comparison of the model with the benchmark. A finite difference, marker -in-cell code that solves for the heat equation will be used from the book by Gerya (2010). This code will be adapted for a subduction zone set up. The markers will allow tracking of different compositions such as water and partial melt. After the thermal model, melting models for the three different melting types will be built. For the flash melting, the hydrous mantle melting parameterisation by Katz et al. (2003) will be used. The hydrous flux melting will be modelled using the method by Davies and Bickle (1991), and

the decompression melting will use the Katz et al. (2003) method. For the initial cases the wedge velocity field will be found using the analytical cornerflow solution (Batchelor, 1967; McKenzie, 1969). For the final case with buoyancy, the wedge velocity field will be solved numerically using Stokes Flow. The initial water content added to the mantle wedge will be varied by changing the fracture size and the radius of the source region it is added to. This will allow for examination of the impact of the initial water content on the melting. Outputs from the models will include; melt fraction, melt productivity rate, melt temperature, water content in the melt and location of the melting. These can all be compared to petrological data to test the hypothesis.

1.8 Thesis Structure

This thesis comprises of eight chapters. This chapter has provided some background and discussed the aim and overview of the thesis. Chapter 2 describes the method for building the thermal model of a subduction zone. The thermal model is then compared to the benchmark by Van Keken et al. (2008). Chapter 3 models flash melting and investigates varying initial water content. The results are compared to petrological data. Chapter 4 examines flash melting followed by hydrous flux melting for different initial water contents. Chapter 5 models flash melting followed by decompression melting and flash melting then flux melting followed by decompression melting. Chapter 6 adds buoyancy into the model. The velocity field is computed using Stokes Flow. This chapter examines flash melting followed by decompression melting, where the partial melt region rises due to buoyancy for two initial water contents. Chapter 7 is a discussion chapter that compares the results from all the models against each other and petrological data, the limitations of the models are also discussed. The final chapter is a summary of the thesis and possible future work.

CHAPTER 2

SUBDUCTION ZONE THERMAL MODEL

2.1 Introduction

The previous chapter discussed the aim and overview of this thesis and also provided some background into subduction zone magmatism and water in subduction zones. The aim of this PhD is to develop and build a computer model that will model subduction zone magmatism due to water being added to the mantle wedge via a hydraulic fracture. The first step is to create a thermal model for a subduction zone. As the intention was to track water and melt in the mantle wedge I decided to use the marker-in-cell technique as used by Taras Gerya e.g. (Gerya and Yuen, 2003). The marker-in-cell techniques will allow the tracking of different compositions within the model and also allows for greater resolution. Once my thermal model has been built I will test it by comparing it to a subduction zone thermal benchmark (Van Keken et al., 2008). This chapter has eight sections. The second section lists the variables and arrays used in the computer model and section three discusses the model set up. The fourth section describes every step of the model process. Section five introduces the subduction zone thermal benchmark by Van Keken et al. (2008) and discusses their results. Sections six and seven are the thermal model results, comparison with the benchmark and

discussion of the reuslts. Finally section eight is a summary of the chapter and introduces the next chapter.

2.2 Variables used in the code

Below is a table of the variables and arrays used in my code. All the model set up parameters such as; horizontal and vertical grid sizes, depth of the overriding plate, slab velocity, dip, initial background and surface temperatures and background density, heat capacity, thermal conductivity and thermal diffusivity use values from Van Keken et al. (2008). Van Keken et al. (2008) is a subduction zone thermal benchmark, by using the same initial set up and model parameters, I will be able to directly compare my thermal model results to the benchmark results.

Parameter	Standard Value	Description
dip	$\pi/4$	dip of the slab in radians
angle	45 $^\circ$	dip of the slab in degrees
U	1.5×10^{-9}	slab velocity [m s^{-1}]
xsize	6.6×10^{5}	horizontal grid size [m]
ysize	6×10^{5}	vertical grid size [m]
xnum	111	number of nodes in horizontal direction
ynum	101	number of nodes in vertical direction
xstp (Δx)	6000	grid step in horizontal direction [m]
ystp (Δy)	6000	grid step in vertical direction [m]
tnum	1000	number of time steps
t50	1.5768×10^{15}	age of oceanic plate [s]
tback (T_b)	1573	initial background temperature [K]
tsurf (T_s)	273	initial surface temperature [K]
MRHO(1)	3300	background medium density [kg m^{-3}]

Parameter	Standard Value	Description
MCP(1)	1250	background medium heat capacity [J kg^{-1} K^{-1}]
MKT(1)	3	background medium thermal conductivity [W m^{-1} K^{-1}]
dsubgridt	1	subgrid diffusion coefficient
corner	0	position of corner of slab at surface [m]
over_plate_y	50	depth of overriding plate [km]
corner_x	50	horizontal position of corner of overriding plate at 50 km depth [km]
xslabmax	600	maximum horizontal position for slab [km]
kappa (κ)	7.2727×10^{-7}	maximum thermal diffusivity [m^2 s_{-1}]
timestep (t)	2.8284×10^{12}	timestep [s]
mxnum	660	total number of markers in the horizontal direction
mynum	600	total number of markers in the vertical direction
mxstep (Δx_m)	1000	step between markers in the horizontal direction
mystep (Δy_m)	1000	step between markers in the vertical direction
marknum	396000	total number of markers

Array	Description
gridx	horizontal nodal point positions
gridy	vertical nodal point positions
xslab	horizontal points on slab
yslab	vertical points on slab
vx	horizontal component of velocity [m s^{-1}]
vy	vertical component of velocity [m s^{-1}]
theta	angle in radians
v_theta	v_θ
v_r	v_r
MX	marker x coordinate [m]
MY	marker y coordinate [m]
MI	marker type
MTK	marker temperature
rho (ρ)	density at the nodes
tk1 (T)	temperature at the nodes
kt	thermal conductivity
cp (Cp)	heat capacity
ntimestep	number of time steps
wtnodes ($w_{m(i,j)}$)	weight of the nodes
mm1	number of markers
xn	horizontal index for upper left node in cell where marker is
yn	vertical index for upper left node in cell where marker is
dx	normalised horizontal distance from marker to the upper left node
dy	normalised vertical distance from marker to the upper right node
MRHOCUR	material density from marker type

Array	Description
MCPCUR	material heat capacity from marker type
MKTCUR	material thermal conductivity from marker type
L	Matrix of coefficients for implicit matrix solving
R	Right hand side for implicit matrix solving
k	global index
S	solution of matrix
tk2	new temperature after matrix solution
dtk1	temperature change
dtkn	subgrid temperature changes
dtkm	nodal-marker subgrid temperature difference
ktm	thermal conductivity at the marker interpolated from the nodes
rhocpm	density $\rho \times C_p$ at the marker interpolated from the nodes
tdm	local thermal diffusion timescale for the marker
sdif	subgrid diffusion
vxm	horizontal component of velocity for marker
vym	vertical component of velocity for marker

2.3 Model set up

The thermal model is adapted from a finite difference, marker-in-cell code to solve the heat equation by Gerya (2010). To adapt it for a subduction zone setting I changed the model size, boundary conditions, recycling method and added in a velocity field.

2.3.1 Finite Difference Method

Partial differential equations (PDEs) can be solved by two methods: analytical and numerical. In my subduction zone thermal model I use both methods; the velocity field is solved analytically and the heat equation is solved numerically. To solve the heat equation numerically I use a first order finite difference method, which represents derivatives using linear mathematical expressions. For example the gradient $\frac{\partial y}{\partial x}$ can be calculated, to a degree of accuracy depending on the spacing, as follows

$$\frac{\partial y}{\partial x} = \frac{\Delta y}{\Delta x} = \frac{y_2 - y_1}{x_2 - x_1} \tag{2.1}$$

where $\Delta y = y_2 - y_1$ and $\Delta x = x_2 - x_1$ are the differences between the y coordinate and x coordinates between points 1 and 2. The smaller the spacing Δ between the points the more accurate the calculation. In my model I use a grid of points with a constant spacing. By decreasing the spacing I can increase the accuracy of the calculations but it is computationally more expensive. I have to find a balance between accuracy and the time it will take for the model to run. This grid represents the distribution of the variables used in space and time. There are two types of numerical grid points: Eulerian and Lagrangian. An Eulerian grid is fixed and does not deform. A Lagrangian grid deforms as the medium deforms and the Lagrangian points move with the local flow. Eulerian grids have the advantage of being fixed so the grid geometry does not change over the model runtime. However it is necessary to

take account of advection which can cause problems numerically such as numerical diffusion. A Lagrangian grid however can account for advection as it deforms as the model deforms. As a Lagrangian grid deforms this means the grid could ultimately need regridding due to the deformation. In this model a combination of an Eulerian grid with Lagrangian points is used.

Finite differences allows us to transform partial differential equations PDEs by approximating derivatives. PDEs can be applied to every point of a continuum which is an infinite number of points. By transforming them into a series of equations applied to fixed number of grid points Gerya (2010) set out the steps for applying finite difference as follows:

1. Replacing an infinite number of points with a finite number of grid points
2. At these points the physical properties are defined,
3. Substituting PDEs by linear equations which are defined by finite differences. The physical properties defined at the grid points are related via the linear equations
4. Solve the linear equations to obtain the unknown values for the grid points.

2.3.2 Code structure

The computer code to calculate the thermal structure of a subduction zone has been separated into 10 sections as shown in Figure 2.1. Each of these sections is a different process involved in solving the temperature equation. The first 3 sections of the code take place outside of the time loop, as they are all things that do not need to be calculated at every time step, so this reduces the computing time required. Sections 4 - 10 take place over a time loop that runs for a set number of time steps. The following sections describes each process on the flow chart.

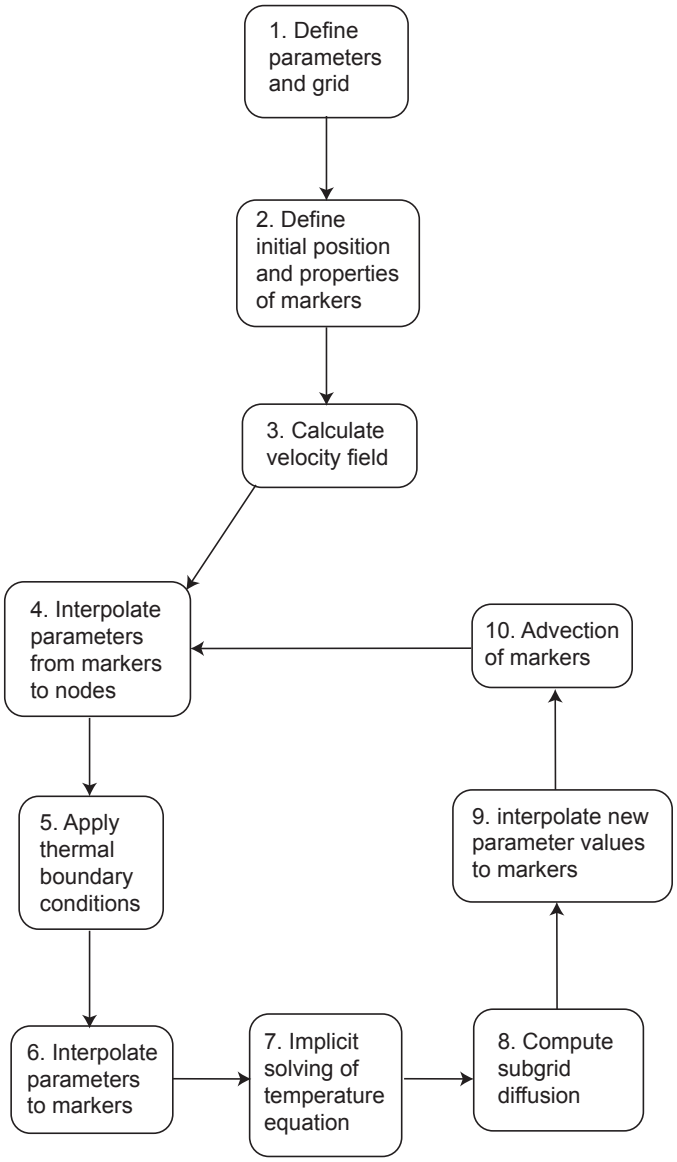

Fig. 2.1 Flowchart showing the different processes involved in modelling the thermal structure of a subduction zone. Sections 1-3 take place outside the time loop where as sections 4-10 are run over a loop for a set number of time steps.

2.4 Thermal Model Processes

I will now go through and explain each step of the flow chart in Figure 2.1.

2.4.1 Calculate velocity field

To allow temperature to advect in the thermal model a velocity field for the subduction zone region needs to be created.

2.4.1.1 Boundary Conditions

The two boundary conditions that are used in the model are the free slip and no slip conditions.

1. For free slip on the boundary, both the normal velocity is zero and shear stress is zero. Since viscosity can be assumed to be constant across the boundary, this implies that the shear strain rate is zero and hence that the tangential velocity components do not change across the boundary. For example the free slip condition is as follows for the boundary orthogonal to the x axis

$$v_x = 0$$

$$\frac{\partial v_y}{\partial x} = \frac{\partial v_z}{\partial x} = 0$$

2. For a no slip condition all the velocity components are zero on the boundary

$$v_x = v_y = v_z = 0$$

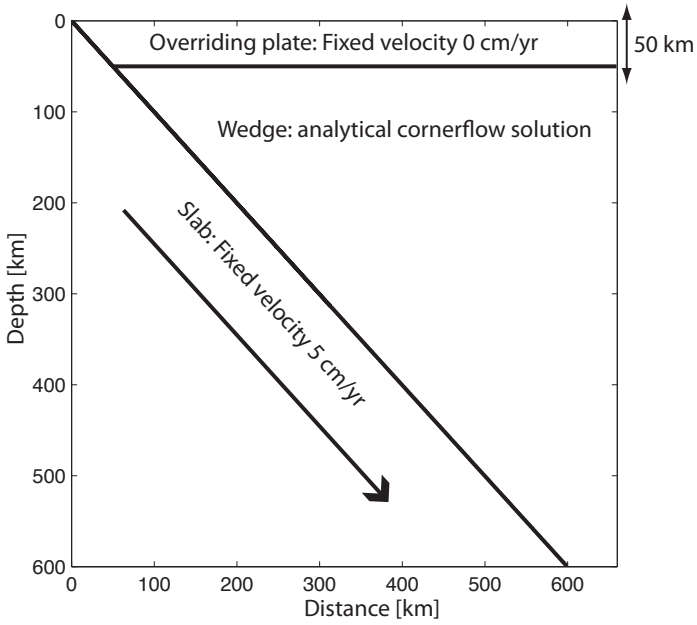

Fig. 2.2 Velocity structure of the model. The overriding plate which is the shallowest 50 km of the model is fixed and has zero velocity. The slab also has a fixed velocity of 5cm/yr and the wedge velocity is calculated using an analytical solution.

2.4.1.2 Mantle wedge velocities

To solve for the mantle wedge velocities we use the analytical solution for corner flow (Batchelor, 1967; McKenzie, 1969), this is done by finding the solution to equation (2.2) where v is written in terms of the stream function Ψ.

$$v = (v_r, v_\theta) = \left(\frac{1}{r} \frac{\partial \Psi}{\partial \theta}, -\frac{\partial \Psi}{\partial \theta} \right) \tag{2.2}$$

A solution for the stream function needs to be found starting with equation (2.3)

$$\nabla^4 \Psi = 0 \tag{2.3}$$

A solution to equation (2.3) is required which satisfies boundary conditions of the form:

$$\mathbf{v} = \mathbf{a}_r \times constant \tag{2.4}$$

Where $\mathbf{a}_r$ = radial unit vector at specified values of θ.

A solution is found by the separation of variables, by substituting $\Psi = r\Theta(\theta)$ into $\nabla^4\Psi$ using $\nabla^4\Psi = \nabla^2(\nabla^2\Psi) = 0$.

$$\nabla^2 \left[\frac{1}{r} \frac{\partial}{\partial r} \left(\frac{r \partial \Psi}{\partial r} \right) + \frac{1}{r^2} \frac{\partial^2 \Psi}{\partial \theta^2} \right] = 0$$

$$\nabla^2 \left[\frac{1}{r} \frac{\partial}{\partial r} \left(\frac{r \partial \Psi}{\partial r} \right) + \frac{1}{r} \frac{\partial}{\partial \theta} \left(\frac{\partial \Psi}{r \partial \theta} \right) \right] = 0$$

Substitute $\Psi = r\Theta(\theta)$

$$\nabla^2 \left[\frac{1}{r} \frac{\partial}{\partial r} \left(\frac{r \partial (r\Theta)}{\partial r} \right) + \frac{1}{r} \frac{\partial}{\partial \theta} \left(\frac{\partial (r\Theta)}{r \partial \theta} \right) \right] = 0$$

$$\nabla^2 \left(\frac{\Theta}{r} + \frac{1}{r} \frac{\partial^2 \Theta}{\partial \theta^2} \right) = 0 \tag{2.5}$$

$$\Theta + \frac{2\partial^2 \Theta}{\partial \theta^2} + \frac{\partial^4 \Theta}{\partial \theta^4} = 0 \tag{2.6}$$

A general solution to (2.6) is found by substituting $\Theta = e^{m\theta} + \theta e^{p\theta}$:

$$\Theta = A \sin\theta + B \cos\theta + C\theta \sin\theta + D\theta \cos\theta \tag{2.7}$$

A, B, C and D are constants that need to be evaluated to find the stream function, Ψ, for the mantle wedge above the subducting slab using the following boundary conditions

$$\mathbf{v} = 0 \text{ at } \theta = 0$$

$$\mathbf{v} = U\mathbf{a}_r \text{ at } \theta = \theta_d \tag{2.8}$$

The details of how Ψ is evaluated is found in Appendix A. For the mantle wedge above the subducting slab the stream function Ψ is

$$\Psi = \frac{Ur[(\theta_d - \theta)\sin\theta_d \sin\theta + \theta_d\theta\sin(\theta_d - \theta)]}{\theta_d^2 - \sin^2\theta_d} \tag{2.9}$$

The grid for the model is in cartesian coordinates so it is necessary to calculate velocities in terms of v_x and v_y. This is done by calculating v_r and v_θ from the stream function, then resolving to get the cartesian components. Using equations (2.2) and (2.9), v_r and v_θ are

$$v_\theta = -\frac{U[(\theta_d - \theta)\sin\theta\sin\theta_d + \theta_d\theta\sin(\theta_d - \theta)]}{{\theta_d}^2 - \sin^2\theta_d} \tag{2.10}$$

$$v_r = \frac{U[(\theta_d - \theta)\cos\theta\sin\theta_d - \sin\theta_d\sin\theta + \theta_d\sin(\theta_d - \theta) + \theta_d\theta\cos(\theta_d - \theta)]}{{\theta_d}^2 - \sin^2\theta_d} \tag{2.11}$$

Then by using the coordinates axes shown in Figure 2.3 we resolve to get v_x and v_y

$$v_x = v_r\cos\theta - v_\theta\sin\theta \tag{2.12}$$

$$v_y = v_r\sin\theta + v_\theta\cos\theta \tag{2.13}$$

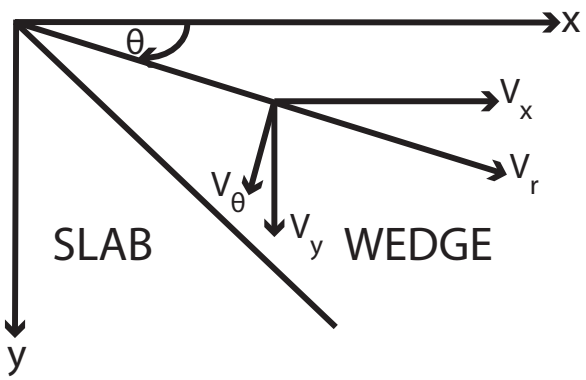

Fig. 2.3 Coordinate axes of the model region. The velocities are calculated in terms of V_Θ and V_r. They then need to be resolved into cartesian coordinates to get V_x and V_y.

2.4.1.3 Slab and overriding plate velocities

Both the slab and overriding plate have fixed velocities. The overriding plate is fixed so it has zero velocity, this condition extends for the shallowest 50 km depth on the mantle wedge side. The slab side also has a fixed velocity of 5 cm/yr at a 45° dip.

Once all the velocities have been calculated for the different sections an overall velocity field is created. Figure 2.4 shows the velocity streamlines of the overall velocity field.

2.4.2 Markers set up

To minimise numerical diffusion this model uses a combination of a fixed Eulerian grid with advecting Lagrangian points (known as particles, tracers or markers). Initially the markers

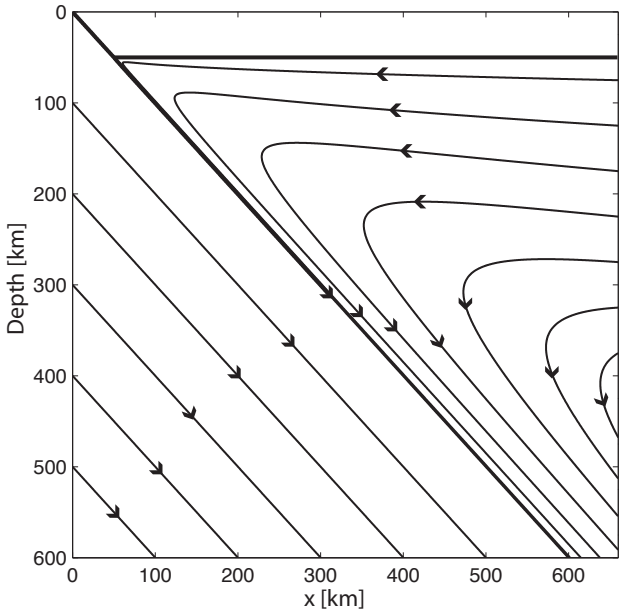

Fig. 2.4 Velocity field of the model region shown by streamlines.

are distributed on a regular marker mesh with a small random displacement. The placement for the markers in the horizontal direction is done as follows: first you divide the horizontal grid size by a fixed value to get the total number of markers in the horizontal direction *mxnum*. The horizontal grid size is then divided by *mxnum* to get the size of the step between markers in the horizontal direction $mxstep$. The horizontal position of the markers MX with a random displacement of 0.5 is then calculated

$$MX = xm \times mxstep - \frac{mxstep}{2} + (rand - 0.5) \times mxstep \tag{2.14}$$

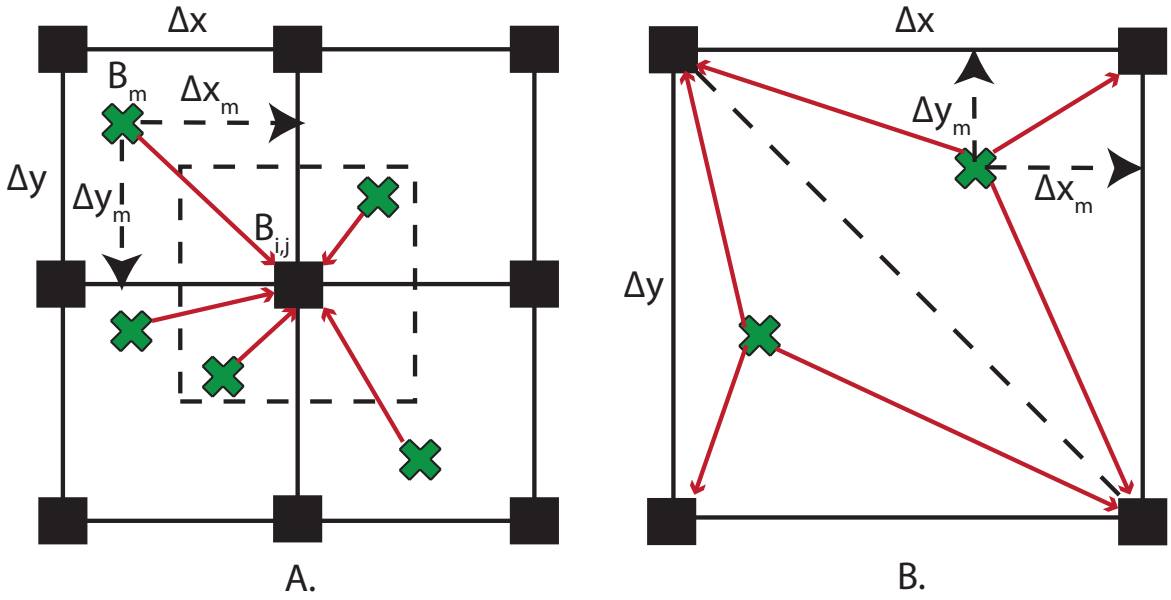

Fig. 2.5 A. Standard and local interpolation of physical properties from markers to nodes. The dashed lines show the area from which marker properties are interpolated to the central node in the case of local interpolation. B. Triangular interpolation of marker properties to nodes. If the marker is located to the left of the dashed line its properties do not get interpolated to the upper right node and if the marker is located to the right of the dashed line its properties do not get interpolated to the lower left node.

where xm is the number of the marker from 1:*mxnum* and *rand* is a random number between 0 and 1. The same method is used to calculate MY for the vertical marker positions. The markers are prescribed values for scalar properties (e.g. T, ρ).

2.4.3 Interpolate parameters from markers to nodes

To interpolate from the Langrangian markers to the Eulerian nodes various schemes can be used. I have tried three interpolation schemes; standard, local and triangular.

2.4.3.1 Standard interpolation

The standard interpolation is a first order, accurate, bilinear scheme to calculate the value of a parameter $B_{i,j}$ interpolated for the ij-th-node. It uses values B_m that are assigned to all the

markers found in the four surrounding grid cells. (Figure 2.5A.)

$$B_{i,j} = \frac{\sum_m B_m w_{m(i,j)}}{\sum_m w_{m(i,j)}} \tag{2.15}$$

$$w_{m(i,j)} = (1 - \frac{\Delta x_m}{\Delta x}) \times (1 - \frac{\Delta y_m}{\Delta y}) \tag{2.16}$$

Where Δx_m and Δy_m are the distances in the x and y directions from the m-th-marker to the ij-th-node and the w_m is the weight of the m-th-marker at the ij-th-nodes. Markers closer to the node will have more "weight". The parameter $B_{i,j}$ is then calculated taking into account the weight of the markers using equations (2.15) and (2.16).

2.4.3.2 Local interpolation

For local interpolation, the marker is interpolated to a node based on its Δx_m and Δy_m distances. The same equations are used as for the standard interpolation method. Local interpolation is shown by the dashed line in Figure 2.5A. The condition for the marker being interpolated to a certain node are as follows:

Upper left node:

$$\text{If} \qquad x_m \leq \frac{\Delta x}{2} \,\&\, y_m \leq \frac{\Delta y}{2}$$

Lower left node:

$$\text{If} \qquad x_m \leq \frac{\Delta x}{2} \,\&\, y_m \geq \frac{\Delta y}{2}$$

Upper right node:

$$\text{If} \qquad x_m \geq \frac{\Delta x}{2} \,\&\, y_m \leq \frac{\Delta y}{2}$$

Lower right node:

$$\text{If} \qquad x_m \geq \frac{\Delta x}{2} \,\&\, y_m \geq \frac{\Delta y}{2}$$

2.4.3.3 Triangular interpolation

The triangular interpolation method uses the same interpolation equations as the standard interpolation technique. In this method the marker properties from all markers are added to the upper left node and lower right nodes. Whether the marker is interpolated to the upper right or lower left node depends on the location of the markers in relation to the diagonal line between the upper left and lower right node as shown in Figure 2.5B. As the grid has equal spacing and $xstp$ equals $ystp$ the gradient of the diagonal line is 1. Therefore any marker located above this line will have a y_m/x_m value of < 1. In this case the properties of the marker are added to the upper right node. If the marker lies below the line then its y_m/x_m value will be > 1. The properties of the marker in this location will be added to the lower left node.

2.4.4 Thermal boundary conditions for nodes

The four sides of the grid all have different thermal boundary conditions. These boundary conditions are the same as used in the benchmark paper by Van Keken et al. (2008).

2.4.4.1 Upper boundary

For the upper boundary of the grid I assume:

$$T = T_o$$

where $T_o = 0°C$ or $273K$, this will be represented in the code as

$$tk1(1,:) = tsurf$$

where $tsurf$ is a constant temperature value.

2.4.4.2 Lower boundary

The lower boundary has an insulating boundary condition (i.e. zero heat flux). This means there is no conductive heat flux across the boundary, implying that there is no temperature gradient i.e.

$$q_y = -k\frac{\partial T}{\partial y} \Rightarrow \frac{\partial T}{\partial y} = 0$$

which will be represented in the code as

$$tk1(ynum, j) = tk1(ynum - 1, j).$$

Simply put the temperature at the lower boundary will equal the temperature one row above in the grid.

2.4.4.3 Left Boundary

The boundary condition is prescribed by the error function from the oceanic half space cooling model and increases from the surface temperature T_o ($0^\circ C$) to the background temperature T_b ($1300^\circ C$) i.e.

$$T(y) = T_o + (T_b - T_o)(erf(\frac{y}{2\sqrt{kt_{50}}}))$$

Where t_{50} is the age of a 50 million year old oceanic plate in seconds.

2.4.4.4 Right boundary

The right boundary has three boundary conditions applied to it for different sections along the boundary. For the overriding plate defined by

$$y \leq 50km$$

the temperature is defined by an adiabatic temperature gradient starting at T_o at the surface and linearly increasing to T_b at 50 km depth.

$$T(y) = T_o + y\frac{\mathrm{d}T}{\mathrm{d}y}$$

where dT/dy is the temperature gradient. The other two boundary conditions for the region below the overriding plate are dependent on the velocity field. At the incoming boundary

$$vx(y) < 0$$

the boundary condition is a constant temperature of the background temperature *tback*

$$T(y) = T_b$$

At the outgoing boundary

$$vx(y) >= 0$$

the boundary condition is an insulating boundary condition

$$\frac{\mathrm{d}T}{\mathrm{d}x} = 0$$

so the temperature on the boundary is the same as the temperature one column in on the grid.

2.4.5 Interpolate initial nodal temperatures back to markers

As well as interpolating properties from markers to nodes, interpolation of physical parameters (e.g. velocity, temperature) from the nodes to the markers is also required. One method is to use the values of the parameter B, which has been defined at the four nodes surrounding a chosen marker. Using the first order bilinear interpolation scheme, a value of the parameter

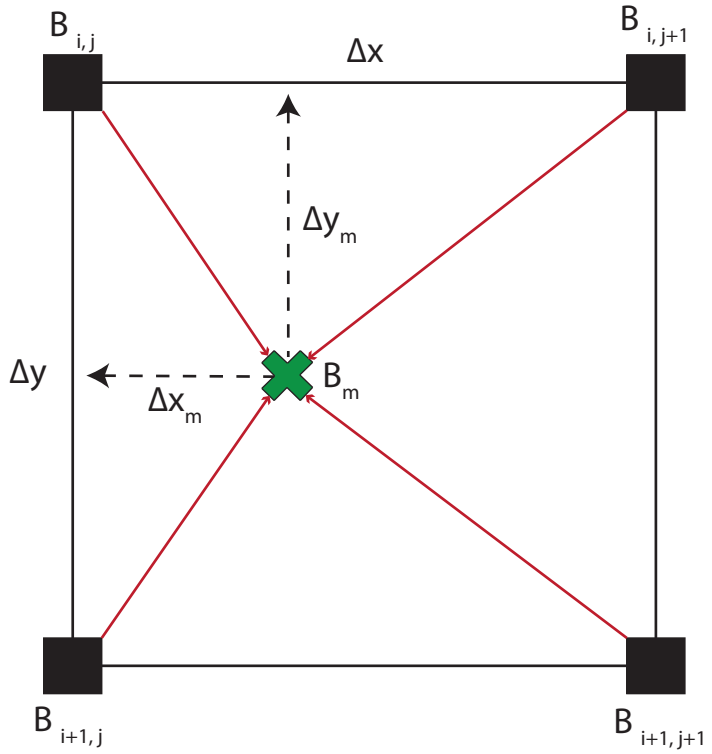

Fig. 2.6 Interpolation of physical properties from the four surrounding nodes to a marker.

B can be calculated for the m-th-marker as follows:

$$\begin{aligned} B_m =& B_{i,j}\left(1-\frac{\Delta x_m}{\Delta x}\right)\left(1-\frac{\Delta y_m}{\Delta y}\right)+B_{i,j+1}\frac{\Delta x_m}{\Delta x}\left(1-\frac{\Delta y_m}{\Delta y}\right) \\ &+B_{i+1,j}\left(1-\frac{\Delta x_m}{\Delta x}\right)\frac{\Delta y_m}{\Delta y}+B_{i+1,j+1}\frac{\Delta x_m \Delta y_m}{\Delta x \Delta y}, \end{aligned} \tag{2.17}$$

where the parameter B for the m-th-marker is denoted by B_m.

2.4.6 Numerical solution of the heat conservation equation

As the model may have different material compositions, the method used to solve the heat equation needs to take into account variable thermal conductivity. For variable thermal conductivity conservative finite difference discretisation can be used, as it allows a cor-

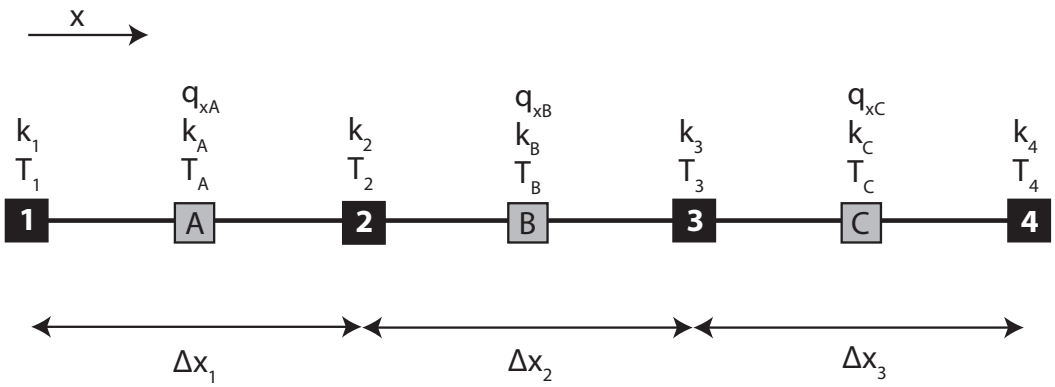

Fig. 2.7 1D grid with 4 grid nodes numbered 1-4 and 3 additional nodes labeled A-C that are located half way between the grid nodes. The additional nodes are used if there is variable thermal conductivity. There the heat fluxes are defined. The temperature equation is solved at the grid nodes.

rect numerical solution by ensuring conservation of energy between nodal points (Gerya, 2010). There are three rules that a conservative finite difference scheme for the solving the temperature equation follows. Lets illustrate for a 1D case, see Figure 2.7.

1. Heat fluxes at the grid nodes are used to initially discretise the temperature equation,

$$\text{node } 2: \left(\rho C_p \frac{DT}{Dt}\right)_2 = 2\frac{q_{x\mathrm{B}} - q_{x\mathrm{A}}}{(\Delta x_1 + \Delta x_2)},$$

$$\text{node } 3: \left(\rho C_p \frac{DT}{Dt}\right)_3 = 2\frac{q_{x\mathrm{C}} - q_{x\mathrm{B}}}{(\Delta x_2 + \Delta x_3)}.$$

2. The heat fluxes are formulated in terms of grid nodes,

$$\text{node A}: q_{x\mathrm{A}} = -k_{\mathrm{A}}\frac{T_2 - T_1}{\Delta x_1},$$

$$\text{node B}: q_{x\mathrm{B}} = -k_{\mathrm{B}}\frac{T_3 - T_2}{\Delta x_2},$$

$$\text{node C}: q_{x\mathrm{C}} = -k_{\mathrm{C}}\frac{T_4 - T_3}{\Delta x_3}.$$

At the additional nodes (A, B, C) we have to use thermal conductivity values k_A, k_B and k_C. These values can be calculated by averaging the thermal conductivity values from the grid nodes (1, 2, 3, 4)

$$k_A = \frac{k_1 + k_2}{2},$$

$$k_B = \frac{k_2 + k_3}{2},$$

$$k_C = \frac{k_3 + k_4}{2}.$$

3. For different grid nodes identical formulations of heat fluxes are used for the temperature equation. Conservative finite differences are not formulated in terms of thermal diffusivity (κ) but in terms of thermal conductivity (k) where:

$$\kappa = \frac{k}{\rho Cp}$$

This is to stop the occurrence of artificial variations in heat fluxes due to spatial variations in heat capacity (Cp) and/or density (ρ). Heat capacity and density should always be taken from the grid node where the equation is being formulated. The conservative finite difference formulation can be derived for the Lagrangian temperature equation in 2D by using these rules (Figure 2.8)

$$\rho_3 Cp_3 \left(\frac{DT}{Dt}\right)_3 = -\left(\frac{\partial q_x}{\partial x}\right)_3 - \left(\frac{\partial q_y}{\partial y}\right)_3, \tag{2.18}$$

$$\rho_3 Cp_3 \frac{T_3^n - T_3^0}{\Delta t} = -2\frac{q_{xB} - q_{xA}}{\Delta x_1 + \Delta x_2} - 2\frac{q_{xD} - q_{xC}}{\Delta y_1 + \Delta y_2} \tag{2.19}$$

$$\rho_3 Cp_3 \frac{T_3^n}{\Delta t} + 2\frac{q_{xB} - q_{xA}}{\Delta x_1 + \Delta x_2} + 2\frac{q_{xD} - q_{xC}}{\Delta y_1 + \Delta y_2} = \rho_3 Cp_3 \frac{T_3^0}{\Delta t}, \tag{2.20}$$

where

$$q_{x\mathrm{A}} = -k_{\mathrm{A}} \frac{(T_3^n - T_1^n)}{\Delta x_1},$$
$$q_{x\mathrm{B}} = -k_{\mathrm{B}} \frac{(T_5^n - T_3^n)}{\Delta x_2},$$
$$q_{y\mathrm{C}} = -k_{\mathrm{C}} \frac{(T_3^n - T_2^n)}{\Delta y_1},$$
$$q_{y\mathrm{D}} = -k_{\mathrm{D}} \frac{(T_4^n - T_3^n)}{\Delta y_2},$$

As the thermal conductivity values at the heat flux nodes (A, B, C, D) are not known they can be computed by averaging the thermal conductivity values from the grid nodes i.e.

$$k_{\mathrm{A}} = \frac{k_1 + k_3}{2},$$
$$k_{\mathrm{B}} = \frac{k_3 + k_5}{2},$$
$$k_{\mathrm{C}} = \frac{k_2 + k_3}{2},$$
$$k_{\mathrm{D}} = \frac{k_3 + k_4}{2}.$$

2.4.7 Interpolate temperature and velocity from nodes to markers

Numerical diffusion is introduced by interpolating between nodes and markers. When it is required to interpolate back and forth the same time dependent parameter (e.g. temperature), the problem can become particularly significant. By interpolating the incremental values and not the absolute values from the nodes to the markers the diffusion can be minimised. So if B

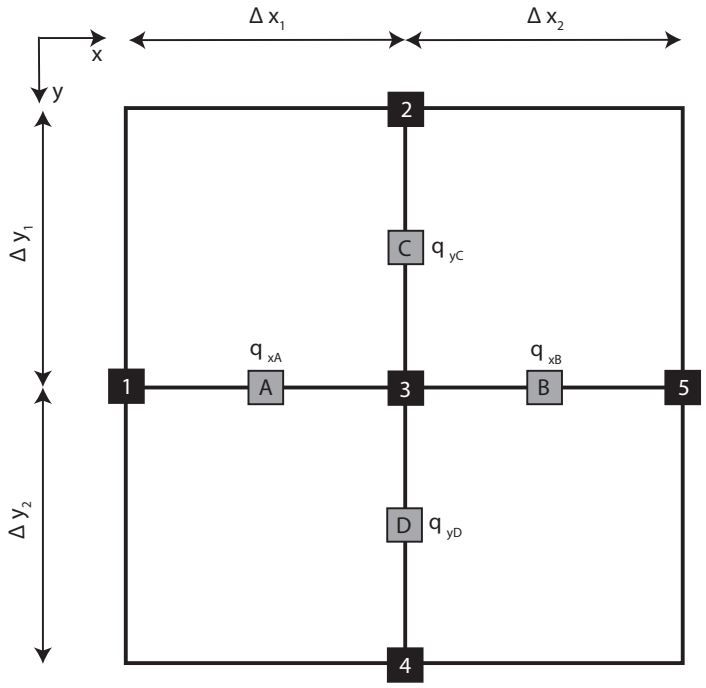

Fig. 2.8 2D grid used to discretise the temperature equation implicitly with variable thermal conductivity. The black numbered squares are the grid nodes which hold the physical parameters (ρ, Cp, T, k). The grey lettered squares are the additional nodes where the heat fluxes are defined. The central node is the node for which the temperature equation is formulated. The number or letter of the node indicate the indices of the parameters at that node e.g. node 1 will have parameters T_1, k_1 etc.

is the value needing interpolating, I apply the following to interpolate from nodes to markers:

$$B_m^{t+\Delta t} = B_m^t + \left(B_{i,j}^{t+\Delta t} - B_{i,j}^t\right)\left(1 - \frac{\Delta x_m}{\Delta x}\right)\left(1 - \frac{\Delta y_m}{\Delta y}\right) + \left(B_{i,j+1}^{t+\Delta t} - B_{i,j+1}^t\right)$$

$$\times \frac{\Delta x_m}{\Delta x}\left(1 - \frac{\Delta y_m}{\Delta y}\right) + \left(B_{i,+1,j}^{t+\Delta t} - B_{i+1,j}^t\right)\left(1 - \frac{\Delta x_m}{\Delta x}\right)\frac{\Delta y_m}{\Delta y}$$

$$+ \left(B_{i+1,j+1}^{t+\Delta t} - B_{i+1,j+1}^t\right)\frac{\Delta x_m \Delta y_m}{\Delta x \Delta y}, \tag{2.21}$$

where t is the current time step and $t + \Delta t$ is the next time step. After solving the temperature equation in the previous section, temperature and velocity of each node need to be interpolated

to the markers for the advection process. To avoid numerical diffusion of temperature the temperature increments are used for the interpolation. First the temperature field changes at the grid nodes are calculated:

$$\Delta T_{i,j} = T_{i,j}^{t+\Delta t} - T_{i,j}^{t} \tag{2.22}$$

Then using the interpolation of increments from nodes to markers method as set out in equation (2.21), the temperature increments for the markers ΔT_m are interpolated allowing the new marker temperatures $T_m^{t+\Delta t}$ as:

$$T_m^{t+\Delta t} = T_m^t + \Delta T_m \tag{2.23}$$

2.4.8 Compute subgrid diffusion for markers

A problem with using the incremental marker update scheme for advection-diffusion processes is that on a sub grid scale, small scale thermal variations may appear (i.e. temperature differences between markers close together). Grid scale corrections can not damp out these oscillations. For example in the case of thermal convection which causes the markers to be chaotically mixed, it may cause the thermal field for the adjacent markers to produce numerical oscillations. These oscillations do not damp out with time. Gerya (2010) uses a sub grid diffusion to solve this problem. In the method temperature changes calculated from equation (2.22) are decomposed into a subgrid part $\Delta T_{i,j}^{subgrid}$ and a remaining part $\Delta T_{i,j}^{remaining}$

$$\Delta T_{i,j} = \Delta T_{i,j}^{subgrid} + \Delta T_{i,j}^{remaining} \tag{2.24}$$

To calculate the sub grid part, sub grid diffusion is applied over a characteristic local heat diffusion timescale Δt_{diff} to the markers, then the temperature changes are interpolated back to the nodes. Equation (2.25) shows how sub grid temperature changes are calculated for

markers

$$\Delta T_m^{subgrid} = (T^t_{m(nodes)} - T^t_m)[1 - exp(-d\frac{\Delta t}{\Delta t_{diff}})] \tag{2.25}$$

where

$$\Delta t_{diff} = \frac{Cp_m \rho_m}{k_m(\frac{2}{\Delta x^2} + \frac{2}{\Delta y^2})}$$

where t_{diff} is defined for the grid cell where the marker is located; d is a dimensionless numerical diffusion coefficient in the range of $0 \leq d \leq 1$. $T^t_{m(nodes)}, Cp_m, \rho_m$ and k_m are interpolated for a given marker from $T^t_{(i,j)}, Cp_{(i,j)}, \rho_{(i,j)}$ and $k_{(i,j)}$values for the nodes surrounding the marker using the relation as set out in equation (2.17). After calculating $\Delta T_m^{subgrid}$ for all markers, $\Delta T_{(i,j)}^{subgrid}$ are calculated by interpolation from markers to nodes using equation (2.15). Then $\Delta T_{(i,j)}^{remaining}$ is calculated by rearranging equation (2.24) so that

$$\Delta T_{(i,j)}^{remaining} = \Delta T_{(i,j)} - \Delta T_{(i,j)}^{subgrid} \tag{2.26}$$

Finally the corrected marker temperatures $T^{t+\Delta t}_{m(corrected)}$ are calculated by modifying equation (2.23) to take into account equations (2.24) to (2.26) therefore removing the subgrid oscillations.

$$T^{t+\Delta t}_{m(corrected)} = T^t_m + \Delta T_m^{subgrid} + \Delta T_m^{remaining} \tag{2.27}$$

where $T_m^{subgrid}$ is calculated from equation (2.25) and $\Delta T_m^{remaining}$ is interpolated from $\Delta T_{(i,j)}^{remaining}$ from the surrounding nodes using equation (2.17). Equation (2.25) needs the differences between the marker temperatures and interpolated nodal temperature values to decay according to the characteristic timescale of local heat diffusion. The temperature values $\Delta T_{(i,j)}$ calculated from the heat conservation equation are not changed by the sub grid diffusion. Unrealistic sub grid oscillations are removed by the sub grid diffusion without affecting the accuracy of the numerical solution of the temperature equation. This scheme will preserve realistic sub grid oscillations.

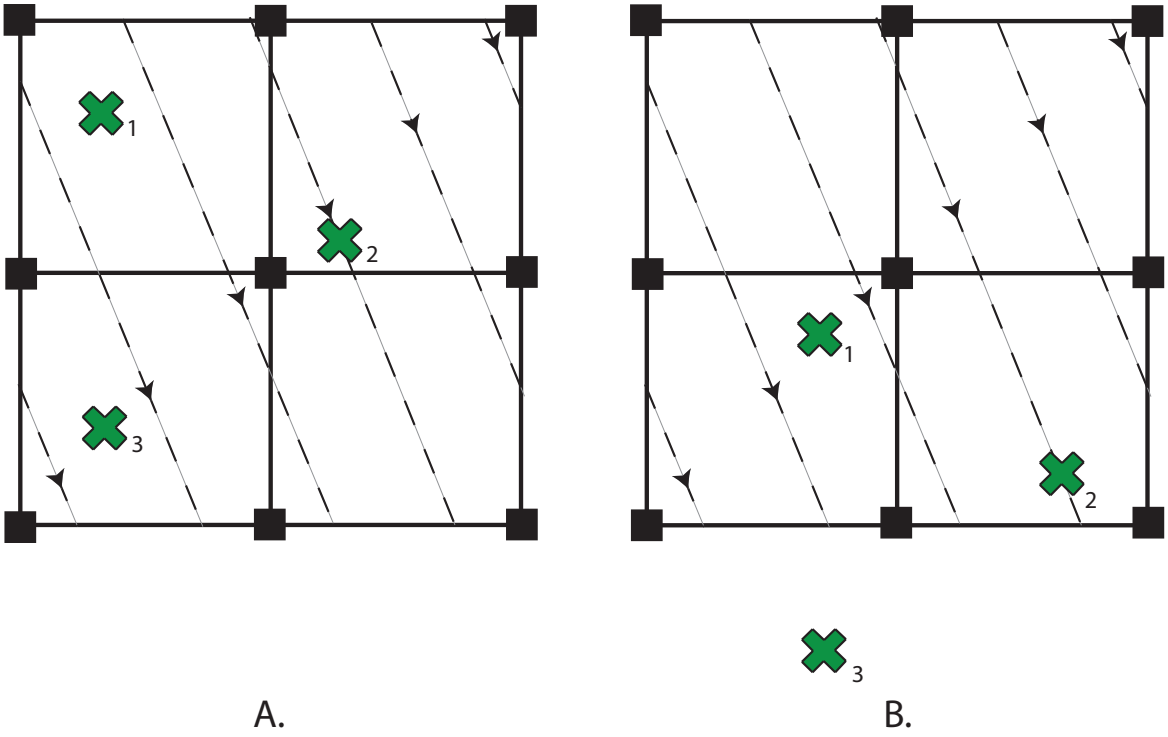

Fig. 2.9 A. shows the original position of the markers before they are moved by the velocity field. B. shows the location of the new marker positions after they have been moved by the velocity field. The velocity field is shown by the dashed line.

2.4.9 Advection of markers

The markers are moved by the velocity field according to the timestep (Figure 2.9).

$$MX(new) = MX(old) + timestep \times vx(marker)$$

$$MY(new) = MY(old) + timestep \times vy(marker)$$

2.4.9.1 Recycling of markers

Movement of the markers by the velocity field may cause some of the markers to move beyond the grid boundaries as shown in Figure 2.9 where the marker numbered 3 moves

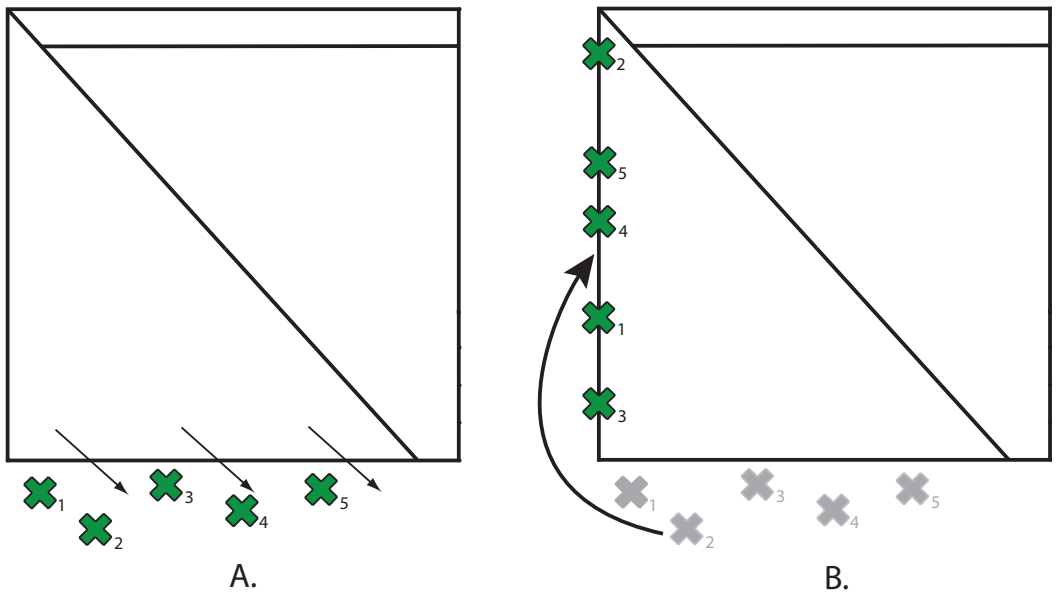

Fig. 2.10 A. the markers shown have been moved by the velocity beyond the lower boundary. B. The markers are recycled back into the grid and randomly distributed along the left hand boundary.

outside the grid. They need to be recycled back into the grid as the total number of markers needs to remain constant. The method I have chosen moves the markers that have gone beyond the grid boundaries back to the boundaries, so they can be given the boundary conditions at the next time step. To prevent clustering of markers, or regions not having any markers, I randomly distribute the markers along the boundaries. If the markers move beyond the lower boundary to the left of the slab, they are randomly distributed along the left hand boundary (Figure 2.10). If the markers go beyond the right hand boundary or beyond the lower boundary to the right of the slab, they are randomly distributed along the right hand boundary (Figure 2.11).

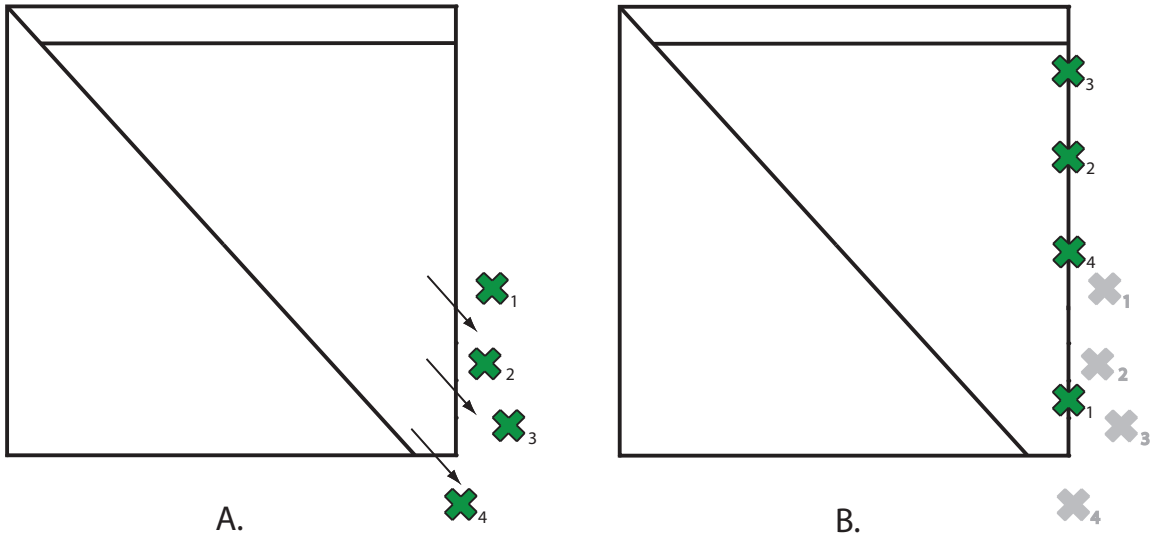

Fig. 2.11 A. The markers shown have been moved by the velocity field beyond the lower boundary to the right of the slab and beyond the right hand boundary. B. The markers are recycled back into the grid and randomly distributed along the right hand boundary.

2.5 Subduction zone thermal model benchmark

2.5.1 Overview of subduction zone benchmark

In the paper by Van Keken et al. (2008), a benchmark was developed that compared numerical models for the thermal structure and dynamics of subduction zones. There was five different benchmark cases that were examined all using the same model geometry:

1. Analytical corner flow model
2. Dynamical flow in isoviscous wedge
3. Dynamical flow in isoviscous wedge with prescribed boundary conditions for stress at the inflow and outflow boundaries
4. Dynamical flow with diffusion creep
5. Dynamical flow with dislocation creep

The first three cases examine the effect of an isoviscous wedge and the last two cases explore the effects of stress and temperature dependent rheology in the mantle wedge. The case that I am comparing to is the first case, which uses the analytical expression for corner flow to prescribe the velocities in the mantle wedge (Batchelor, 1967; McKenzie, 1969). The paper compiles the contributions from the seven different groups involved all with independent codes which are listed as follows along with a short identifier:

1. Mark Behn (WHOI) used Comsol 3.2b, which is a finite element code.
2. Amandine Cagniocle and Marc Parmentier (Brown) used a mixed finite volume and finite element approach.
3. Claire Currie, Jiangheng He and Kelin Wong (PGC) used the code PGCtherm which uses the finite element method.

4. Richard Katz and Marc Spiegelman (LDEO) used an uniform finite volume code which employs the Portable Extensible Toolkit for Scientific Computing (PETSc).

5. Scott King (VT) used CONMAN, his finite element code.

6. Shu-Chuan Lin (NTU) employed a finite volume discretization method.

7. Peter Van Keken (UM) used a code based on the Sepran software, which employs the finite element method.

None of the codes that contributed to the benchmark used the finite difference marker-in-cell technique that I utilise in my code. I will use this benchmark to check this method and my code. I could not find a benchmark demonstration of this method in the literature.

2.5.2 Benchmark Results

Van Keken et al. (2008) focused on the temperature field in the mantle wedge in the corner of the corner flow region and the top of the slab, as this region is most relevant for the chemical and physical processes that lead to seismicity and volcanism. Figure 2.12a is the model result of the temperature field from the UM group for the analytical corner flow case. Figure 2.12b is a close up of the corner of the wedge.

To allow for easy comparison between different groups model results each group provided the temperature field as T_{ij} on a 6 km by 6 km grid. The values were stored in a 111 x 101 matrix with the top left value the starting value. Using these temperature grid the following measurements were extracted to allow for direct comparison:

1. The temperature value located at coordinates (60, 60 km) which is $T_{11,11}$ in the temperature field grids. This point is located on the slab wedge interface just down from the corner point of the wedge. Figure 2.13 (a) plots the temperature at (60,60 km) for different grid resolutions, for each of the different groups. As the grid resolution increases the results start to converge.

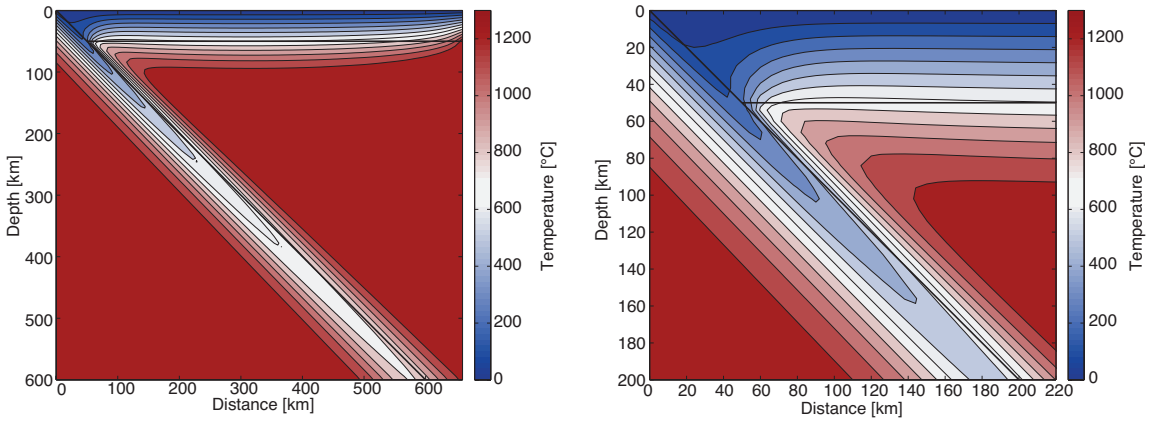

(a) (b)

Fig. 2.12 (a) Model result for temperature field from the UM group, temperature is in °C. (b) A close up of the mantle wedge corner temperature field. (http://www.earth.lsa.umich.edu/ keken/subduction/benchmark/)

2. The L2 norm value of the slab wedge interface temperature between 0-210 km depth given by:

$$\|T_{slab}\| = \sqrt{\frac{\sum_{i=1}^{36} T_{ii}^2}{36}} \tag{2.28}$$

Figure 2.13(b) plots the L2 norm slab value against grid resolution with the results converging as the grid resolution goes towards 0 km.

3. The L2 norm of the temperature in the tip of the wedge between 54 and 120 km depth:

$$\|T_{wedge}\| = \sqrt{\frac{\sum_{i=10}^{21} \sum_{j=10}^{i} T_{ij}^2}{78}} \tag{2.29}$$

Figure 2.13(c) shows the L2 norm value for the wedge section against grid resolution and the results converge as the grid spacing decreases.

Table 2.3 Selected temperature values

Code	$T_{11,11}$	$\|T_{slab}\|$	$\|T_{wedge}\|$
Brown	393.51	520.14	866.52
LDEO	396.63	506.43	855.58
NTU	388.87	507.43	852.99
PGC	388.21	503.69	854.34
UM	388.24	503.77	852.89
VT	379.87	502.26	852.05
WHOI	388.26	503.75	854.37
Average	389.1	506.8	855.5

All values are in °C. For each the code the values at the highest resolution are listed (Van Keken et al., 2008).

Table 2.3 is the temperature values of the three measurement points. These are all for the highest resolution in each code. At the bottom of the table I have calculated the average of these values which I will use to compare my results to the benchmark results.

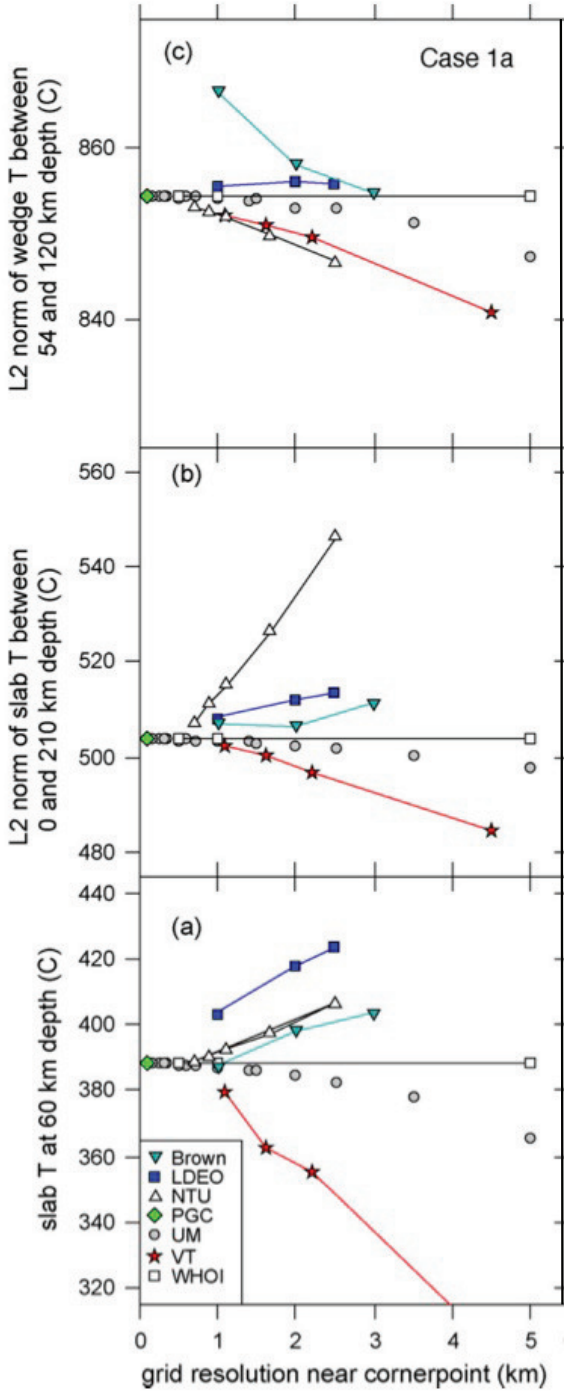

Fig. 2.13 Grid resolution plotted against temperature for the different group model results for the following measurements; (a) slab T at 60 km depth, (b) L2 norm of slab between 0 and 210 km and (c) L2 norm of wedge between 54 and 120 km depth.

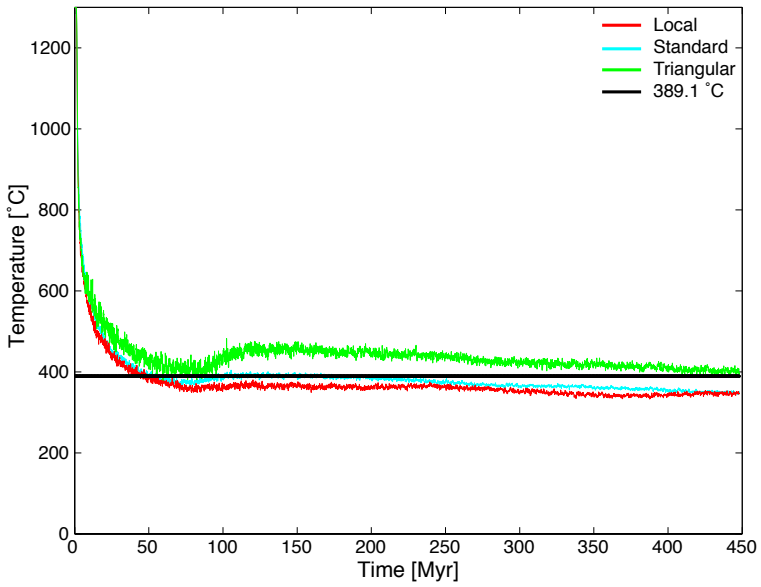

Fig. 2.14 Plot of temperature at 60 km depth on the slab against time for the three different interpolation schemes, local, standard and triangular all with 3km grid resolution. The black line represents the average benchmark value for 60 km depth on the slab taken from 2.3 Standard and local are very similar but converge to a temperature lower than the average value. The triangular interpolation converges towards the average benchmark value.

2.6 Model Results

2.6.1 Different interpolation schemes

I plotted graphs of how the three temperature values changed over time for the different interpolation schemes. Figure 2.14 is the temperature value at (60, 60 km) plotted against time. All three interpolation schemes quickly trend towards the average benchmark value, with triangular interpolation being the closest. In Figure 2.15 the L2 norm temperature of the

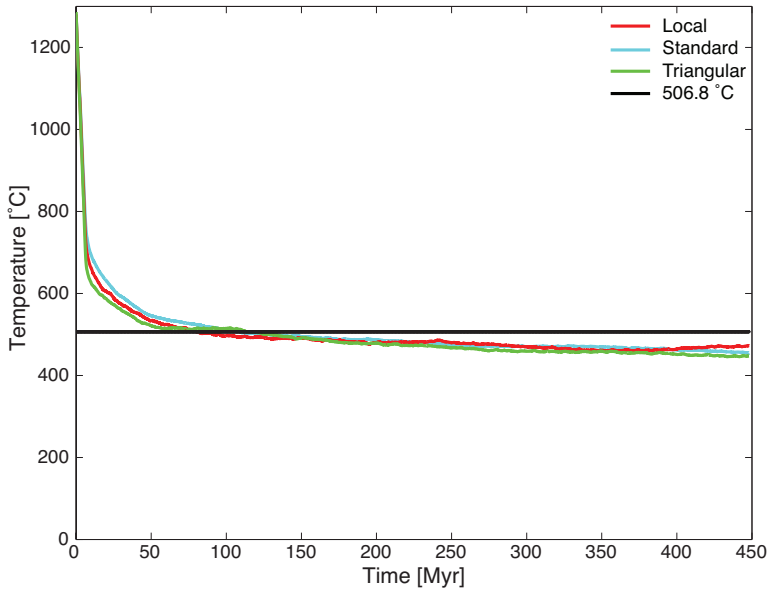

Fig. 2.15 Plot of L2 norm temperature of slab between 0 and 210 km against time for the three different interpolation schemes, local, standard and triangular all with 3km grid resolution. The black line represents the average benchmark value for L2 norm temperature of the slab between 0 and 210 km taken from Table 2.3 Triangular, standard and local interpolation lines are very similar but converge to a temperature lower than the average benchmark value.

slab is plotted against time and all three lines are very similar. In Figure 2.16 the L2 norm temperature of the wedge is plotted against time; and triangular interpolation trends closest to the average benchmark value, followed by local interpolation and standard interpolation is the worst fit. Standard interpolation is the weakest of the results due to it interpolating values from the four surrounding grid cells. Local interpolation is better as it interpolates values from a smaller area equivalent to 1 grid cell. This allows the slab wedge interface temperature contrast to be more sharply defined. Even with local interpolation the temperature contrast was not being as sharply defined. As the slab wedge interface is on a diagonal, I designed a triangular interpolation scheme (see triangular interpolation in Section 2.4.3).

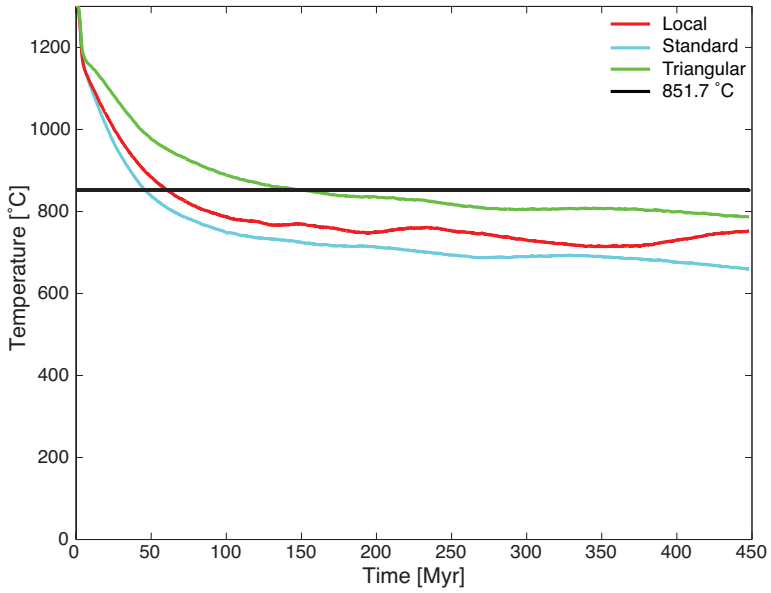

Fig. 2.16 Plot of L2 norm temperature of the wedge between 54 and 120 km depth against time for the three different interpolation schemes, local, standard and triangular all with 3km grid resolution. The black line represents the average benchmark value for L2 norm temperature of the wedge between 54 and 120 km depth taken from Table 2.3 All three lines move below the average value however the triangular interpolation line is the closest to the average benchmark value.

2.6.2 Initial background temperature

The initial background temperature can either start from the surface temperature (0°C) or the mantle background temperature (1300°C). Figure 2.17 shows the results converge which means it does not have much effect which initial starting temperature is used.

2.6.3 Change in resolution

Increasing the resolution causes the average temperature values to tend towards the benchmark average value. The benchmark average value was calculated for the highest resolution from each groups results which is much higher than my highest resolution. The 2 km resolution provided the best result for the L2 norm temperature of the wedge value, but it was very

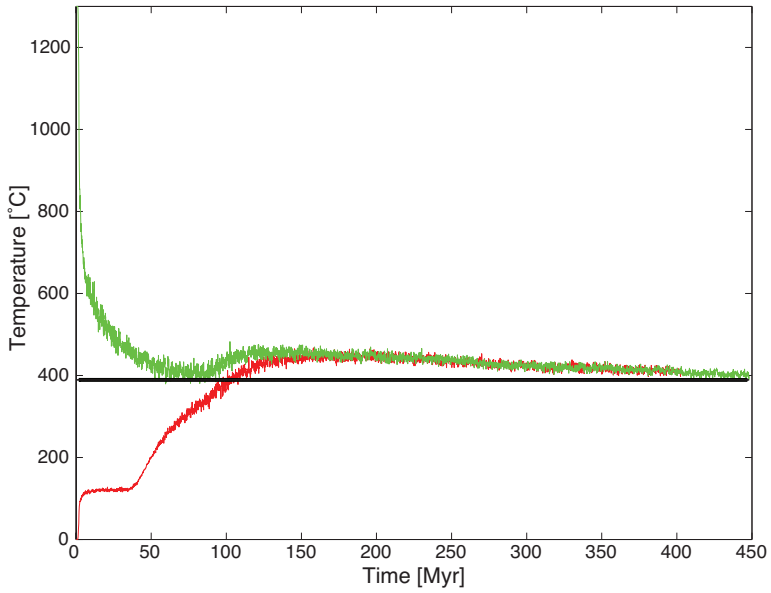

Fig. 2.17 Model runs with 3km grid resolution. The red line represents model starting with a surface initial temperature of 0°C and the green line starts with a mantle background initial temperature 1300°C. The two lines converge together.

computationally expensive. The 3 km resolution was computationally much less expensive but was still close to the benchmark average.

2.6.4 Final Result

My final result is a 3 km resolution, triangular interpolation with the starting background temperature of 1300 °C. I decided this would produce the best result whilst not being too computationally expensive. Figure 2.20a is my final temperature field for this model and Figure 2.20b is a close up of the wedge region. At the start of the model the temperature field is the background temperature of 1300 °C, then as the model runs over time the overriding plate starts to cool and the subducting slab pulls colder temperatures down the slab.

As the temperature values oscillate, rather than selecting the final temperature value, I average the final 20 time steps to get my temperature value. From this average temperature field I calculate my three average values as:

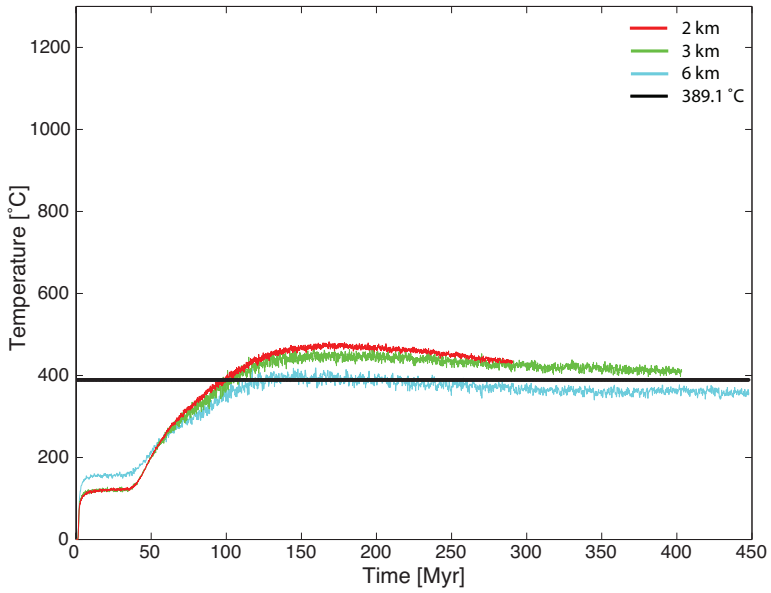

Fig. 2.18 Plot of temperature at 60 km depth on the slab against time for the three different grid resolutions, 2km, 3km and 6km. The black line represents the average value for 60 km on the slab taken from Table 2.3 All three lines trend towards the average value.

Table 2.4

	Model Average	Benchmark Average
$T_{11,11}$	401.2	389.1
$\|\|T_{slab}\|\|$	462.0	506.8
$\|\|T_{wedge}\|\|$	781.3	851.7

All values are in °C.

2.6.5 Comparison of model results with benchmark

Visual comparison of Figure 2.21a with Figure 2.21b and Figure 2.22a with Figure 2.22b shows that my temperature field is visually very similar to the UM group model result. Numerical comparison of my average values with the average benchmark values show that my values do not match the average benchmark values. However the average benchmark values were calculated from the highest resolution results from the different groups, so it is expected for my values to not fit them exactly.

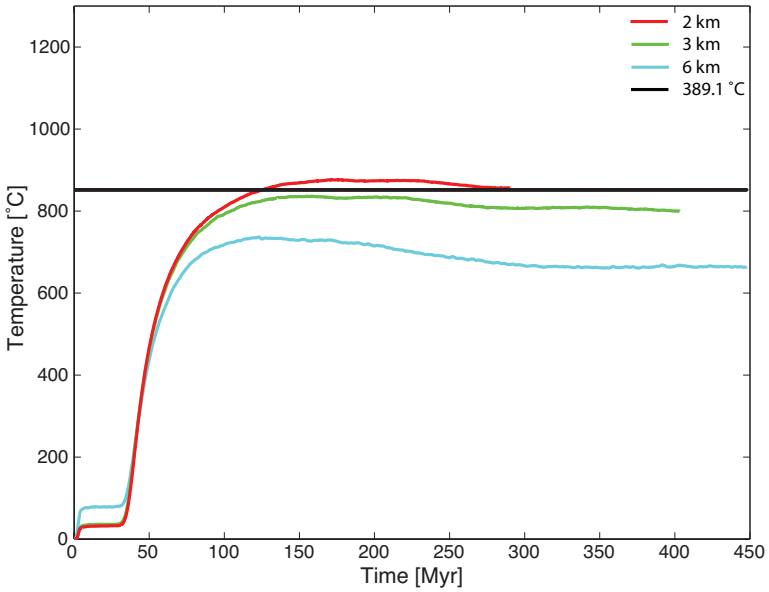

Fig. 2.19 Plot of L2 norm temperature of the wedge between 54 and 120 km depth against time for the three different grid resolutions, 2km, 3km and 6km. The black line represents the average value for L2 norm temperature of the wedge between 54 and 120 km depth taken from Table 2.3 The 2km line trends towards the average value and the 3km line is just below the average benchmark value.

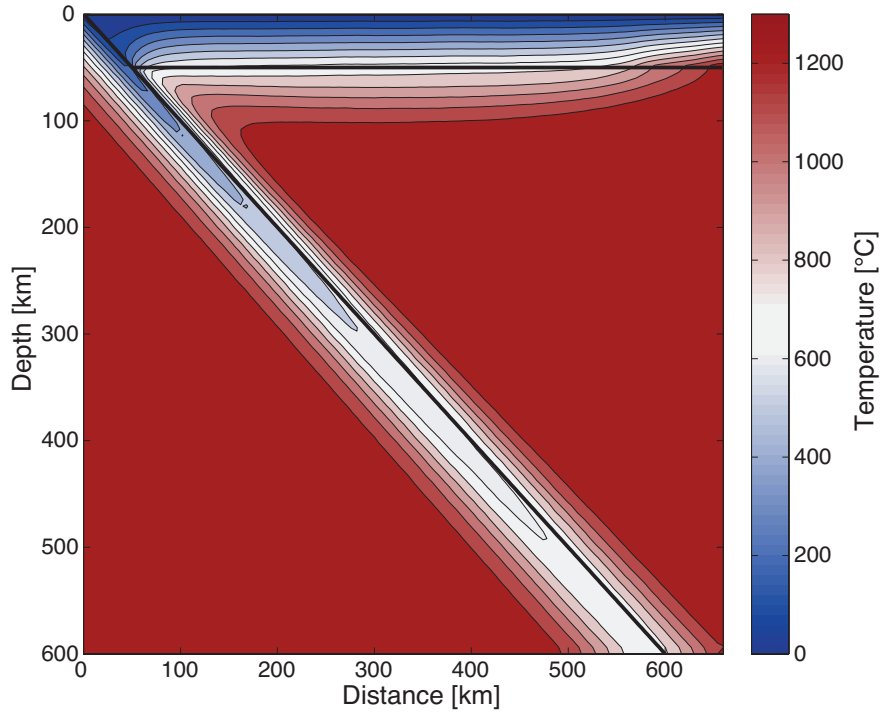

(a)

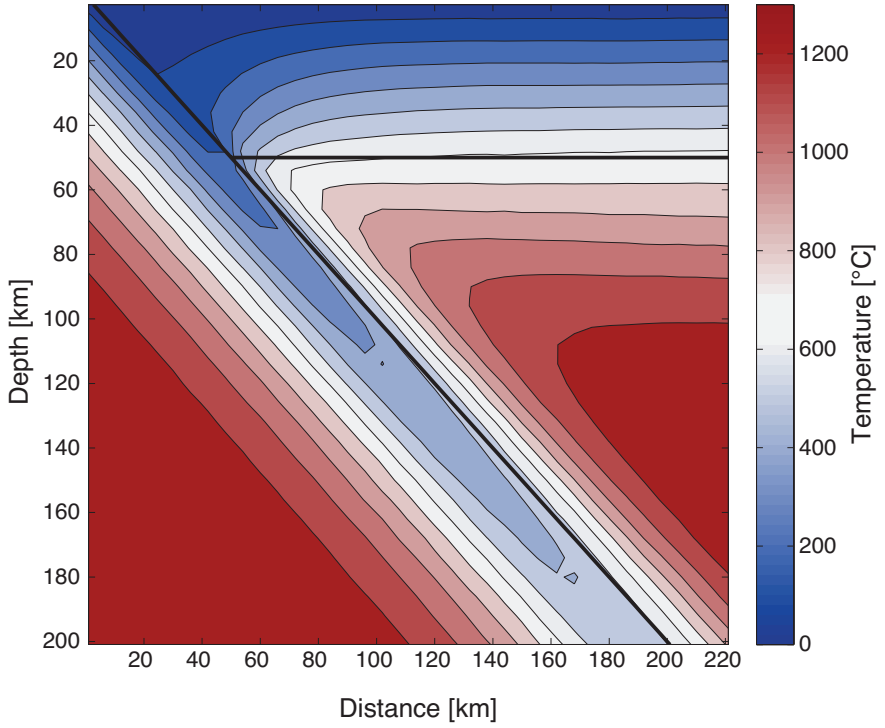

(b)

Fig. 2.20 (a) Model result for a triangular interpolation, 3km grid resolution run. (b) The model result but zoomed into the corner part of the wedge.

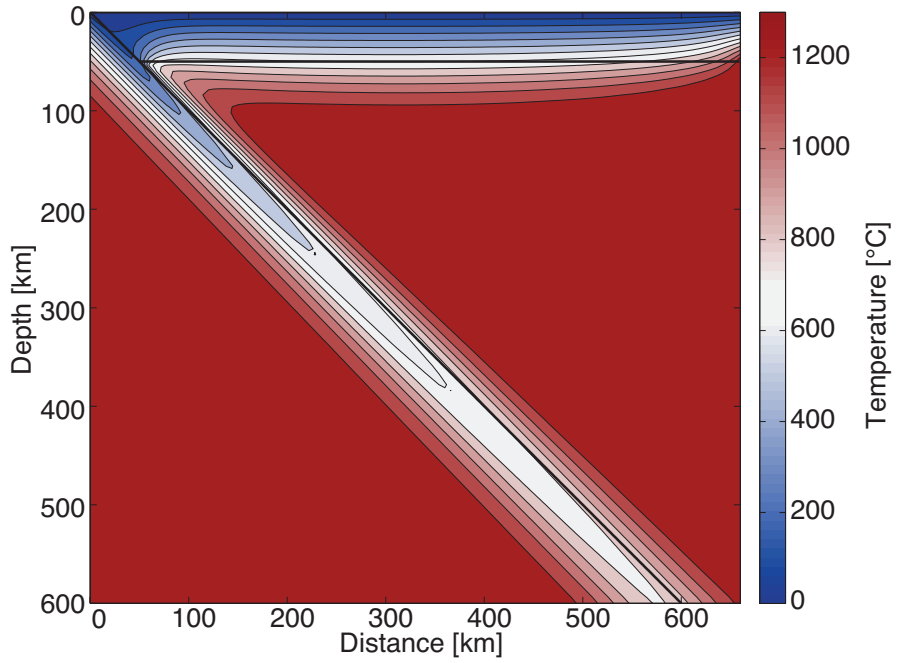

(a)

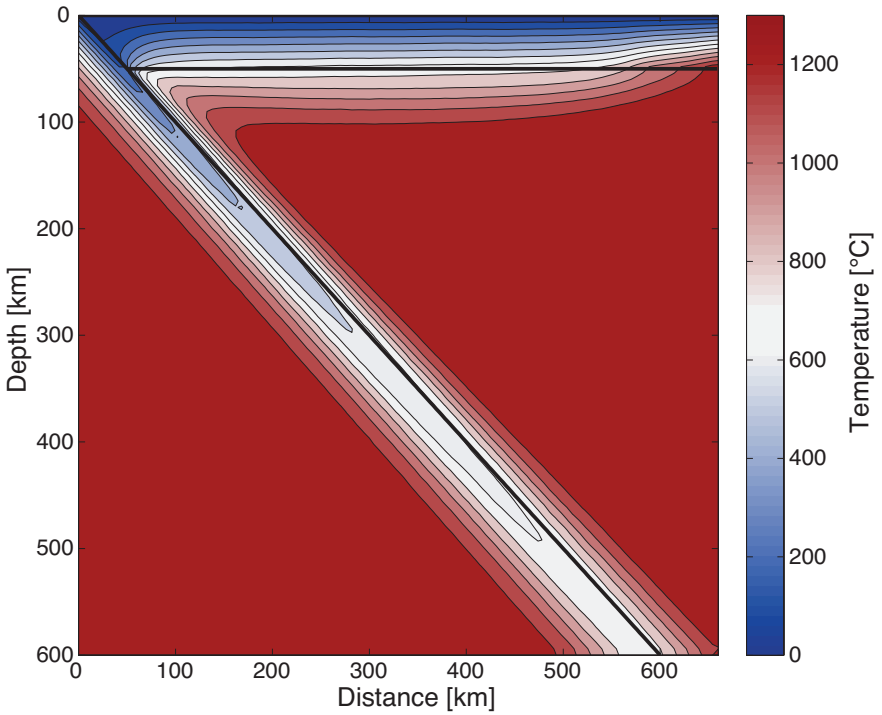

(b)

Fig. 2.21 (a) temperature field by (Van Keken et al., 2008) (b) model result. Visually they look very similar.

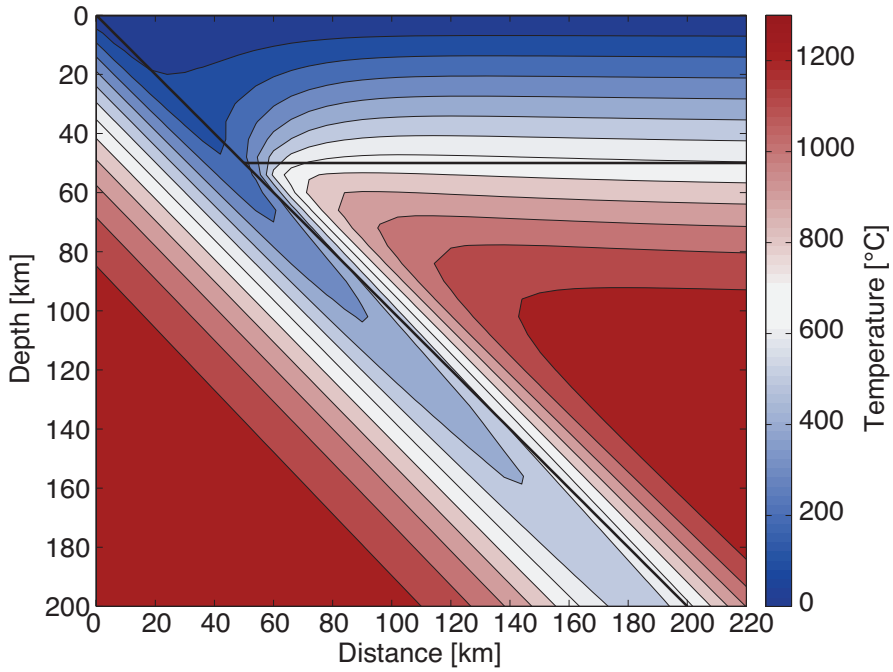

(a) Van keken zoom

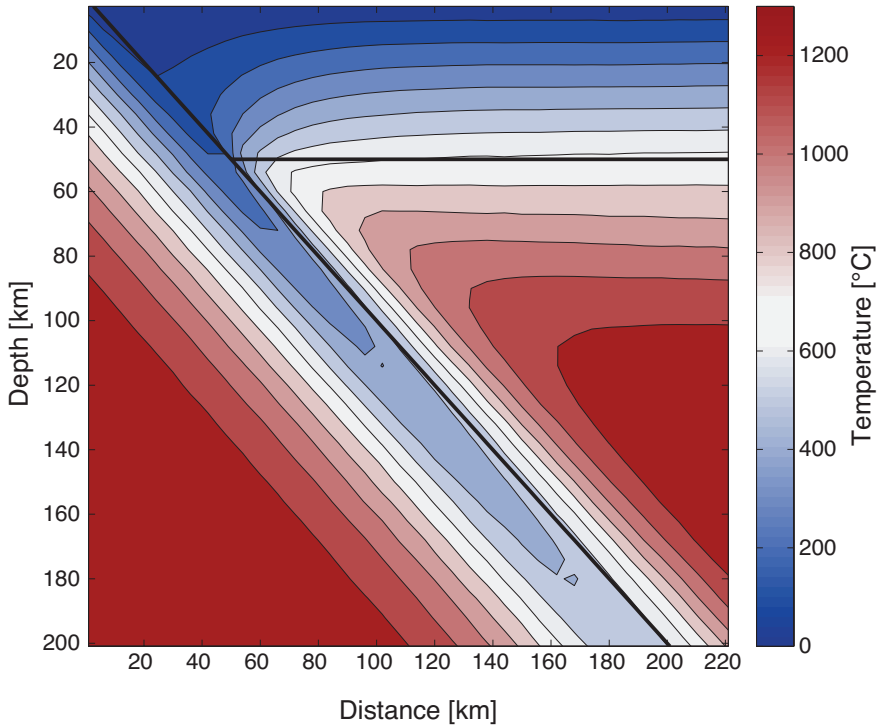

(b) Zoom in of model result

Fig. 2.22 Close up of wedge corner of temperature field from (Van Keken et al., 2008). (b) close up of model result.

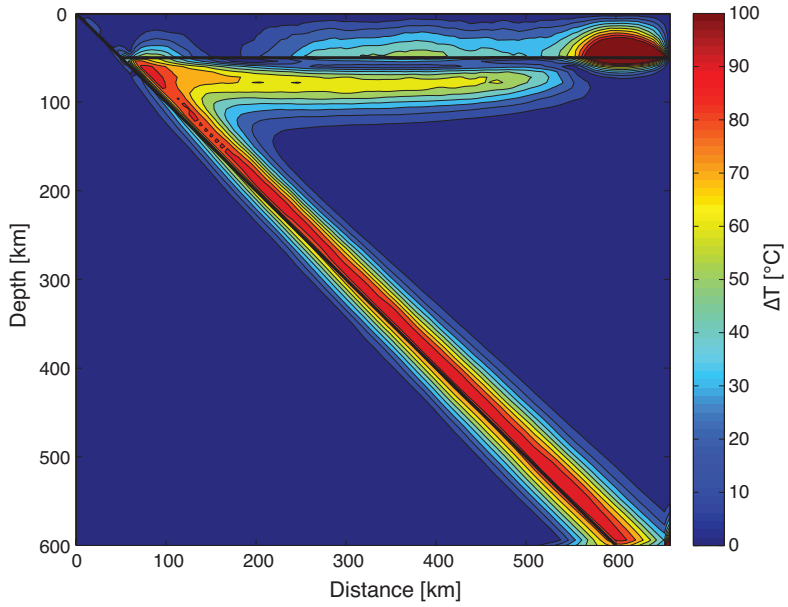

Fig. 2.23 Temperature difference between the thermal model result and the benchmark result from Van Keken et al. (2008). The largest temperature difference is closest to the slab and the core of the wedge has little to no temperature difference.

2.7 Discussion

The graphs of temperature of the 3 benchmark values show that the model temperature field does not fit the benchmark values. Whilst decreasing the grid size seemed to have some impact and cause the model temperatures to be closer to the benchmark values, the temperature change is not large enough. We cannot make the grid size any smaller, as it would be too computationally expensive. However if we look at the model temperature field as a whole and not just the three benchmark values, then the model temperature field is more similar to the benchmark temperature field. By subtracting the benchmark temperature field from the model temperature field we can see which regions have the greatest temperature differences compared to the benchmark temperature field. In Figure 2.23 we can see the edge of the subducting slab is the region with the largest temperature difference to the benchmark temperature field. However as the region closest to the slab has lower temperatures than the

rest of the wedge, melting is unlikely to occur here. Estimates of melt temperatures using geothermometers are in the range of 1200-1400 °C (Kelley et al., 2010; Kohut et al., 2006). This temperature range is found in the core of the mantle wedge where the temperature difference is very low compared to the benchmark. Consequently I have decided that although the thermal model does not match the benchmark values; the temperature difference between the thermal model and the benchmark in the core of the wedge is low enough to justify using this thermal model in melting calculations.

2.8 Summary

In this chapter I built a thermal model for a subduction zone using a finite difference, marker-in-cell method. The first part of the chapter covered the processes innvolved in building the thermal model. A thermal benchmark for subduction zones by Van Keken et al. (2008) was introduced. Parameters such as grid resolution, starting temperature and interpolation technique were investigated, and the final model used a 3km grid resolution, triangular interpolation with a starting background temperature of 1300°C. Higher resolutions would produce better results but are computationally more expensive. Visual comparison of my model result with the benchmark temperature field showed that my temperature field is very similar to the benchmark. However numerical comparision of the average values show that they do not fit the benchmark average values. However by plotting the difference in temperature between the thermal model and the benchmark, the largest temperature difference is closest to the slab, where the cooler temperatures make melting unlikely. The core of the mantle wedge where melting is most likely to occur, has little to no temperature difference between the thermal model and the benchmark. Based on this I have decided to use this thermal model moving forwards. The next step is to add water into the model via a hydraulic fracture and see whether melting occurs. The fracture path, melting parameterisation and incorporating them into the thermal model will be covered in the next chapter.

CHAPTER 3

FLASH MELTING

3.1 Introduction

The previous chapter showed the method for creating a thermal model for a subduction zone region. The model used a finite difference, marker-in-cell technique to solve the heat equation, with the advection being carried out by the markers. Comparison of the thermal model with the subduction zone temperature benchmark by Van Keken et al. (2008), showed that the model did not closely match the three benchmark values that were provided for comparison. However the temperature difference between the model and the benchmark in the region where melting is most likely to occur is small. As a consequence I decided to use the steady state temperature field for the next step of adding water to initiate melting.

In this chapter I test an extreme end member of the Davies (1999) hypothesis, that hydraulic fractures might transport water out into the mantle wedge. In this end member I consider that a fracture transports water immediately to the source region of subduction magmatism, generating partial melt instantaneously. I term this 'Flash melting'. The partial melt is then rapidly transported vertically to the surface, this melting scenario is shown in Figure 3.1 To implement this test, I use a hydrous melting parameterisation by Katz et al. (2003) to calculate the melting from the water added to the mantle wedge by a hydraulic

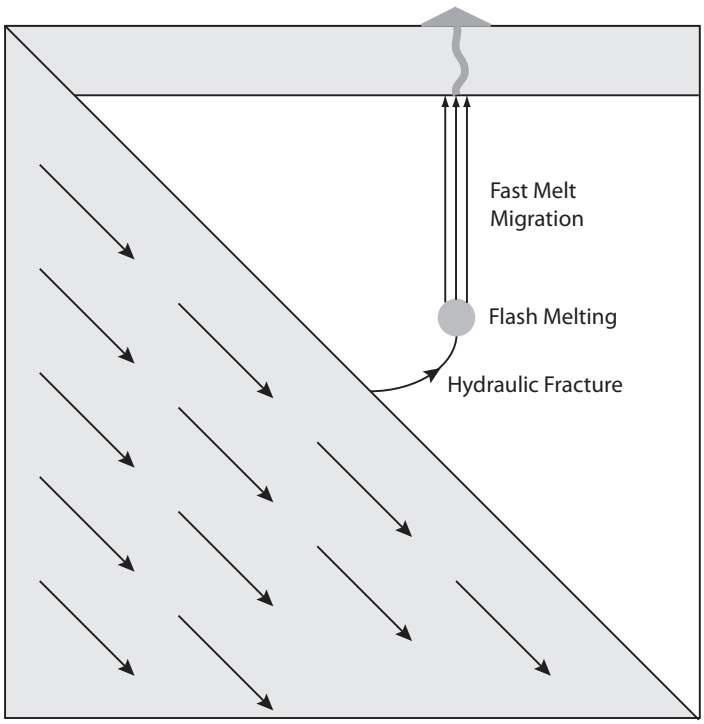

Fig. 3.1 Flash melting scenario. Water is added to the wedge via a hydraulic fracture causing instanteous melting. This is followed by rapid melt transport to the surface.

fracture. Different size fractures and source regions are used, giving 12 different bulk water contents. This will allow me to examine the effect bulk water content has on melting in the source region.

Structurally this chapter has six sections. The first section discusses the possible causes of hydraulic fracturing in the subducting slab and the path the hydraulic fracture will propagate. The second section focuses on the hydrous melting parameterisation I have chosen to use and covers the method and testing of the parameterisation. The third section is the method of combining the first and second sections with the steady state temperature field from the previous chapter to create a flash melting model. This section also discusses the water contents of the subducting slab, which leads to a range of water content inputs being chosen. The final three sections are firstly the results of the combined model for twelve different bulk water content cases, followed by a discussion of the results and finally a summary of the chapter.

3.2 Hydraulic fractures

I this section I discuss the hypothesis from Davies (1999), of hydraulic fractures being a way of transporting water from the subducting slab to the mantle wedge. First I cover possible causes of the hydraulic fracture and evidence for them occurring. Then I examine the direction the propagation of the hydraulic fractures would take in the mantle wedge.

3.2.1 Causes of hydraulic fractures in subduction zones

Davies (1999) hypothesised that intermediate depth seismicity (70-300 km deep) is caused by water released from dehydrating minerals. He used the theory from Green and Houston (1995) that decreasing the friction by high pore pressure could aid faulting. The hypothesis from Davies (1999) is that the high pore pressure is caused by non-percolating water. The faulting that occurs as a consequence interconnects the water pores, a hydrofracture then occurs when the water interconnects to a sufficient height. The hydrofracture would transport the water from the slab out into the mantle wedge. This addition of water to the mantle wedge would generate subduction zone magmatism. Peacock (2001) proposed a similar theory that intermediate depth earthquakes are triggered by serpentine dehydration reactions that occur tens of kilometres into the subducting plate. In this case the serpentine dehydration can encourage brittle failure by increasing the pore pressure (Meade and Jeanloz, 1991).

For hydraulic fractures to occur there needs to be water in the subducting slab. Peacock (2001) suggested that water could enter the subducting slab by faulting, caused by the subducting slab bending. At these bend faults seawater can infiltrate into the subducting slab causing the serpentinization. Ranero et al. (2003) used multibeam bathymetry and seismic data to show that bending related faulting occurs across the ocean trench slope. This promotes percolation of water deep into the slab enabling hydration. In the seismic data the reflectivity of the deep penetrating faults could be caused by water percolation and mineral

alteration along the fault planes. Ranero et al. (2003) suggest that serpentinized bend faults may rupture several times during their descent, due to increased relative concentrations of hydrous minerals. As the dimensions of the rupture area of intermediate depth earthquakes is similar to the depth penetration and along strike lengths of the bend faults, the implication is that this region is the subducted bend faults.

3.2.2 Direction of propagation of fractures

Davies and Stevenson (1992) derived an equation for the path of a hydraulic fracture based on the stress field, for the cornerflow solution, for a mantle wedge. They state that the least compressive stress controls the direction of propagation of fractures. The fracture will widen in this direction but will propagate perpendicular to the least compressive stress (Davies, 1999). This case is for a corner flow regime where the velocity field can be calculated exactly (Batchelor, 1967). Davies and Stevenson (1992) derived the following corner flow equations in a similar manner to the derivation by McKenzie (1969). Using Ψ as the stream function the velocity can be given by

$$(v_r, v_\theta) = (\frac{1}{r}\frac{\partial \Psi}{\partial \theta}, -\frac{\partial \Psi}{\partial r}) \tag{3.1}$$

then using the coordinate system as shown in Figure 3.2 we can find Ψ using an acute angle θ_d

$$\Psi = \frac{rv[(\theta_d - \theta)\sin(\theta_d)\sin(\theta) - \theta_d \theta \sin(\theta_d - \theta)]}{\theta_d^2 - \sin^2 \theta d} \tag{3.2}$$

Davies and Stevenson (1992) also state that the stress regime can be solved given the velocity field and a constant viscosity rheology with the deviatoric stresses as follows

$$\sigma_{rr} = 2\eta(\frac{\partial v_r}{\partial r}) \tag{3.3}$$

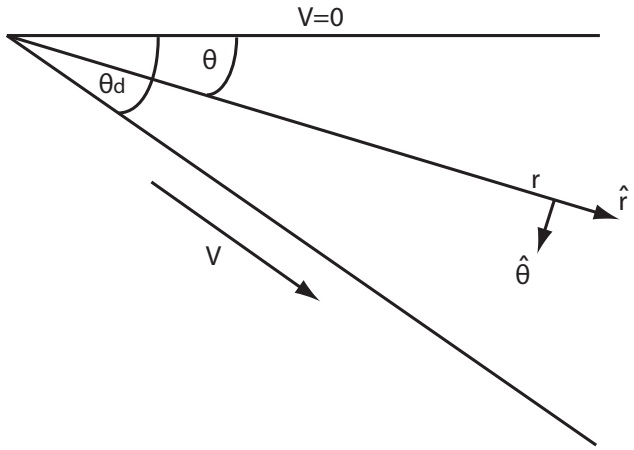

Fig. 3.2 Coordinate system used to calculate fracture path

$$\sigma_{\theta\theta} = 2\eta\left(\frac{1}{r}\frac{\partial v_\theta}{\partial \theta} + \frac{v_r}{r}\right) \tag{3.4}$$

$$\sigma_{r\theta} = \eta\left(\frac{1}{r}\frac{\partial v_r}{\partial \theta} + \frac{\partial v_\theta}{\partial r} - \frac{v\theta}{r}\right) \tag{3.5}$$

For this case:

$$\sigma_{rr} = \sigma_{\theta\theta} = 0 \tag{3.6}$$

and

$$\sigma_{\theta r} = \frac{2v\eta\left[\theta_d \cos(\theta_d - \theta) - \sin\theta_d \cos\theta\right]}{r(\theta_d^2 - \sin^2\theta_d)} \tag{3.7}$$

Equation (3.6) tells us that the normal stress perpendicular to the $r = constant$ and $\theta = constant$ surfaces is zero. Since we are dealing with deviatoric stresses, these surfaces must also be the surface of maximum shear stress (Twiss and Moores, 1992). Therefore since the planes that maximise the shear stress are always at 45° to the principal planes, the principal planes (and their perpendicular principal axes) are, in this case at 45° to the $r = constant$

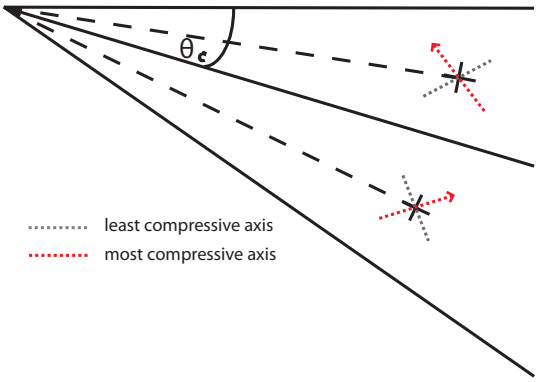

Fig. 3.3 Figure showing the orientation of the most and least compressive axes.

and $\theta = constant$ surfaces. In Figure 3.3 the least compressive axes are shown with the grey dotted lines and the most compressive axes shown with the red dotted lines. When the shear stress is positive, the maximum compressive axis is between the two coordinates axes, while the minimum compressive axis is between the two coordinate axes when the shear stress is negative. The line separating the two regimes is at an angle θ_c, called the critical angle. The critical angle is calculated using the dip as shown in equation (3.8). The arrows in Figure 3.3 indicate the general direction the fracture would propagate depending on its location above or below the critical angle.

$$\theta_c = \tan^{-1}\left(\frac{\sin\theta_d - \theta_d \cos\theta_d}{\theta_d \sin\theta_d}\right) \tag{3.8}$$

The equations from Davies and Stevenson (1992) for the path of the fracture are

$$r = r' \exp[(\theta_d - \theta)] \tag{3.9}$$

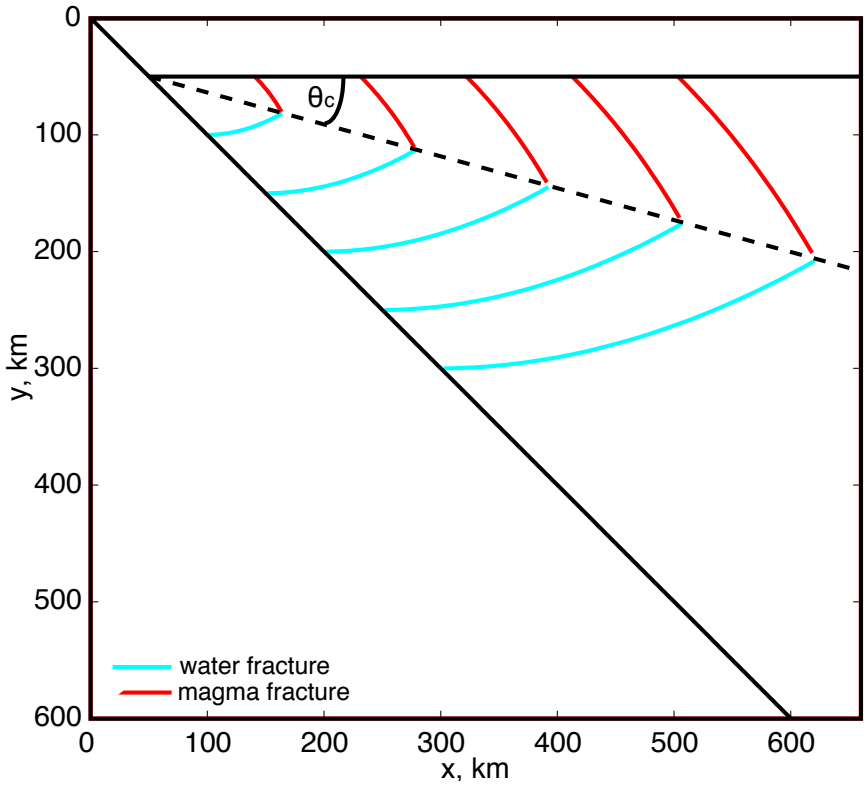

Fig. 3.4 Potential fracture paths plotted for starting points on subducting slab of 50, 100, 150, 200 and 250 km from the wedge corner respectively. For $\theta > \theta_c$ I assume a hydrofracture shown by the blue lines. For $\theta < \theta_c$ a magma fracture is assumed with the path shown with a dark red line.

for $\theta > \theta_c$ and

$$r = r_o \exp[\theta] \tag{3.10}$$

for $\theta < \theta_c$ with r' the point of intersection with the slab and r_o is the point of intersection of the overriding plate with the curve. However, as I will always start the curve from the slab I have changed r_o to be the intersection of the curve with the line $\theta = \theta_c$. Equation (3.10) then becomes

$$r = r_o \exp[-1(\theta_c - \theta)] \tag{3.11}$$

Fracture paths for different start points on the slab are shown in Figure 3.4

3.3 Wet melting parameterisation

In this section I discuss the hydrous melting parameterisation from Katz et al. (2003), and go through the method they use to find the melt fraction.

3.3.1 Structure of parameterisation

Parameter	For Calculating	Value	Units
A_1	$T_{solidus}$	1085.7	°C
A_2		132.9	°C GPa^{-1}
A_3		-5.1	°C GPa^{-2}
B_1	$T^{lherz}_{liquidus}$	1475.0	°C
B_2		80.0	°C GPa^{-1}
B_3		-3.2	°C GPa^{-2}
C_1	$T_{liquidus}$	1780.0	°C
C_2		45.0	°C GPa^{-1}
C_3		-2.0	°C GPa^{-2}
r_1	R_{cpx}	0.5	cpx/melt
r_2		0.08	cpx/melt/GPa
β_1	F	1.5	
β_2		1.5	
K	$\Delta T(X_{H_2O})$	43	°C wt%$^{-\gamma}$
γ		0.75	
D_{H_2O}		0.01	
χ_1	$X^{sat}_{H_2O}$	12.0	wt% GPa$^{-\lambda}$
χ_2		1.0	wt% GPa$^{-\lambda}$
λ		0.6	

Table 3.1 Parameters and their values used in the parameterisation. Reproduced from Katz et al. (2003).

The parameterization by Katz et al. (2003) has the form $F = f(P,T,X_{H_2O},M_{cpx})$. F is the weight fraction of melt, P is pressure in GPa, T is the temperature in degrees Celsius, X_{H_2O} is the weight fraction of water in the melt and M_{cpx} is the modal clinopyroxene (cpx) of the residual (or unmelted) peridotite. The parameters in Table 3.1 are used in the parameterisation. The following seven concepts and principles are incorporated into the parameterisation:

1. F, the isobaric melting function should increase monotonically, with $\partial F/\partial T|_{P,X_{H_2O}}$ the isobaric productivity increasing as a function of T (Hirschmann et al., 1999). Despite the existing experimental data not clearly showing this effect, Katz et al. (2003) use this constraint as long as the phase assemblage remains constant.

2. When the major phases are exhausted from the residue $F(T)$ should be kinked. At this point productivity should decrease then increase, as it does for melting in a low-F regime (Hirschmann et al., 1999).

3. The melt reaction coefficient of cpx is only a function of pressure for a peridotite with fertile mineral compositions. Therefore given the pressure of melting and the modal cpx of the peridotite being melted, $F_{cpx-out}$ can be predicted (Longhi, 2002; Pickering-Witter and Johnston, 2000).

4. F should monotonically increase at constant P and T due to the addition of water in a peridotite system. For small $X_{H_2O}^{bulk}$, $F(X_{H_2O})$ should approximately be a linear increasing function at constant P and T. Also with increasing T the slope of the curve should increase (Hirose, 1997; Hirschmann et al., 1999).

5. The solidus should lower in proportion with X_{H_2O} due to the addition of water to a peridotite system. The liquidus of the solid should also lower. For modest bulk water contents and melt fractions near one, at the liquidus the weight percent dissolved water is small as it is diluted by silicate melt. Therefore the liquidus can only be lowered significantly by extreme water contents.

6. Katz et al. (2003) assume that water may be treated as an incompatible element after Asimow and Langmuir (2003). The addition of water depresses the solidus until saturation of the melt occurs. The amount of water at saturation is dependent on the pressure. Productivity above the wet solidus stays low until a temperature near the dry

solidus. This is because as melting occurs the amount of water in the liquid decreases, the influence of water decreases (Hirschmann et al., 1999).

7. Experiments show at atmospheric pressure, $X_{H_2O}^{saturated}$ is zero, at 1 GPa it is about 13wt% and rises as pressure increases (Mysen and Wheeler, 2000).

3.3.2 Anhydrous Melting

The first step of the Katz et al. (2003) parameterisation is to look at the parameterisation of dry melting or anhydrous melting. Prior to the exhaustion of cpx, F_{cpx} is the degree of melting. $F_{cpx}(T,P)$ is difficult to determine directly. Katz et al. (2003) use a similar technique to McKenzie and Bickle (1988), where instead F_{cpx} is calculated in terms of a dimensionless temperature T' in this case it is parameterised as a power law:

$$F_{cpx}(T') = [T'(T,P)]^{\beta_1} \tag{3.12}$$

where

$$T'(T,P) = \frac{T - T_{solidus}(P)}{T_{liquidus}^{lherz}(P) - T_{solidus}(P)} \tag{3.13}$$

T' is the fractional distance in temperature between the solidus and lherzolite liquidus. The temperature T is in Kelvin and the pressure dependence is contained within $T_{solidus}$ and $T_{liquidus}^{lherz}$. These are calculated using the same form suggested by Hirschmann (2000):

$$T_{solidus} = A_1 + A_2P + A_3P^2 \tag{3.14}$$

$$T_{liquidus}^{lherz} = B_1 + B_2P + B_3P^2 \tag{3.15}$$

with pressure in GPa. The lherzolite liquidus $T_{liquidus}^{lherz}$ was introduced by Katz et al. (2003) to create a kinked melting function. This can be thought as the temperature the liquidus would

have if the melting from equation (3.12) continued to $F = 1$. This is if cpx remained in the residue. Cpx-out occurs before $F = 1$, at this point there is a change in the productivity of the system. For a batch (closed) system;

$$F_{cpx-out} = \frac{M_{cpx}}{R_{cpx}(P)} \tag{3.16}$$

where M_{cpx} is the weight fraction of cpx being isobarically melted in the solid peridotite and R_{cpx} is the reaction coefficient for cpx. Katz et al. (2003) used experimental results from Longhi (2002), Pickering-Witter and Johnston (2000) and Walter (1998) to give the reaction coefficient R_{cpx} a pressure dependence as follows;

$$R_{cpx} = (P) = r_0 + r_1 P \tag{3.17}$$

When $F > F_{cpx-out}$, mostly orthopyroxene (opx) is consumed as the melting reaction changes with the melting function;

$$F_{opx}(T) = F_{cpx-out} + (1 - F_{cpx-out} \left[\frac{T - T_{cpx-out}}{T_{liquids} - T_{cpx-out}} \right]^{\beta_2} \tag{3.18}$$

where

$$T_{cpx-out} = F_{cpx-out}^{\frac{1}{\beta_1}} \left(T_{liquidus}^{lherz} - T_{solidus} \right) + T_{solidus} \tag{3.19}$$

where $T_{liquidus}$ is the liquidus of the modal peridotite system which is dependent on pressure as follows;

$$T_{liquidus} = C_1 + C_2 P + C_3 P^2 \tag{3.20}$$

Figure 3.5 shows the shape of the melting function at different pressure. The curves are clearly kinked which is the point of cpx-out.

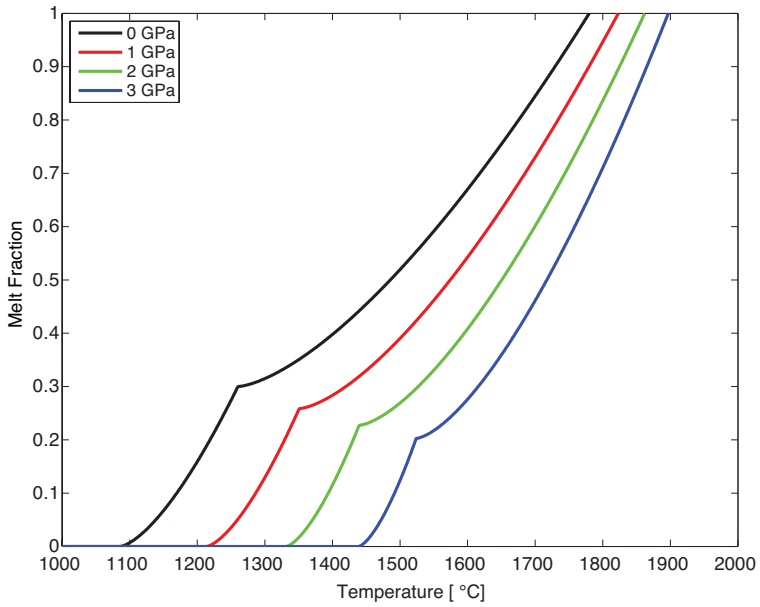

Fig. 3.5 Plots of melt fraction against temperature for different pressures. The curves are clearly kinked which is the point of cpx-out. This is a reproduction of Figure 2 from Katz et al. (2003) using my MATLAB code.

3.3.3 Hydrous Melting

Once Katz et al. (2003) had parameterized anhydrous melting they extended it to include the addition of water to the system. They specify the weight fraction of dissolved water in the melt (X_{H_2O}) and the weight fraction of bulk water ($X^{bulk}_{H_2O}$). They made the following changes to the anhydrous parameterization:

$$T_{solidus}(P) \rightarrow T_{solidus}(P) - \Delta T(X_{H_2O}) \tag{3.21}$$

$$T^{lherz}_{liquidus}(P) \rightarrow T^{lherz}_{liquidus}(P) - \Delta T(X_{H_2O}) \tag{3.22}$$

$$T_{liquidus}(P) \rightarrow T_{liquidus}(P) - \Delta T(X_{H_2O}) \tag{3.23}$$

where $T(X_{H_2O})$ is the decrease in temperature due to the water content in the melt X_{H_2O} . This function must satisfy the following two conditions:

$$\Delta T(X_{H_2O} = 0) = 0 \tag{3.24}$$

$$\Delta T(X_{H_2O} \geq X^{sat}_{H_2O}) = \Delta T(X^{sat}_{H_2O}) \tag{3.25}$$

where $X^{sat}_{H_2O}(P)$ is the weight percent of water in a saturated melt. Katz et al. (2003) use the condition in equation (3.25) as water is not computed as a separate vapour phase beyond the saturation of the melt, it is accounted for in the fluid phase that includes the saturated melt. Katz et al. (2003) use this condition as the water content beyond saturation has no effect on the thermodynamic properties, such as liquidus of the melt. The simplification also enabled them to use a standard two-phase fluid mechanical formulation for melt transport (McKenzie, 1984). Katz et al. (2003) chose a form for $\Delta T(X_{H_2O})$ that at low water contents has a steep slope and after that grows more slowly. This fits the data within their uncertainties shown in Figure 3.6. The form for $\Delta T(X_{H_2O})$ is as follows;

$$\Delta T(X_{H_2O}) = K X^{\gamma}_{H_2O}, \quad 0 < \gamma < 1 \tag{3.26}$$

Figure 3.7 shows the solidus for a range of bulk water contents. Below 2 GPa the water saturation concentration is constrained by the experiments of Mysen and Wheeler (2000). At higher pressures, Katz et al. (2003) estimate the water saturation concentration by requiring it to be consistent with the results of Kawamoto and Holloway (1997) for the water saturated solidus. Their water saturation concentration $X^{sat}_{H_2O}$ takes the form;

$$X^{sat}_{H_2O} = \chi_1 P^{\lambda} + \chi_2 P, \quad 0 < \lambda < 1 \tag{3.27}$$

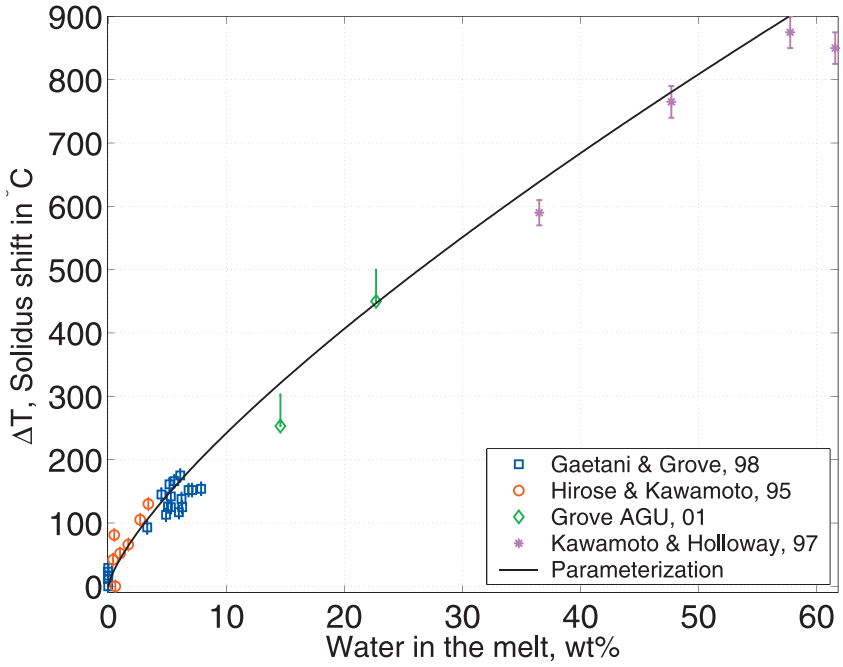

Fig. 3.6 Figure 8a. from Katz et al. (2003) showing the calibration of $\Delta T(X_{H_2O})$. For the additional references used for the data points refer to Katz et al. (2003).

Katz et al. (2003) decided to treat water as a regular trace element and use a bulk distribution coefficient (D_{H_2O}) to model the equilibrium partition between the solid and melt. Using D_{H_2O}, X_{H_2O} takes the form;

$$X_{H_2O} = \frac{X^{bulk}_{H_2O}}{D_{H_2O} + F(1 - D_{H_2O})} \tag{3.28}$$

To preserve simplicity in the parameterisation Katz et al. (2003) chose a constant D_{H_2O} value of 0.01.

The melting function for $F \leq F_{cpx-out}$ is;

$$F\left(P,T,X^{bulk}_{H_2O}\right) = \left[\frac{T - \left(T_{solidus} - \Delta T\left(X_{H_2O}\left(X^{bulk}_{H_2O},P,F\right)\right)\right)}{T^{lherz}_{liquidus} - T_{solidus}}\right]^{\beta_1} \tag{3.29}$$

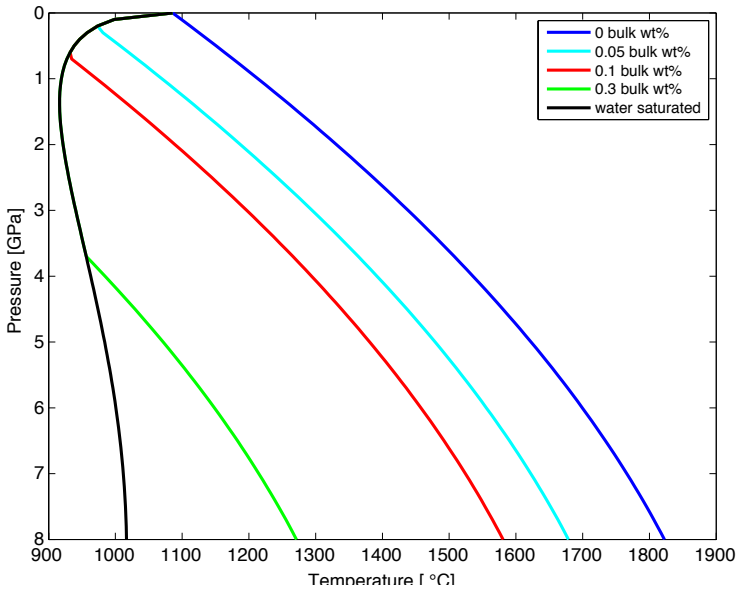

Fig. 3.7 The solidus for different bulk water weight percentages. The solidus depression is linear with dissolved water. The solidus lines are bounded by the saturation value of water in the melt, which is dependent on pressure. Reproduced from Katz et al. (2003) using my MATLAB code.

as ΔT depends on F, equation (4.13) has F on both sides of the equation. There is no analytical solution for F, so it must be solved for numerically. This is done using a root finder, in this case the Matlab function FZERO was used.

Figure 3.8 shows the melting curves for pressure of 1 GPa with different bulk water contents. The solidus decreases greatly with small increases in water content but with little additional melting. At low temperatures of the 0.3 wt% bulk water content the water saturation levels are exceeded causing F to sharply increase with temperature. Figure 3.9 shows the degree of melting against bulk water content holding the pressure and temperature constant. As bulk water increases the degree of melting increases, and the degree of melting is greater for higher temperatures.

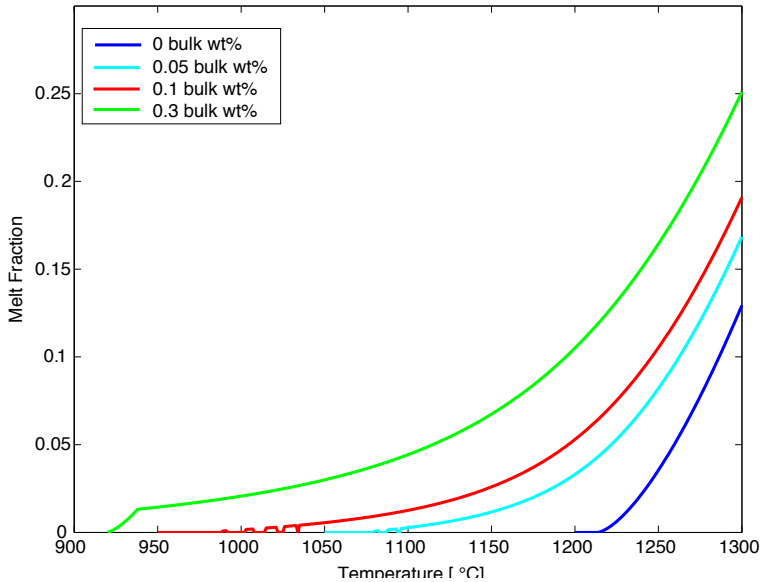

Fig. 3.8 Melting curves with different bulk water contents at 1GPa. The melting curve for 0.3 wt% bulk water content is saturated at the solidus. Reproduced from Katz et al. (2003) using my MATLAB code.

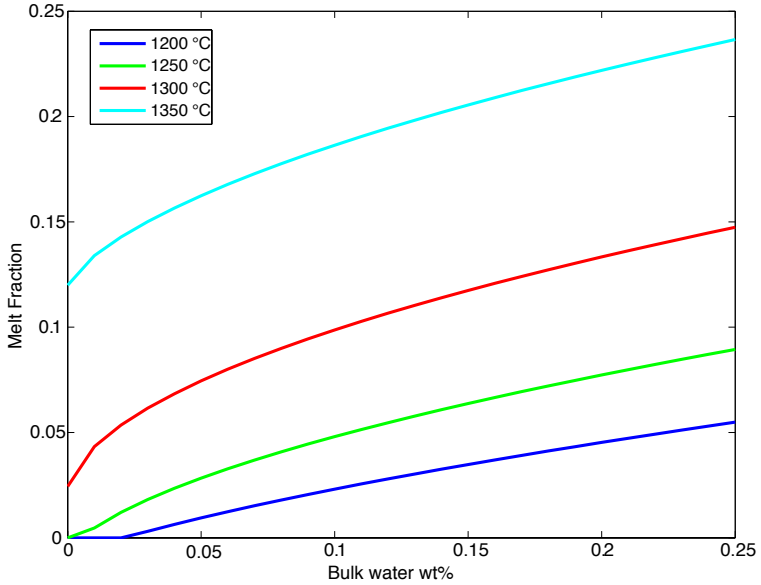

Fig. 3.9 Melt fraction as a function of $X_{H_2O}^{bulk}$ holding the pressure constant for 4 different temperatures. Reproduced from Katz et al. (2003) using my MATLAB code.

3.4 Modelling the melting due to hydraulic fracture

The next step is to combine the hydrous melting parameterisation, fracture path propagation and the steady state temperature field, to allow modelling of the melting due to hydraulic fracture. First I need to calculate the bulk water weight fraction to use in the hydrous melting parameterisation. Estimating the water flux from a subduction zone is difficult, there have been many different estimates of the input and output flux of water from a subduction zone. Some of these values have been summarised in Table 3.2. In my calculations I will use the global water flux estimate from van Keken et al. (2011) for the case with 2 km serpentinised upper mantle. I will use the sum of the water flux for depth down to 230 km which is 6.6×10^8 Tg Myr^{-1}.

	P90	B95	J03	SP03	R04	H08	VK11 ws	VK11 w/os
Subduction zone H_2O input								
Sediment	0.7	0.3-1.4	1.2		1.6	1.5	0.7	0.7
Igneous crust	8	9-18	6		4.6	6.1	6.3	6.3
Mantle				4.9-8.6	2.4-12	5.7	3.0	0
Total input	8.7	9-19		9-12	9-18	13	10.0	7
Slab H_2O output to wedge								
$<$100 km depth				4.8-7.5			3.2	3.2
100-150 km				1.8-8.0			1.4	3.2
150-230 km				1.6-3.6			2.0	0.6
$>$230 km				0-10			3.4	2.2

Table 3.2 Estimates of global subduction zone water flux in 10^8 Tg Myr^{-1}. P90, Peacock (1990); B95, Bebout (1995); J03, Jarrard (2003); SP03, Schmidt and Poli (2003); R04, Rüpke et al. (2004); H08, Hacker (2008); VK11, van Keken et al. (2011); w s, with 2km serpentinised upper mantle (2 wt %); w/o s, without serpentinised upper mantle. Table reproduced from van Keken et al. (2011).

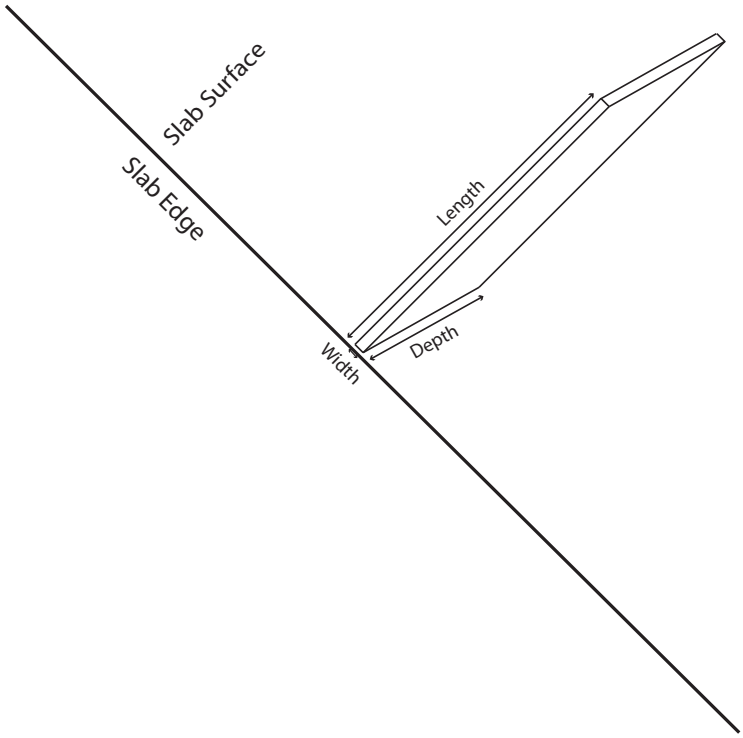

Fig. 3.10 Schematic of the hydraulic fracture dimensions.

3.4.1 Weight fraction of water

The weight percentage of bulk water is calculated using two parameters; fracture size and the area of the mantle that the water affects, which will be called the search radius. By varying the fracture size and search radius, I can calculate a range of bulk water weight percentage.

For the fracture size Dahm (2000) chose a length of 400 m with a cross sectional area of 20 m^2 for the water filled fractures and 14 km length and a cross sectional area of 5×10^4 m^2 for magma fractures. The fracture size I choose should fall within this range. The fracture size has three dimensions, length , width and depth/strike as shown in Figure 3.10 so even though our model is in 2D I need to take account of the depth of the fracture in the calculations.

To find the mass of the mantle inside the search radius I need to find the volume of the region. This is the area of the search radius multiplied by the fracture depth. For all fractures the assumed depth is 1 km. I then multiplied by the density of the mantle to calculate the mass of this region. The mass of the water in the fracture is calculated by multiplying the volume of the fracture by the density of water. To find the bulk water content $X_{H_2O}^{bulk}$, equation (3.30) is used:

$$X_{H_2O}^{bulk} = \frac{M_w}{M_m + M_w} \times 100 \tag{3.30}$$

Where M_w is the mass of the water and M_m is the mass of the mantle.

Iwamori (1998) used a range of $X_{H_2O}^{bulk}$ varying from 0 - 5 wt% in his models, so I tried to fit this range by choosing different fracture sizes and search radii to calculate the $X_{H_2O}^{bulk}$ values. The calculated $X_{H_2O}^{bulk}$ weight percentages are shown in Table 3.3. The $X_{H_2O}^{bulk}$ weight percentages vary from 0.086 wt% for the largest search radius and smallest fracture size to 2.996 wt% for the smallest search radius and largest fracture size. The fracture sizes were larger than the water filled fracture sizes of Dahm (2000), but they are smaller than the magma filled fracture sizes that he used. Using smaller search radii would have allowed for smaller fracture sizes however as the grid size of the model is 3km by 3km containing on average 35 markers per grid cell, there would be increased chance that no markers would be found within the smaller search radii.

		Search radius		
		0.5 km	1 km	1.5 km
Fracture size	2km x 1km x 10 m	0.766 %	0.193 %	0.086 %
	4km x 1km x 10 m	1.52 %	0.385 %	0.171 %
	6km x 1km x 10 m	2.264 %	0.576 %	0.257 %
	8km x 1km x 10 m	2.996 %	0.763 %	0.342 %

Table 3.3 Bulk water weight percentages calculated for a range of fracture sizes and search radii.

3.4.2 Method for modelling the melting

The following method is used to calculate the melting, due to water being added by a hydraulic fracture:

1. Find the hydrofracture end point. I chose a random start point on the slab with the depth varying from 50 km to 230 km. This depth region is where intermediate depths earthquakes occur (Davies, 1999). Then by choosing a random angle between the critical angle and the dip, equation (3.11) is used to calculate the point along the fracture path, which will be the fracture end point.

2. Add water to markers, within the search radius, from the fracture end point. Once the fracture end point has been found the grid cell that it is located in is found. In case the fracture end point is near a grid cell boundary, the grid cell either side of the grid cell with the fracture end point are found. For this region all the markers are tested to see if their distance from the fracture end point is less than the search radius. If the distance is less than the search radius then the marker is given the marker composition of 2, which is 'water added'. The marker now has a bulk weight water percentage taken from Table 3.3.

3. Calculate melt fraction. The hydrous melting parameterisation from section 3 is used to calculate the melt fraction. Equation (4.13) is turned into a function so that the Matlab function FZERO can be used to find the root of the equation which gives the melt fraction. The temperature T is taken from the marker temperatures of the steady state temperature field of the thermal model. As noticed when testing the parameterisation from Katz et al. (2003), the FZERO function struggles to find low values for a single initial search value. To overcome this, FZERO searches over a possible range of F from 0 - 0.2 with an increment of 0.001. This allows the values near zero to be found.

4. Check for water saturation. Equation (3.28) is used to calculate the water content percentage in the melt. This is compared with the water saturation concentration calculated using equation (3.27). If the water content percentage is greater than the water saturation concentration, the melt fraction is recalculated using the water saturated concentration instead.

For each of the twelve different $X_{H_2O}^{bulk}$ values, the melt fractions were found for markers within the corresponding search radius for 1000 random fracture end points. The results for these twelve cases are shown in the next section. For these cases the assumption is that once melt occurs it is transported vertically to the surface and is removed from the system.

3.5 Results

This section shows the results for the twelve cases each run for 1000 random fracture end points. I will examine the differences in melt fraction, melt volume and water content in the melt between the different cases.

3.5.1 Melt Fraction

In Figure 3.11, I have plotted melt fraction against distance for each of the twelve $X_{H_2O}^{bulk}$ values. The plots are all to the same scale to allow visual comparison. The plots correspond to search radius increasing left to right and fracture size increasing top to bottom. The highest melt fractions recorded were for the highest bulk water weight percentage of 2.996 %. The lowest bulk water weight percentage of 0.086 % did not cause any melt in any of the 1000 runs, so the water content must have been too low to cause melting. The melt fractions increase from right to left and from top to bottom which corresponds to an increase in fracture size but a decrease in search radius. Overall the higher the bulk water weight percentage the higher the melt fraction values.

For the markers within the search radius for each of the fracture end points I have plotted their location with the colour of the dot representing the melt fraction. I did this for three different $X_{H_2O}^{bulk}$ values; 0.766 wt% shown in Figure 3.12, 1.52 wt% shown in Figure 3.13 and 2.996 wt% shown in Figure 3.14. For all three Figures the region with the largest melt fraction was the area between 100 and 200 km depth and 150 to 400 km distance. The melt fraction values in Figure 3.14 show melt fractions that are $\sim$ four times higher than Figure 3.12. The region of melting increases with $X_{H_2O}^{bulk}$ but all three Figures show that the region directly next to slab does not melt even with a higher $X_{H_2O}^{bulk}$ value.

3.5.2 Melt Volume

To calculate the mass of the markers we assume the depth of the fracture is the depth of the whole region so the volume of the region is the area multiplied by the depth. To calculate the mass of each marker, I multiply the background density (3300 kg m^{-3}) by the volume of the region. This is then divided by the total number of markers to get the mass of the individual markers. I am assuming that all the markers have the same mass. To calculate the melt volume the mass of the marker is divided by the density, then multiplied by the melt fraction. Figure 3.15 is a bar chart of the total melt volume in km^3 as a function of horizontal distance. The bins of horizontal distance are 10 km wide. To do this I found the average melt volume for each fracture end point then found which ten km bin it corresponded to. The melt volumes in each bin were then summed to give the total volume for each bin. As with the melt fraction the melt volume increases with fracture size and smaller search radii. The largest total melt volumes occured between 150 km and 300 km distance. The total melt volume for each $X_{H_2O}^{bulk}$ is found by finding the sum of each bin from Figure 3.15. Figure 3.16 plots the total volume in km^3 against $X_{H_2O}^{bulk}$ values. A best fit line was plotted through the data that shows the total volume of the partial melt increases linearly with $X_{H_2O}^{bulk}$ values.

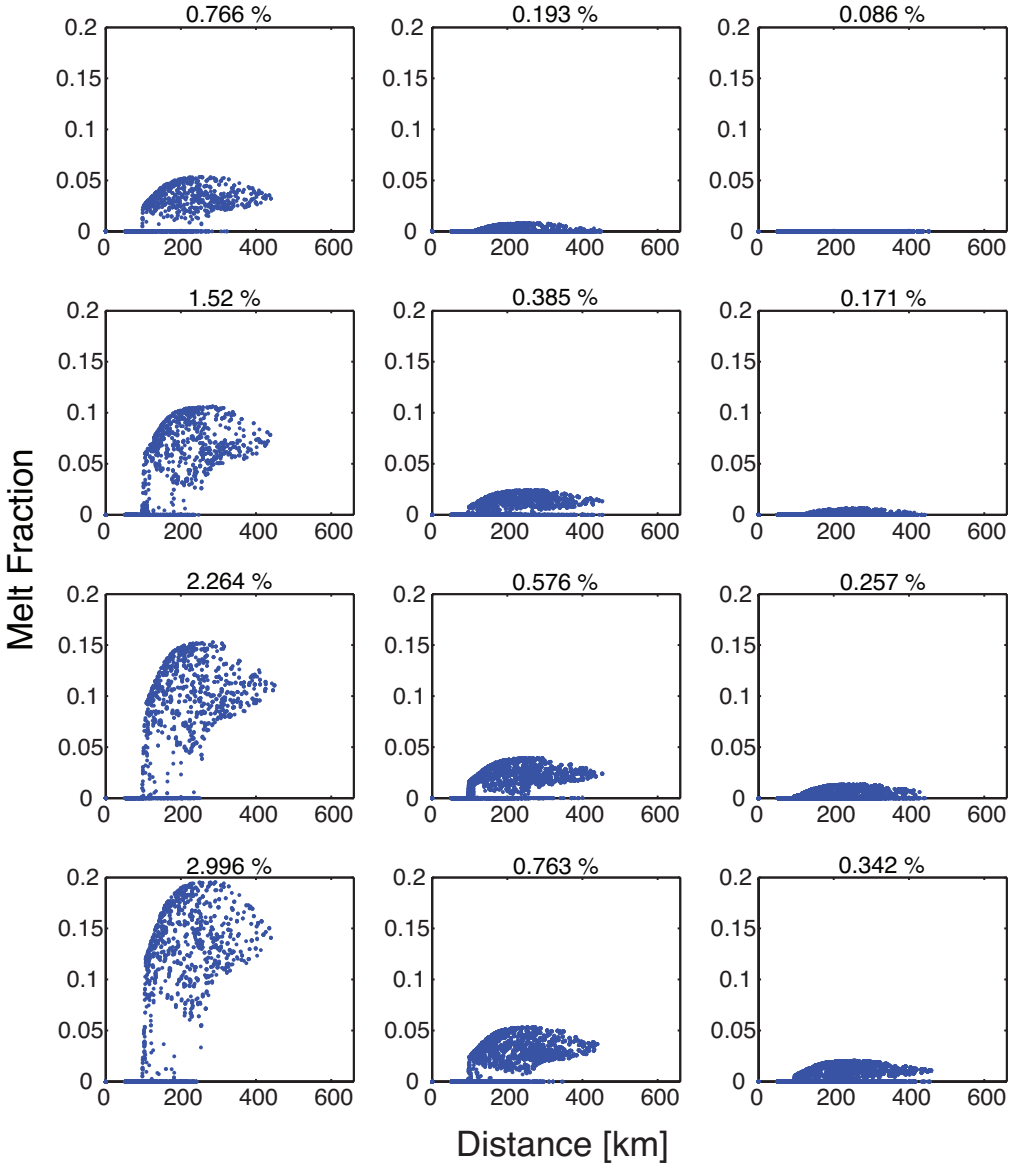

Fig. 3.11 Melt fraction as a function of distance for the 12 different $X_{H_2O}^{bulk}$ (labelled at the top of individual subplots).

3.5.3 Water Content in the Melt X_{H_2O}

I calculated the water content in the melt based on step 4 from the method in Section 5.

Figure 3.17 plots the X_{H_2O} for each fracture end point against distance for each of the twelve

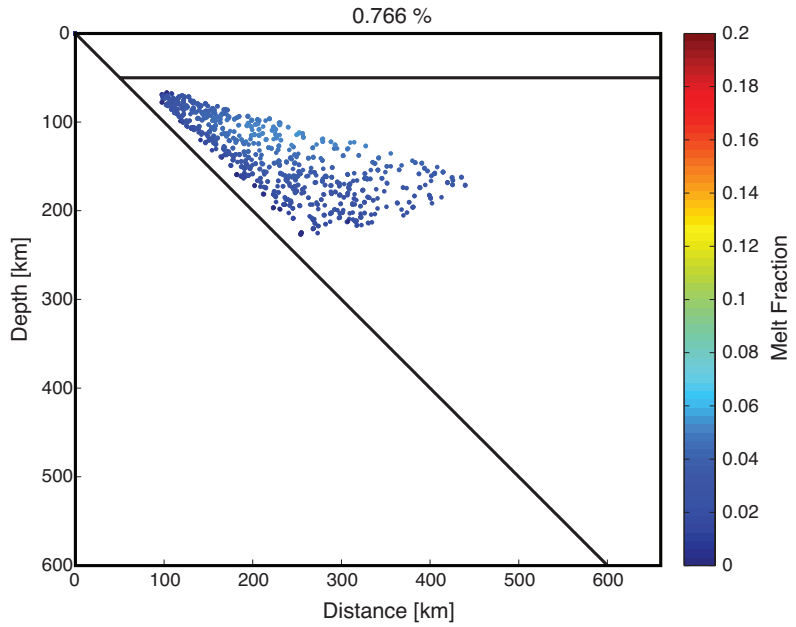

Fig. 3.12 Scatter plot of melt fraction for $X_{H_2O}^{bulk}$ of 0.766 wt%

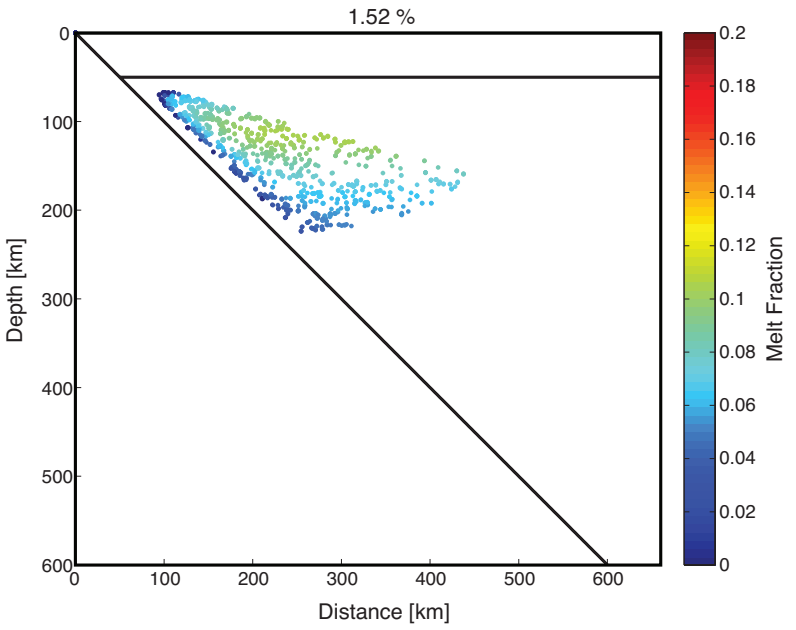

Fig. 3.13 Scatter plot of melt fraction for $X_{H_2O}^{bulk}$ of 1.52 wt%

$X_{H_2O}^{bulk}$ values. There is less difference in X_{H_2O} between each of the cases compared to melt

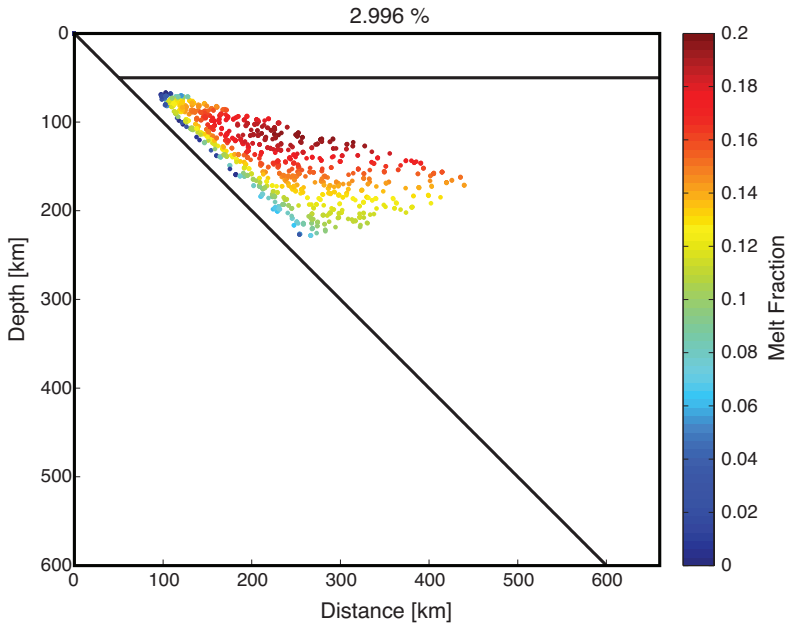

Fig. 3.14 Scatter plot of melt fraction for $X_{H_2O}^{bulk}$ of 2.996 wt%

fraction or melt volume, only the lowest values of $X_{H_2O}^{bulk}$ have a small range of X_{H_2O} values. The X_{H_2O} varies between $\sim$ 15 and $\sim$ 50 % for most of the cases.

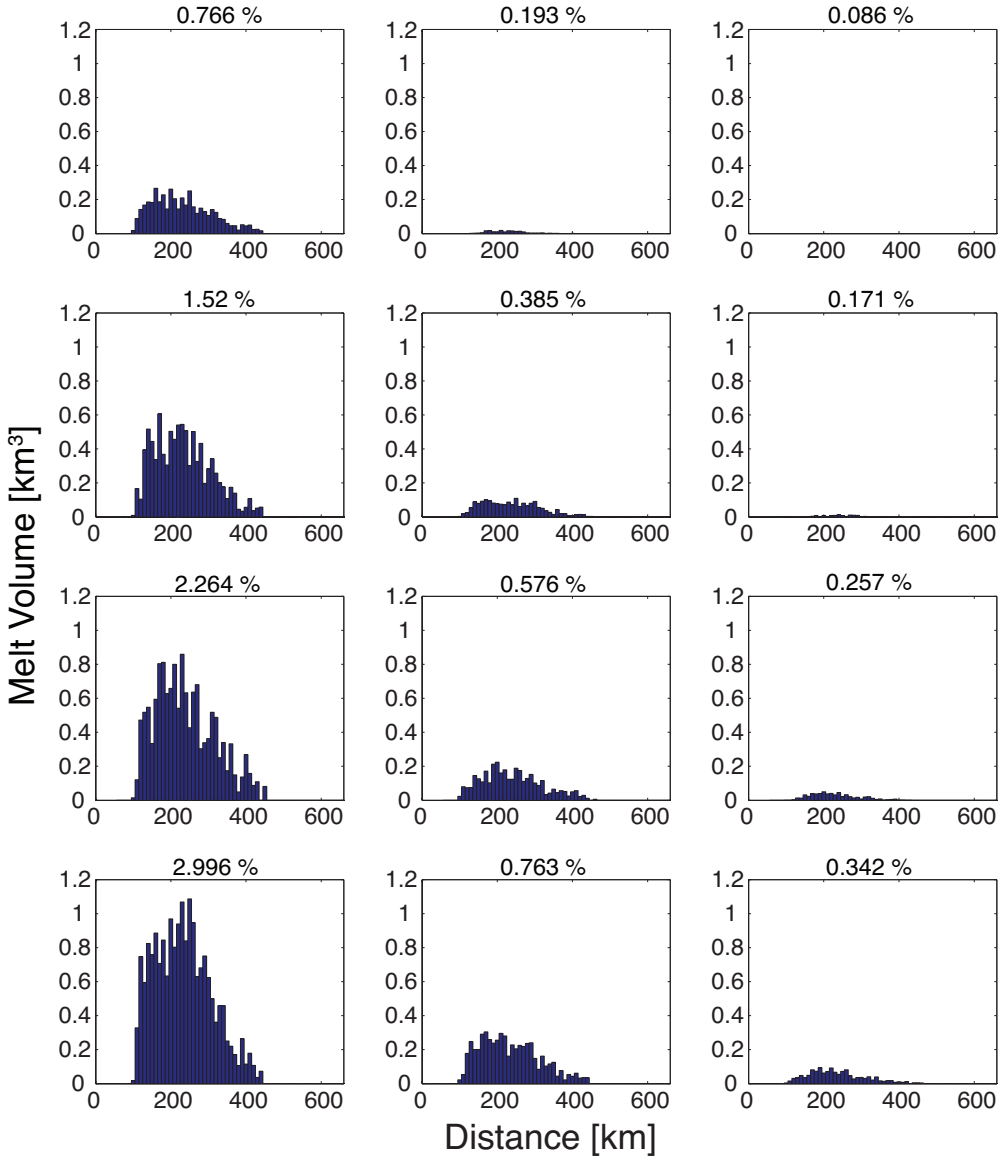

Fig. 3.15 Total melt volume found for 10 km sized bins for 12 different $X_{H_2O}^{bulk}$

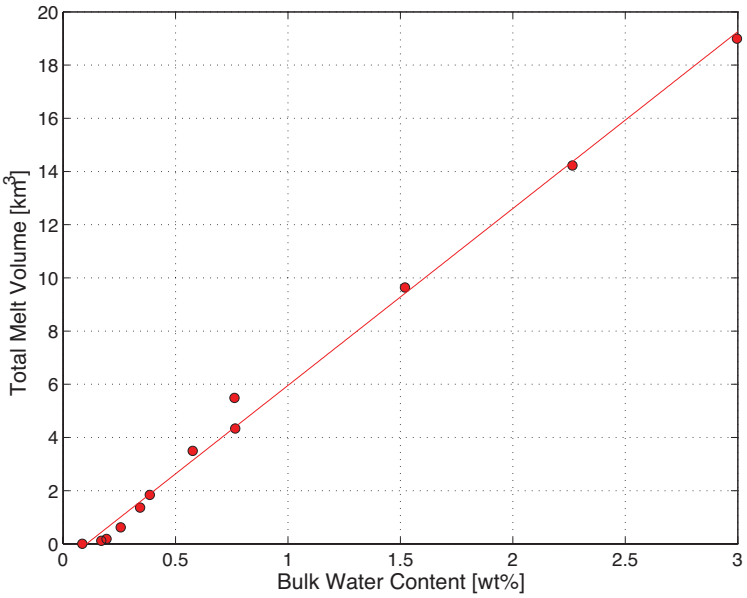

Fig. 3.16 Total melt volume of all the partial melt events plotted against $X_{H_2O}^{bulk}$

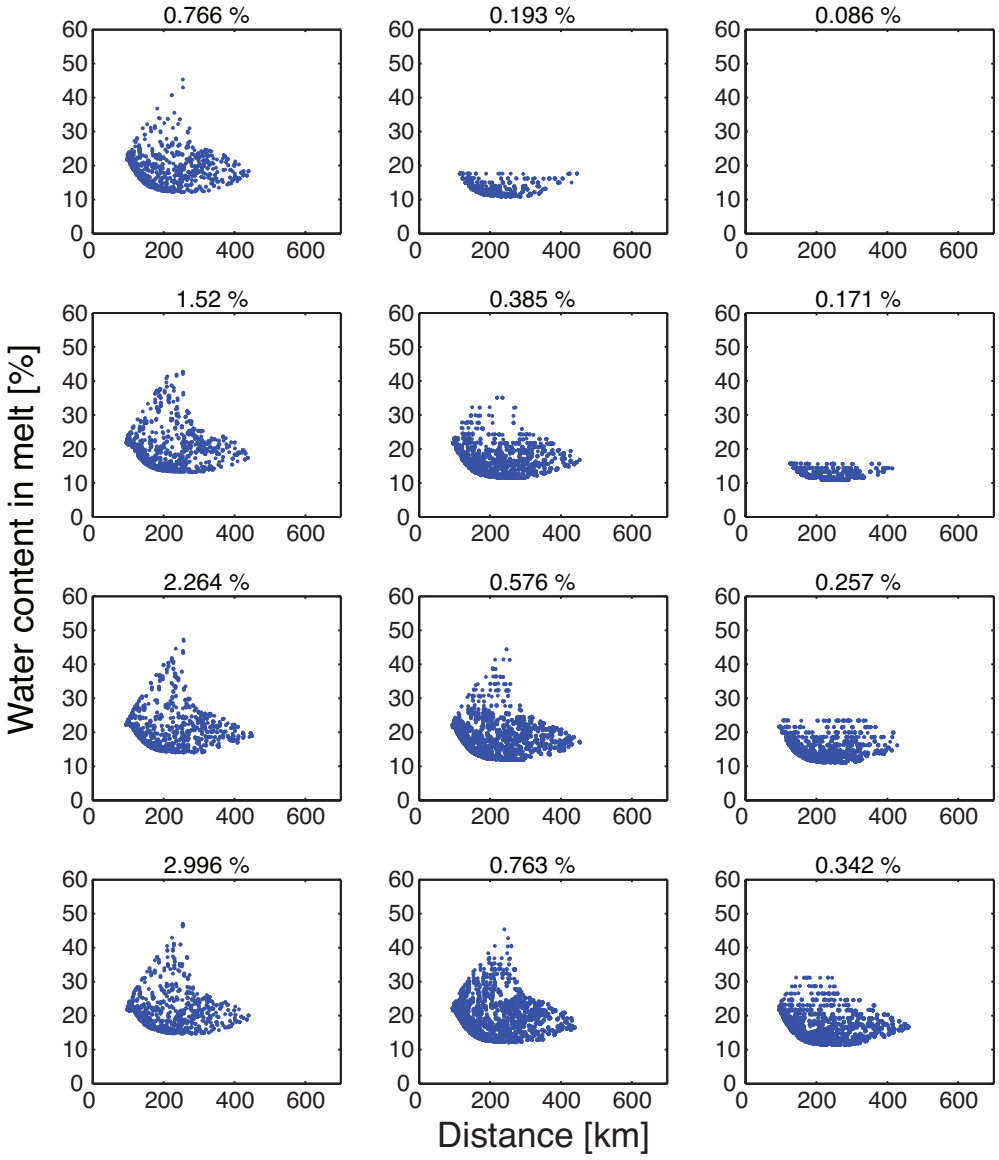

Fig. 3.17 X_{H_2O} against distance for 12 different $X_{H_2O}^{bulk}$ (labeled at the top of each plot).

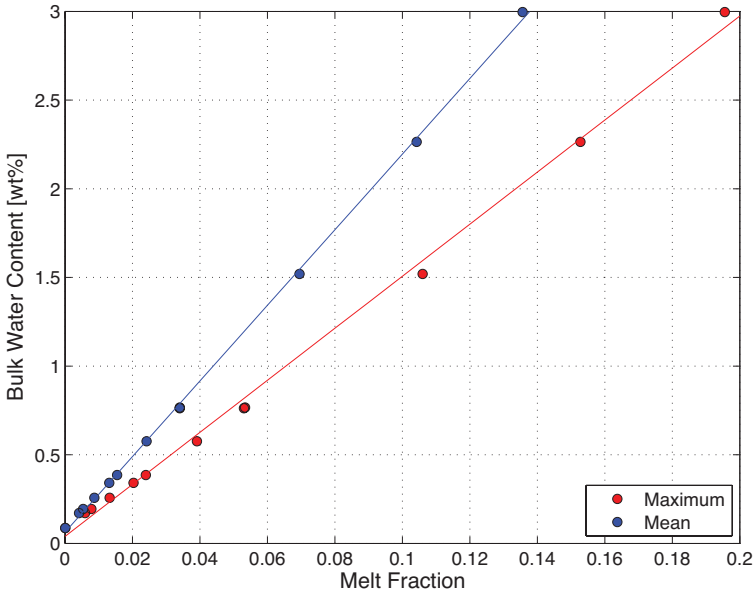

Fig. 3.18 Plot of $X_{H_2O}^{bulk}$ against melt fraction. The red points are the maximum melt fraction for each $X_{H_2O}^{bulk}$ and the blue points are the average melt fraction of all the melt events

3.6 Discussion

The trend established in the Results section was that increasing the $X_{H_2O}^{bulk}$ increases the melt fraction, melt volume and to a lesser extent the X_{H_2O} in the melt. I now need to compare the model results to published data. As well as comparing melt fraction and water content, I will compare the melt production rate, melt temperature and pressure.

3.6.1 Comparison with data

3.6.1.1 Melt Fraction

In Figure 3.18 the average melt fraction for each $X_{H_2O}^{bulk}$ is plotted in blue and the maximum melt fraction for each $X_{H_2O}^{bulk}$ is plotted in red. Both have best fit lines plotted through the values. The best fit lines shows that both sets of melt fractions increase linearly with $X_{H_2O}^{bulk}$ values, with the maximum melt fractions having a shallower trend. The distance between the

two lines increases with $X_{H_2O}^{bulk}$, which corresponds with the wide spread of melt fractions shown in Figure 3.11. Kelley et al. (2010) plotted $X_{H_2O}^{bulk}$ against melt fraction as shown in Figure 7.3. The melt fractions for different regions of the Mariana Arc were plotted against $X_{H_2O}^{bulk}$ ($C_{H_2O}^{o}$ in Figure 7.3). The results from Figure 7.3 shows higher melt fractions for equivalent $X_{H_2O}^{bulk}$ compared to Figure 3.18. A melt fraction of 0.1 is found between $X_{H_2O}^{bulk}$ of 0-0.5 wt%, whereas in Figure 3.18 a melt fraction of 0.1 is the maximum melt fraction for a $X_{H_2O}^{bulk}$ of $\sim$1.5 wt% and the average melt fraction for a $X_{H_2O}^{bulk}$ of ~ 2.2 wt%. Portnyagin et al. (2007) found a melt fraction of 0.1 corresponded to a $X_{H_2O}^{bulk}$ of $\sim 0.2 - 0.3$ wt% for the Kamchatka arc. Comparison of the model melt fractions with Kelley et al. (2010) and Portnyagin et al. (2007) suggest that whilst partial melting is occurring, it not as high as observed values from subduction zones. The hypothesis was that large hydraulic fractures would transport water to the source region and cause melting. Figure 3.20 plots the number of fracture events that produced melting as a percentage for each $X_{H_2O}^{bulk}$. The lowest $X_{H_2O}^{bulk}$ have the lowest success rate and the larger $X_{H_2O}^{bulk}$ all fall between 50 - 70 %. As the end locations of the fractures are random there is no correlation between $X_{H_2O}^{bulk}$ and success rate for the larger $X_{H_2O}^{bulk}$.

3.6.1.2 Melt temperature and pressure

Figure 3.21 plots the temperature of the maximum melt fraction in red and the average temperature of all melt events in blue, for each $X_{H_2O}^{bulk}$ value. The temperature of the maximum melt varies between 1250-1270 °C. The average temperature are lower with most of them under 1200 °C. This distance between the two set of values indicate the melting occurs over a range of temperatures. Figure 3.22 plots the pressure of the maximum melt fraction in red and the average pressure of all the melt events in blue for each $X_{H_2O}^{bulk}$. Nearly all of the maximum melt pressures occur between 3.6-3.8 GPa. The average pressure values are higher with most being above 4 GPa. This indicates the maximum melting occurred quite high

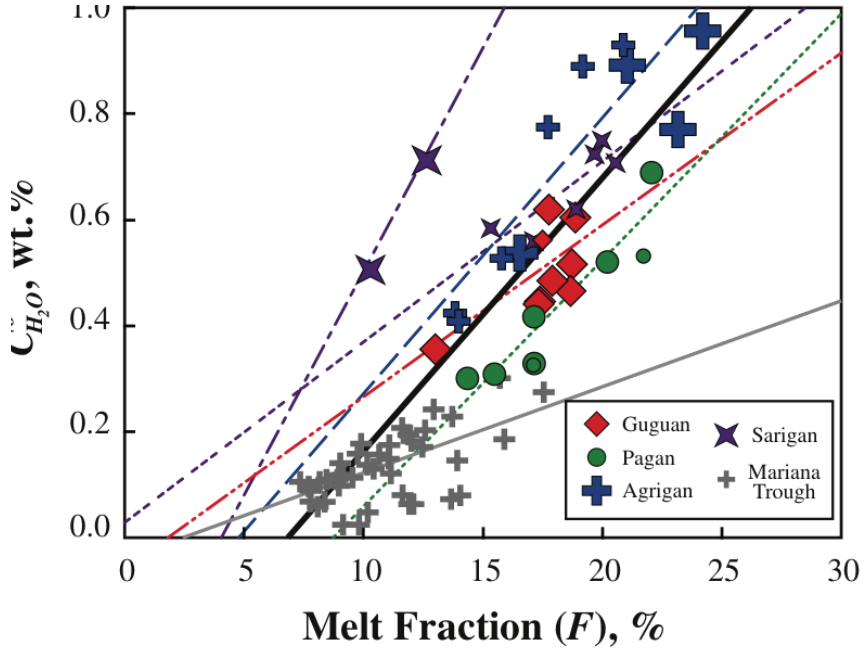

Fig. 3.19 Figure from Kelley et al. (2010) of plot of melt fraction against original water content $C^{O}_{H_2O}$ for the Mariana arc and trough modelled data. The lines shown are least-sqaures linear regressions for the back arc basin, whole arc and each island. The grey line is the Mariana Trough, the bold black line is all the Mariana arc data, the dotted line is Pagan Island, the double dot-dash line is Guguan Island, the long dash line is Agrigan Island, the dot-dash is smaple S93 and triple dot line is Sarigan Island.

in the melt region, with most of the melt occurring at lower depths. This is corroborated by the melt scatter plots in Figures 3.12, 3.13 and 3.14, which show the maximum melt region is in a similar location for each $X^{bulk}_{H_2O}$ at around $\sim$ 120 km depth. Some studies have estimated the melt temperature and pressure of the Mariana Arc using geothermometers (Kelley et al., 2010; Kohut et al., 2006). Kelley et al. (2010) estimated melt temperatures between 1200-1400 $\pm \sim$ 40 °C and pressures between 1.0-2.4 $\pm$ 0.2 GPa. Kohut et al. (2006) estimated a higher magmatic temperature of $\sim$1367 °C at 1-1.5 GPa. The maximum melt temperatures from Figure 3.21 are at the lower end of the temperature range suggested by Kelley et al. (2010) but are lower than the estimate by Kohut et al. (2006). The average melt temperature from Figure 3.21 is lower that both estimated values. The maximum and average melt pressures are both lower than the estimates of Kelley et al. (2010) and Kohut

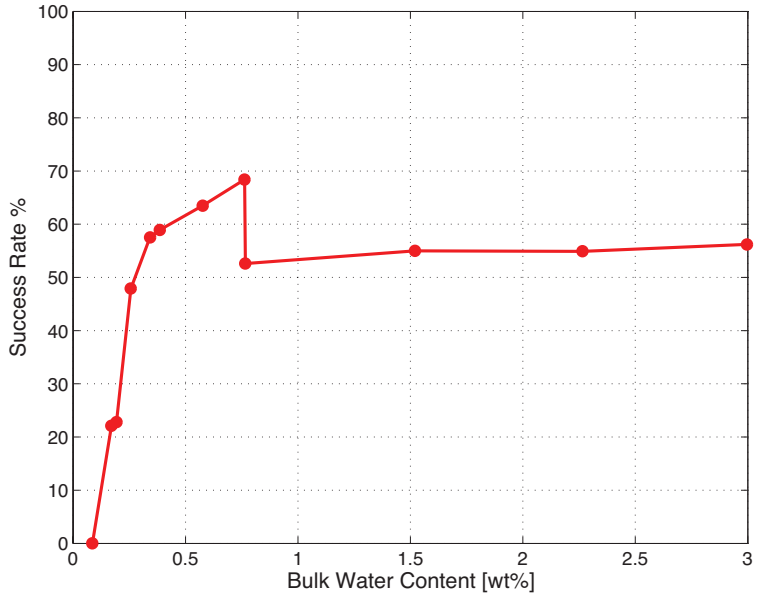

Fig. 3.20 Percentage of hydraulic fracture events that cause flash melting against $X_{H_2O}^{bulk}$

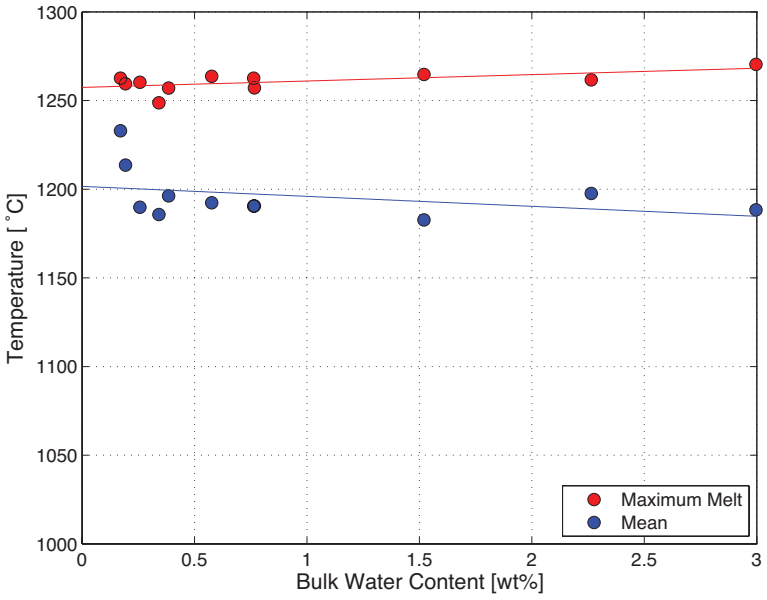

Fig. 3.21 Plot of temeprature against $X_{H_2O}^{bulk}$. The blue points are the average partial melt temperature and the red points are the temperature of the maximum melt fraction.

et al. (2006), indicating the melting occurs too deep in the mantle wedge compared to the Mariana Arc.

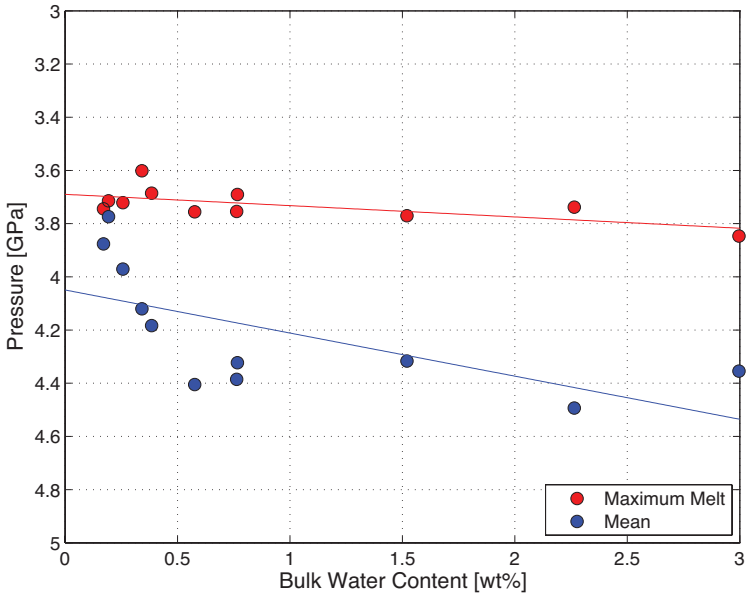

Fig. 3.22 Plot of pressure against $X_{H_2O}^{bulk}$. The blue points are the average partial melt pressure and the red points are the pressure of the maximum melt fraction.

3.6.1.3 Melt Production Rate

The melt production rate is the volume of melt that is created over a certain time. The time is calculated based on the flux of water from the slab. By using the global water flux estimate from van Keken et al. (2011) down to 230 km of 6.6×10^8 Tg Myr^{-1}, I can estimate the length of time required for 1000 hydraulic fractures assuming they occur one after the other. To get the estimated water flux per arc length of subduction zone, the global estimate is divided by the total arc length of all subduction zones. The total arc length used is 38500 km from van Keken et al. (2011), this gives an estimated water flux per arc of 1.71×10^{13} g Myr^{-1} m^{-1}. By calculating the volume of water that can be contained in a fracture, the number of fractures per Myr can be calculated. Note that the water flux quoted is per metre

Fracture Size	Mass of water per fracture kg	Number of fractures per Myr	Time in Myr for 1000 fractures
2km x 1km x 10 m	2×10^{10}	857	1.17
4km x 1km x 10 m	4×10^{10}	429	2.33
6km x 1km x 10 m	6×10^{10}	286	3.5
8km x 1km x 10 m	8×10^{10}	214	4.67

Table 3.4 Mass of water in each fracture, number of fractures per Myr and time in Myr for 1000 fractures for each fracture size.

along strike, while I am assuming my fractures have a 1 km along strike (depth) length. Clearly the water flux per km will be 1000 times greater than per m. Table 3.4 shows the mass of water, the number of fractures per Myr per km along strike and the time in Myr for 1000 fractures to occur per km along strike, for each fracture size. Dividing the total volume of all the melt events for each $X_{H_2O}^{bulk}$ (Figure 3.16) by the time for 1000 fractures gives the melt production rate in km^3 Myr^{-1} km^{-1}. Figure 3.23 plots the melt production rate for each $X_{H_2O}^{bulk}$. There were four different fracture sizes used; the red points are the 2 km length fractures, the blue points are 4 km length, green are 6 km length and the light blue are the 8 km length values. Best fit lines are plotted through the four sets of data. what is noticeable is as fracture length increases the melt production rate increases at a smaller rate with $X_{H_2O}^{bulk}$ compared to lower fracture lengths, this is due to the larger fracture lengths needing a longer time for 1000 fractures to occur. Holbrook et al. (1999) and Lizarralde et al. (2002) estimated the melt production rate at the Eastern Aleutian to be $\sim$67 km^3 km^{-1} Myr^{-1}. Wada and Wang (2009) used the volcanic output rate to estimate melt production rate for 17 subduction zones. They found the melt production rate varied from 24 km^3 Myr^{-1} up to 11000 ± 1000 km^3 Myr^{-1}. The values from Wada and Wang (2009) are per arc whereas the melt production rate values I calculate are per km of arc so it is difficult to compare them directly. All the melt production rates from Figure 3.23 are lower than 4.5 km^3 Myr^{-1} km^{-1} which are lower than the estimates. This suggests more melting needs to occur in the same length of time to increase the rate.

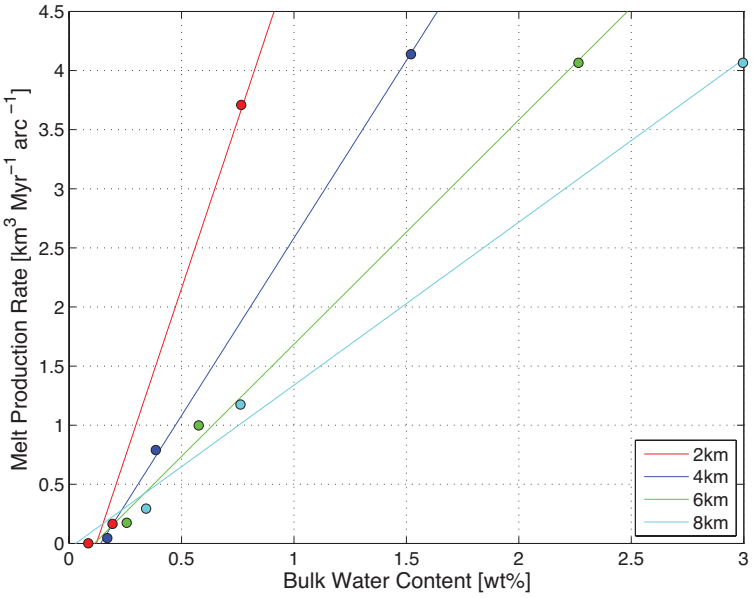

Fig. 3.23 Plot of melt production rate against $X_{H_2O}^{bulk}$. The red points are the melt production values for a fracture length of 2 km, the blue points are for a fracture length of 4 km, the green points are for a fracture length of 6 km and the light blue points are for a fracture length of 8 km.

3.6.1.4 Water Content in the melt X_{H_2O}

Figure 3.24 plots X_{H_2O} against $X_{H_2O}^{bulk}$ values. The blue points are the average X_{H_2O} for each $X_{H_2O}^{bulk}$ and the red point are the X_{H_2O} for the maximum melt fraction, which is the minimum X_{H_2O} value. The average X_{H_2O} increase steeply with low $X_{H_2O}^{bulk}$ and then the rate steadies after $\sim$1 wt%. The minimum X_{H_2O} have a steady increase with $X_{H_2O}^{bulk}$ from $\sim$11 wt% to $\sim$15 wt%. The large spread in X_{H_2O} shown in Figure 3.17 is reflected in the large distance between the average X_{H_2O} and minimum X_{H_2O} values. Estimates of X_{H_2O} in arc magmas can be made from melt inclusion trapped in crystals that rapidly cool at the surface. Plank et al. (2013) estimated X_{H_2O} for seven different arc locations and found averages of $\sim$4 wt% and a range of $\sim 1.0 - \sim 7.0$ wt%. None of the X_{H_2O} values in Figure 3.24 are as low as 4 wt%, all values are above 10 wt%. However some studies have found larger X_{H_2O} values. Carmichael (2002) found X_{H_2O} values of $\sim$10 wt% in the Mexican volcanic belt. Grove et al. (2003) and

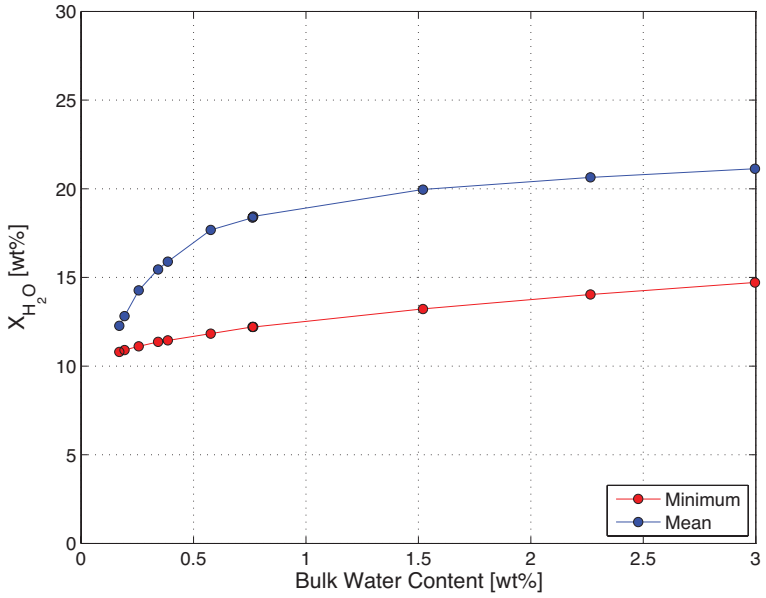

Fig. 3.24 Plot of X_{H_2O} against $X_{H_2O}^{bulk}$. The red points are the X_{H_2O} for the maximum melt fraction for each $X_{H_2O}^{bulk}$ and the blue points are the average X_{H_2O} of all the melt events

Krawczynski et al. (2012) estimated X_{H_2O} values between $\sim 10-\sim 14$ wt% from magmas from Mt Shasta. Nearly all of the minimum X_{H_2O} fall in this range, and the three lowest $X_{H_2O}^{bulk}$ also fall in this range of the average X_{H_2O} values. For each $X_{H_2O}^{bulk}$ I found the number of X_{H_2O} values that were ≤ 14 wt% and calculated the percentage of melt events that produced X_{H_2O} lower than 14 wt% as shown in Figure 3.25. The percentage decreases rapidly as $X_{H_2O}^{bulk}$ increases. The fact that no melt event produces X_{H_2O} values lower than 7 wt% suggests more melting needs to occur, as melt fraction and X_{H_2O} are connected via equation (3.28).

3.7 Model Limitations

The first limitation is the fracture size, they are large compared to the estimates of water filled fractures by Dahm (2000). Smaller fracture sizes would produce more fractures per Myr which would impact the melt production rate. However as the $X_{H_2O}^{bulk}$ is calculated from the fracture size and the radius of the source region, a decrease in fracture size would require

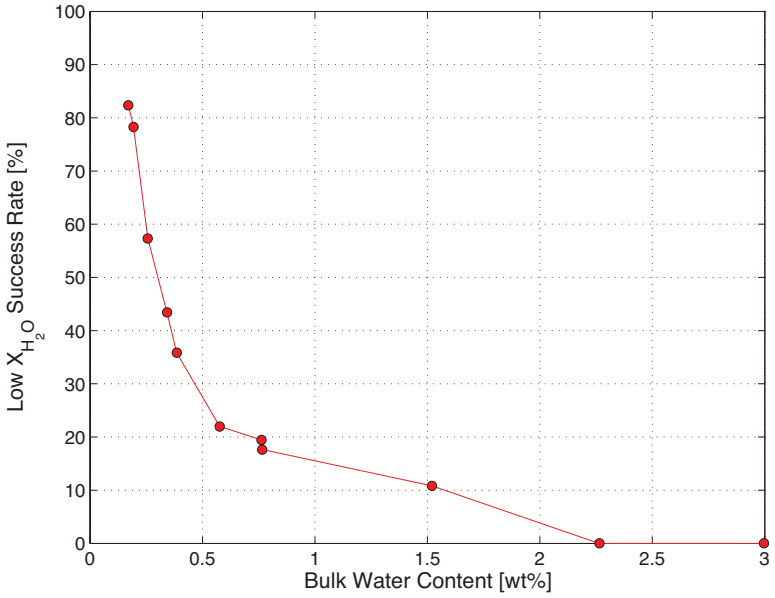

Fig. 3.25 Percentage of partial melt events that produce $X_{H_2O} \leq 14$ wt% against $X_{H_2O}^{bulk}$

a decrease in the radius to get a similar $X_{H_2O}^{bulk}$. The smallest radius used in this model was 0.5 km, if this was to decrease further then the chances of no markers being found within that radius increases. An option would be to increase the number of markers in the model but that would make the model more computationally expensive. Another thing to consider is the end point of the fractures, this was found by choosing a random point on the slab and a random angle. Whilst this is a good initial estimate of water release locations from the slab, in reality it may be that more water is released at certain depths compared to others. This would require more investigation into the release depths of water. Once the water is added to the mantle wedge the markers within the source radius are given the marker composition of 2 for 'water added'. If this water then produces melting the marker composition becomes 3 for 'partial melt'. The focus in this model has been on the partial melt markers. In the model the markers with water added that do not melt will be advected with the velocity field with all the other markers. If in this new location the water then causes melting the marker composition number will change to 3. In Figures 3.12, 3.13 and 3.14, the region of

no melting is close to the slab and the tip of the wedge. If the water added in these locations does not produce melting then when the markers are advected they will likely still be in a region where no melting will occur. The success rate percentage for most of the $X^{bulk}_{H_2O}$ in Figure 3.20 was between 50-70 %, this means that 30-50 % of the fracture events do not produce melting and stay as water markers. Transport of the water other than by solid flow should be considered. A lateral transport mechanism was suggested by Davies and Stevenson (1992) and recent work by Cagnioncle et al. (2007) and Wilson et al. (2014) have the water ascend through porous flow. Future work could consider adding in one of these water transport mechanisms to increase the melting success rate. A final limitation is that the hydrous melting parameterisation by Katz et al. (2003) was constrained with experimental data that only went up to 2 GPa, so they had to extrapolate for the higher pressures. This creates some uncertainty in the melting calculation as most of the melting occurred at higher pressures than 2 GPa.

3.7.1 Conclusions

The hypothesis being tested was from Davies (1999), that a large hydraulic fracture would transport water from the slab to the mantle wedge and cause instantaneous melting. Figure 3.20 shows that melting does occur due to water added via a hydraulic fracture, with most of the $X^{bulk}_{H_2O}$ values having a success rate percentage between 50-70 %. However whether the melting produced is sufficient compared to observations from arcs is another question. Comparisons of the melt fraction, melt production rate and X_{H_2O} with observations showed that the amount of melting produced was too low. None of the X_{H_2O} values were within the range suggested by Plank et al. (2013) of between 1-7 wt%. Lower $X^{bulk}_{H_2O}$ values had X_{H_2O} values under 14 wt% which matches observations by Grove et al. (2003) and Krawczynski et al. (2012), but their X_{H_2O} estimates are for one locations whereas Plank et al. (2013) is a global estimate based on seven different arc regions. This suggests more melting needs

to occur at the same $X_{H_2O}^{bulk}$, which would increase the melt fraction and production rate and lower the X_{H_2O} wt% accordingly. Therefore other melting processes need to be considered to supplement the flash melting. Two possible melting mechanisms are hydrous flux melting and decompression melting. In both cases the partial melt will be transported vertically whilst undergoing more melting. Comparison of the melt temperature and pressure of the maximum melt fractions indicate the flash melting occurs too deep and at slightly lower temperatures, than results estimated using geothermometers. By having either hydrous flux melting or decompression melting occur after flash melting would transport the partial melt to lower depths and maybe higher temperatures (note that the partial melt temperature is constrained by the maximum thermal model temperature of 1300 °C). Other evidence that another melting mechanism is required is that the flash melting model produces no melt focussing as it occurs over a large region of the mantle wedge. England and Katz (2010b) suggested melt focussing towards the tip of the anhydrous solidus explained the consistent depth to the slab from volcanic arc, melt focussing was also suggested by Cagnioncle et al. (2007). Having another melting mechanism occur after the flash melting may focus the melt into a smaller region of the wedge.

3.8 Summary

In this chapter I used a hydrous melting parameterisation by Katz et al. (2003) to calculate the melting from the water added to the mantle wedge by a hydraulic fracture. I calculated the fracture path using the equations from Davies and Stevenson (1992) to find the fracture end points to use in the model. The model used the temperature field taken from the thermal model discussed in the previous chapter and a range of $X_{H_2O}^{bulk}$, that were calculated from varying fracture sizes and search radii. Overall as the fracture size increased and the search radius decreased; melt fractions, melt volumes and X_{H_2O} all increased. This also corresponded to higher $X_{H_2O}^{bulk}$. Comparison of the model results with data showed that the X_{H_2O} from the

model were much higher than the global average, but fitted results from the Mount Shasta region. I also showed that the melt fractions were lower than data for the same $X_{H_2O}^{bulk}$ and that the melt production rate was low compared to melt production rate in literature. The conclusion from this is that more melting needs to occur to decrease the water content in the melt. The maximum melt pressures and temperatures also indicated the melting occurs lower than estimated at arcs. Another melting mechanism needs to occur after the flash melting to produce more melting, and also transport the melt to a higher location in the mantle wedge. Two possible melt mechanisms were suggested; hydrous flux melting and decompression melting. The next chapter is going to examine hydrous flux melting occurring after flash melting to see if this can produce sufficient melting.

CHAPTER 4

HYDROUS FLUX MELTING

4.1 Introduction

In the previous chapter I investigated flash melting using the hydrous melting parameterisation by Katz et al. (2003). Whilst the addition of water to the mantle wedge, by a hydraulic fracture did produce melting, the melt fractions and melt production rates were too low compared to petrological data. Some of the water content in the melt X_{H_2O} values were within the range by Grove et al. (2003) but none of the X_{H_2O} values were as low as the range estimated by Plank et al. (2013). I decided that whilst flash melting could play a part in subduction zone magmatism, another melting process also needed to occur to increase the melting and consequently lower the water content in the melt. Two melting processes that could take place in subduction zones are hydrous flux melting and adiabatic decompression melting.

This chapter is going to focus on hydrous flux melting. Hydrous flux melting is caused by water moving or fluxing upwards into hotter mantle temperatures. As the water rises into hotter temperature and lower pressure, more melting occurs. The method I am using to calculate hydrous flux melting is from Davies and Bickle (1991) . The aim is to see if

hydrous flux melting can cause more melting than flash melting, and also see if the results fit petrological data.

This chapter is set out in five sections. The first section discusses the paper by Davies and Bickle (1991) and their hydrous fluxing method. The second section covers the method of how I implemented the hydrous flux melting in the model, then the third section shows the results from the model. Next is the discussion section which compares the hydrous flux melting results to petrological data. Lastly the final section is a summary of the chapter.

4.2 Davies and Bickle hydrous fluxing method

In their method to calculate melting due to hydrous fluxing Davies and Bickle (1991) first start with the parameterisation for dry melting by McKenzie and Bickle (1988). They then extend it to handle wet melting, then finally calculate the flux melting.

4.2.1 Dry melting parameterisation

The dry melting parameterisation by McKenzie and Bickle (1988) is in the form $F(T,P)$, where F is the melt fraction, T is the temperature in $^\circ$ C and P is pressure in GPa. The pressure is used to calculate the solidus and liquidus temperatures. The equation for the solidus temperature T_s is:

$$P = \frac{(T_s - 1100)}{(136 + 4.968 \times 10^{-4} \exp(1.2 \times 10^{-2}(T_s - 1100)))} \tag{4.1}$$

Equation (4.1) gives $P(T_s)$ so $T_s(P)$ is found using iteration. The liquidus temperature T_l is found by:

$$T_l = 1736.2 + 4.343P + 180 \tan^{-1}\left(\frac{P}{2.2169}\right) \tag{4.2}$$

The solidus and liquidus temperatures for a range of pressures are plotted in Figure 4.1

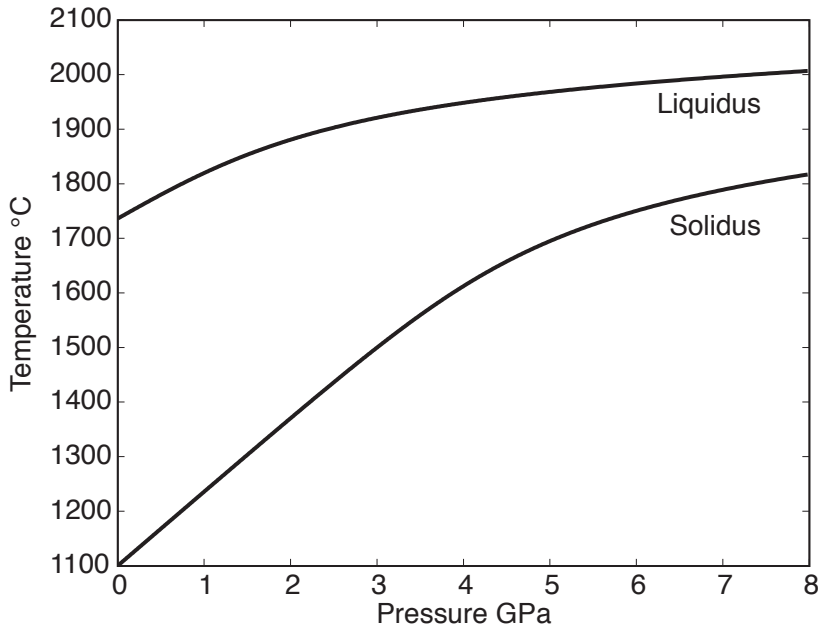

Fig. 4.1 Solidus and liquidus curves for different pressures generated from equations (4.1) and (4.2).

To determine F the first step is to assume that $F = 0$ when $T = T_s$ and $F = 1$ when $T = T_l$. A dimensionless temperature T' is then defined:

$$T' = \frac{(T - (T_s + T_l)/2)}{T_l - T_s} \tag{4.3}$$

Using the assumptions for T_s and T_l, $T' = -0.5$ when $F = 0$ and $T' = 0.5$ for $F = 1$. There is a general polynomial which satisfies these conditions to find F:

$$F - 0.5 = T' + (T'^2 - 0.25)((a_0 + a_1 T' + a_2 T'^2) \tag{4.4}$$

McKenzie and Bickle (1988) use two coefficients in their final equation for F:

$$F = 0.5 + T' + (T'^2 - 0.25)((a_0 + a_1 T') \tag{4.5}$$

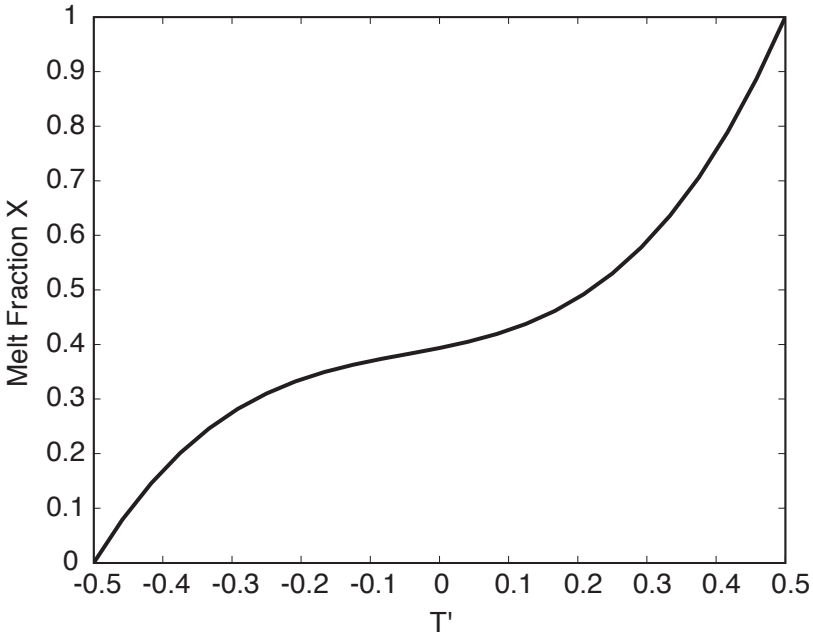

Fig. 4.2 Melt fraction of rock X plotted as a function of T'.

where:

$$a_0 = 0.4256$$

$$a_1 = 2.988$$

F as a function of T' is plotted in Figure 4.2

4.2.2 Wet Melting

Davies and Bickle (1991) then expanded the dry parameterisation from McKenzie and Bickle (1988) to include wet melting. From conservation of energy, the amount of melting is calculated. Davies and Bickle (1991) balanced the heat advected in by solid flow with the latent heat of melting. To achieve this they needed to calculate the weight fraction of peridotite, which melts as a function of water content and temperature. Increasing the melt fraction causes an increase in wet melt temperature. This is done by relating the dry melt

temperature to the wet melt temperature, at the same melt fraction and pressure by:

$$T_w = T_d - b_1 X_w^m \tag{4.6}$$

where T_w is the wet melt temperature, b_1 is a constant, X_w^m is the mole fraction content of water and T_d is the dry melt temperature which is T in equation (4.3). Davies and Bickle (1991) found a larger value of b_1 of 642°C described correctly the separation between the dry and water saturated solidi. The equation for the mole fraction content of water in the melt is:

$$X_w^m = \frac{M_e}{18.02(1 - W_w^m)/W_w^m + M_e} \tag{4.7}$$

where Me is the mole equivalent mass for melt and W_w^m is the weight fraction of water in the melt. The maximum solubility of water in the melt is taken to be 25% at 3 GPa (Green, 1973; Stern and Wyllie, 1973). Therefore if $W_w^m > 0.25$ then it is classed as saturated and the W_m^w saturated value of 0.25 is used. W_w^m is calulated for different $X_{H_2O}^{bulk}$ by:

$$W_w^m = \left(\frac{X_{H_2O}^{bulk}}{F} \right) / 100 \tag{4.8}$$

Davies and Bickle (1991) approximate the relationship between melt fraction, water content and melt temperature, by a one dimensional column of partial melt that rises into hotter mantle temperatures. Into the sides of the column hot unmelted dry mantle flows, this reacts with the wet magma and any excess water flowing up the column and melts. A temperature drop is caused by the latent heat of melting so cooler partly melted mantle leaves the region of melting. Davies and Bickle (1991) assumed steady state with a constant flux of water up the one dimensional column. The same velocity is assumed for melt, water in the melt and excess water. They also state that the melt is in local thermal equilibrium with the solid. Also the conduction of heat up the column and the advection of heat by the melt were

ignored. Heat advected into the column would be reduced by the heat conducted horizontally into the column.

4.2.3 Flux melting

The final step was to calculate the melt due to fluxing up a one dimensional column. The conservation of energy equation is:

$$L\frac{\mathrm{d}M}{\mathrm{d}t} = \frac{v_s C_p \rho_s (T_i - T_w)}{\Delta y} \tag{4.9}$$

where L is the latent heat of melting, $\mathrm{d}M/\mathrm{d}t$ is the mass rate of melting per cubic metre, v_s is the matrix velocity, C_p is the specific heat capacity at constant pressure, ρ_s is the density of the mantle, Δy is the source width and T_i is the mantle temperature just before it enters the source region.

From conservation of mass, the melt flux gradient is related to the melting rate by:

$$\frac{\mathrm{d}M}{\mathrm{d}t} = \frac{\mathrm{d}W}{\mathrm{d}z} \tag{4.10}$$

where z is the height above the base of the melting column and W is the melt flux (kg m^{-2} s^{-1}).

By substituting equations (4.6) and (4.10) into equation (4.9) we get:

$$\frac{\mathrm{d}W}{\mathrm{d}z} = \left(\frac{v_s C_p \rho_s}{L \Delta y}\right)(T_i - T_d + b_1 X_m^w) \tag{4.11}$$

The degree of melting is the ratio of the melting rate to solid flux:

$$F = \frac{\left(\frac{\mathrm{d}W}{\mathrm{d}z}\Delta y\right)}{\rho_s v_s} \tag{4.12}$$

Substituting equation (4.11) into equation (4.12) gives the final equation for F:

$$F = \frac{C_p}{L}(T_i - T_w) \tag{4.13}$$

Equation (4.13) must be solved by iteration as to get T_w requires T_d, which is dependent on F.

Davies and Bickle (1991) assumed that the melts rise slowly through the source region, remaining in thermal and hydrous equilibrium.

4.3 Method

I am wanting to calculate the flux melting that occurs due to the melt from the flash melting events rising through the mantle wedge. To do this I need to combine the flash melting events as calculated in the previous chapter, with the flux melting equations from Davies and Bickle (1991).

4.3.1 Flash melting data

Following on from the previous chapter I have made a few changes to the flash melting cases. Instead of 12 cases with different water contents, I have decided to only have 9 cases. I am removing the water contents calculated for the smallest fracture size, as the 0.086 wt% case produced no melting and the 0.766 wt % case is very similar in value to the 0.763 wt % case. By removing this row of water contents the rest are unchanged and are reshown in Table 4.1.

For each of the nine cases, I had the melt fractions of the markers and the corresponding marker positions for the 1000 fracture events. I averaged the melt fraction and marker positions for each fracture event. For each fracture event I found the grid node nearest to the averaged marker position. Not all of the 1000 fracture events caused flash melting, as I am

		Search radius		
		0.5 km	1 km	1.5 km
Fracture size	4km x 1km x 10 m	1.52 %	0.385 %	0.171 %
	6km x 1km x 10 m	2.264 %	0.576 %	0.257 %
	8km x 1km x 10 m	2.996 %	0.763 %	0.342 %

Table 4.1 Bulk water weight percentages calculated for a range of fracture sizes and search radii.

only looking at flux melting that occurs after flash melting, I removed any fracture event that produced no melting.

4.3.2 Interpolation of data

Currently the data is on a grid with 3 km spacing in both x and y directions. When calculating hydrous flux melting, Davies and Bickle (1991) used a much smaller grid spacing in the vertical direction of 300 m. Therefore I need to change the grid spacing in the y direction from 3 km to 300m. With the new grid spacing in the y direction, the temperature field from the thermal model is interpolated onto this new grid.

4.3.3 Calculating hydrous flux melting

For each flash melting event the nearest node is known in the x and y direction. Hydrous flux melting will occur at the grid nodes vertically above the flash melting node. The maximum height of the hydrous flux melting column will be the node with the highest temperature, as the assumption is that the melting will cease once the temperature starts to decrease. For each node that contained a flash melting event, the node with the maximum temperature vertically above it was found. This gives for each flash melt event the height of the column the flux melting is going to take place over. As I am examining the effect of flash melting followed by flux melting, any flash melting event that occured on a node that had no higher temperature above was removed as no flux melting would occur.

Next the parameterisation by Davies and Bickle (1991) is used to calculate the flux melting with the following steps.

1. For a range of F from 0 to 1, find the corresponding values of T' using the Matlab function FZERO to find the root of (4.14):

$$T' + (T'^2 - 0.25)((a_0 + a_1 T') - F + 0.5 = 0 \tag{4.14}$$

2. Calculate the pressure for each node and iterate over a range of T, to find the corresponding solidus temperature $T_s(P)$ value.

3. For the first point in the column set the melt fraction and water content in the melt to the flash melt values, as this is the fracture end point node.

4. For the range of T' find T_d using equation (4.15), with T_l found using equation (4.2).

$$T_d = (T'(T_l - T_s)) + \frac{(T_s + T_l)}{2} \tag{4.15}$$

5. For each value of F find the corresponding weight fraction of water in the melt using equation (4.8). Then use equation (4.7) to find the mole fraction content of water in the melt.

6. A range T_w is then calculated using equation (4.6) for the range of T_d and X_w^m.

7. Using the temperature of the node T_i and the range of T_w find the range of F values using equation (4.13).

8. Each of the new F values is calculated from one of the original F values, so the normalised difference is found between each pair of F.

9. The pair of F with the normalised difference closest to zero is the chosen pair, the F value given to the node is the F calculated by equation (4.13)

4.4 Results

This section shows the results for the nine cases, each ran for 1000 random fracture end points. For the fracture end points where flash melting occurs, hydrous flux melting is calculated for the region vertically above the fracture end point node, stopping at the maximum temperature. I will examine the differences in melt fraction, melt volume and water content in the melt between the different cases.

4.4.1 Melt Fraction

In Figure 4.3 I have plotted melt fraction against distance for each of the nine water contents. The plots are all to the same scale to allow visual comparison. The plots correspond to search radius increasing left to right and fracture size increasing top to bottom. The melt fraction values increase in columns up to a maximum degree of melting. This is the melt fraction values increasing as the hydrous fluxing melting takes place in a column above the fracture end point node. The higher melt fraction values are seen for the cases with higher bulk water contents with 2.996% having the highest melt fractions.

For the fracture end point node and the melt points in the vertical column above, I have plotted the position of the node and the colour of the point corresponds to the melt fraction. I did this for three different water contents; 0.763 % shown in Figure 4.4, 1.52 % shown in Figure 4.5 and 2.996 % shown in Figure 4.6. For all three figures, the region with the largest melt fraction was the area between 100 and 160 km depth and 120 to 250 km distance. The melt fraction values in Figure 4.6 show melt fractions that are $\sim$ three times higher than Figure 4.4. All three figures clearly show the increase in melt fraction as the hydrous fluxing occurs upwards from the fracture end node.

As the hydrous flux melting increases as it moves up the column the melt fractions values that will be most useful are the final melt fraction values at the top of each column, which

will be the maximum melt fraction for that column. In Figure 4.7 I have plotted the maximum melt fraction for each hydrous fluxing column against distance. For each of the nine cases the melt fraction increases with distance to $\sim$ 160 km distance. After this point the melt fraction decreases with distance. The range of maximum melt fraction values is larger for the cases with higher bulk water content with the 2.996% case having the largest range in the melt fraction maximum values. When the melt fraction starts to decrease there is more scatter in the melt fraction values, compared to the region where the melt fraction values are increasing. This could be due to the original flash melt values being large as this region is the hottest temperature wise. This could cause the original melt fractions values to be the maximum melting value in the column as opposed to the top of the column. Comparison with the flash melting values will show if this is the case.

4.4.2 Melt Volume

I assume that each fracture end node is one marker, so the melt volume for each node is the mass of the marker, as calculated in the previous chapter, divided by the density of the mantle then multiplied by the melt fraction. I found the melt volume for each top node in a melting column to give the final melt volume. Figure 4.8 is a plot of the final melt volume in km^3 as a function of horizontal distance. The highest melt volumes are found in the cases with higher bulk water content. In all cases the total melt volume in the bin increases to $\sim$ 200 km distance, then it decreases with distance. The total melt volume for each $X_{H_2O}^{bulk}$ is found by finding the sum of each bin from Figure 4.8. Figure 4.9 plots the total volume in km^3 against $X_{H_2O}^{bulk}$ values. I found that by plotting the $X_{H_2O}^{bulk}$ on a log scale, the total volume values then plotted to a straight line. This shows the total volume of flux melting increases exponentially with $X_{H_2O}^{bulk}$ values.

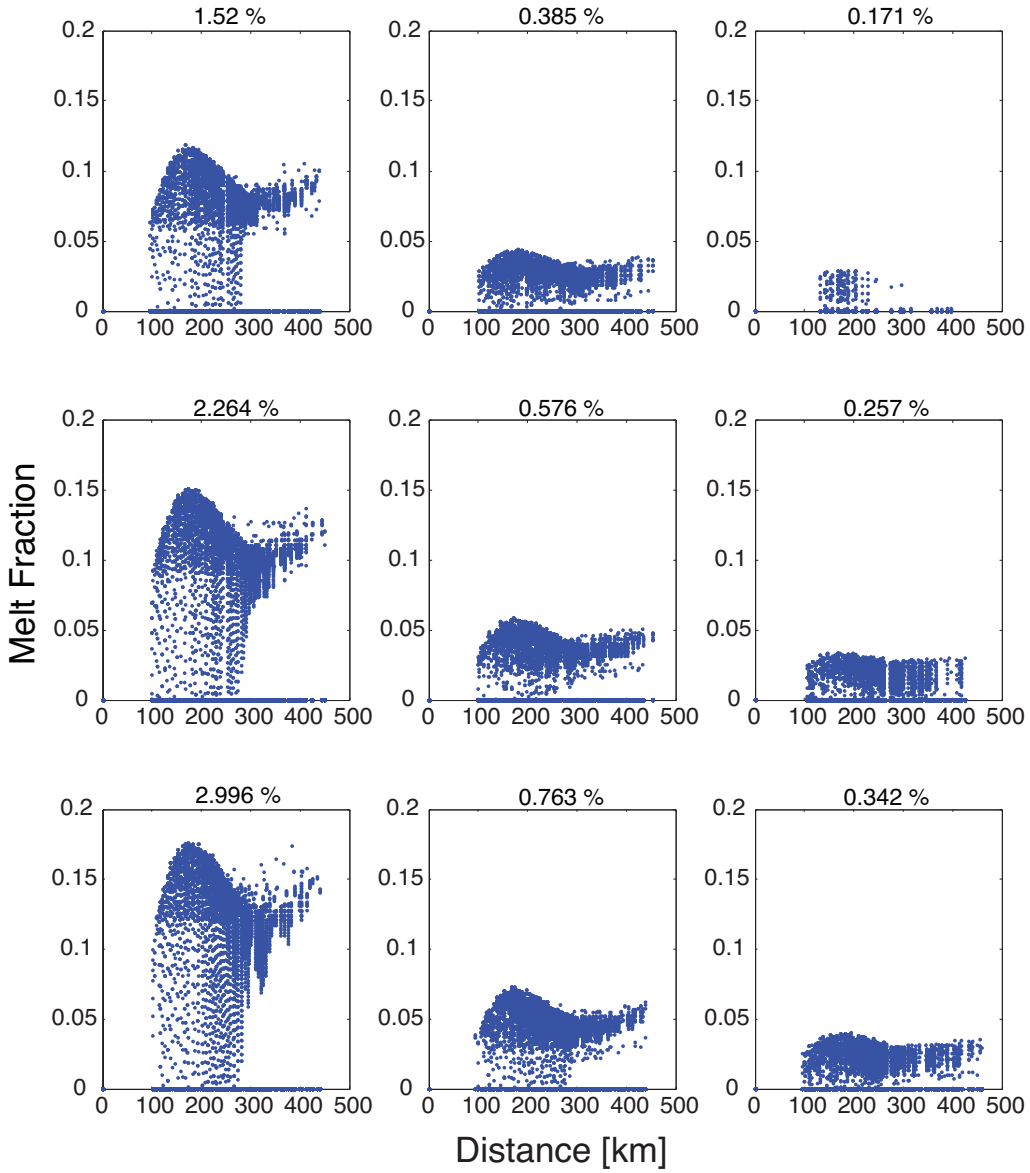

Fig. 4.3 Melt fraction as a function of distance for the 9 different bulk water weight percentages (labelled at the top of individual subplots).

4.4.3 Water Content in the Melt

The water content in the melt is found by dividing the bulk water content by the melt fraction.

Figure 4.10 plots the water content in the melt for each fracture end point against distance

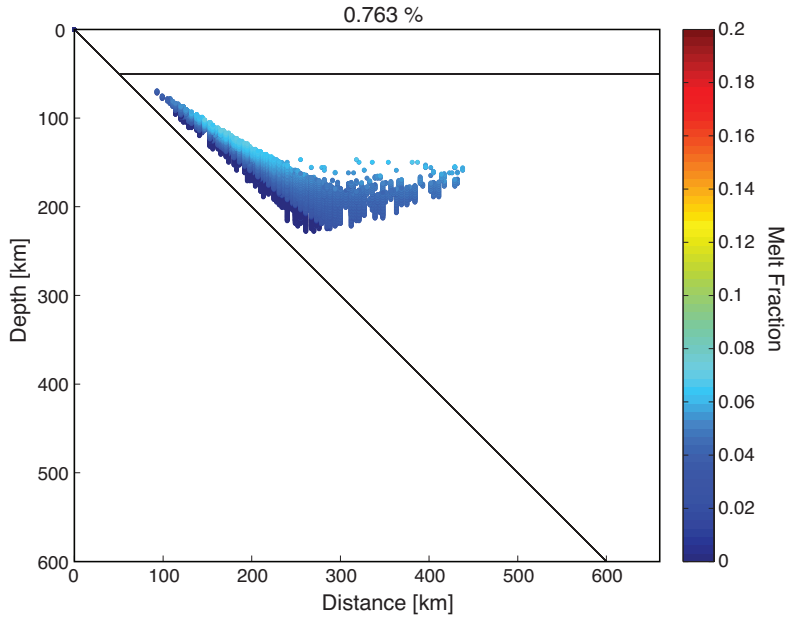

Fig. 4.4 Scatter plot of melt fraction for initial water content of 0.766%

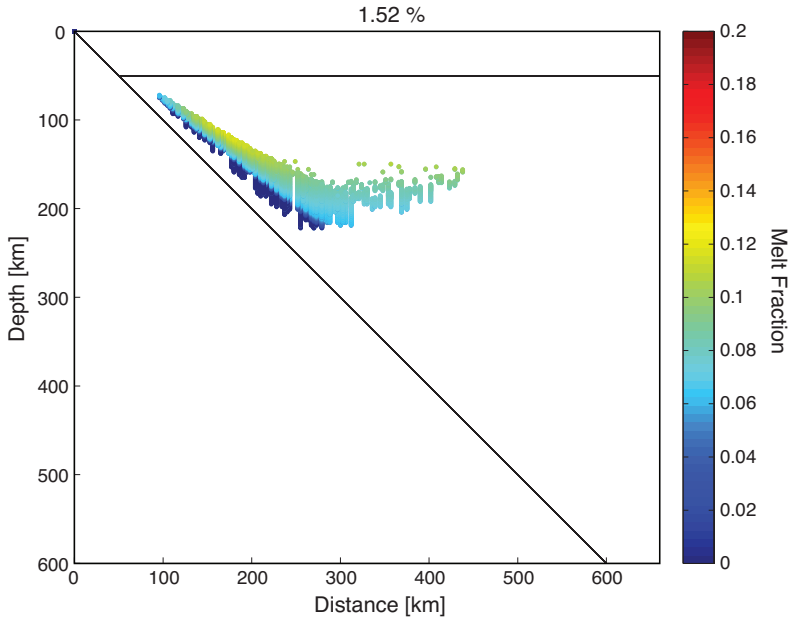

Fig. 4.5 Scatter plot of melt fraction for initial water content of 1.52%

for each of the nine bulk water weight percentages. The water content values decrease in columns from the saturated value of 25%. As the maximum melt fraction values at the top of the melting column and therefore are the values of interest, the corresponding water content

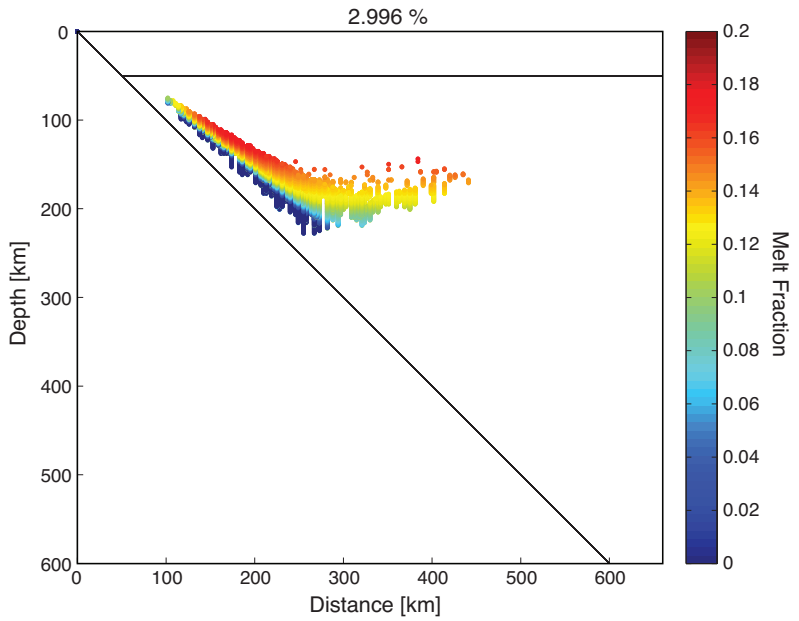

Fig. 4.6 Scatter plot of melt fraction for initial water content of 2.996%

of the melt for these melt fractions are found and plotted against distance in Figure 4.11. In each of the nine cases the water content decreases with distance to $\sim$ 160 km, then the water content values become more scattered, but there is some increase in water content with distance after 160 km. As the highest melt fractions were found for the cases with the largest bulk water contents; we would expect the lowest water contents in the melt to be found for the same cases. However the cases with the lower bulk water contents actually show the lowest water content in melt values, so this is something that needs to be explored in more detail.

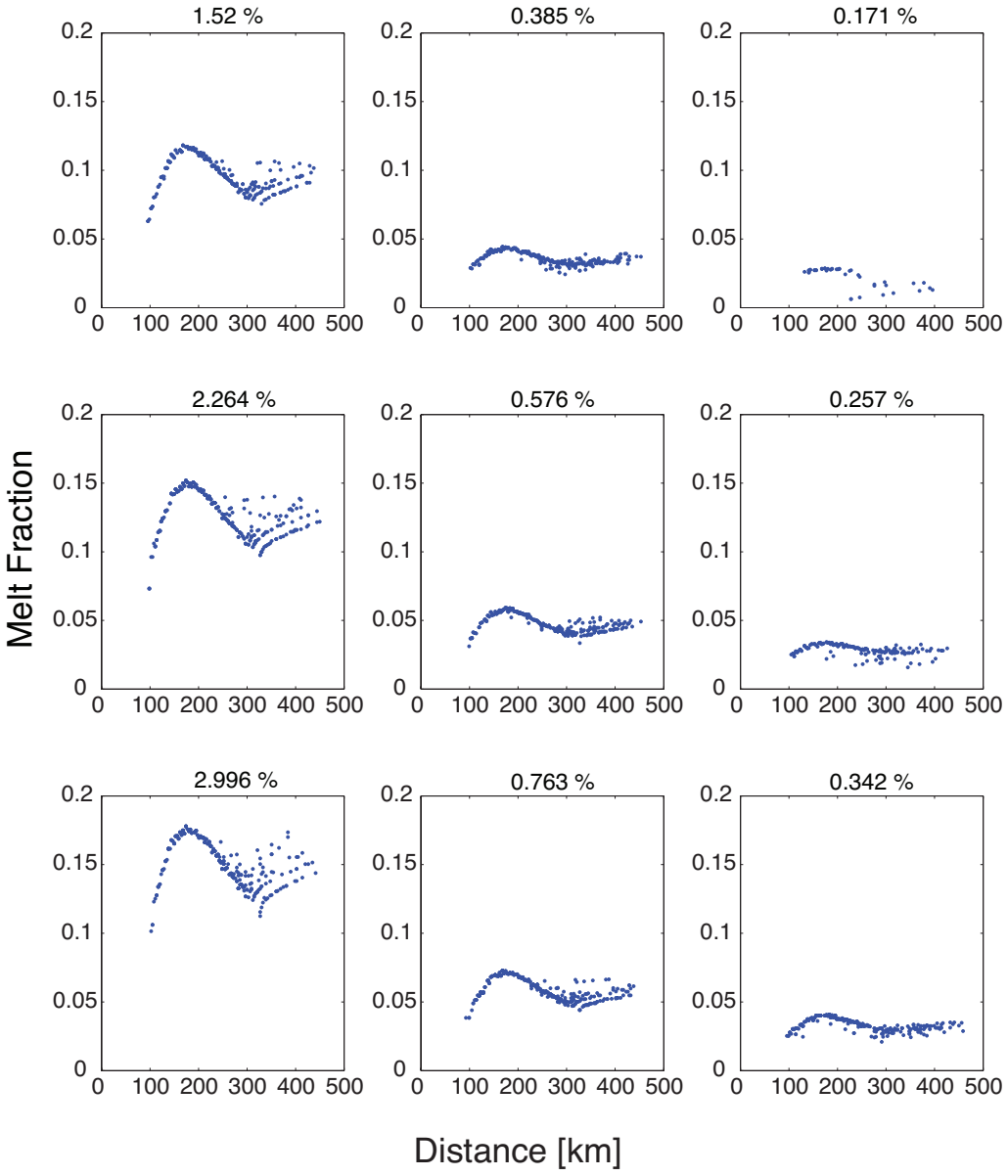

Fig. 4.7 Melt fraction at the top of each melting column as a function of distance for the 9 different bulk water weight percentages (labelled at the top of individual subplots).

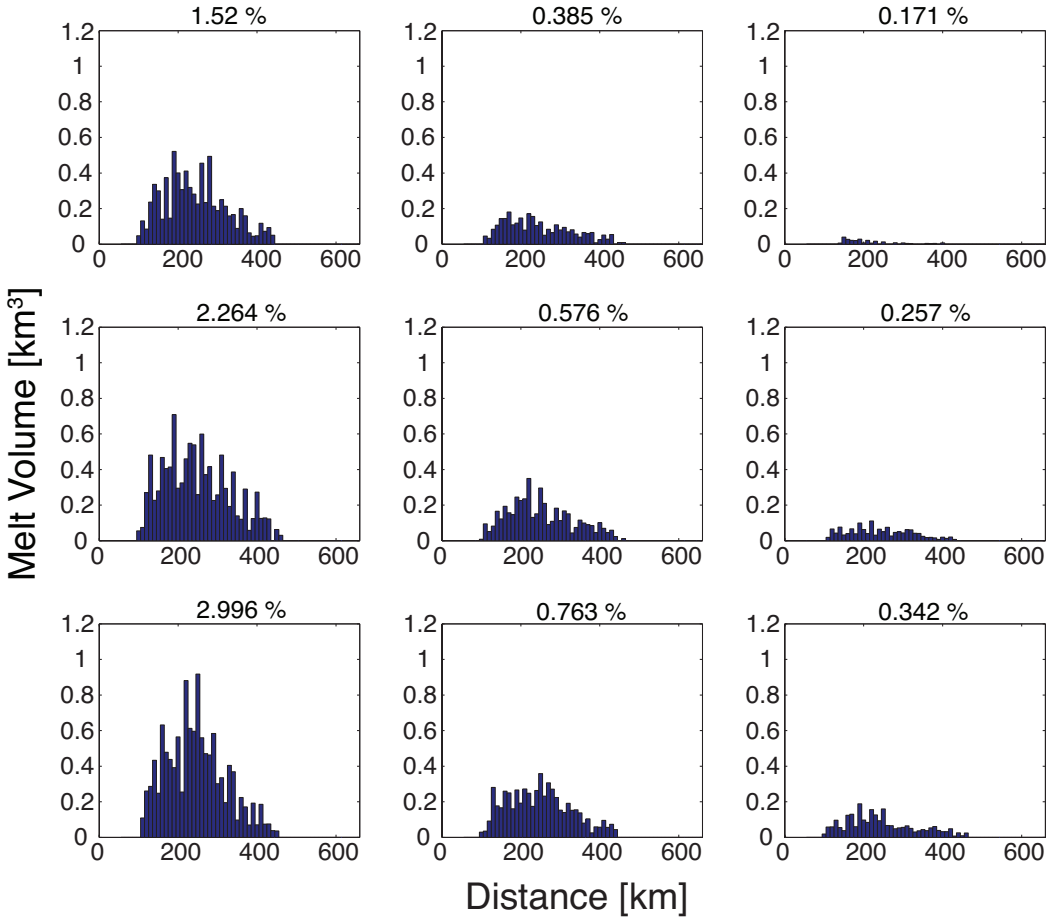

Fig. 4.8 Total melt volume found for 10 km sized bins for 9 different bulk water weight percentages

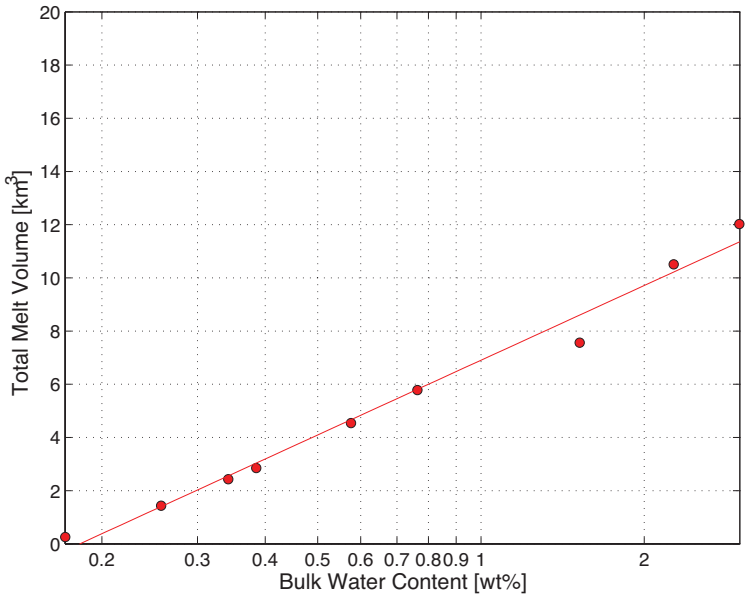

Fig. 4.9 Total melt volume of all the hydrous flux melt events plotted against $X_{H_2O}^{bulk}$ with x axis plotted on a log scale.

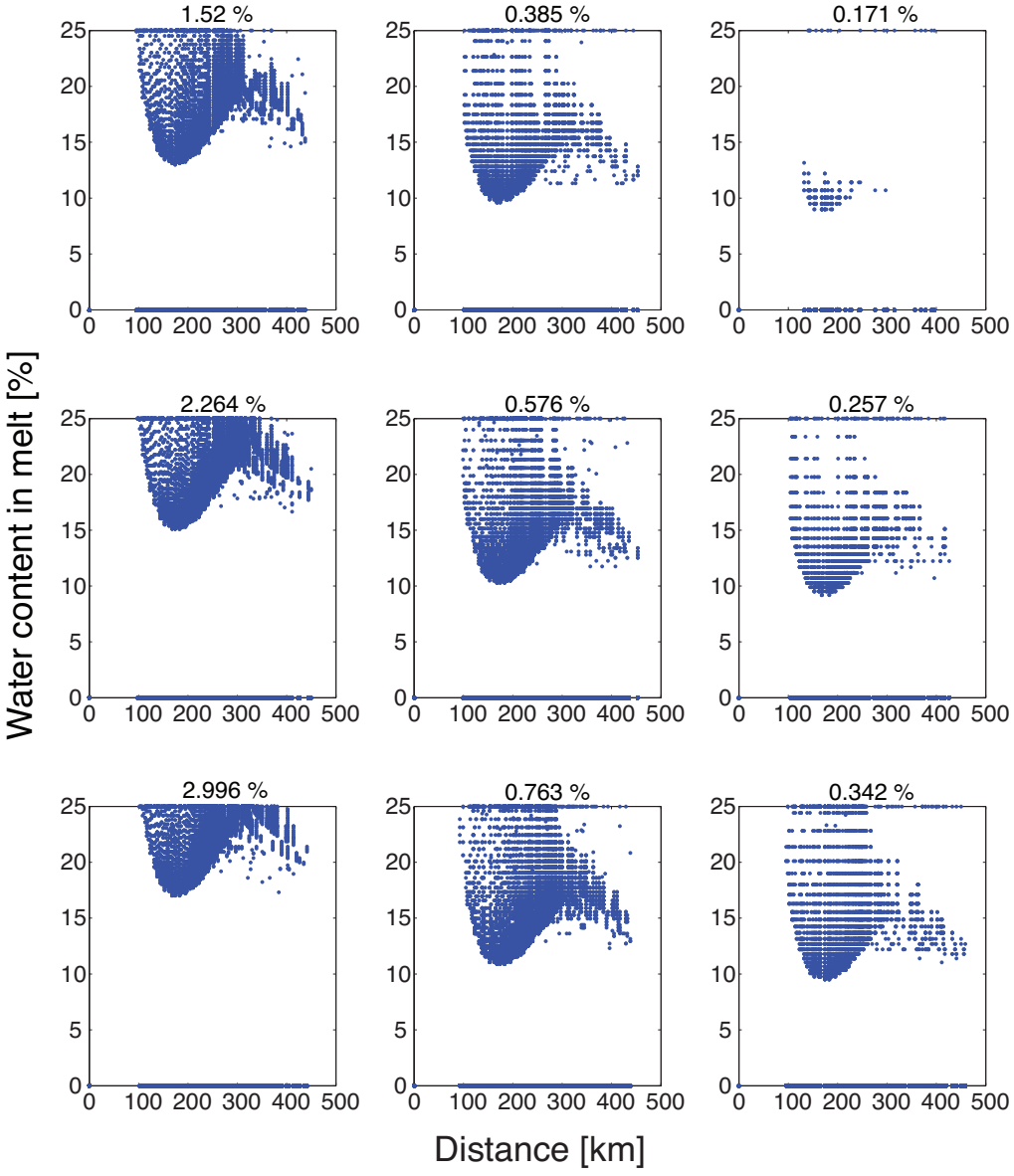

Fig. 4.10 Water content in the melt against distance for 9 different bulk water weight percentages.

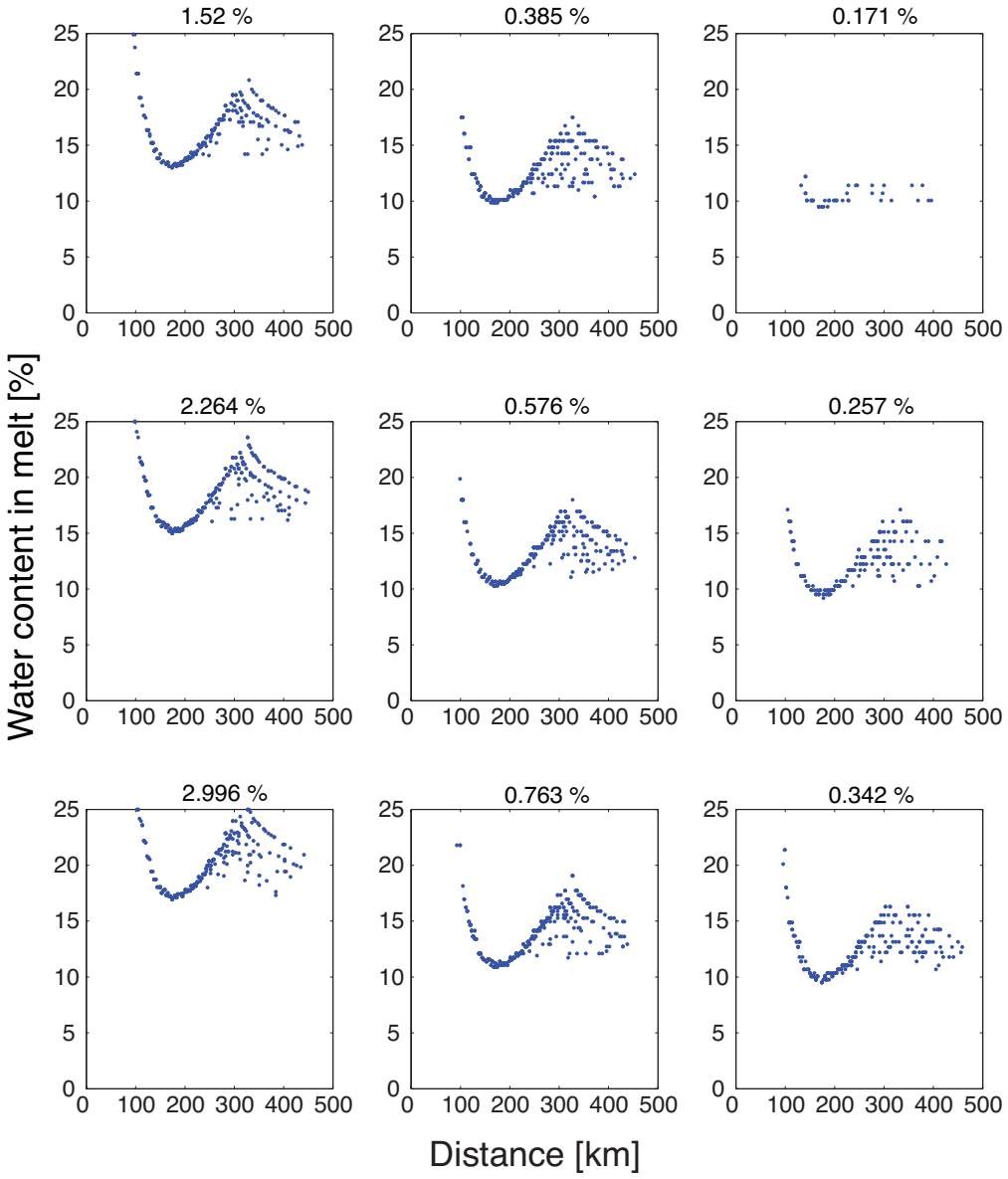

Fig. 4.11 Water content in the melt at the top of each melting column against distance for 9 different bulk water weight percentages.

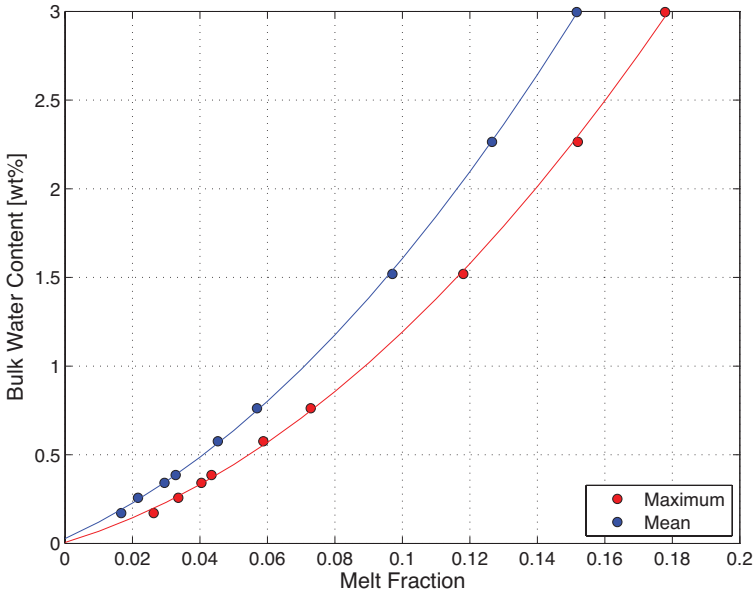

Fig. 4.12 Plot of $X_{H_2O}^{bulk}$ against melt fraction for hydrous flux melting. The red points are the maximum melt fraction for each $X_{H_2O}^{bulk}$ and the blue points are the average melt fraction of all the melt events

4.5 Discussion

4.5.1 Comparison with Petrological Data

4.5.1.1 Melt Fraction

In Figure 4.12 the average melt fraction for each $X_{H_2O}^{bulk}$ is plotted in blue and the maximum melt fraction for each $X_{H_2O}^{bulk}$ is plotted in red. Both have best fit curves plotted through the values. The best fit curves shows that both sets of melt fractions increase with $X_{H_2O}^{bulk}$ values, with the maximum melt fractions having a greater increase in melt fraction with increasing $X_{H_2O}^{bulk}$ values. The distance between the two lines increases with $X_{H_2O}^{bulk}$ values. Kelley et al. (2010) plotted $X_{H_2O}^{bulk}$ against melt fraction for different regions of the Mariana Arc. In Kelley et al. (2010) a melt fraction of 0.1 was found between $X_{H_2O}^{bulk}$ of 0-0.5 wt% whereas in Figure 4.12 a melt fraction of 0.1 is the maximum melt fraction for a $X_{H_2O}^{bulk}$ of $\sim$1.2 wt% and the

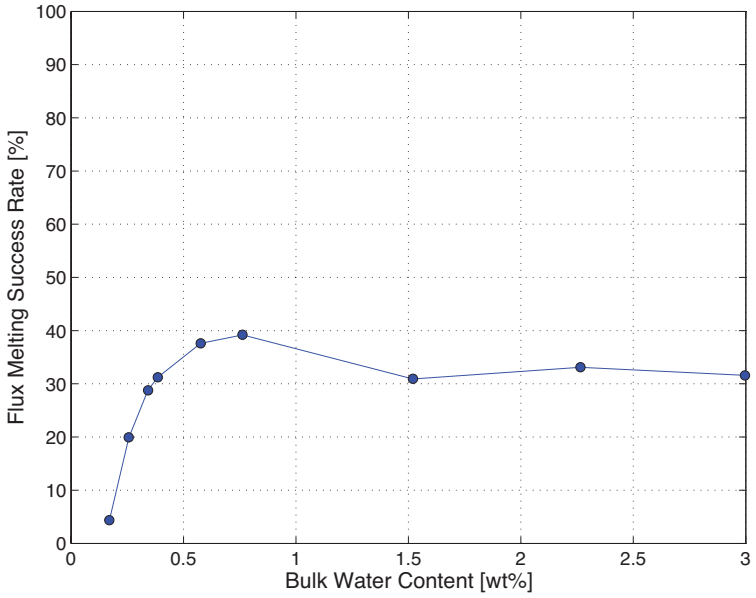

Fig. 4.13 Percentage of hydraulic fracture events that cause hydrous flux melting following flash melting against $X_{H_2O}^{bulk}$

average melt fraction for a $X_{H_2O}^{bulk}$ of ~ 1.6 wt%. Portnyagin et al. (2007) found a melt fraction of 0.1 corresponded to a $X_{H_2O}^{bulk}$ of $\sim 0.2-0.3$ wt% for the Kamchatka arc. Comparison of the model melt fractions with Kelley et al. (2010) and Portnyagin et al. (2007) suggest that whilst partial melting is occurring, it not as high as observed values from subduction zones. Figure 4.13 plots the number of fracture events that produced hydrous flux melting after the inital flash melting as a percentage for each $X_{H_2O}^{bulk}$. The lowest $X_{H_2O}^{bulk}$ have the lowest success rate and the larger $X_{H_2O}^{bulk}$ all fall between 30 - 40 %. As the success rate for flash melting was between 50-70 % for the larger bulk $X_{H_2O}^{bulk}$ this suggest that ~ 50 % of the flash melting events then undergo hydrous flux melting.

4.5.1.2 Melt temperature and pressure

Figure 4.14 plots the wet melt temperature T_w of the maximum melt fraction in red and the average T_w of all melt events in blue, for each $X_{H_2O}^{bulk}$ value. Note that in the hydrous fluxing parameterisation by Davies and Bickle (1991) the wet melt temperature T_w can be calculated

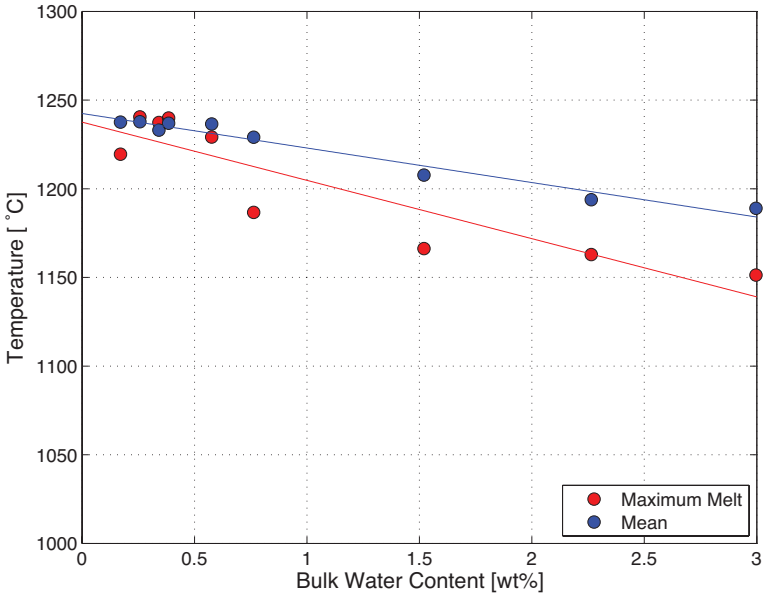

Fig. 4.14 Plot of temperature against $X_{H_2O}^{bulk}$. The blue points are the average partial melt temperature and the red points are the temperature of the maximum melt fraction of hydrous flux melting.

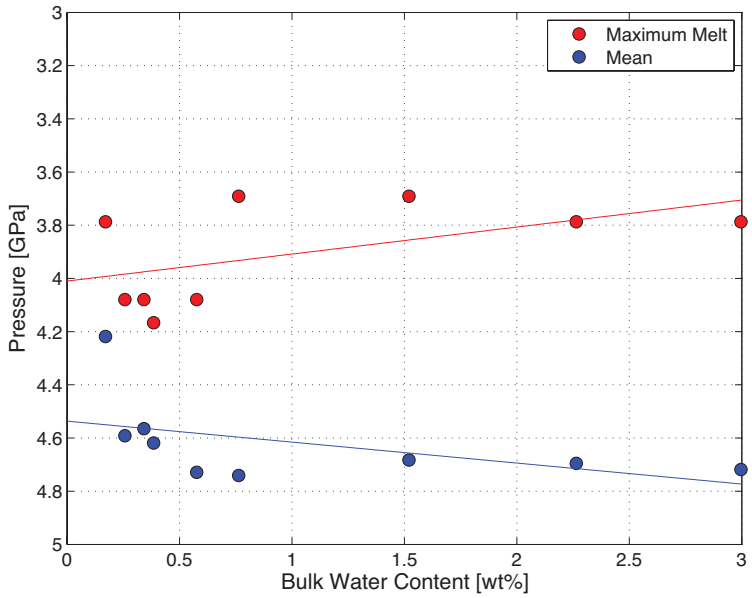

Fig. 4.15 Plot of pressure against $X_{H_2O}^{bulk}$. The blue points are the average partial melt pressure and the red points are the pressure of the maximum melt fraction for hydrous flux melting.

using (4.6), I will examine this instead of the thermal model temperature. The T_w of the maximum melt varies between 1150-1240 °C. The average T_w values are higher between 1190-1240 °C. There was no linear relationship between $X_{H_2O}^{bulk}$ and maximum melt T_w , but the average T_w seems to decreases linearly with $X_{H_2O}^{bulk}$ values. Figure 4.15 plots the pressure of the maximum melt fraction in red and the average pressure of all the melt events in blue for each $X_{H_2O}^{bulk}$ value. The maximum melt pressures occur between 3.7-4.2 GPa. The average pressure values are higher with all being above 4.5 GPa.

In Figure 4.14 the average T_w were higher than the T_w at the maximum melt fractions. This is unusual as we would expect the highest melt fractions to be associated with the highest T_w , so this needs to be explored further. The first step is to look at where the final melt events take place as shown in Figure 4.16. There are two distinct trends in the final melt locations. The first is a diagonal line of final melt locations in the region marked A. The second is the final melt events plotting on a horizontal line in the region marked B. If T_w is plotted against distance as shown in Figure 4.17, we can see that again there are two distinct regimes that correspond to the regions marked in Figure 4.16. In Figure 4.17 the region marked A has an increase in T_w with distance. In region B, T_w remains constant as the distance increases. In Figure 4.18 the melt fraction is plotted against T_w for four different $X_{H_2O}^{bulk}$ cases; 0.342 wt% in light blue, 0.763 wt% in red, 1.52 wt% in blue and 2.996 wt% in green. On the green values I have also marked the two regions A and B, all the other cases have the same trend. For all $X_{H_2O}^{bulk}$ cases the A region is distinguished by a gradual increase in F as T_w increases, it is not a completely straight line as the melt fractions starts to decrease at the T_w . Region B is distinguished by a linear decrease in melt fraction as T_w increases. It is noticeable that the four B regions all plot on a line. It should be noted that the B region is located in the core of the mantle wedge, therefore the thermal model temperature at these locations is the maximum background temperature of 1300 °C. Region B has higher T_w values than region A but lower melt fractions. This explains why the average T_w values in

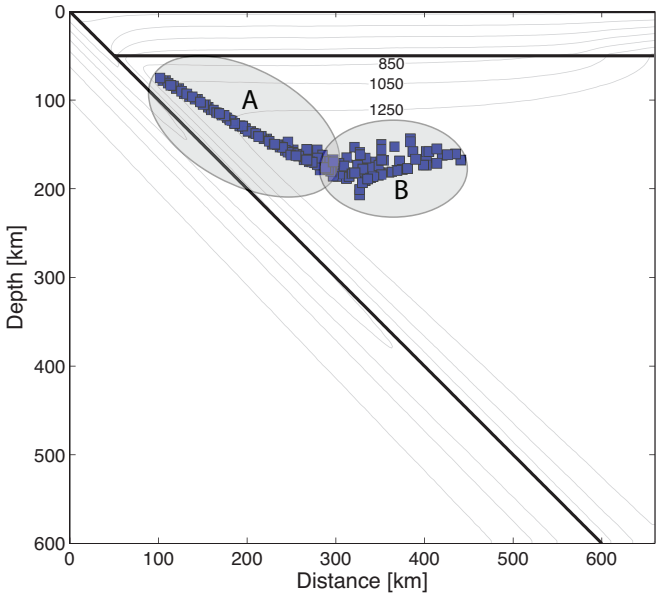

Fig. 4.16 Locations of the final hydrous flux melt events for the 2.996 wt% $X^{bulk}_{H_2O}$ case. The final melt events are located in two regions shown by the grey ellipses and marked A and B.

Figure 4.14 were higher than the T_w values for the maxmimum melt fractions. As the two regions are so distinct, it is better to consider the region separately, rather than the average T_w .

Some studies have estimated the melt temperature and pressure of the Mariana Arc using geothermometers (Kelley et al., 2010; Kohut et al., 2006). Kelley et al. (2010) estimated melt temperatures between 1200-1400 $\pm \sim 40$ °C and pressures between 1.0-2.4 $\pm$ 0.2 GPa. Kohut et al. (2006) estimated a higher magmatic temperature of ∼1367 °C at 1-1.5 GPa. The T_w from Figure 4.18 are at the lower end of the temperature range suggested by Kelley et al. (2010) but are lower than the estimate by Kohut et al. (2006). However Sisson and Grove (1993) estimated lower magmatic temperature between 950 - 1250 °C. In this case the T_w from Figure 4.18 fit in this range. The maximum and average melt pressures are both lower than the estimates of Kelley et al. (2010) and Kohut et al. (2006). This indicates the melt that occurs is too deep in the mantle wedge. If the pressure decreased but T_w remained the same the melt fraction should increase and X_{H_2O} would decrease.

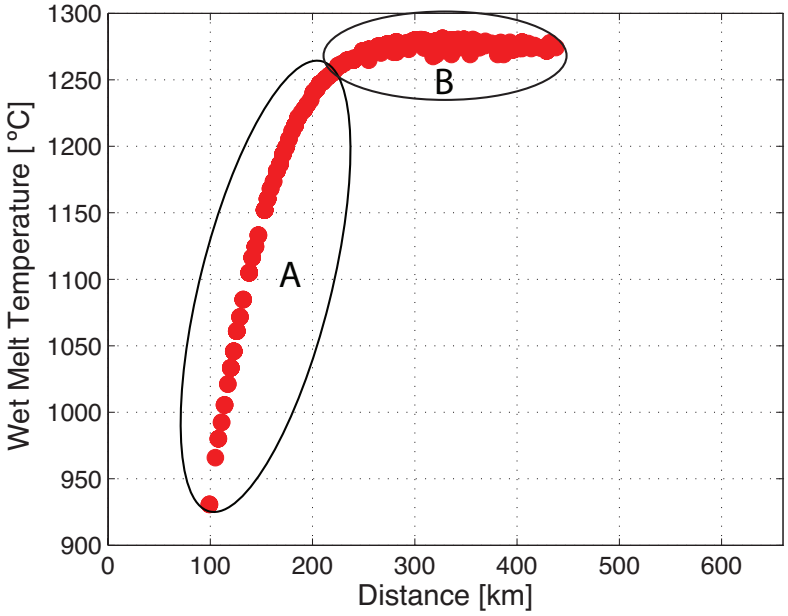

Fig. 4.17 Wet melt temperature T_w against distance for the 0.763 wt% $X_{H_2O}^{bulk}$ case. The T_w are located in two regions shown by the ellipses and marked A and B.

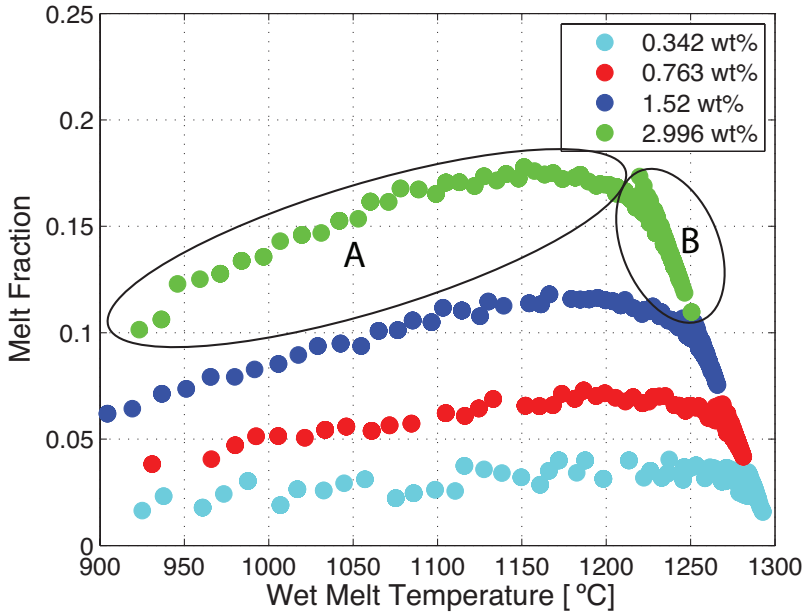

Fig. 4.18 Melt fraction against T_w for four $X_{H_2O}^{bulk}$ cases; 0.342 wt% in light blue, 0.763 wt% in red, 1.52 wt% in blue and 2.996 wt% in green. The melt fractions values are located in two regions shown by the ellipses and marked A and B on the green line.

4.5.1.3 Melt Production Rate

I used the same method as the previous chapter to calculate the melt production rate. I took the total volume values from Figure 4.9 and divided by the time in Myr for 1000 fractures to occur, as calculated in the previous chapter. Figure 4.19 plots the melt production rate for each $X_{H_2O}^{bulk}$. There were three different fracture sizes used; the red points are the 4 km length fractures, the blue points are 6 km length, and the green are the 8 km length values. By plotting the $X_{H_2O}^{bulk}$ on a log scale best fit lines could be plotted through the three sets of data. This shows the melt production rate increases exponentially with $X_{H_2O}^{bulk}$ values. For larger fracture lengths the melt production rate increase at a smaller rate with $X_{H_2O}^{bulk}$ compared to lower fracture lengths, this is due to the larger fracture lengths having a larger time for 1000 fractures to occur. Holbrook et al. (1999) and Lizarralde et al. (2002) estimated the melt production rate at the Eastern Aleutian to be $\sim$67 km^3 km^{-1} Myr^{-1}. All the melt production rates from Figure 4.19 are lower than 3.5 km^3 Myr^{-1} km^{-1} which are lower than the estimates. This suggests more melting needs to occur in the same length of time to increase the rate.

4.5.1.4 Water Content in the melt X_{H_2O}

Figure 4.20 plots X_{H_2O} against $X_{H_2O}^{bulk}$ values. The blue points are the average X_{H_2O} for each $X_{H_2O}^{bulk}$ and the red point are the X_{H_2O} for the maximum melt fraction, which is the minimum X_{H_2O} value. The average X_{H_2O} increase linearly with $X_{H_2O}^{bulk}$ from $\sim$10 wt% to $\sim$20 wt%. The minimum X_{H_2O} have a steady increase with $X_{H_2O}^{bulk}$ from $\sim$9 wt% to $\sim$17 wt%. As with the previous chapter none of the X_{H_2O} values from Figure 4.20 match estimates from Plank et al. (2013), of a range between $\sim 1.0- \sim 7.0$ wt%. However all the values below 1 wt % $X_{H_2O}^{bulk}$ fit in the range suggested by Grove et al. (2003) and Krawczynski et al. (2012) of $\sim 10- \sim 14$ wt%. For each $X_{H_2O}^{bulk}$ I found the number of X_{H_2O} values that were $\leq$ 14 wt% and calculated the percentage of melt events that produced X_{H_2O} lower than 14 wt% as shown in Figure 4.21.

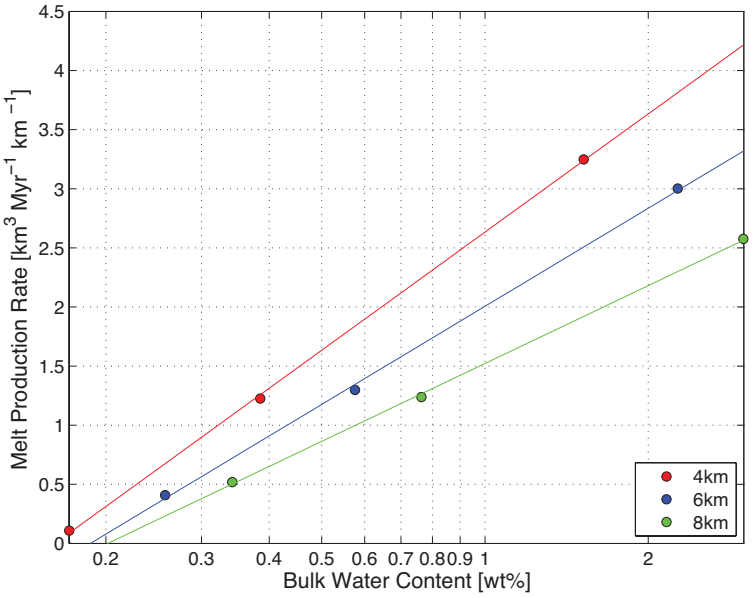

Fig. 4.19 Plot of melt production rate for hydrous flux melting against $X_{H_2O}^{bulk}$. The red points are the melt production values for a fracture length of 4 km, the blue points are for a fracture length of 6 km and the green points are for a fracture length of 8 km. x axis is plotted on a log scale.

The percentage decreases rapidly as $X_{H_2O}^{bulk}$ increases, all the $X_{H_2O}^{bulk}$ values below 1 wt% have over a 50 % success rate.

4.5.2 Model Limitations

The main limitation is the melting is moved to the nodes in this calculation rather than at the markers. This will produce some loss in resolution of the final melt as partial melting will now only occur at the grid nodes that are horizontally spaced at 3km. If the flux melting was calculated at the markers there would need to be a method to determine how far the markers would rise at each step in the melting column. If a vertical water transport mechanism was added into the model such as porous flow, then hydrous flux melting could be calculated at the markers as they move vertically upwards. Another limitation is finding the maximum temperature in the melting column, where the melting stops. Figure 4.16 shows that the final

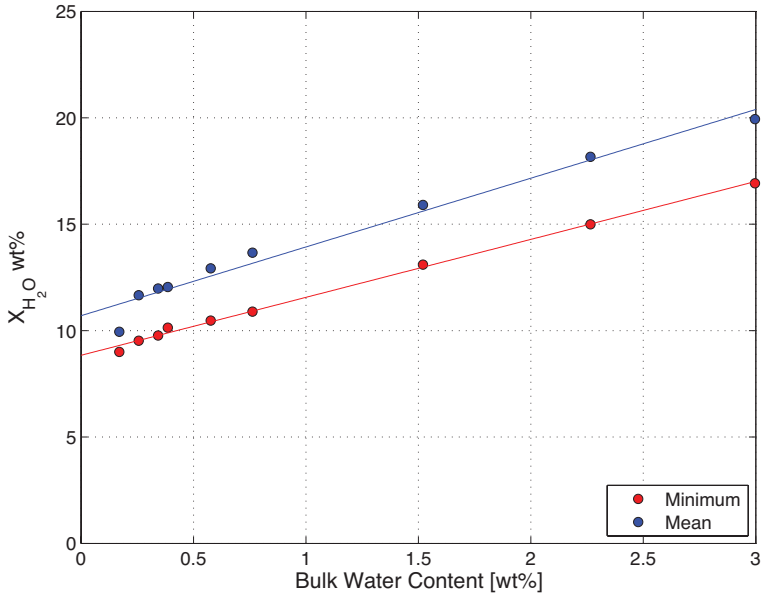

Fig. 4.20 Plot of X_{H_2O} against $X_{H_2O}^{bulk}$. The red points are the X_{H_2O} for the maximum melt fraction for each $X_{H_2O}^{bulk}$ and the blue points are the average X_{H_2O} of all the hydrous flux melting events.

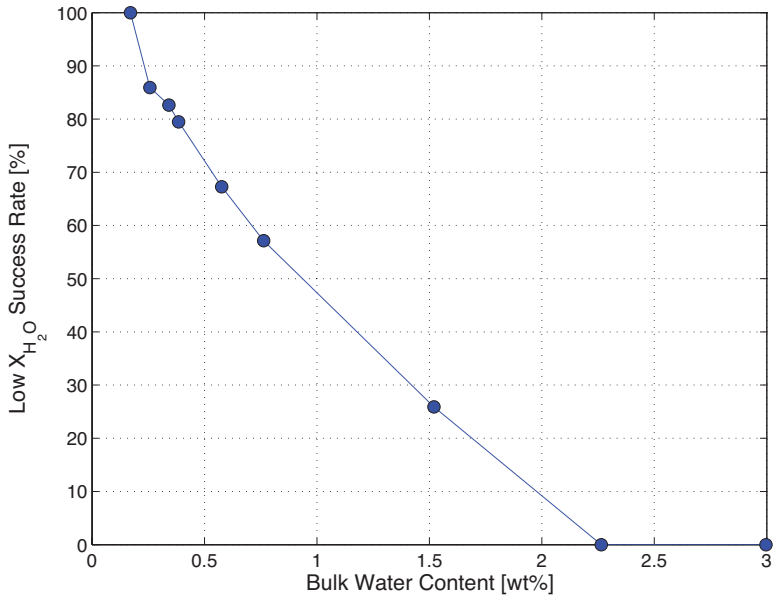

Fig. 4.21 Percentage of partial melt events that produce $X_{H_2O} \leq 14$ wt% against $X_{H_2O}^{bulk}$

melting locations plot to a line close to the wedge corner, but out in the core of the wedge the final flux melitng locations are scattered. In the core of the wedge the temperature will be close to or be 1300 °C. Small changes in the temperature within the region will cause the maximum temperature locations to be scattered. I did try to account for this by rounding the temperature to the nearest tenth of a degree but the scatter still occurred. Finally the melt production rates calculated for for hydrous flux melting used the time for 1000 fractures. Figure 4.13 showed that for most of the $X_{H_2O}^{bulk}$ values, 30-40 % of the fractures produced flux melting. The assumption made is that we do not know which of the 1000 fractures will produce flux melting, so the end member is used that it will take all 1000 fractures to produce the 30-40 % flux melting events. The other end member would be the hydrous flux melting occured within the first 30-40 % of fractures. This would lower the time required, which would increase the melt production rate by over 50%.

4.5.3 Conclusions

The aim of this chapter was to investigate hydrous flux melting occuring after flash melting to see if this produced higher melt fractions and lower corresponding X_{H_2O} . Comparisons of the melt fraction, melt production rate and X_{H_2O} with observations showed that the amount of melting produced was too low. None of the X_{H_2O} values were within the range suggested by Plank et al. (2013) of between 1-7 wt%. $X_{H_2O}^{bulk}$ values under 1 wt % had over 50 % of X_{H_2O} values under 14 wt%, which matches observations by Grove et al. (2003) and Krawczynski et al. (2012) The suggestion from the previous chapter was more melting needs to occur at the same $X_{H_2O}^{bulk}$ which would increase the melt fraction and production rate and lower the X_{H_2O} wt% accordingly. Hydrous flux melting does not appear to have acheived this. Therefore another melting process need to be considered to supplement the flash melting. Another possible melting mechanism is decompression melting. Comparison of the pressure of the maximum melt fractions indicate the hydrous flux melting occurs too deep. By having

decompression melting occur after flash melting this transport the partial melt to lower depths. England and Katz (2010b) suggested melt focussing towards the tip of the anhydrous solidus explained the consistent depth to the slab from volcanic arc, melt focussing was also suggested by Cagnioncle et al. (2007). Partial melt is focussed along a line as shown in Figure 4.16, however it still covers a large depth range, decompression melting could focus melt to a lower depth.

4.6 Summary

In this chapter I used the hydrous flux melting method by Davies and Bickle (1991) to calculate melting up a column of increasing temperature. I used the flash melting results from the previous chapter as the starting point of the hydrous flux melting column. I calculated hydrous flux melting for a range of bulk water contents. Overall as $X_{H_2O}^{bulk}$ increased the melt fraction increased. The final melt events were located in two distinct regions each with different melt fractions, X_{H_2O} values and T_w trends. Comparison of the model results with data showed that the X_{H_2O} values from the model were much higher than the global average, but fitted results from Grove et al. (2003) and Krawczynski et al. (2012) . I also showed that the melt fractions were lower than data for the same $X_{H_2O}^{bulk}$ and that the melt production rate was low, compared to melt production rate in literature. The conclusion from this is that hydrous flux melting occuring after flash meting does not increase the melt fraction or decrease the X_{H_2O} sufficiently. This suggests another melting process needs to occur either after flash melting or after the hydrous flux melting. Another melting mechanism needs to occur after the flash melting to produce more melting. A possible melt mechanism is decompression melting. The next chapter is going to examine decompression melting occurring after flash melting and also after hydrous flux melting to see if this can produce sufficient melting.

CHAPTER 5

HYDROUS DECOMPRESSION MELTING

5.1 Introduction

The previous chapter examined the flash melting followed by hydrous flux melting (flash-flux) scenario, where the flux melting was calculated using the parameterisation by Davies and Bickle (1991). Whilst the water content in the melt values for the flash-flux case were ~ 10 wt% and fitted with some petrological observations Krawczynski et al. (2012), lower water content values of ~ 4 wt% have been observed (Plank et al., 2013) . As the flash-flux melting scenario does not produce water content in the melt values this low, I need to examine other melting scenarios.

The other melting process that could occur in subduction zones is decompression melting and there is evidence from tomography that suggests decompression melting does take place. Tomographic studies of the north eastern Japanese arc show a seismic low velocity, high attenuation zone in the mantle wedge, that is nearly parallel to the slab. This has been interpreted as an upwelling flow that contains water released by dehydration of the slab. In this region melt is formed by the addition of water and by decompression melting (Hasegawa et al., 2005). I am going to use the parameterisation for decompression melting that has been extended to include hydrous melting from Katz et al. (2003). This parameterisation is based

on the dry adiabatic decompression melting parameterisation from McKenzie (1984). I am going to be examining two melting scenarios in this chapter; the first will be flash melting followed by decompression melting (flash-ad) and the second is flash melting then hydrous flux melting followed by decompression melting (flash-flux-ad).

This chapter will have five main sections. The first will discuss the adiabatic decompression wet melting parameterisation by Katz et al. (2003). The second section will discuss the two melting scenarios and the method for calculating the melting. The next section is the results section which will be the final melt fractions and X_{H_2O} values for each melting scenario. This is followed by the discussion section, where I compare both melting cases to observations from volcanic arcs. Finally is a summary of this chapter.

5.2 Adiabatic Decompression Melting Parameterisation

The melting produced by a reduction of pressure at constant entropy was defined by McKenzie (1984) as:

$$\left.\frac{\mathrm{d}F}{\mathrm{d}P}\right|_S = \frac{\dfrac{-C_p}{T}\left(\dfrac{\partial T}{\partial P}\right)\Big|_F + F\dfrac{\alpha_f}{\rho_f} + (1-F)\dfrac{\alpha_s}{\rho_s}}{\Delta S + \dfrac{C_p}{T}\left(\dfrac{\partial T}{\partial F}\right)\Big|_P} \tag{5.1}$$

Katz et al. (2003) use equation (5.1) but they also include their wet melting parameterisation. By rearranging their wet melting equation for F in terms of T, $\frac{\mathrm{d}T}{\mathrm{d}P}$ and $\frac{\mathrm{d}T}{\mathrm{d}F}$ can be found. As the water content in the melt cannot exceed the saturated water content there are two sets of equations; the first for $X_{H_2O} \leq X^{sat}_{H_2O}$ and the second for $X_{H_2O} > X^{sat}_{H_2O}$. These are as follows:

If $X_{H_2O} \leq X^{sat}_{H_2O}$

$$T = F^{\frac{1}{\beta_1}}\left(T^{lherz}_{liquidus} - T_{solidus}\right) + T_{solidus} - K\left(\frac{X^{bulk}_{H_2O}}{D_{H_2O} + (1 - D_{H_2O})F}\right)^{\gamma} \tag{5.2}$$

$$\left.\frac{\mathrm{d}T}{\mathrm{d}F}\right|_P = \beta_1^{-1} F^{\frac{(1-\beta_1)}{\beta_1}} \left(T_{liquidus}^{lherz} - T_{solidus}\right) + \gamma K \frac{(X_{H_2O}^{bulk})^{\gamma}(1-D_{H_2O})}{(D_{H_2O}+(1-D_{H_2O})F)^{\gamma+1}} \tag{5.3}$$

$$\left.\frac{\mathrm{d}T}{\mathrm{d}P}\right|_F = F^{\frac{1}{\beta_1}} \left(\frac{\partial T_{liquidus}^{lherz}}{\partial P} - \frac{\partial T_{solidus}}{\partial P}\right) + \frac{\partial T_{solidus}}{\partial P} \tag{5.4}$$

If $X_{H_2O} > X_{H_2O}^{sat}$

$$T = F^{\frac{1}{\beta_1}} \left(T_{liquidus}^{lherz} - T_{solidus}\right) + T_{solidus} - K\left(\chi_1 P^{\lambda} + \chi_2 P\right)^{\gamma} \tag{5.5}$$

$$\left.\frac{\mathrm{d}T}{\mathrm{d}F}\right|_P = \beta_1^{-1} F^{\frac{(1-\beta_1)}{\beta_1}} \left(T_{liquidus}^{lherz} - T_{solidus}\right) \tag{5.6}$$

$$\left.\frac{\mathrm{d}T}{\mathrm{d}P}\right|_F = F^{\frac{1}{\beta_1}} \left(\frac{\partial T_{liquidus}^{lherz}}{\partial P} - \frac{\partial T_{solidus}}{\partial P}\right) + \frac{\partial T_{solidus}}{\partial P} - \lambda K\left(\chi_1 P^{\lambda} + \chi_2 P\right)^{\lambda-1}\left(\lambda\chi_1 P^{\lambda-1} + \chi_2\right) \tag{5.7}$$

For both cases $\frac{\partial T_{solidus}}{\partial P}$ and $\frac{\partial T_{liquidus}^{lherz}}{\partial P}$ are found by differentiating the equations for $T_{solidus}$ and $T_{liquidus}^{lherz}$ respectively:

$$\frac{\partial T_{solidus}}{\partial P} = A_2 + 2A_3 P \tag{5.8}$$

$$\frac{\partial T_{liquidus}^{lherz}}{\partial P} = B_2 + 2B_3 P \tag{5.9}$$

By integrating equation (5.10) simultaneously with equation (5.1) the pressure temperature path of the adiabat can be calculated. This is done using a 4th order Runge Kutta scheme

(Press et al., 1992).

$$\left.\frac{\mathrm{d}T}{\mathrm{d}P}\right|_S = T\left(\frac{F\frac{\alpha_f}{\rho_f} + (1-F)\frac{\alpha_s}{\rho_s} - \Delta S\left.\frac{\mathrm{d}F}{\mathrm{d}P}\right|_S}{C_p}\right) \tag{5.10}$$

To integrate equations (5.1) and (5.10) they are defined in terms of functions f and g:

$$\frac{\mathrm{d}F}{\mathrm{d}P} = f(P,F,T) \tag{5.11}$$

$$\frac{\mathrm{d}T}{\mathrm{d}P} = g(P,F,T) \tag{5.12}$$

The first point is at a given pressure and temperature where $F = 0$. The step size h is the decrease in pressure at each step:

$$h = P_{i+1} - P_i \tag{5.13}$$

$$k_1 = hf(P,F,T) \tag{5.14}$$

$$k_2 = hf(P+\frac{h}{2}, F+\frac{k_1}{2}, T+\frac{m_1}{2}) \tag{5.15}$$

$$k_3 = hf(P+\frac{h}{2}, F+\frac{k_2}{2}, T+\frac{m_2}{2}) \tag{5.16}$$

$$k_4 = hf(P+h, F+k_3, T+m_3) \tag{5.17}$$

$$m_1 = hg(P,F,T) \tag{5.18}$$

$$m_2 = hg(P + \frac{h}{2}, F + \frac{k_1}{2}, T + \frac{m_1}{2}) \tag{5.19}$$

$$m_3 = hg(P + \frac{h}{2}, F + \frac{k_2}{2}, T + \frac{m_2}{2}) \tag{5.20}$$

$$m_4 = hg(P + h, F + k_3, T + m_3) \tag{5.21}$$

$$F_{i+1} = F_i + \frac{k_1}{6} + \frac{k_2}{3} + \frac{k_3}{3} + \frac{k_4}{6} \tag{5.22}$$

$$T_{i+1} = T_i + \frac{m_1}{6} + \frac{m_2}{3} + \frac{m_3}{3} + \frac{m_4}{6} \tag{5.23}$$

By integrating equations (5.1) and (5.10) the temperature pressure curves and melt fraction pressure curves are plotted in Figure 5.1, for three different potential temperatures. The solid lines are for a $X_{H_2O}^{bulk}$ of 0 wt% and the dashed line are for a $X_{H_2O}^{bulk}$ of 0.02 wt%.

5.3 Melting Scenarios

In this chapter there are two melting scenarios that I am going to examine; the first is flash melting followed by adiabatic decompression melting and the second is flash melting, then hydrous flux melting followed by adiabatic decompression melting.

5.3.1 Flash melting then Adiabatic Decompression Melting

The first scenario, shown in Figure 5.2, is flash melting due to water being added to the mantle wedge by a hydraulic fracture, followed by adiabatic decompression melting as the melt rises towards the overriding plate. In this case the flash melting is calculated using the

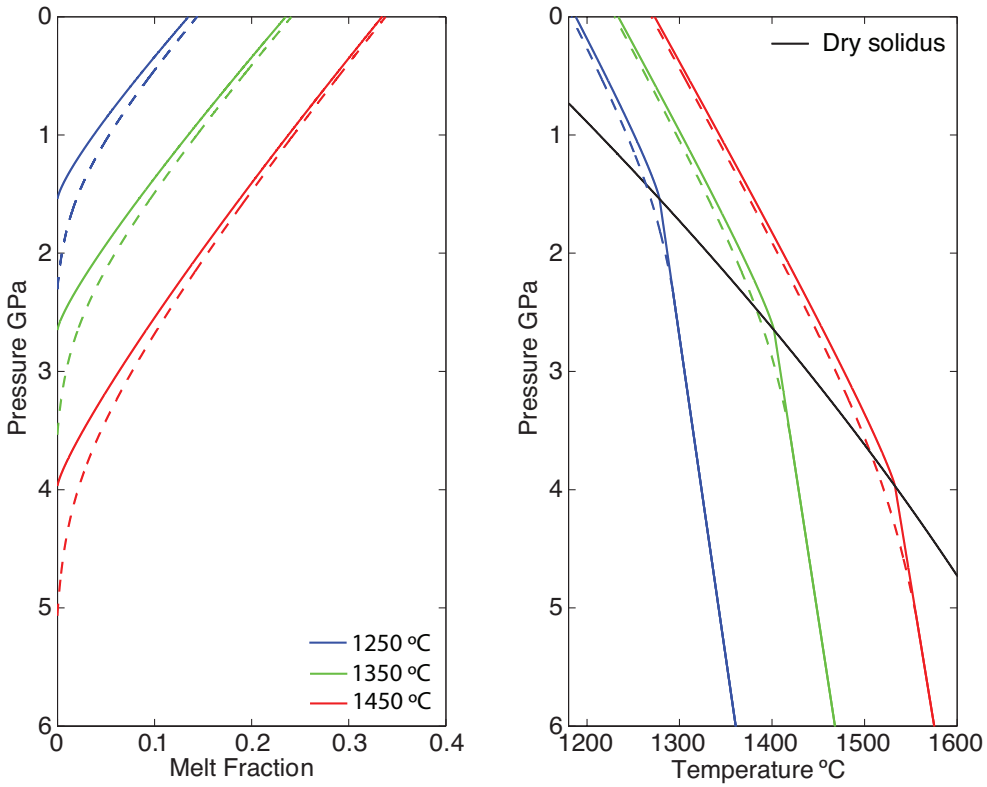

Fig. 5.1 Results of integrating equations (5.1) and (5.10) for $X^{bulk}_{H_2O}$ of 0 shown by the solid line and $X^{bulk}_{H_2O}$ of 0.02 wt% shown by the dashed lines. Three potential temperatures were used 1250 °C in blue, 1350 °C in green and 1450 °C in red. Reproduced from Katz et al. (2003).

method from Chapter 3, where the hydraulic fracture end point is calculated from a random start point on the slab and a random angle. Water is added at this point to a certain size radius around the endpoint. The radius and fracture size dictates the initial water content as set out in the Flash melting chapter. From the initial water content the melt fraction is calculated for all the markers affected. To get the initial conditions for the adiabatic decompression melting the nearest grid node is found for the markers with a melt fraction. The average melt fraction is then calculated and the pressure and temperature at that grid node are used as the starting (F,P,T) values.

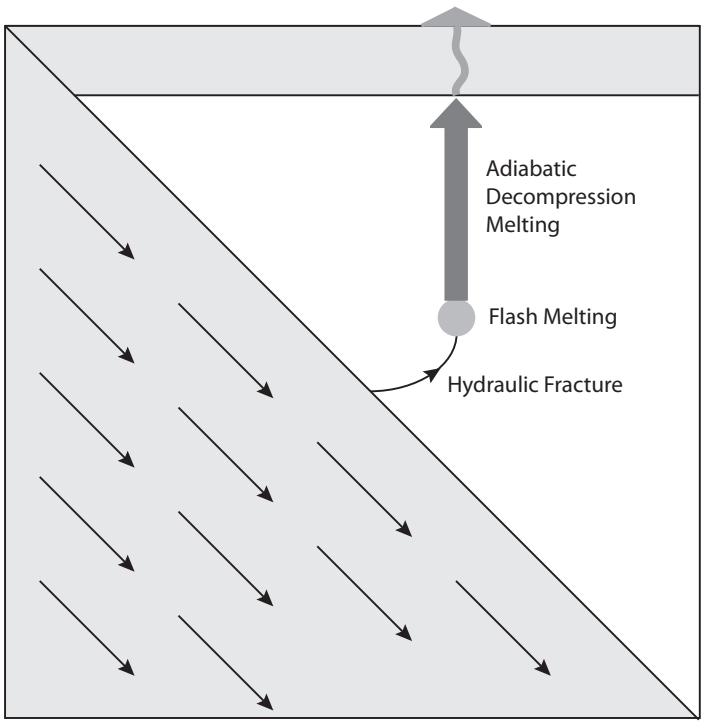

Fig. 5.2 Schematic of flash melting followed by adiabaitic decompression melting scenario.

5.3.2 Flash Melting then Hydrous flux melting, then Adiabatic Decompression Melting

The second scenario, shown in Figure 5.3, is flash melting due to a hydraulic fracture, followed by hydrous flux melting to the point of maximum temperature and then adiabatic decompression melting to the overriding plate. In this case the average flash melt fraction and corresponding pressure and temperature from that grid node are used as the starting point of the hydrous flux melting. The hydrous flux melting then is calculated using the method from Chapter 4 up to the point of maximum temperature vertically above the initial grid node. The final melt fraction and pressure and temperature at that grid node are then used as the initial (F,P,T) conditions for the adiabatic decompression melting.

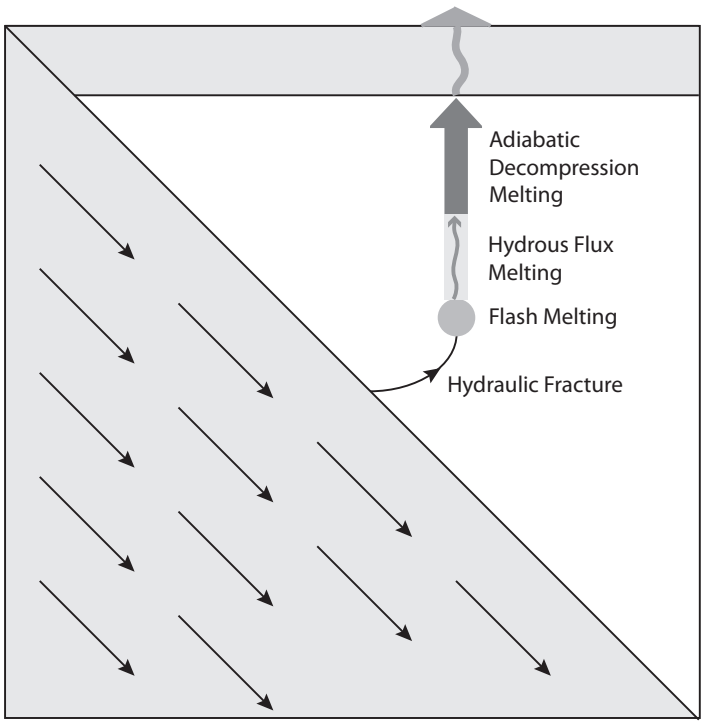

Fig. 5.3 Schematic of flash melting, then hydrous flux melting followed by adiabaitic decompression melting scenario.

5.3.3 Temperature used in Melting Calculation

The adiabatic decompression melting will be calculated on a 300 m grid spacing, similar to hydrous flux melting. The initial conditions of (F,P,T) required for adiabatic decompression melting are found using the steps set out for each melting scenario from the previous section. Adiabatic decompression melting is traditionally used to calculate melting at mid ocean ridges where the temperature decreases towards the surface making the use of the adiabatic temperature gradient appropriate. However in subduction zone regions you get the temperature increasing towards the core of the mantle wedge, then the temperature decreases towards the surface. The two pressure-temperature regimes are shown in Figure 5.4. As they both start at the same temperature the adiabatic temperature is lower than the subduction zone temperature for the initial values. If this was to happen the melt would 'freeze' as it would be at a lower temperature than the surrounding mantle; accordingly, I will use the

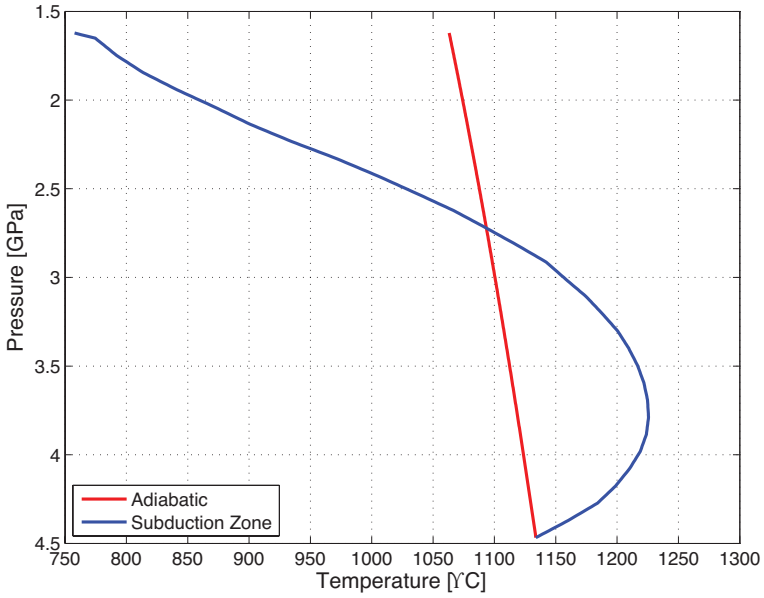

Fig. 5.4 Pressure-Temperature paths for a decompression melting calculation using the adiabatic temperature gradient plotted in red and the thermal model temperature in blue. The thermal model temperature increases as pressure decreases before decreaisng, where the adiabaitc temeprature is a constant decrease with pressure.

thermal model temperatures as the temperature input into the model. This means equation (5.1) will no longer need to integrated simultaneously with (5.10) as the temperature will be known. The traditional Runge Kutta method is therefore used for one function only as follows:

$$\frac{\mathrm{d}F}{\mathrm{d}P} = f(P,F) \tag{5.24}$$

$$k_1 = hf(P,F) \tag{5.25}$$

$$k_2 = hf(P+\frac{h}{2},F+\frac{k_1}{2}) \tag{5.26}$$

$$k_3 = hf(P+\frac{h}{2},F+\frac{k_2}{2}) \tag{5.27}$$

$$k_4 = hf(P+h, F+k_3) \tag{5.28}$$

$$F_{i+1} = F_i + \frac{k_1}{6} + \frac{k_2}{3} + \frac{k_3}{3} + \frac{k_4}{6} \tag{5.29}$$

5.4 Results

The melt fraction, melt volume and X_{H_2O} values are caluclated for both the flash-ad and the flash-flux-ad cases.

5.4.1 Melt Fraction

5.4.1.1 Flash Melting Followed by Adiabatic Decompression Melting

Figure 5.5 plots the final melt fraction against distance for each of the 9 $X_{H_2O}^{bulk}$, for the flash-ad case. In Figure 5.5 the general trend is the melt fraction increases with distance until $\sim$ 200 km. After 200 km the melt fraction no longer increases. As $X_{H_2O}^{bulk}$ increases the greater the maximum melt fraction value. For the fracture end point node and the melt points in the vertical column above, I have plotted the position of the node and the colour of the point corresponds to the melt fraction. I did this for three different water contents; 0.763 wt% shown in Figure 5.6, 1.52 wt% shown in Figure 5.7 and 2.996 wt% shown in Figure 5.8. For all three Figures the region with the largest melt fraction was the area between the overriding plate and 100 km depth and after 200 km distance. The three figures show that the melt fraction increases with $X_{H_2O}^{bulk}$ values. All three figures clearly show the increase in melt fraction as the decompression melting occurs upwards from the fracture end node.

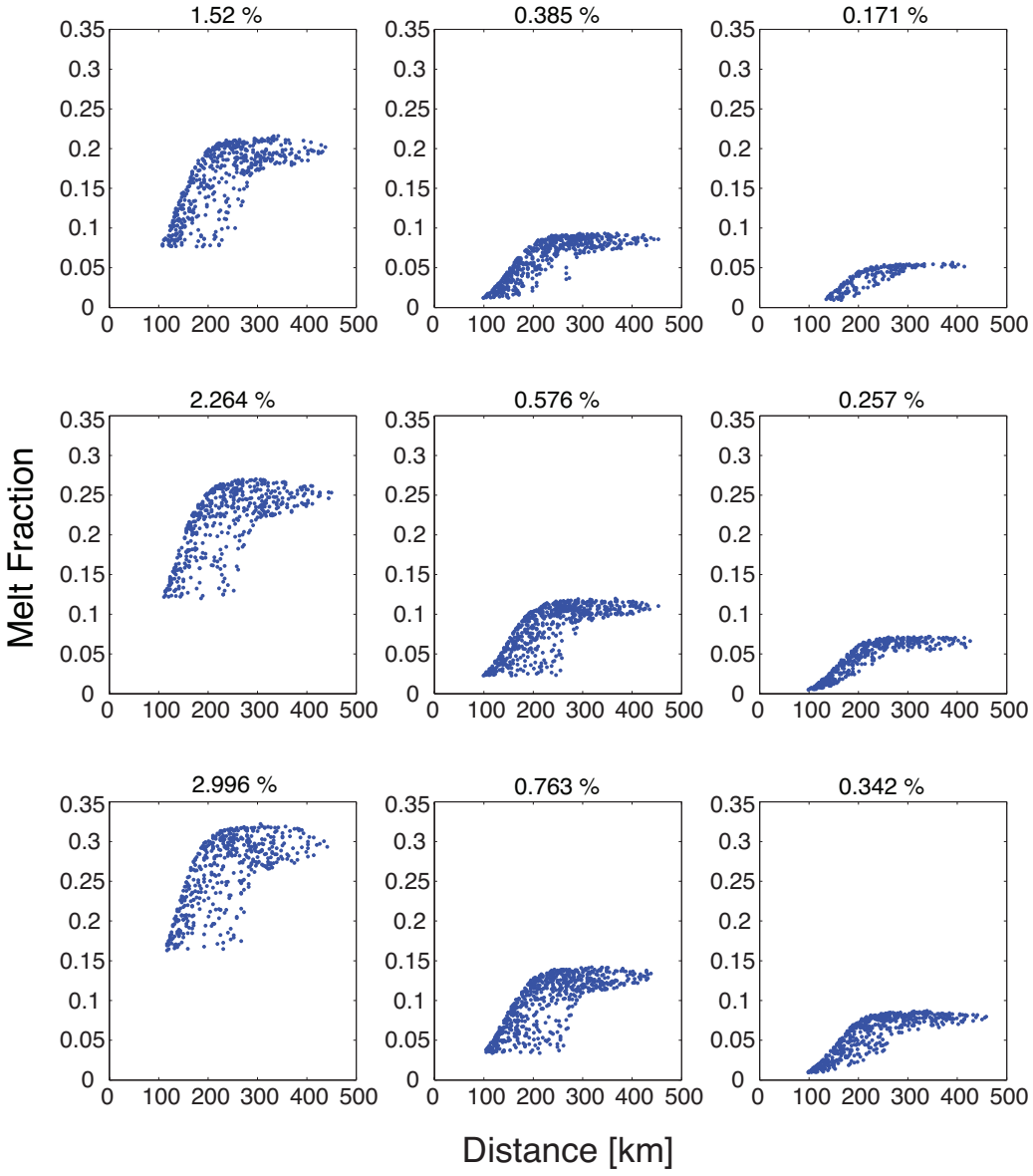

Fig. 5.5 Final melt fraction against distance for 9 $X_{H_2O}^{bulk}$ values for the flash-ad melting scenario using the thermal model temperature

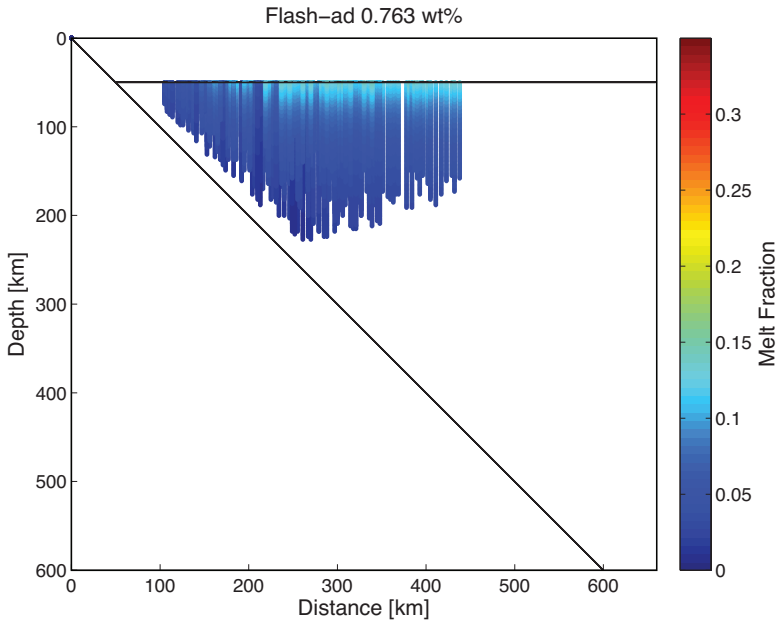

Fig. 5.6 Scatter plot of melt fraction for $X_{H_2O}^{bulk}$ of 0.766 wt% for a flash-ad case

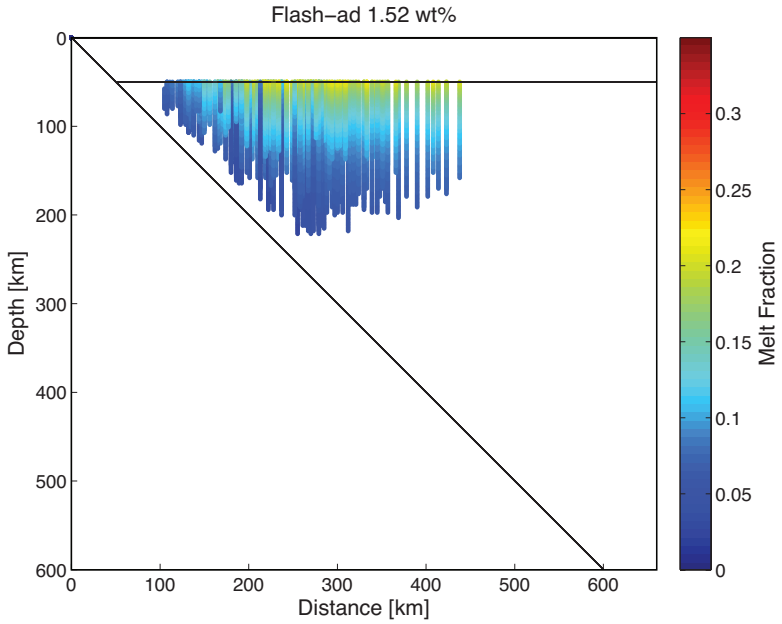

Fig. 5.7 Scatter plot of melt fraction for $X_{H_2O}^{bulk}$ of 1.52 wt% for a flash-ad case

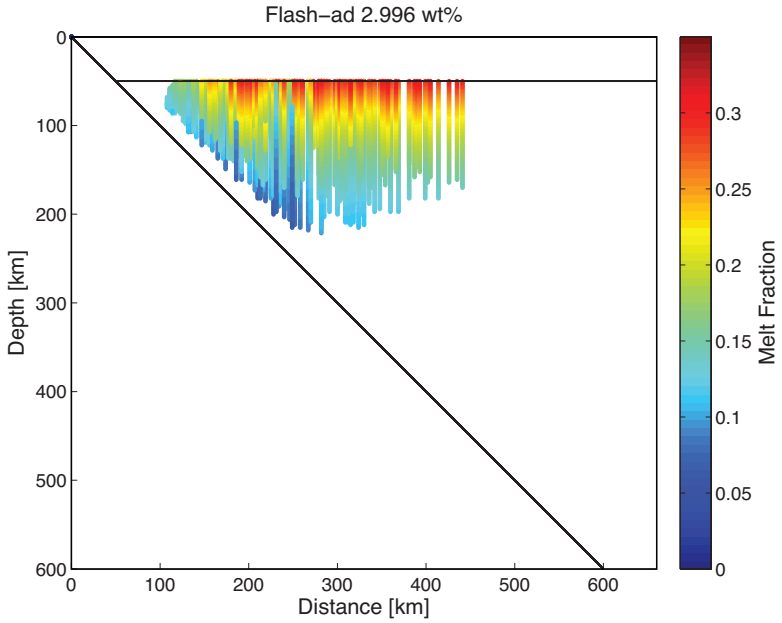

Fig. 5.8 Scatter plot of melt fraction for $X_{H_2O}^{bulk}$ of 2.996 wt% for a flash-ad case

5.4.1.2 Flash Melting then Hydrous Flux Melting, Followed by Adiabatic Decompression Melting

Figure 5.9 plots the final melt fraction against distance for the flash-flux-ad case. The general trend is the melt fraction increases with distance. For $X_{H_2O}^{bulk}$ values < 0.5 wt% the maximum melt fraction is at ~ 300 km distance. For initial water contents of > 0.5 wt% the melt fraction increases with distance to ~ 200 km distance then becomes constant. As $X_{H_2O}^{bulk}$ increases the spread of the melt fraction values decreases. The spread of values is also a lot smaller compared to the flash-ad melt fraction values shown in Figure 5.5. For $X_{H_2O}^{bulk}$ values of < 1 wt% the maximum melt fractions are similar, whereas for $X_{H_2O}^{bulk}$ values > 1 wt% the maximum melt fraction increases with $X_{H_2O}^{bulk}$ values. I plotted scatter plots of the melt fractions in the mantle wedge for three different water contents for the decompression melting portion; 0.763 wt% shown in Figure 5.10, 1.52 wt% shown in Figure 5.11 and 2.996 wt% shown in Figure 5.12. For all three figures the region with the largest melt fraction was the area between the overriding plate and 100 km depth and after 150 km distance. The three figures show that the melt fraction increases with $X_{H_2O}^{bulk}$ values. All three figures clearly show the increase in melt fraction as the decompression melting occurs upwards from the fracture end node. Compared with figures 5.6, 5.7, and 5.8, these three melt scatter plots show that higher melt fractions occur lower in the mantle wedge for equal $X_{H_2O}^{bulk}$ values.

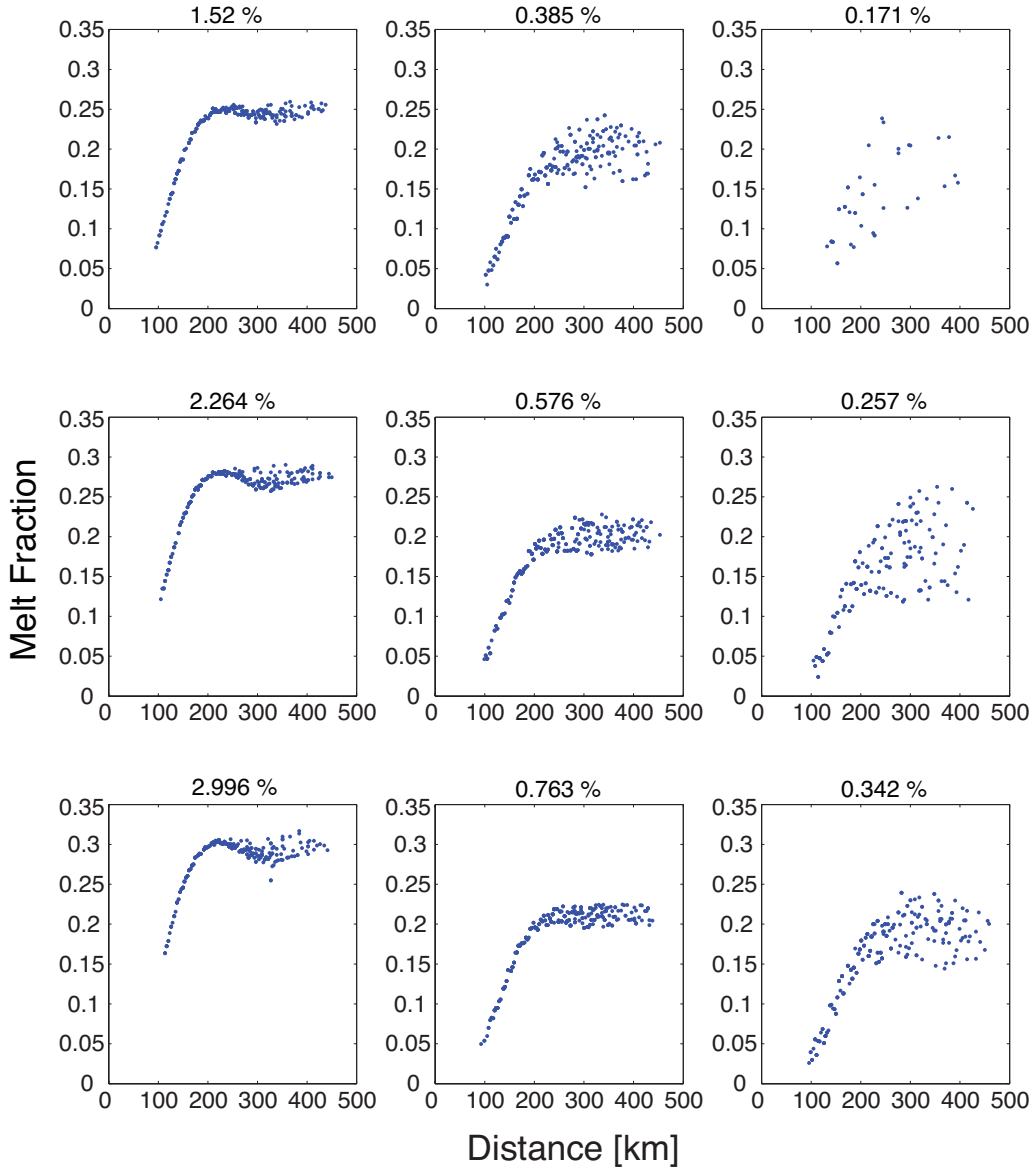

Fig. 5.9 Final melt fraction against distance for 9 $X_{H_2O}^{bulk}$ values for the flash-flux-ad melting scenario using the thermal model temperature

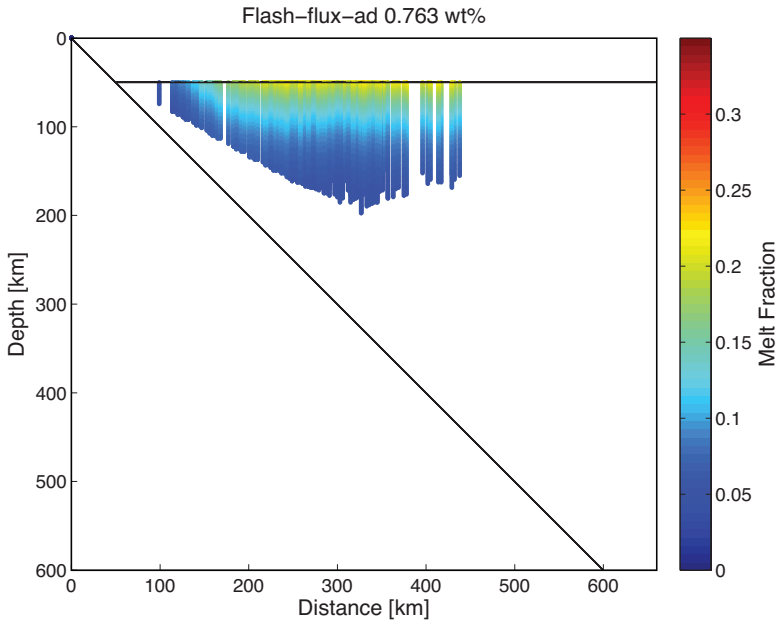

Fig. 5.10 Scatter plot of melt fraction for $X_{H_2O}^{bulk}$ of 0.766% for a flash-flux-ad case

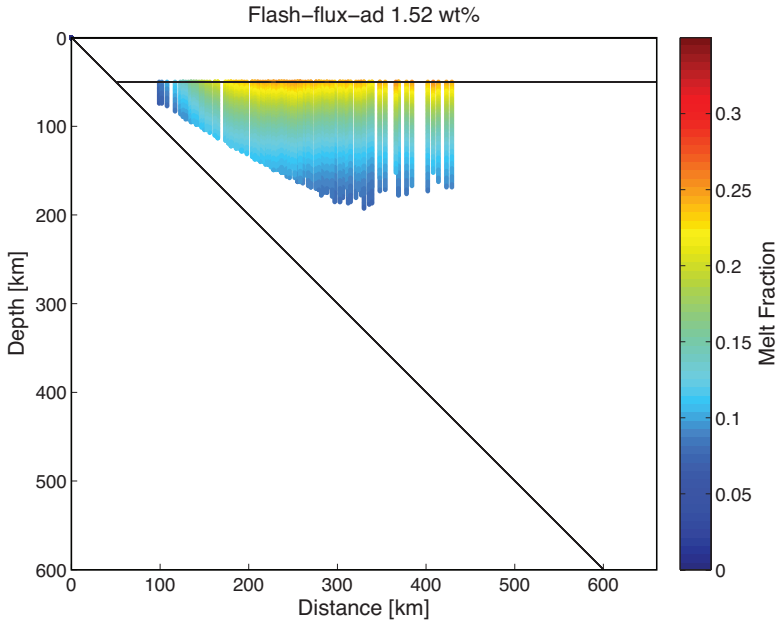

Fig. 5.11 Scatter plot of melt fraction for $X_{H_2O}^{bulk}$ of 1.52% for a flash-flux-ad case

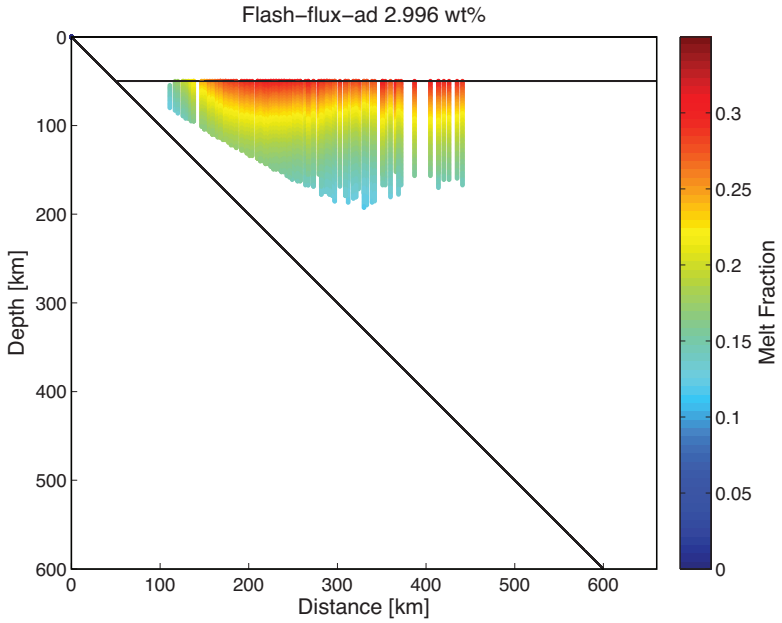

Fig. 5.12 Scatter plot of melt fraction for $X_{H_2O}^{bulk}$ of 2.996% for a flash-flux-ad case

5.4.2 Melt Volume

As with the previous chapter, I assume that each fracture end node is one marker so the melt volume for each node is the mass of the marker divided by the density of the mantle, then multiplied by the melt fraction. I found the melt volume for each top node in a melting column to give the final melt volume. Figure 5.13 is a plot of the final melt volume in km^3 as a function of horizontal distance for the flash-ad case, and Figure 5.14 is a plot of the final melt volume in km^3 as a function of horizontal distance for the flash-flux-ad case. For both figures the highest melt volumes are found in the cases with higher $X_{H_2O}^{bulk}$ values. In all cases the total melt volume in the bin increases to $\sim$ 300 km distance, then it decreases with distance. The total melt volume for each $X_{H_2O}^{bulk}$ is found by finding the sum of each bin from Figures 5.13 and Figure 5.14. Figures 5.15 and Figures 5.16 plots the total volume in km^3 against $X_{H_2O}^{bulk}$. I plotted both the figures on a log scale for the x axis. For Figure 5.15 the total volume values then plotted to a straight line. This shows the total volume of flux melting increases exponentially with $X_{H_2O}^{bulk}$ values. Figure 5.16 has linear fit with exponentially increasing $X_{H_2O}^{bulk}$ for lower values of $X_{H_2O}^{bulk}$, but the trend starts to curve at higher $X_{H_2O}^{bulk}$ values and the rate of increase decreases with exponential increase in $X_{H_2O}^{bulk}$ value. The total volumes in Figure 5.15 are lower than those in Figure 5.16 for $X_{H_2O}^{bulk}$ values under 1 wt%, above 1wt% the total volume values in Figure 5.15 are higher.

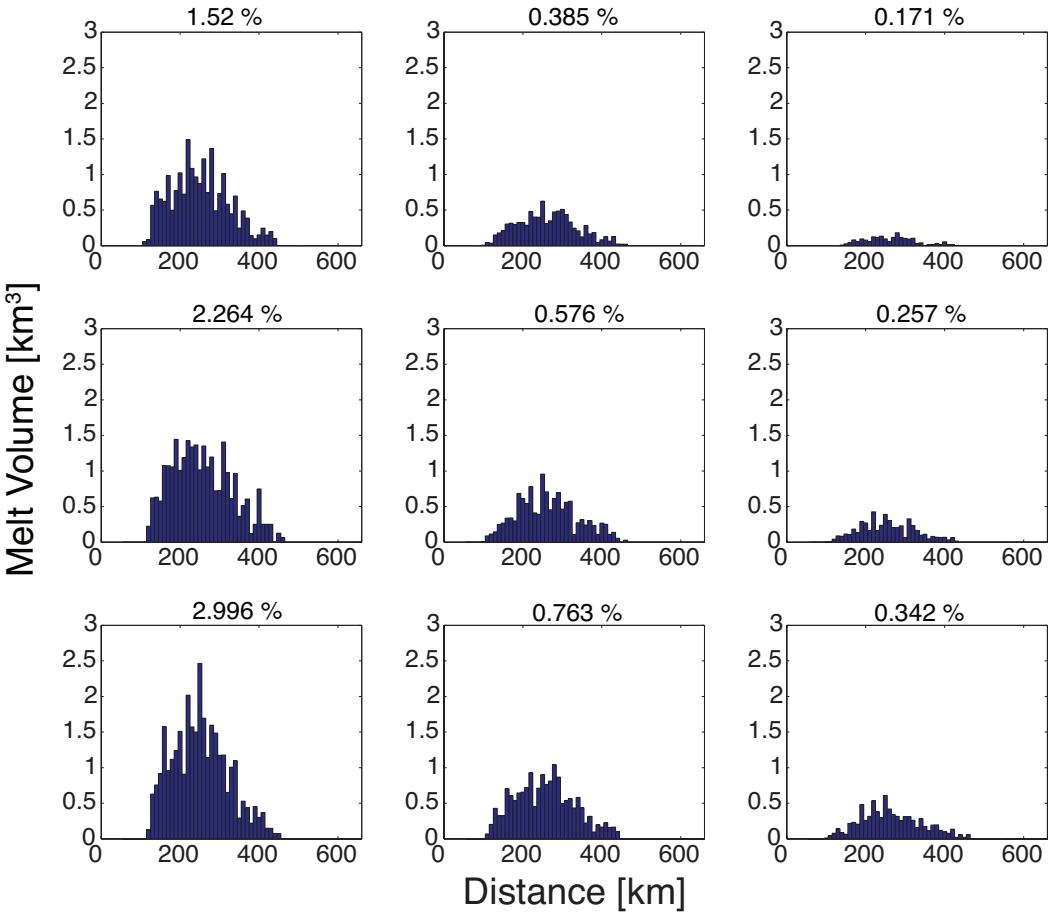

Fig. 5.13 Total melt volume found for 10 km sized bins for 9 different $X_{H_2O}^{bulk}$ values for the flash-ad case

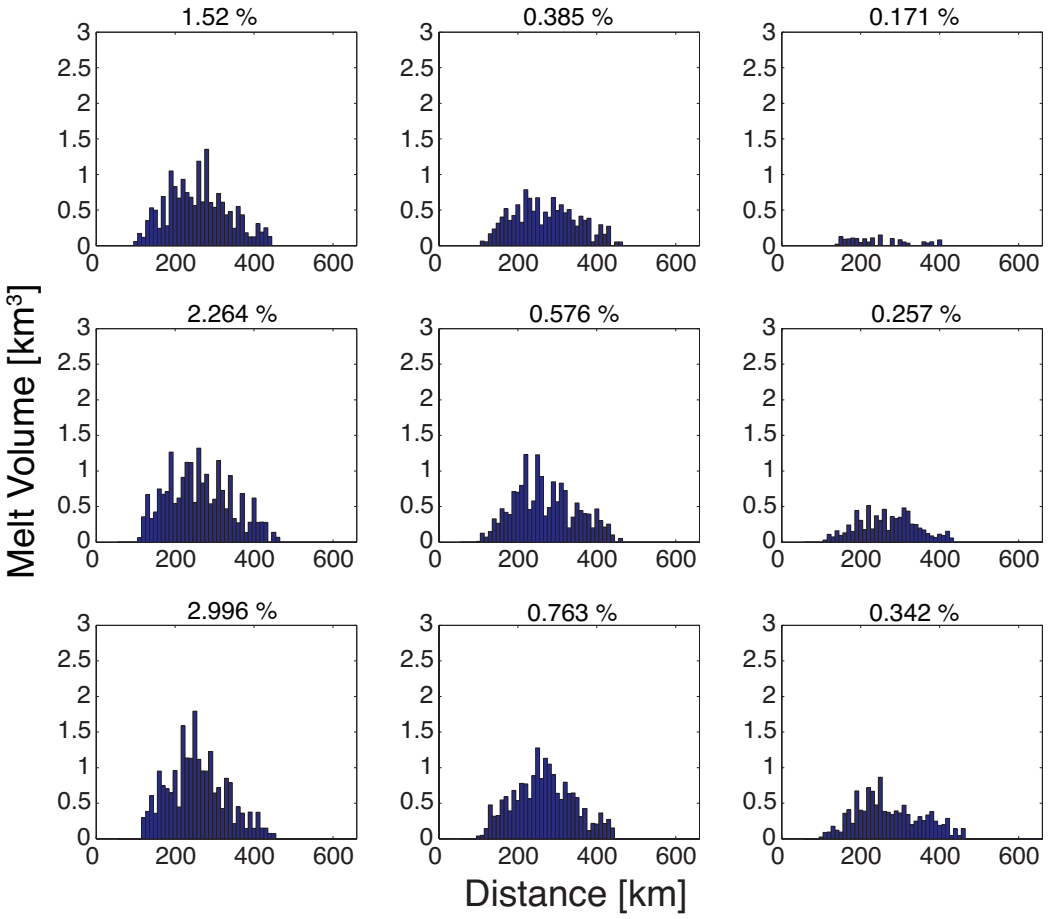

Fig. 5.14 Total melt volume found for 10 km sized bins for 9 different $X_{H_2O}^{bulk}$ values for the flash-flux-ad case

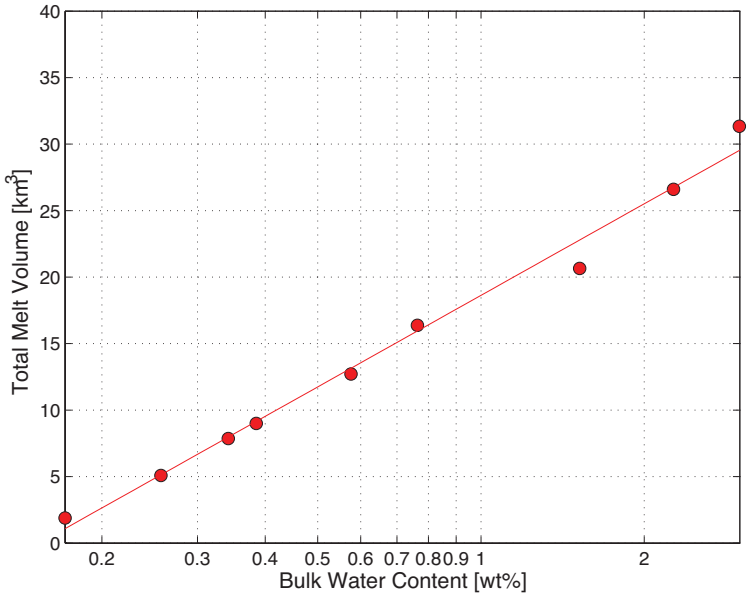

Fig. 5.15 Total melt volume of the final flash-ad melting events plotted against $X_{H_2O}^{bulk}$ with x axis plotted on a log scale.

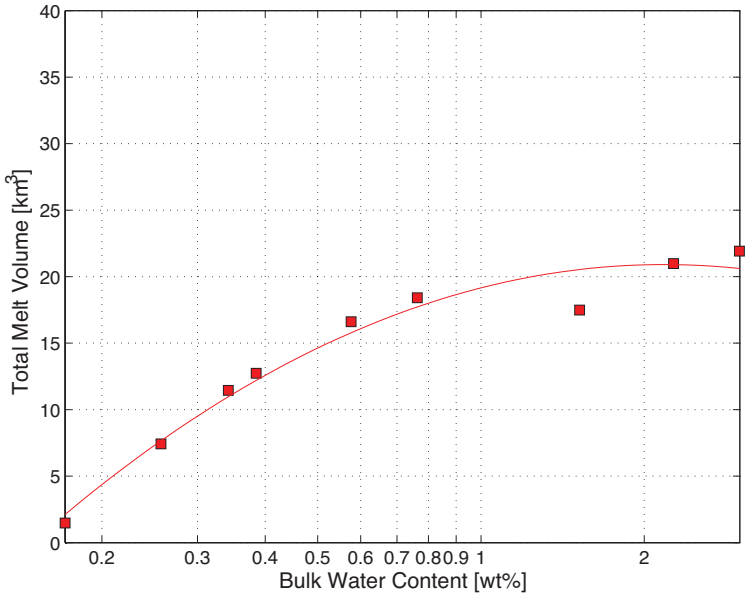

Fig. 5.16 Total melt volume of the final flash-flux-ad melting events plotted against $X_{H_2O}^{bulk}$ with x axis plotted on a log scale.

5.4.3 Water Content in the Melt

5.4.3.1 Flash Melting Followed by Adiabatic Decompression Melting

Figure 5.17 plots X_{H_2O} against distance for nine different $X_{H_2O}^{bulk}$ values for the flash-flux-ad cases. The general trend is the X_{H_2O} decreases with distance to $\sim$ 200 km distance then becomes constant. The smaller $X_{H_2O}^{bulk}$ values have lower minimum X_{H_2O} values of $\sim$ 4 wt% and the larger $X_{H_2O}^{bulk}$ minimum values of $\sim$ 8 wt%.

5.4.3.2 Flash Melting then Hydrous Flux Melting Followed by Adiabatic Decompression Melting

Figure 5.18 plots X_{H_2O} against distance for nine $X_{H_2O}^{bulk}$ values for the flash-flux-ad cases. In general the X_{H_2O} decreases with distance to $\sim$ 200 km distance then becomes constant. As $X_{H_2O}^{bulk}$ increases the minimum X_{H_2O} increases. Figure 5.18 has less spread in the X_{H_2O} values compared to the flash-ad case shown in Figure 5.17. The smaller $X_{H_2O}^{bulk}$ values have lower minimum X_{H_2O} values of $\sim$ 2 wt% and the larger $X_{H_2O}^{bulk}$ minimum X_{H_2O} values of $\sim$ 6-8 wt%.

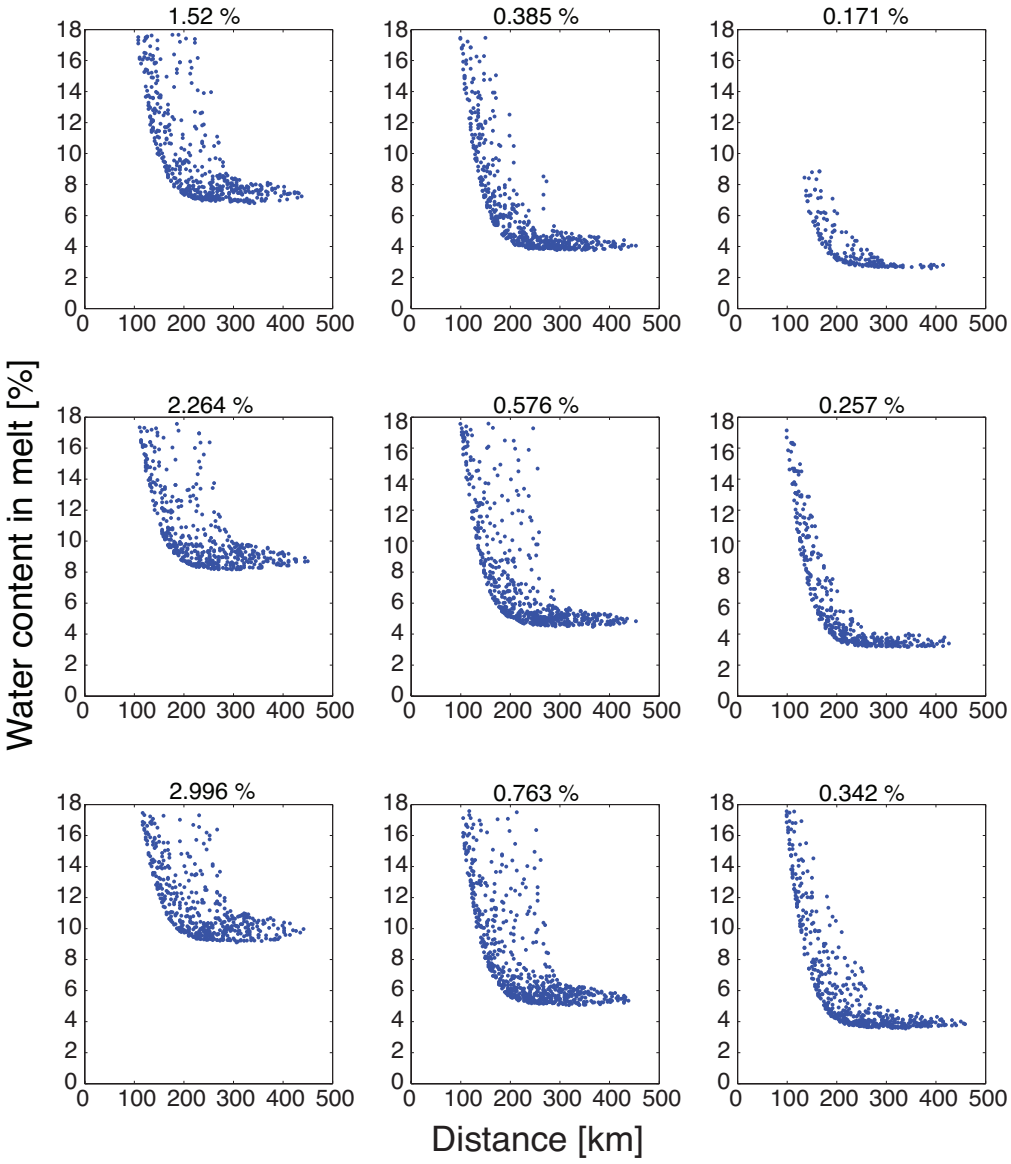

Fig. 5.17 Final water content in the melt against distance for 9 $X_{H_2O}^{bulk}$ values for the flash-ad melting scenario using the thermal model temperature

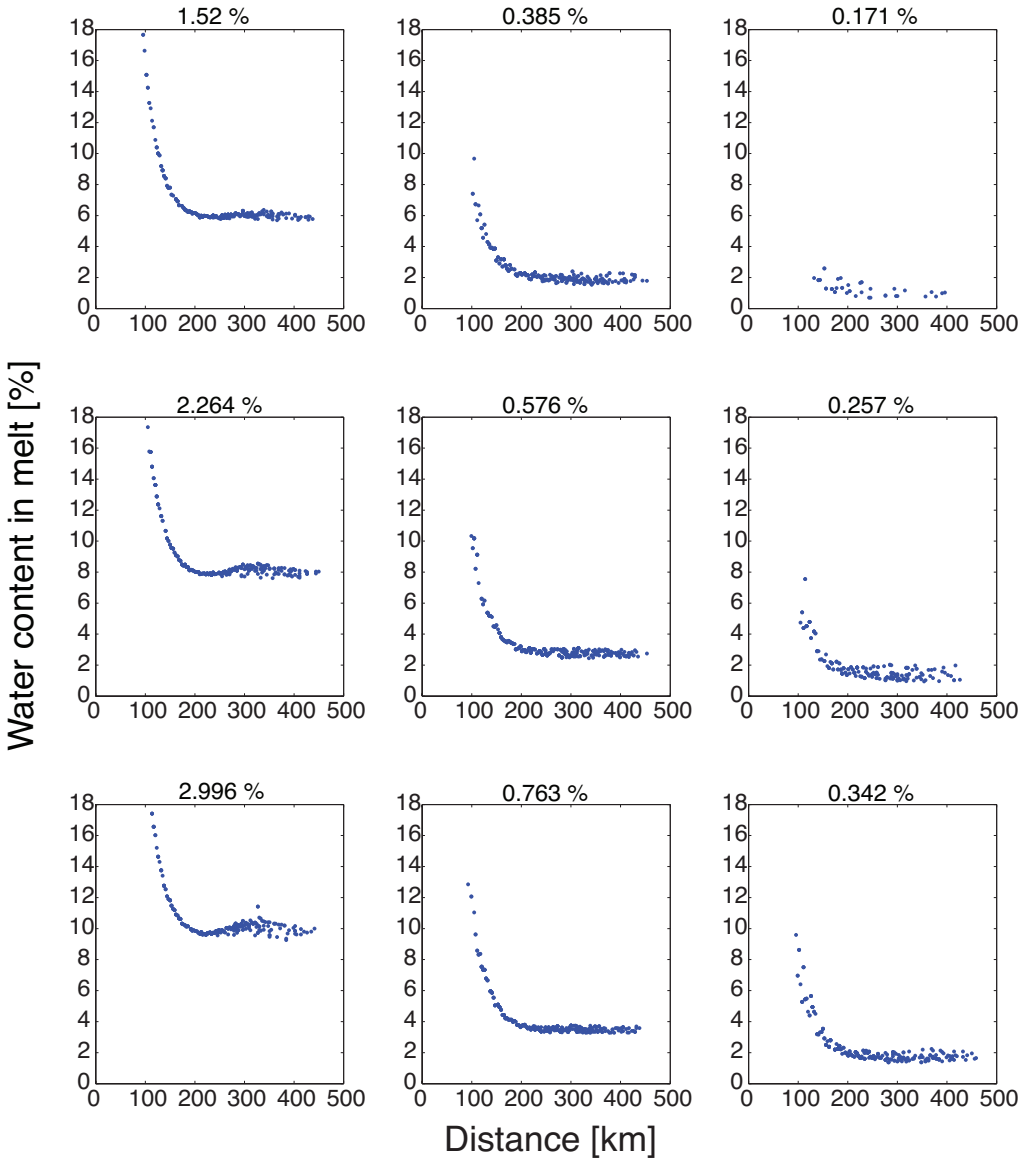

Fig. 5.18 Final X_{H_2O} value against distance for 9 $X_{H_2O}^{bulk}$ values for the flash-flux-ad melting scenario using the thermal model temperature

5.5 Discussion

In this section I will compare the maximum and average melt fractions, the melt production rate and the minimum and average X_{H_2O} values, for both the flash-ad case and the flash-flux-ad case. The flash-ad case will always be plotted with circles and the flash-flux-ad case will be plotted with squares. Their values will be compared to results observed form arcs.

5.5.1 Comparison with Petrological Data

5.5.1.1 Melt Fraction

In Figure 5.19 the average melt fraction for each $X^{bulk}_{H_2O}$ is plotted in blue and the maximum melt fraction for each $X^{bulk}_{H_2O}$ is plotted in red for the flash-ad case. A line of best fit is plotted through each set of values with both showing a steady increase in melt fraction as $X^{bulk}_{H_2O}$ increases. Figure 5.20 plots the average melt fractions and maximum melt fraction for the flash-flux-ad case. Whilst best fit lines were plotted through both sets of values, the maximum values do not have a good to fit to the line of best fit. The maximum melt fractions initially decrease with $X^{bulk}_{H_2O}$ before increasing. The average melt fractions increase with $X^{bulk}_{H_2O}$, with the rate increasing rapidly initially before becoming steady. Portnyagin et al. (2007) found a melt fraction of 0.1 corresponded to a $X^{bulk}_{H_2O}$ of $\sim 0.2 - 0.3$ wt% for the Kamchatka arc, in Figure 5.19 a maximum melt fraction of 0.1 occured for a $X^{bulk}_{H_2O}$ of ~ 0.5 wt% so a slightly higher water content. All the melt fractions in Figure 5.20 are above 0.1, but Portnyagin et al. (2007) also estimate melt fractions between 0.2-0.25 for a $X^{bulk}_{H_2O}$ of 0.8 wt%. In Figure 5.20 these melt fractions fall between the maximum values and average values, so this range fits with the values. In Kelley et al. (2010) a melt fraction of 0.1 was found between a $X^{bulk}_{H_2O}$ of 0-0.5 wt% for the Mariana Arc, this corresponds with the best fit line for the maximum melt fraction in Figure 5.19. For a $X^{bulk}_{H_2O}$ of 0.8 wt% in Kelley et al. (2010) the estimated melt fraction range was between $\sim$0.12 and $\sim$0.25. The maximum melt fractions in 5.19 are at

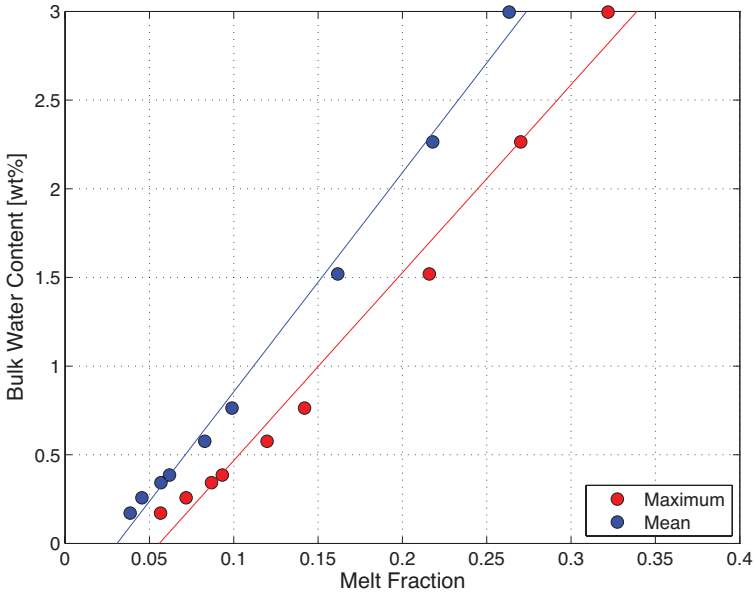

Fig. 5.19 Plot of $X_{H_2O}^{bulk}$ against melt fraction for the flash-ad case. The red points are the maximum melt fraction for each $X_{H_2O}^{bulk}$ and the blue points are the average melt fraction of all the melt events

the low end of this range. The melt fractions values from 5.20 for a $X_{H_2O}^{bulk}$ of 0.8 wt% fall in this range for both sets of values. Comparison of the model melt fractions with Kelley et al. (2010) and Portnyagin et al. (2007) suggest that partial melting is occurring in a similar amount as observed values from subduction zones.

5.5.1.2 Melt temperature and pressure

In the model the decompression melting occurs up to the overriding plate so the pressure at this depth is the pressure of the final melting. The lower edge of the overriding plate in the model is situated at 50 km depth, which corresponds to $\sim$ 1.6 GPa. As the thermal model temperature was used in the decompression melting caluclation, the temperature along the lower edge of the overriding plate is the final melting temperature range. For the region of melting this is between 750 - 800 °C. The temperature range is lower than the estimates from Kelley et al. (2010) and Kohut et al. (2006) of 1200-1400 $\pm \sim$ 40 °C and $\sim$1367 °C

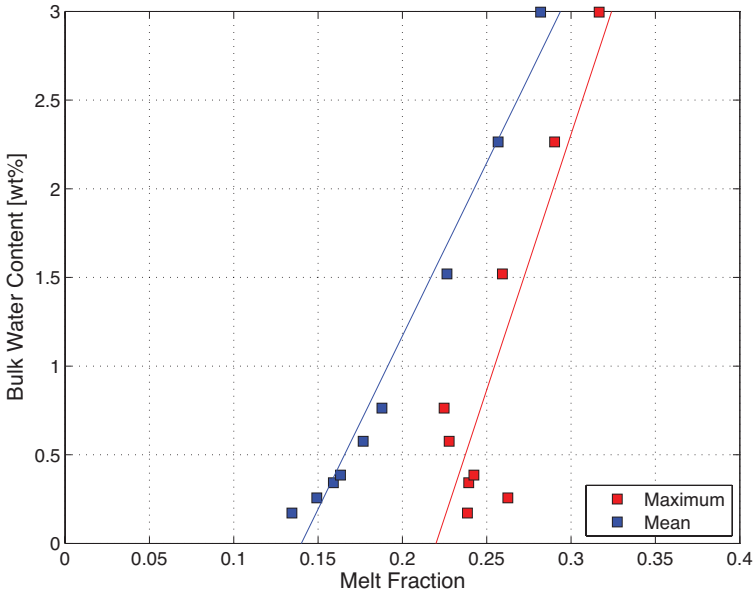

Fig. 5.20 Plot of $X_{H_2O}^{bulk}$ against melt fraction for the flash-flux-ad case. The red points are the maximum melt fraction for each $X_{H_2O}^{bulk}$ and the blue points are the average melt fraction of all the melt events

respectively. However their pressure estimates were between 1.0-2.4 $\pm$ 0.2 GPa from Kelley et al. (2010) and between 1-1.5 GPa for Kohut et al. (2006). The pressure estimate of 1.6 GPa from the melting models fits within the estimate by Kelley et al. (2010) and is just outside the range by Kohut et al. (2006). This shows the melting is now occuring at the depth that observations from arcs suggest but the temperature is still too low.

5.5.1.3 Melt Production Rate

I used the same method as the two previous chapters to calculate the melt production. I took the total volume values from Figures 5.15 and 5.16 and divided by the time in Myr for 1000 fractures to occur, as calculated in the Chapter 3. Figure 5.21 plots the melt production rate for each $X_{H_2O}^{bulk}$ for the flash-ad case. There were three different fracture sizes used; the red points are the 4 km length fractures, the blue points are 6 km length, and the green are the 8 km length values. By plotting the $X_{H_2O}^{bulk}$ on a log scale, best fit lines could be plotted

through the three sets of data. This shows the melt production rate increases exponentially with $X_{H_2O}^{bulk}$ values. For larger fracture lengths the melt production rate increases at a smaller rate with $X_{H_2O}^{bulk}$ compared to lower fracture lengths, this is due to the smaller fracture lengths requiring less time for 1000 fractures to occur. Figure 5.22 plots the melt production rate for each $X_{H_2O}^{bulk}$ for the flash-flux-ad case. The red points are the 4 km length fractures, the blue points are 6 km length, and the green are the 8 km length. The $X_{H_2O}^{bulk}$ values were plotted on a log scale similar to Figure 5.21, however a best fit curve fitted the three sets of data rather than lines of best fit. This shows the melt production rate does not increase linearly with as $X_{H_2O}^{bulk}$ exponentially increases. Wada and Wang (2009) used estimated melt production rate for 17 subduction zone which varied form 24 km^3 Myr^{-1} up to 11000 ± 1000 km^3 Myr^{-1}. Holbrook et al. (1999) and Lizarralde et al. (2002) estimated the melt production rate at the Eastern Aleutian to be $\sim$67 km^3 km^{-1} Myr^{-1}. All the melt production rates from Figure 5.21 and Figure 5.22 are lower than the estimates. As the melt fractions produced by the melting models fit observations this suggest that the time for the melting needs to decrease. Lowering the fracture size would decrease the time for 1000 fractures accordingly.

5.5.1.4 Water Content in the melt X_{H_2O}

Figure 5.23 plots X_{H_2O} against $X_{H_2O}^{bulk}$ for the flash-ad case. The blue points are the average X_{H_2O} for each $X_{H_2O}^{bulk}$ and the red points are the X_{H_2O} for the maximum melt fraction, which is the minimum X_{H_2O} value. By plotting the $X_{H_2O}^{bulk}$ values on a log axis, both sets of values plotted along lines of best fit. This shows the X_{H_2O} values increase linearly with exponential increase of $X_{H_2O}^{bulk}$ values. Figure 5.24 plots X_{H_2O} against $X_{H_2O}^{bulk}$ for the flash-flux-ad case. The blue points are the average X_{H_2O} for each $X_{H_2O}^{bulk}$ and the red points are the X_{H_2O} for the maximum melt fraction, which is the minimum X_{H_2O} value. I found best fit curves plotted along the both set of values better than lines of best fit. For both sets of values, X_{H_2O} increases with $X_{H_2O}^{bulk}$ more rapidly for lower $X_{H_2O}^{bulk}$ values than higher $X_{H_2O}^{bulk}$ values. All the

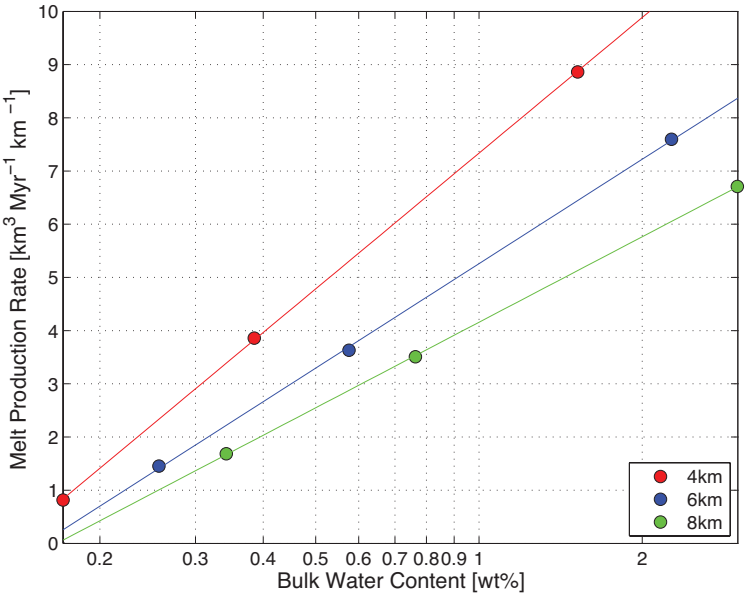

Fig. 5.21 Plot of melt production rate for flash-ad case against $X_{H_2O}^{bulk}$. The red points are the melt production values for a fracture length of 4 km, the blue points are for a fracture length of 6 km and the green points are for a fracture length of 8 km. x axis is plotted on a log scale.

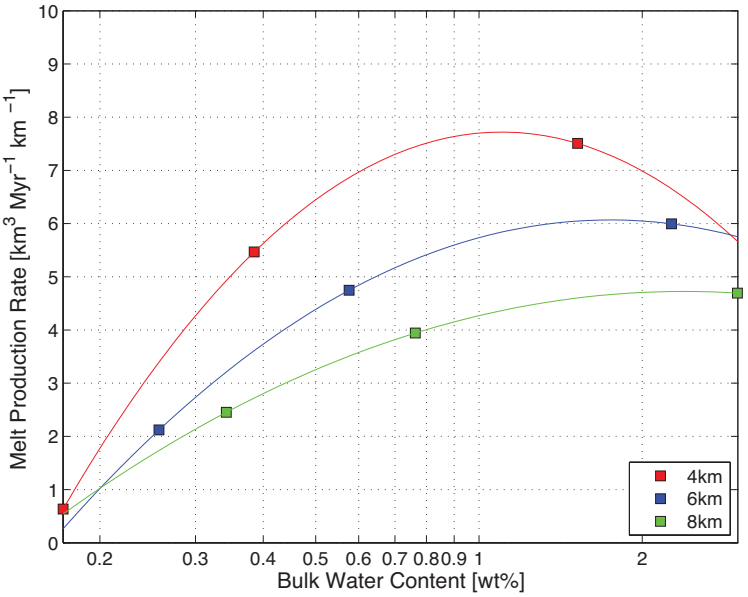

Fig. 5.22 Plot of melt production rate for flux-ad case against $X_{H_2O}^{bulk}$. The red points are the melt production values for a fracture length of 4 km, the blue points are for a fracture length of 6 km and the green points are for a fracture length of 8 km. x axis is plotted on a log scale.

values in Figures 5.23 and 5.24 are below 14 wt% so are lower than the upper X_{H_2O} estimate from Grove et al. (2003) and Krawczynski et al. (2012). Plank et al. (2013) suggested an average X_{H_2O} of $\sim$4 wt% and a range of 1-7 wt%. In Figure 5.23 the lowest $X_{H_2O}^{bulk}$ values have average X_{H_2O} values under 7 wt%, and for the minimum X_{H_2O} values only the two highest $X_{H_2O}^{bulk}$ values had higher X_{H_2O} values. In Figure 5.24 only the two highest $X_{H_2O}^{bulk}$ values have mininum and average X_{H_2O} values higher than 7 wt%. For each melting case I found the percentage of melt events that produced X_{H_2O} values under 14 wt%, and also found the percentage of melt events that produced X_{H_2O} values under 7 wt%. Figure 5.25 plots the percentage of melt events that produced X_{H_2O} values under 14 wt% in red and the percentage of melt events that produced X_{H_2O} values under 7 wt% in blue. The percentage of melt events that produced 14 wt% X_{H_2O} and under was very high for all $X_{H_2O}^{bulk}$, varying between 85-100 %. The $X_{H_2O}^{bulk}$ values under 1 wt% had a success rate of $\sim 60- \sim 90$ %, for producing X_{H_2O} values under 7 wt%. For $X_{H_2O}^{bulk}$ values above 1 wt% the success rate drops to 0-5 %. Figure 5.26 plots the percentage of melt events that produced X_{H_2O} values under 14 wt% in red and the percentage of melt events that produced X_{H_2O} values under 7 wt% in blue. The percentage of melt events that produced 14 wt% X_{H_2O} and under was very high for all $X_{H_2O}^{bulk}$, varying between 95-100 %. The two highest $X_{H_2O}^{bulk}$ values had no X_{H_2O} values under 7 wt%, but all the other $X_{H_2O}^{bulk}$ values had a high success rate that varied between 80-100 %.

5.5.1.5 Focussing of the Partial Melt Region

In the two decompression melting model cases, the partial melt is focussed along the lower edge of the overriding plate as shown in Figures 5.6, 5.7, 5.8 5.10, 5.11 and 5.12. However whilst they are focussed to a certain depth the distance of the partial melt regions is very wide. The long held view of the location of volcanic arcs is that they occur where the depth to the top of the slab is $\sim 120 \pm 40$ km (Gill, 1981; Tatsumi and Eggins, 1995). However newer studies found that between different sections of volcanic arc the depth varies from 80 to 160

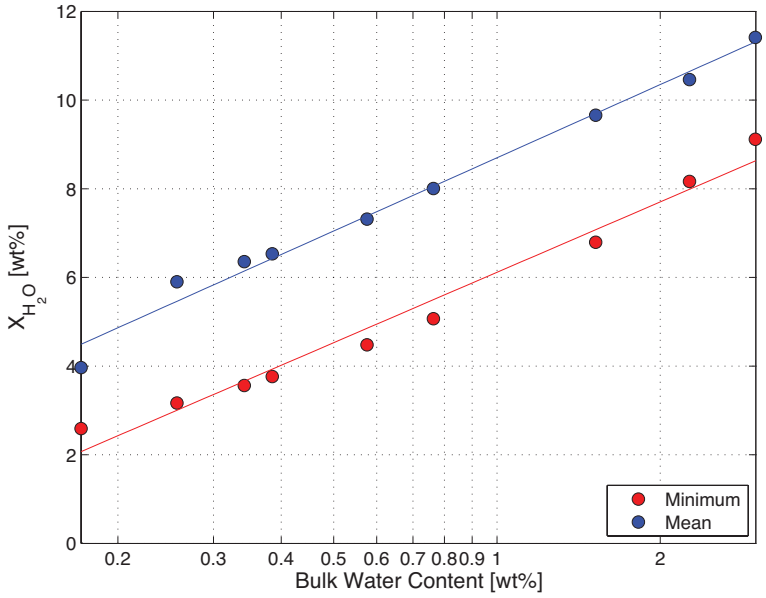

Fig. 5.23 Plot of X_{H_2O} against $X_{H_2O}^{bulk}$ for the flash-ad case. The red points are the X_{H_2O} for the maximum melt fraction for each $X_{H_2O}^{bulk}$ and the blue points are the average X_{H_2O} of all the decompression melting events.

km (England et al., 2004; Syracuse and Abers, 2006) Figure 5.27 shows the distance for the maximum melt fraction for each water content for both melting scenarios. The flash-ad case is shown with the red circles and the flash-flux-ad case is shown with the light blue circles. What is apparent is there is no correlation between bulk water content and maximum melt fraction distance for the flash-ad case. For the flash-flux-ad case there is a decrease in distance with bulk water content but it is not a strong trend. Only a couple of values fall within the 80 - 160 km distance all the rest are higher, with most values varying from $\sim$ 200 km to $\sim$ 400 km distance. What this shows is my location of maximum melt fraction does not correlate with the known location of volcanoes. In this chapter I assumed vertical transport of the melting so this indicates it may not occur. Cagnioncle et al. (2007) suggest the solid flow of the mantle wedge would affect the fluid migration by deflecting it from a vertical trajectory. Taking this idea, the solid flow could also deflect the melt as it rises towards the wedge corner, so the distance of the maximum melt would decrease.

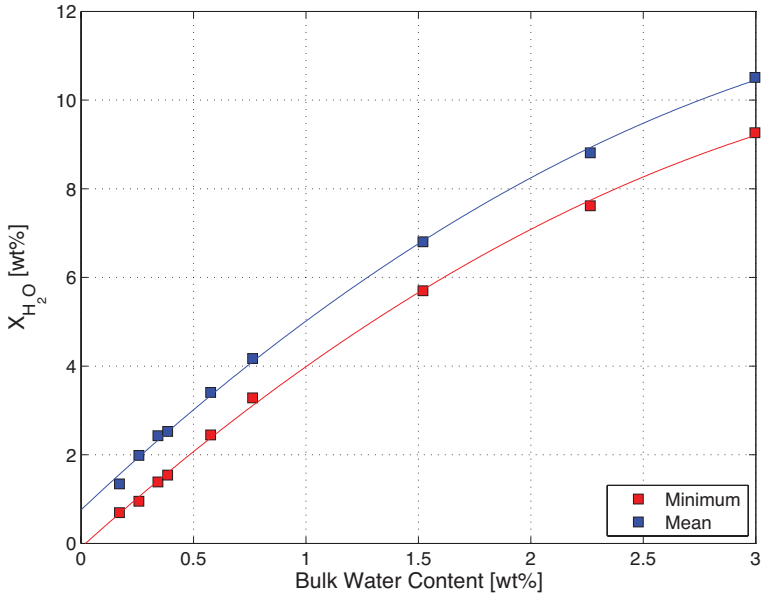

Fig. 5.24 Plot of X_{H_2O} against $X_{H_2O}^{bulk}$ for the flash-flux-ad case. The red points are the X_{H_2O} for the maximum melt fraction for each $X_{H_2O}^{bulk}$ and the blue points are the average X_{H_2O} of all the decompression melting events.

To implement the melt migration being deflected by solid flow, I will need to add buoyancy into my model to allow the melt to rise. I will also need to change the velocity field as it currently fixed, as it will need to take account of the melt rising. To do this I am going to resolve my velocity field using Stokes flow. I will also add in buoyancy to allow the melt to migrate towards the surface. Resolving the velocity field and adding in buoyancy will be covered in the next chapter.

5.5.2 Model Limitations

The main limitation is that by using the thermal model temperature field in the melting calculations the final temperature is much lower than the geothermometer estimates. Decompression melting usually uses an adiabatic temperature gradient, however I showed that if the starting temperature of the adiabaitic gradient is the same as the flash melting temperature, the temperature drops lower than the thermal model temperature. This would cause the melt

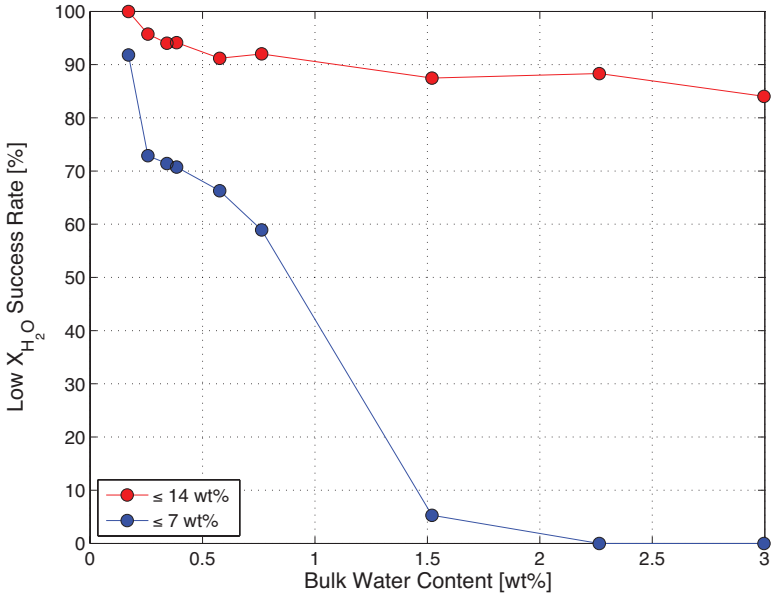

Fig. 5.25 Percentage of decompression melt events that produce $X_{H_2O} \leq 14$ wt% against $X_{H_2O}^{bulk}$ plotted in red and Percentage of decompression melt events that produce $X_{H_2O} \leq 7$ wt% against $X_{H_2O}^{bulk}$ plotted in blue for the flash-ad case

to 'freeze'. In Katz et al. (2003) they used a mantle potential temperature as the starting temperature. If a high enough potetnial temperature was used then the temperature should not fall below the thermal model temperature. However I am unsure as how I would select a suitable temperature and how it would relate to the initial flash melting temperature.

5.5.3 Conclusions

Both the flash-ad and flash-flux-ad melting cases produced melt fractions and X_{H_2O} values that fitted with observations from arcs. This suggests that hydrous decompression melting is a feasible melting mechanism for subduction zones. The melt productivity rates were lower than estimates which suggests that if the fracture sizes were smaller, the time for the 1000 fractures to produce melting would decrease, therefore increasing the melt productivity rate. The decompression melting occured vertically, therefore the partial melt region was over a

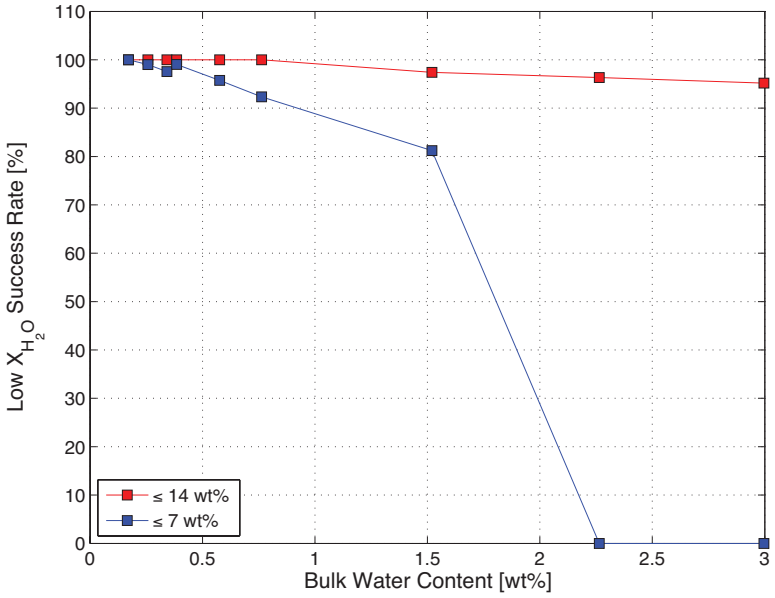

Fig. 5.26 Percentage of decompression melt events that produce $X_{H_2O} \leq 14$ wt% against $X^{bulk}_{H_2O}$ plotted in red and Percentage of decompression melt events that produce $X_{H_2O} \leq 7$ wt% against $X^{bulk}_{H_2O}$ plotted in blue for the flash-flux-ad case

wide distance. To try and focus the partial melt region buoyancy needs to be added to the model to allow the partial melt region migration to be deflected by the solid flow.

5.6 Summary

In this chapter I examined hydrous decompression melting using the method from Katz et al. (2003). I looked at two melting scenarios, flash-ad and flash-flux-ad. The flash-flux-ad case produced higher melt fractions and lower water content in the melt than the flash-ad case. Comparing the results to petrological data the majority of the X_{H_2O} fall within the ranges found in literature. Plotting the distance of the maximum melt fraction showed the values were a lot higher than expected. This led to the conclusion that the transport of the melt may not be vertical, but could be deflected by the solid flow of the mantle wedge. The next

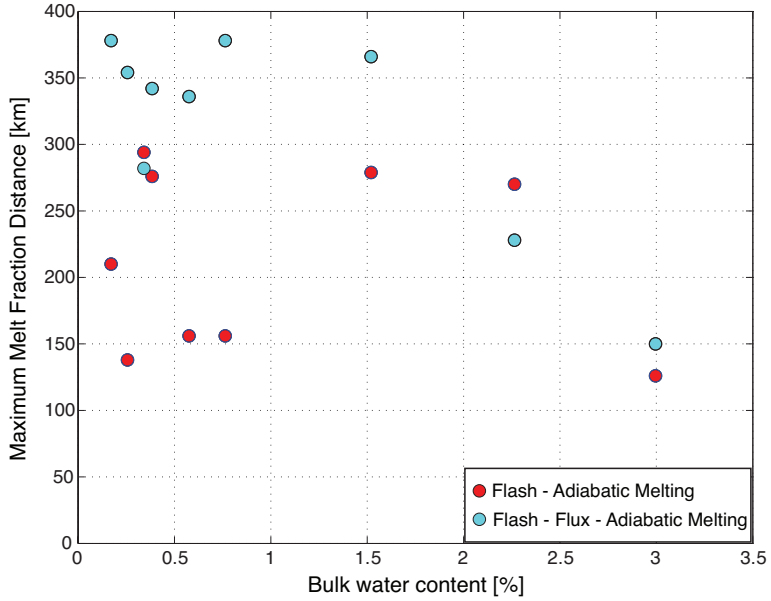

Fig. 5.27 Maximum melt fraction distance against $X_{H_2O}^{bulk}$ for the flash-ad melting scenario and the flash-flux melting scenario. The red circles are the flash-ad values and the light blue circles are the flash-flux-ad values.

chapter is going to examine this idea by introducing buoyancy and solving the velocity field using Stokes flow, to see if the melt migrates towards the wedge corner.

CHAPTER 6

ADDITION OF BUOYANCY

6.1 Introduction

The previous chapter introduced adiabatic decompression melting as a possible melting mechanism in subduction zones. I used the adiabatic decompression melting parameterisation from Katz et al. (2003) which extended the dry adiabatic melting parameterisation from McKenzie (1984) to include hydrous melting. I examined two melting scenarios; flash melting followed by adiabatic decompression melting (flash-ad) and flash melting, then hydrous flux melting followed by adiabatic decompression melting (flash-flux-ad). The flash-flux-ad case produced higher melt fractions and corresponding low water content in the melt values that were within the range from Plank et al. (2013). The flash-ad case had lower melt fractions and therefore higher water contents, but these still matched values from literature such as Grove et al. (2003). For both cases the location of maximum melting was a large distance from the wedge corner outside of the range by Jarrard (1986). In the previous chapter the partially molten region migrated vertically, but the effect of solid flow needs to be taken into account.

In this chapter, buoyancy is added into the model to allow the partially molten region to migrate upwards due to its buoyancy and it can also be affected by the solid flow. The solid

flow should cause the melt trajectory to be upwards but deflected towards the wedge corner. To add in buoyancy the velocity field will be accounted for by Stokes flow that uses density as an input, therefore any density change due to buoyancy will affect the velocity field. With the new velocity field incorporated into the thermal model a new steady state temperature field can be calculated. The next step is to then incorporate melting, initial flash melting followed by adiabatic decompression melting as the partially molten region rises. The melt fraction changes the density causing the partially molten region to be more buoyant and rise.

This chapter has seven main sections. Sections 1 and 2 are calculating the velocity field using Stokes flow and then making a new thermal model. Section 3 discusses the addition of melting and density change due to melting. Section 4 looks at varying the background viscosity, radius of the melt region and their effect on the partially molten region. Then sections 5 and 6 are the results from the two final model runs and a discussion of the results. Finally is a summary of the chapter.

6.2 Velocity field using Stokes Flow

6.2.1 Governing Equations

To solve for the velocity and pressure in the wedge the following need to be solved; the conservation of mass

$$\nabla \cdot \vec{v} = 0 \tag{6.1}$$

and the conservation of momentum for a continuous medium in a gravity field

$$\frac{\partial \sigma_{ij}}{\partial x_j} + \rho g_i = \rho \frac{\mathrm{D}v_i}{\mathrm{D}t} \tag{6.2}$$

where i,j are coordinate indices, σ_{ij} is the total stress, x_j is a spatial coordinate, ρ is the density, g_i is the i-th component of the gravity vector $\vec{g} = (g_x, g_y, g_z)$ and $\frac{\mathrm{D}v_i}{\mathrm{D}t}$ is the time derivative of the i-th component of the velocity vector.

Pressure can be introduced into the momentum equation (6.2) by using equation (6.3) that relates the total stress (σ_{ij}) with the deviatoric stress (σ'_{ij}) as follows:

$$\sigma'_{ij} = \sigma_{ij} + P\delta_{ij} \tag{6.3}$$

This gives the Navier Stokes equation of motion (6.4), which describes the conservation of momentum for a fluid in a gravity field:

$$\frac{\partial \sigma'_{ij}}{\partial x_j} - \frac{\partial P}{\partial x_i} + \rho g_i = \rho \frac{\mathrm{D}v_i}{\mathrm{D}t} \tag{6.4}$$

where P is the dynamic pressure and x_i is a spatial coordinate.

The inertial forces $\rho \frac{\mathrm{D}v_i}{\mathrm{D}t}$ are negligible with respect to viscous resistance and gravitational forces in highly viscous flows. Deformation of highly viscous flows can be described by the Stokes equation for slow flow (6.5):

$$\frac{\partial \sigma'_{ij}}{\sigma x_j} - \frac{\partial P}{\partial x_i} + \rho g_i = 0 \tag{6.5}$$

The background viscosity is going to be constant and the fluid is incompressible so the Stokes equation can be further simplified to (6.6):

$$\eta \frac{\partial^2 v_i}{\partial x_j^2} - \frac{\partial P}{\partial x_i} + \rho g_i = 0 \tag{6.6}$$

where η is the viscosity. The x-stokes equation (6.7) can be written as:

$$\eta \Delta v_x - \frac{\partial P}{\partial x} + \rho g_x = 0 \tag{6.7}$$

and the y-stokes equation (6.8) is:

$$\eta \Delta v_y - \frac{\partial P}{\partial y} + \rho g_y = 0 \tag{6.8}$$

where $\Delta = \frac{\partial^2}{\partial x^2} + \frac{\partial^2}{\partial y^2}$ is the Laplace operator.

To solve these equations numerically I use a Matlab function, Stokes_Continuity_solver_sandbox.m from Chapter 16 in Gerya (2010), that solves the Stokes equations to get a velocity and dynamic pressure field.

6.2.2 Boundary Conditions

In my model the slab has prescribed velocity of 5 cm yr^{-1}, so the region that boundary conditions are to be applied is the wedge. The boundary locations are the bottom of the overriding plate, the edge of the slab, lower edge between 600 and 660 km and the right edge between 50 and 600 km depth. The top boundary condition is a no slip condition such that:

$$v_x = v_y = 0$$

For the lower boundary condition the wedge is prescribed with the analytic solution for cornerflow (Batchelor, 1967).

For the left boundary along the edge of the slab the slab velocity is prescribed below 80 km as the slab velocity. Between the wedge corner at 50 km and 80 km the prescribed velocity is $0.05v_s$ where v_s is the slab velocity. This is the same as the boundary condition from Wilson et al. (2014) and has the effect of partially decoupling the wedge corner from the slab.

For the right boundary I tried two conditions; an open channel boundary condition and a prescribed boundary condition. Both have the ability to allow flow in and out of the grid boundary.

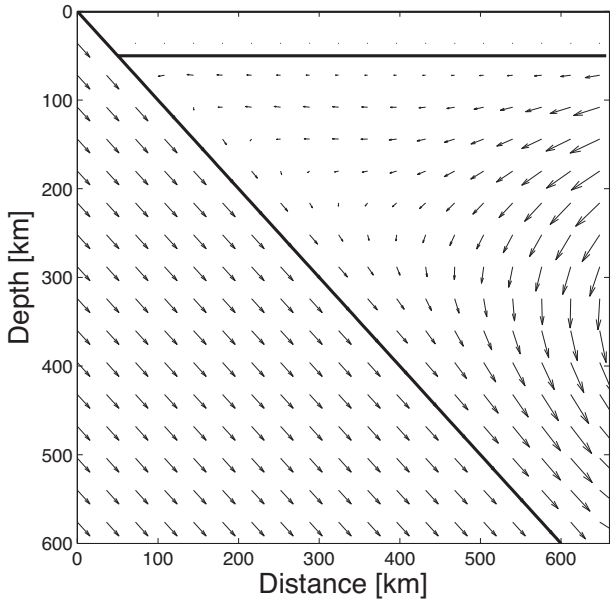

Fig. 6.1 Velocity field for the wedge region solved using a open channel boundary condition on the right hand side and a background viscosity of 10^{23} Pa s.

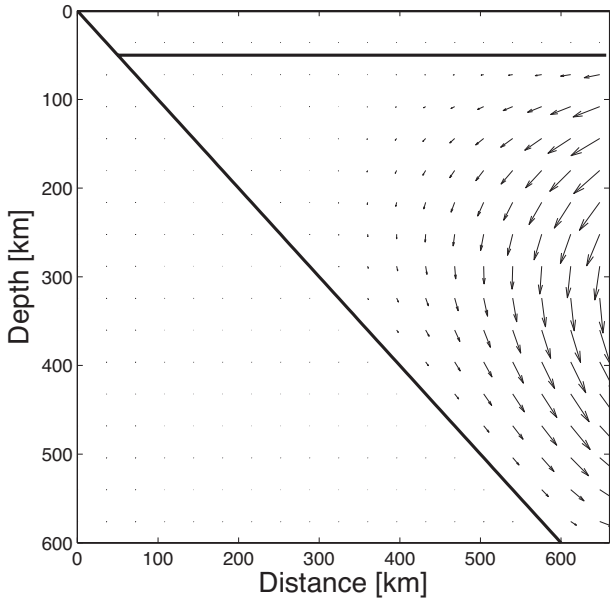

Fig. 6.2 Velocity field for the wedge region solved using a open channel boundary condition on the right hand side and a background viscosity of 10^{21} Pa s.

6.2.2.1 Open Channel Boundary Condition

In the book by Gerya (2010), the flow of a channel in and out of the grid is calculated using an open boundary condition. Having an open boundary on the right implies a horizontal channel and horizontal pressure gradients. To set the open channel boundary condition the nodes on the right hand side of the grid are set to an initial pressure value of 0. $\frac{\partial v_x}{\partial x} = 0, \frac{\partial v_y}{\partial x} = 0$ are also set as conditions on the right boundary. This creates a pressure field that is 0 along the central horizontal axis with negative pressure in the top half and positive pressure in the lower half. This pulls the velocity field into the grid in the top half of the wedge and pushes it out in the lower half.

Figure 6.1 shows the velocity field with the open channel flow boundary condition for the right hand boundary. In the wedge region the velocity field enters in the top half and leaves in the lower region. There is flow into the wedge corner but the flow is stronger towards the right hand boundary. This result was for a background viscosity η of 10^{23} Pa s. This is probably higher than the background viscosity I want, as other studies tend to use lower back ground viscosities of $\sim 10^{21}$ Pa s (Van Keken et al., 2008). Figure 6.2 plots the velocity field using the same boundary conditions as Figure 6.1, but with a background viscosity of 10^{21} Pa s. The channel flow at the right hand side has now become dominant and is much larger than the slab velocity such that the velocity arrows for the slab are not visible.

6.2.2.2 Prescribed boundary condition

Another way to allow the velocity field to flow in and out of the right hand boundary is to prescribe the velocity at the boundary. The velocity that is prescribed is taken from the cornerflow solution (Batchelor, 1967), which was solved for in Chapter 2. To calculate the pressure, one pressure node is initially defined, which then allows the other nodes to be calculated. In Gerya (2010) the standard is to set the top left node as 0, however as the top left node is not located within the wedge region it is better to choose a node located within the wedge. I use the same pressure condition as Van Keken et al. (2008), which is

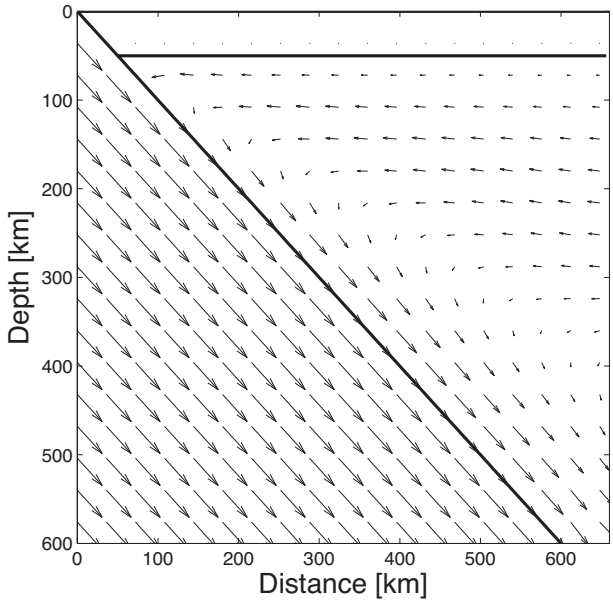

Fig. 6.3 Velocity field for the wedge region solved using a prescribed boundary condition on the right hand side and a background viscosity of 10^{21} Pa s.

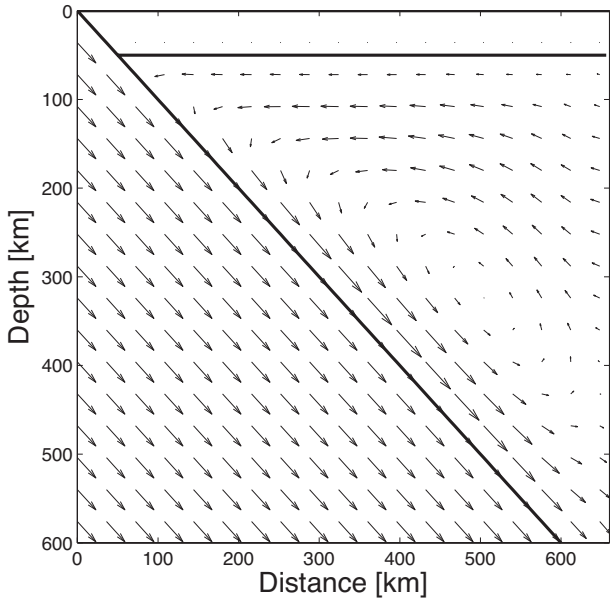

Fig. 6.4 Velocity field for the wedge region solved using a prescribed boundary condition on the right hand side and a background viscosity of 10^{20} Pa s.

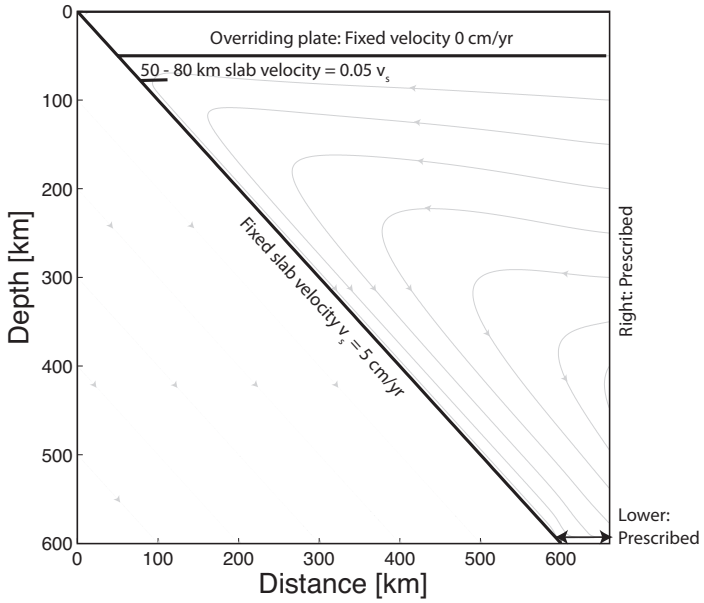

Fig. 6.5 Chosen velocity boundary conditions for the new thermal model. The right and lower boundaries are prescribed with the cornerflow velocities from the velocity field from Chapter 2.

setting the lower right grid node to 0. Figure 6.3 shows the velocity field with the right hand boundary prescribed with the cornerflow solution and a background viscosity of 10^{21} Pa s. The velocity field looks very similar to the analytic cornerflow solution from Chapter 2. A lower background viscosity of 10^{20} Pa s was tried as shown in Figure 6.4, but whilst there is still a corner flow a convection cell is created which would not be suitable.

The right hand boundary condition I have chosen to use is the prescribed boundary condition as it produces a close match to the cornerflow velocity field and it works for viscosities as low as 10^{21} Pa s. The final velocity boundary conditions are shown in Figure 6.5. These boundary conditions are the same as those described in case 1b in Van Keken et al. (2008), apart from the slab condition for which I used the condition from Wilson et al. (2014).

6.3 New Thermal Model

Now that the velocity is calculated using Stokes Flow it can be incorporated into the existing thermal model. First though the density change due to thermal expansion needs to be taken into account.

6.3.1 Density change due to temperature

As the Stokes equations depend on density, changes in density due to temperature need to be calculated as this will affect the buoyancy. The density ρ will change due to temperature T according to the equation:

$$\rho = \rho_0(1 - \alpha(T - T_0)) \tag{6.9}$$

where ρ_0 is the reference density 3300 kg m^{-3}, α is the thermal expansion coefficient chosen to be $3e^{-5}$ as used by Gerya and Yuen (2003). T_0 is the reference temperature which is $T_0 = T_s = 273$ K as used in Gerya (2010).

6.3.2 Thermal Model Structure

With the density now calculated taking into account temperature change, the new thermal model can now incorporate the Stokes solver to calculate the velocity field used for the advection of temperature. The chart in Figure 6.6 shows the new order of processes within the model when calculating the temperature field. The main difference from the thermal model in Chapter 2 is in Figure 6.6 the velocity field is now calculated at each time step using the Stokes solver, and the marker densities are calculated using equation (6.9) before being interpolated to the nodes.

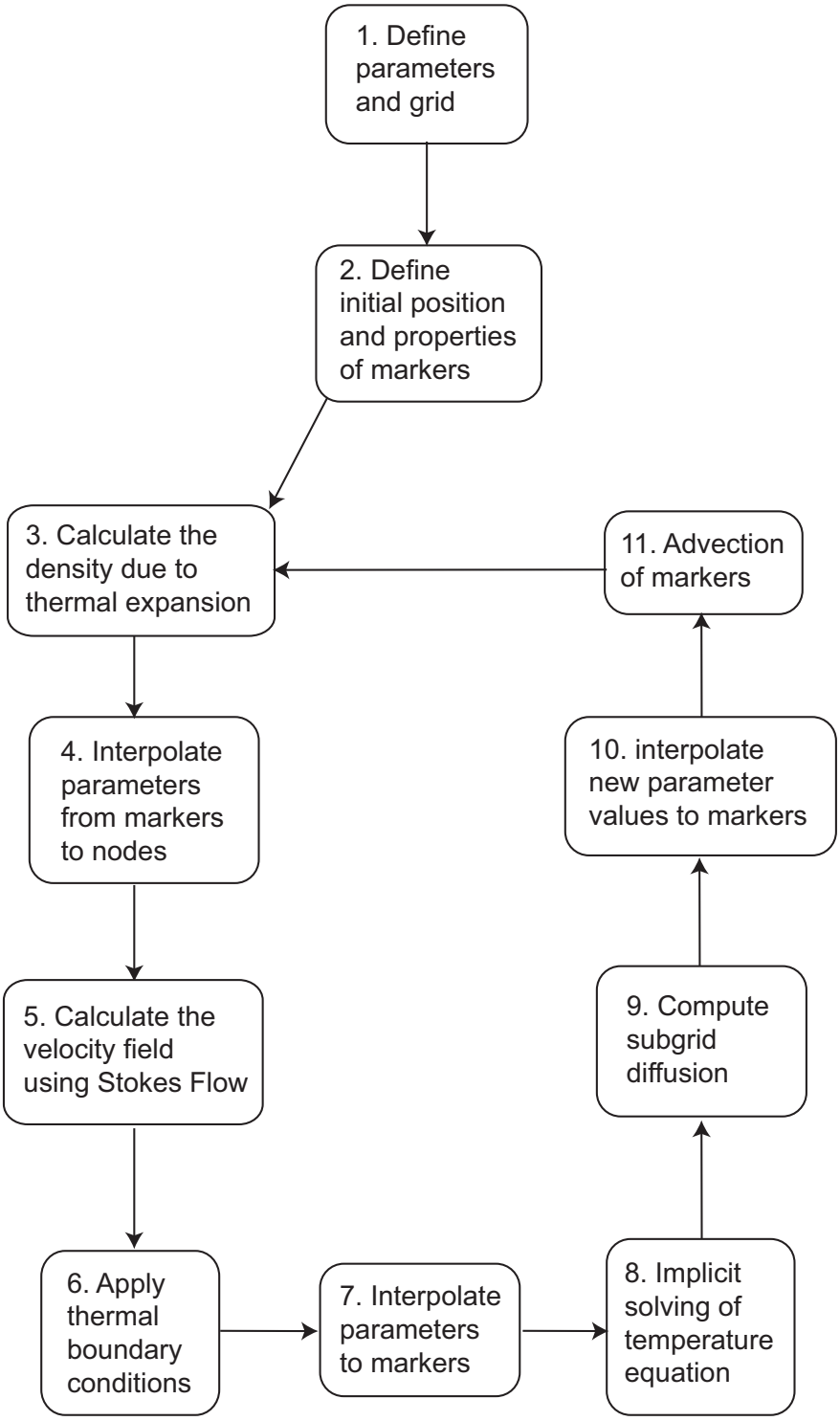

Fig. 6.6 Flowchart of the code structure with addition of calculating the density and calculating the velocity field.

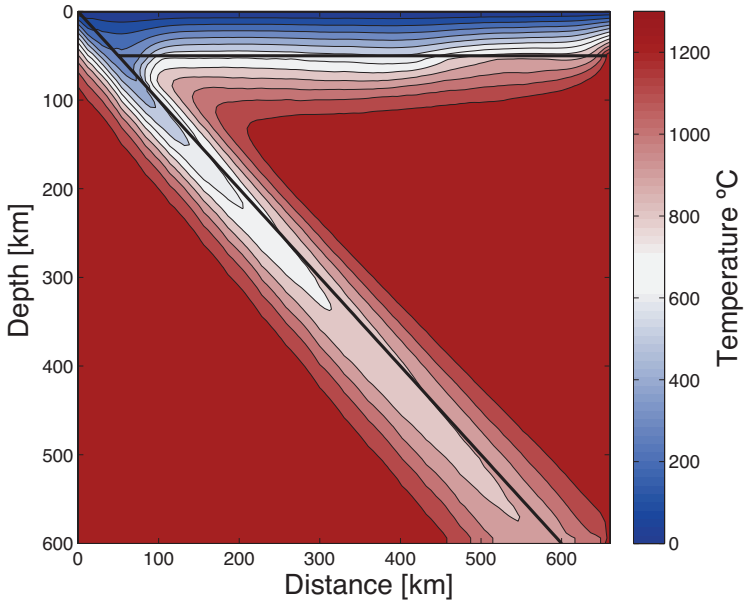

Fig. 6.7 Temperature field of the thermal model with the velocity field solved using Stokes flow. The contours represent 100 ° C. The temperature has cooled downwards from the overriding plate and down along the slab.

6.3.3 New Temperature Field

Using the model structure from Figure 6.6 the thermal model was run, from an starting background temperature T_b of 1573 K, over time until the temperature difference between timesteps was very low, at which point I assumed it had reached steady state. The final temperature field is shown in Figure 6.7. The temperature field in the wedge decreases in temperature towards the overriding plate and also decreases in temperature towards the slab boundary. The overriding plate cools in temperature from T_b over time due to the adiabatic temperature gradient on the right hand boundary on the overrriding plate, which was discussed in Chapter 2. The slab also pulls down colder temperature over time causing cooling in the region close to the slab.

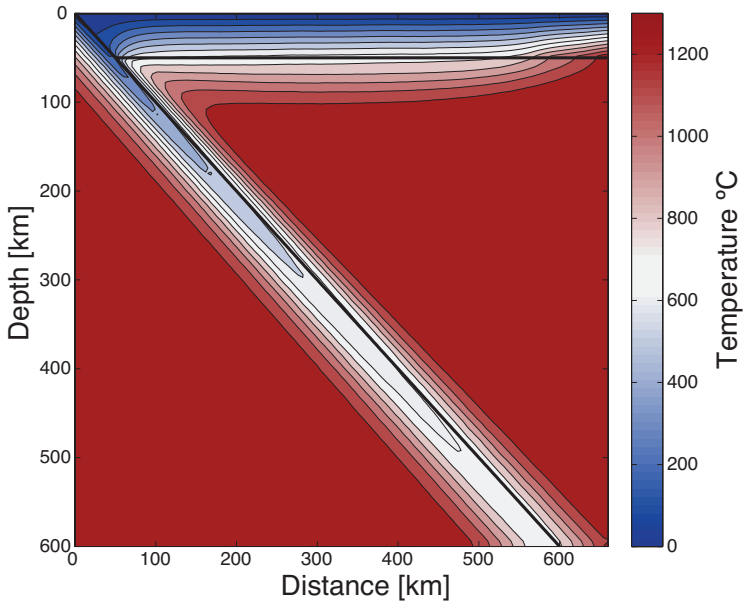

Fig. 6.8 Temperature field of the thermal model from Chapter 2 solved using a analytic cornerflow velocity field.

6.3.3.1 Comparison to Cornerflow Temperature Field

Figure 6.8 is the temperature field calculated using the cornerflow velocity field from Chapter 2. Comparing the new temperature field Figure 6.7 to Figure 6.8 we can see the wedge region is cooler in Figure 6.7 compared to Figure 6.8. The overriding plate has cooled more towards the wedge corner in Figure 6.7, but the temperature along the slab has not cooled as much as Figure 6.8. One reason for the temperature field in Figure 6.7 to be cooler than Figure 6.8 is the grid resolution used in both models. In the thermal model from Chapter 2, a 3 km grid resolution was used. However for the new thermal model the velocity field is numerically solved for by Stokes flow at each time step. This causes the time taken for each time step to run to significantly increase. Due to this I found it was computationally expensive to use a 3km grid resolution in the new thermal model. Instead a 6km grid resolution was used with the consequence of a cooler wedge region. The fact that the temperature may be lower is something to consider, as this could impact the amount of melting.

6.4 Addition of Melting

Now that I have made a new thermal model of a subduction zone with the velocity being solved by Stokes flow, I can add melting and buoyancy into the model.

6.4.1 Density Change due to Melting

In order for the partially molten region to rise, it needs to be more buoyant than the surrounding mantle. Partial melt will have a lower density than mantle rocks and therefore will be more buoyant. To find the density of the partial melt region, I used an equation from Gerya (2010) that calculates the density of the melt ρ_{melt} using the melt fraction values that are calulated:

$$\rho_{melt} = \rho \left(1 - F + F \left(\frac{\rho_f}{\rho_s}\right)\right) \tag{6.10}$$

where ρ is the density calculated due to temperature change from equation (6.9), ρ_f is the density of a complete melt (2800 kg m^{-3})and ρ_s is the reference density of the mantle (3300 km m^{-3}). For the region of interest in the mantle wedge the density initially calculated from equation (6.9) is $\sim$ 3175 kg m^{-3}. If we take a reference melt fraction of 0.1 we can calculate what the ρ_{melt} will be:

$$\rho_{melt} = 3175 \left(1 - 0.1 + 0.1 \left(\frac{2800}{3300}\right)\right)$$

$$\rho_{melt} = 3127$$

This gives a density change $\Delta\rho$ of 48 kg m^{-3}. This is quite a small change. In addition to a reduction in density due to the presence of melt, melting can also reduce the density by changing the density of the remaining solid residue. Note equation (6.10) can be reaaranged

as:

$$\rho_{melt} = \rho(1 - F\rho_{meltfac})$$

where $\rho_{meltfac}$ is the density melt reduction factor ($\frac{\rho_s - \rho_f}{\rho_s}$).

The equation including this affect and the effect of the residue is:

$$\rho_{melt} = \rho(1 - F\rho_{meltfac} - F\rho_{resfac}) \tag{6.11}$$

where ρ_{resfac} is the density reduction factor due to the effect of melting on the solid density. From the experimental work of Schutt and Lesher (2006) and Jordan (1978) estimates of the ρ_{resfac} lie between 0.05 and 0.1. I will use the Schutt and Lesher (2006) ρ_{resfac} of 0.05 in my calculations. Using this value and the previous constants for a melt of 0.1, the ρ_{melt} is now 3111 kg m^{-3}, which is a difference of 64 kg m^{-3}. Equation (6.11) calculates the density of the melt, which then is used in the Stokes solver to calculate the velocity field with the melt buoyancy included. The next step is to add in melting.

6.4.2 Melting Process

The melting scenario I am going to examine in this chapter is similar to the flash-ad case from the previous chapter. In this melting scenario flash melting will occur, followed by adiabatic decompression melting. However in this case the partially molten region due to adiabatic decompression melting does not migrate vertically, but moves upwards due to the effect of buoyancy. The velocity field in the mantle wedge should deflect the upward trajectory towards the wedge corner as shown in Figure 6.9.

The flash melting is calculated in the same way as previous chapters; the fracture end point is found, all the markers within a certain radius of the end point are given a bulk water content, and finally the flash melt value is calculated for each marker. Instead of then finding the nearest grid node for the adiabatic decompression melting, as with the previous chapter,

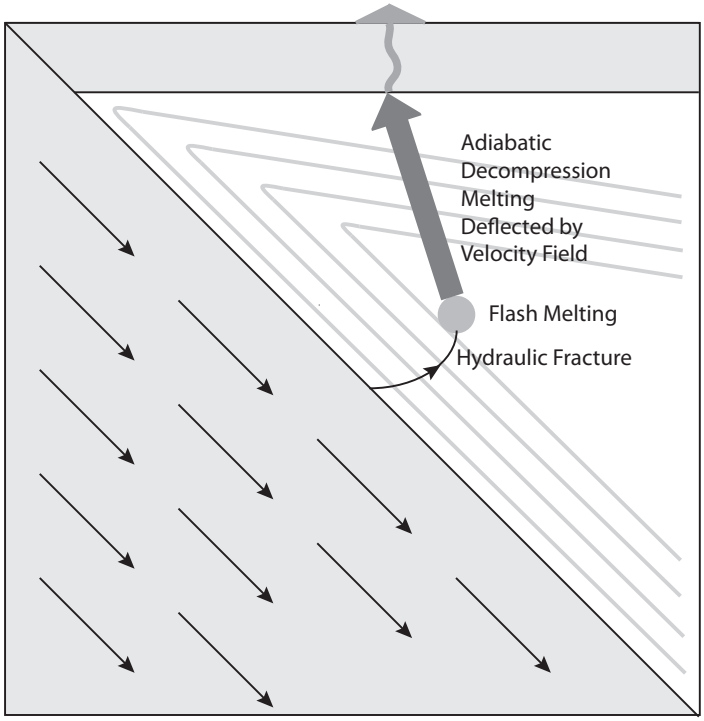

Fig. 6.9 Melting scenario used in this chapter. Water is added to the wedge via an hydraulic fracture which causes flash melting. The partially molten region rises due to buoyancy and undergoes adiabaitc decompressin melting. The partially molten region trajectory is deflected towards the wedge corner by the solid flow.

the melting is going to be calculated at the marker locations. The equation used are the ones from the previous chapter and I am using the thermal model temperature field. In the previous chapter the change in pressure was the step change h and was defined. In this chapter once the markers have been displaced by the velocity field, the change between the old and new marker depth positions are found. This change in depth is then used to find the corresponding change in pressure;

$$\Delta P = \rho_s g \Delta y \tag{6.12}$$

where ΔP is the change in pressure in Pa, ρ_s is the reference density of the mantle, g is the gravitational constant and Δy is the change in marker depth in m. The ΔP is then used as h in the adiabatic decompression melting equations to calculate the melt fraction at the new marker position.

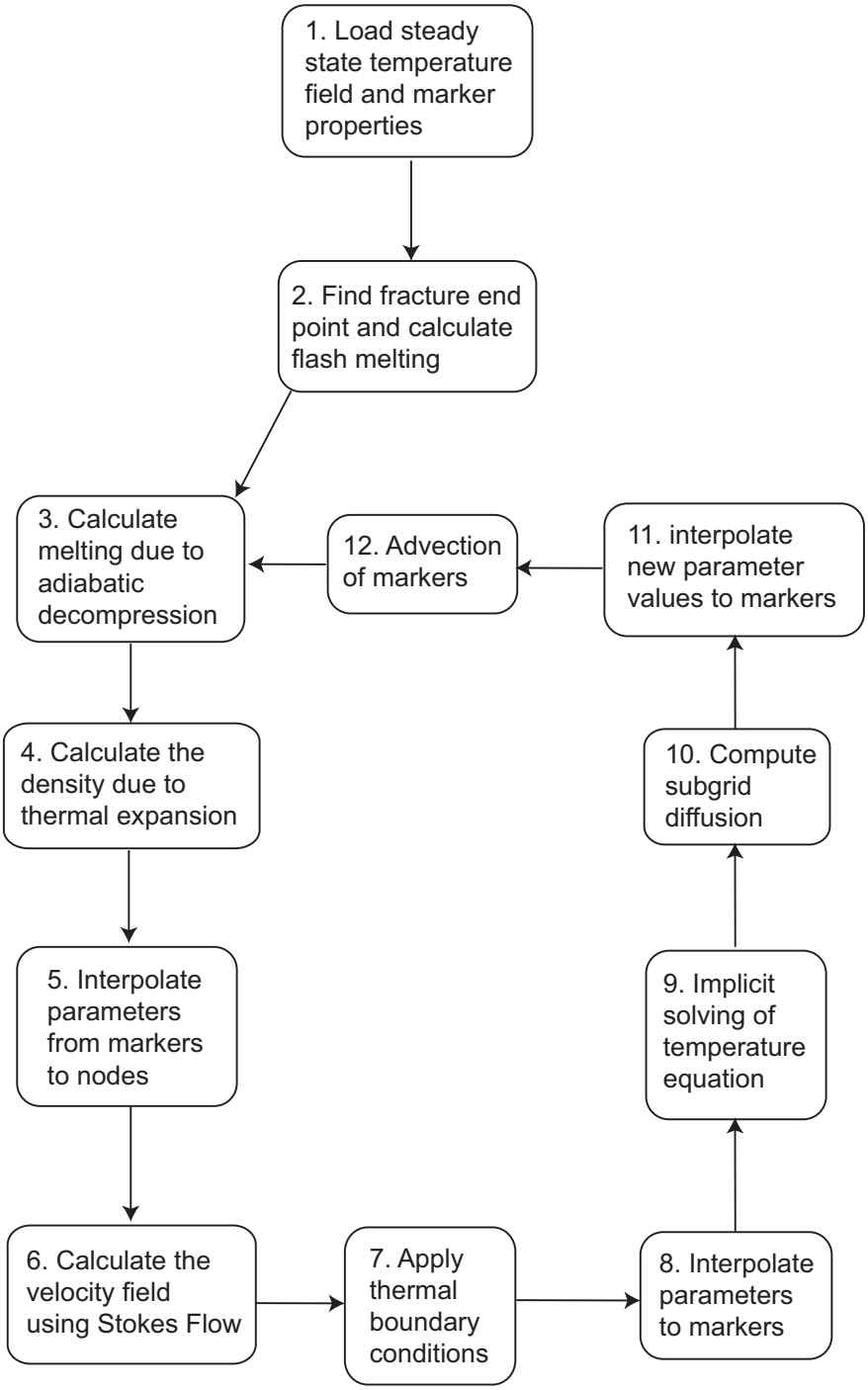

Fig. 6.10 Flowchart of the code structure with addition of calculating the flash melting and adiabatic decompression melting.

6.4.3 Melting Model Structure

The melting sections are added into the existing thermal model in two separate sections; the flash melting calculation and then the adiabatic decompression melting. The first time

step loads in the steady state temperature field from the thermal model described in Section 3. This gives a starting temperature field and an initial velocity that has no buoyancy from melting. The second time step is when flash melting occurs. A fracture end point is chosen and a bulk water content is given to the markers within a certain radius of the end point. The flash melting is then calculated using the water content and the steady state temperature field. Once flash melting has been calculated the density of the melt is found using equation (6.11), which is then used as an input into the Stokes solver to calculate the new velocity field. The temperature is then calculated but as it is steady state the temperature changes are very small. Once the new velocity field is calculated the markers are advected, with the background markers moving with the solid flow and the melt markers should begin to rise due to buoyancy. The following time steps adiabatic decompression melting is calculated instead of flash melting. The code structure after the melting remains the same from the second time step; calculating the melt density, solve for the new velocity field, solve the temperature equation, advection. This structure is shown as a flow chart in Figure 6.10.

6.4.4 First Run of Melting Model

For my first run I chose to select a fracture end point of (300,200) km and a bulk water content of 0.763 wt % to be added to a radius of 1 km around the end point. Figure 6.11 shows four snapshots as the melting progressed. The top left is the initial flash melting event. The four figures are zoomed in as the melt region is small. The next three are taken at 1.2 Myr, 2.4 Myr and 3.6 Myr. What is apparent is the partially molten region is not rising, it seems to be moving downwards, which suggests the buoyancy of the partially molten region is not as strong as the solid flow velocity field. Figures 6.12 and 6.13 are plots of maximum melt fraction against time and average depth of the melt markers with time. In Figure 6.12 the maximum melt fraction decreases over time and in Figure 6.13 the depth of the melt markers increases over times. These figures confirm that the melt is not rising, it is sinking with the

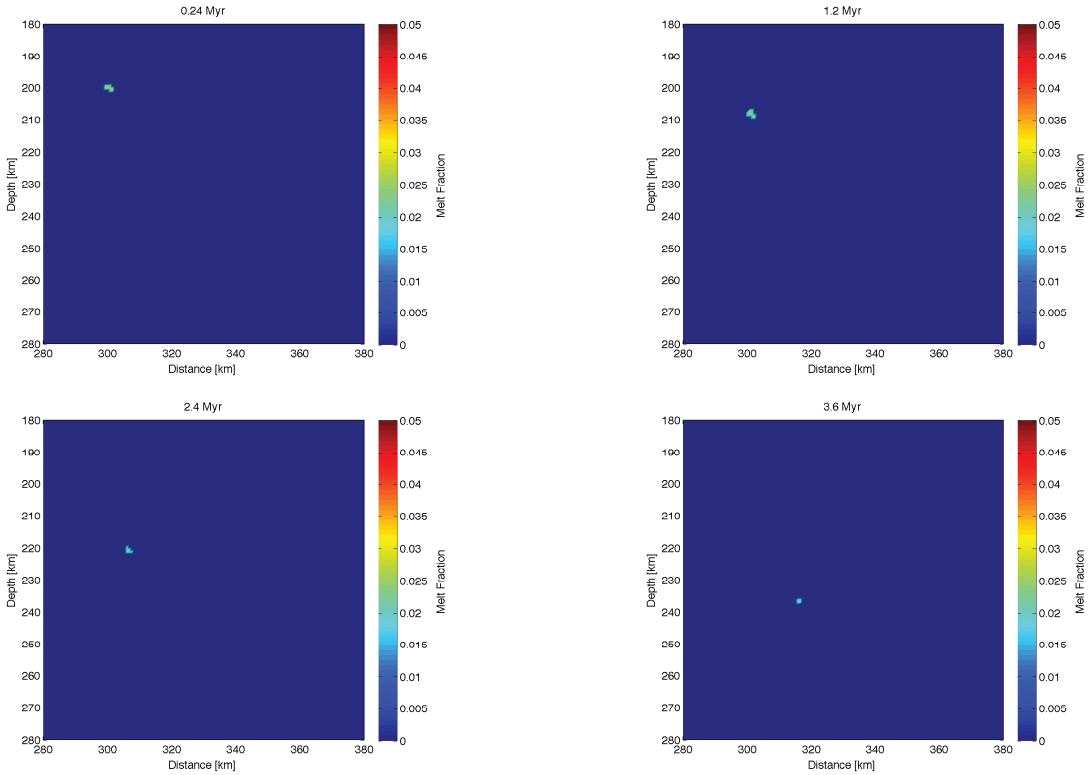

Fig. 6.11 Snapshots of the partially molten region over time. The top left is the initial flash melting event. As the time progresses the partially molten region moves downwards.

adiabatic decompression melting causing the melt fraction to decrease, as the pressure step change is positive instead of negative.

Two possible factors affecting the ability of the partially molten region to rise are; the viscosity of the background material and the melt radius. In the next section I will explore these parameters to see if varying one or more of them could cause the partially molten to rise.

6.5 Varying Viscosity and Radius

The previous section showed that for the radii of the partially molten region I used in previous chapters (1.5, 1 and 0.5 km), the partially molten region did not rise, but was carried by the

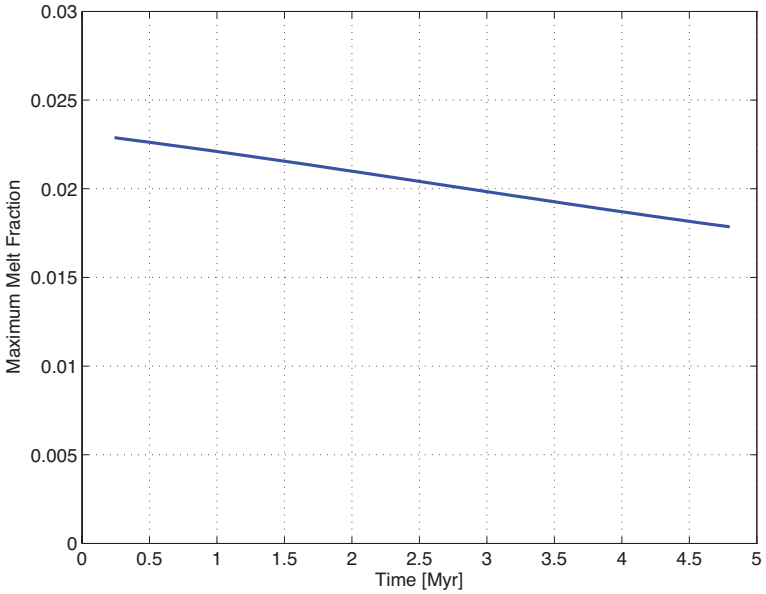

Fig. 6.12 Maximum melt fraction of the partially molten region for each timestep. The melt fraction decreases over time.

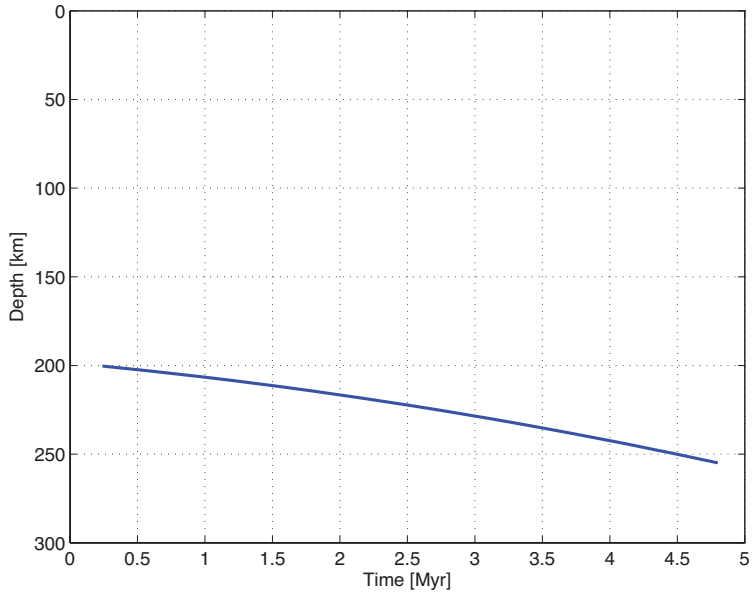

Fig. 6.13 Average depth of the partially region for each timestep. The depth of the partially molten region decreases over time.

velocity field downwards. I therefore need to investigate radii sizes for different viscosities to see what minimum radius is required for the partially molten region to rise. The aim is to see if there is a relationship between minimum radius required for the partially molten region to rise and viscosity.

6.5.1 Method

To examine these relationships I chose two initial fracture end point locations in the mantle wedge shown in Figure 6.14. The first location (A) is located at coordinates (300,200) km, which is at a turning point in the velocity field. The second point (B) is at coordinates (300,160) km, where the flow field is mainly horizontal with very little V_y component. The V_y component is stronger at A than B. It should therefore be harder for the V_y component to change sign at A compared to B, so I expect the results to be different for each location. In both locations the initial V_y is positive (note positive V_y is downwards). I found the nearest grid node for each location and recorded the initial velocity at that grid node. I then added a constant melt fraction of 0.1 to different size radii around that point. From the melt fraction the new density is calculated, which is then used in the Stokes flow equations to calculate the new velocity field. Once the new velocity field had been calculated I compared the V_y velocity component at the grid node to the initial velocity. If the V_y component changed sign from positive to negative then the partially molten region is starting to rise. For six different viscosities; ($5 \times 10^{20}, 10^{21}, 5 \times 10^{21}, 10^{22}, 5 \times 10^{22}$ and 10^{23} Pa s), I varied the radius to find the approximate minimum radius at which the partially molten region would rise. For all cases the melt viscosity was 10^{19} Pa s, as I found that if the viscosity contrast between the background and melt regions was greater then numerical errors occured when using the Stokes solver .

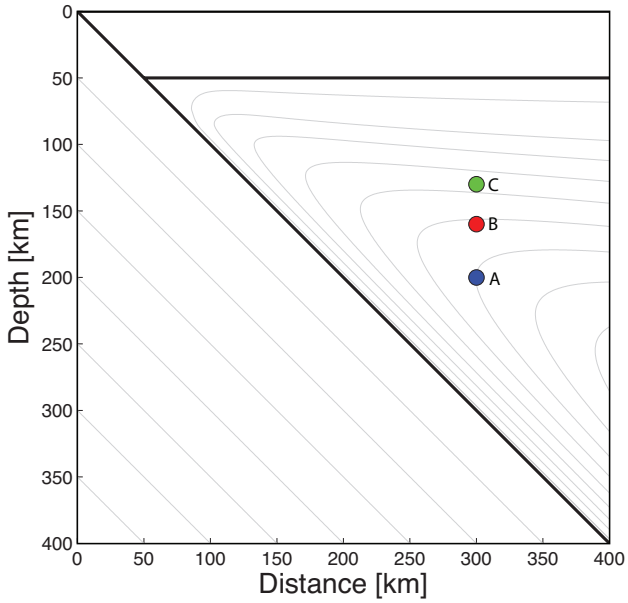

Fig. 6.14 Location of the three initial partial melt locations. Location A at (300,200) km plotted as the blue circle, Location B at (300,160) km plotted as the red circle and Location C (300,130) km plotted as the green circle. The grey lines are streamlines of the velcocity field.

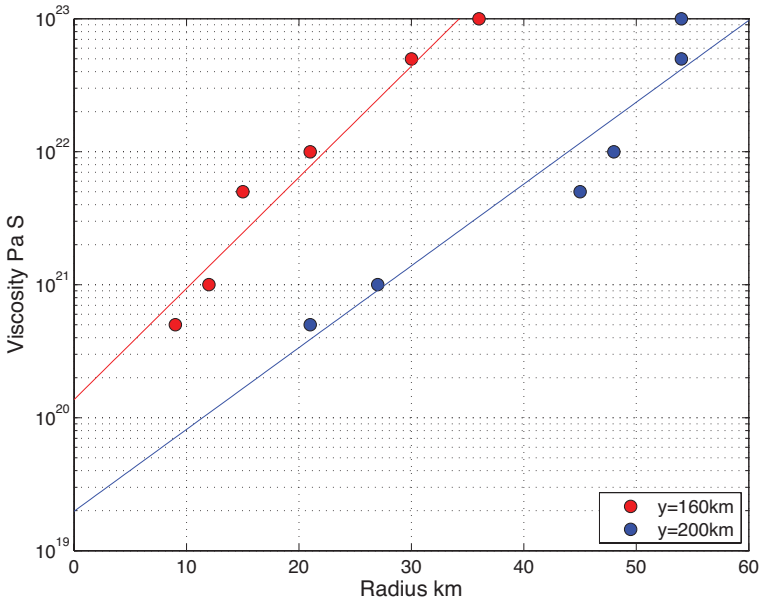

Fig. 6.15 Plot of minimum partial melt radius required for partially molten region to rise against viscosity. Location A is plotted with blue circles and blue best fit line and B is plotted with red circles and a red best fit line. The y axis is a plotted on a log scale.

6.5.2 Varying Viscosity

Figure 6.15 plots the minimum radius against viscosity for the two locations. A is plotted in blue and B is plotted in red. For both sets of data I have plotted a line of best fit through the points. Both sets of data approximately plot a straight line with viscosity plotted on a log scale. The gradient for A is not as steep as the line for B, with A requiring larger minimum radii than B at each viscosity. From the best fit lines a radius of 1 km would need a background viscosity of $\sim 2.3 \times 10^{19}$ Pa s at Location A and $\sim 1.7 \times 10^{20}$ Pa s at Location B to rise. As shown in Section 2 a background viscosity of 10^{20} Pa s does not create a realistic flow field, as a large convection cell occurs. Another point to consider is the line of best fit may not be linear as currently the two lines of best fit cross the y axis, whereas the best fit line should start at (0,0). In this case the best fit line would rapidly increase up to the first data values I have plotted. This implies that the viscosity required for a radius of 1 km to rise could be even smaller than $\sim 2.3 \times 10^{19}$ Pa s.

6.5.3 Rise Velocity

Another thing to consider is the velocity at which the partially molten region will rise. To calculate this rise velocity, I found the mean depth of the partially molten region my_2 at the second time step t_2 when the initial melt fraction of 0.1 is added. I then ran the model for 20 time steps and recorded the mean depth my_{20} at that time t_{20}. Then to find the velocity I used equation (6.13):

$$V_{rise} = \frac{my_{20} - my_2}{t_{20} - t_2} \tag{6.13}$$

where my_{20} and my_2 are in cm and t_{20} and t_2 were in years to give the rise velocity units of cm yr^{-1}. As the depth of the melt region will decrease if the partial melt rises, a negative rise velocity signifies the partially molten region is rising. I started with calculating the rise velocity values used in Figure 6.15 for Location A. However most of the rise velocities

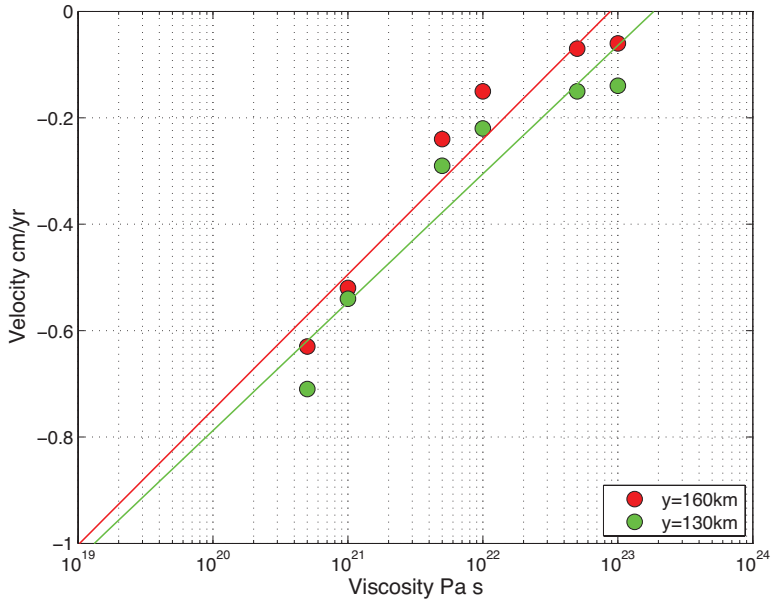

Fig. 6.16 Plot of viscosity against the rise velocity for a depth of 160 km with red circle and a red best fit line and 130 km with green circles and a green best fit lines. x axis is plotted on a log scale.

calculated at 20 time steps were positive indicating the melt region sinks, even though the initial v_y component was negative. I therefore used the minimum radii and viscosity values from Location A at Location B. As Location B has smaller minimum radii, by using the larger radii from Location A the partially molten region should rise. I also used the minimum radii and viscosity values from Location A in a new Location, C which is at (300,130) km.

Figure 6.16 plots the rise velocity calculated from each viscosity. The red circles are the values from Location B and the green circles are the values from Location C. The line of best fit for Location B is plotted in red and plotted in green for Location C. The x axis is plotted on a log scale. Both best fit lines have a similar gradient and position. This shows that between these two locations the rise velocity does not vary much. From previously examining varying the viscosity, a viscosity of $\sim 2 \times 10^{19}$ Pa s would be needed for a 1 km radius partially molten region to rise. From Figure 6.16 we can estimate that the rise velocity

for the 1 km radius region of partial melt at $\sim 2 \times 10^{19}$ Pa s would be ~ -0.9 cm yr^{-1} for an initial melt of 0.1.

6.5.4 Conclusions

From these results it is apparent that a lower background viscosity is required for a partially molten region of radius of 1 km to rise. A viscosity of $\sim 1.7 \times 10^{20}$ Pa s or lower would be needed, however the velocity field for a background viscosity of 10^{20} Pa s is not stable and creates a convection cell. As I have shown that there seems to be a linear relationship between minimum radius and viscosity depending on location, I will use the minimum radius of my chosen background viscosity (10^{21}Pa s). This minimum radius is 27 km. The rise velocity for a viscosity of 10^{21} Pa s for locations B and C was~ -0.55 cm yr^{-1}. This is lower than the estimated rise velocity for a melt radius of 1 km and a viscosity of $\sim 2 \times 10^{19}$ Pa s. This means it is likely that the partially molten region with a radius of 27 km with a background viscosity of 10^{21} Pa s will rise slower than the partially molten region of 1 km at $\sim 2 \times 10^{19}$ Pa s background viscosity.

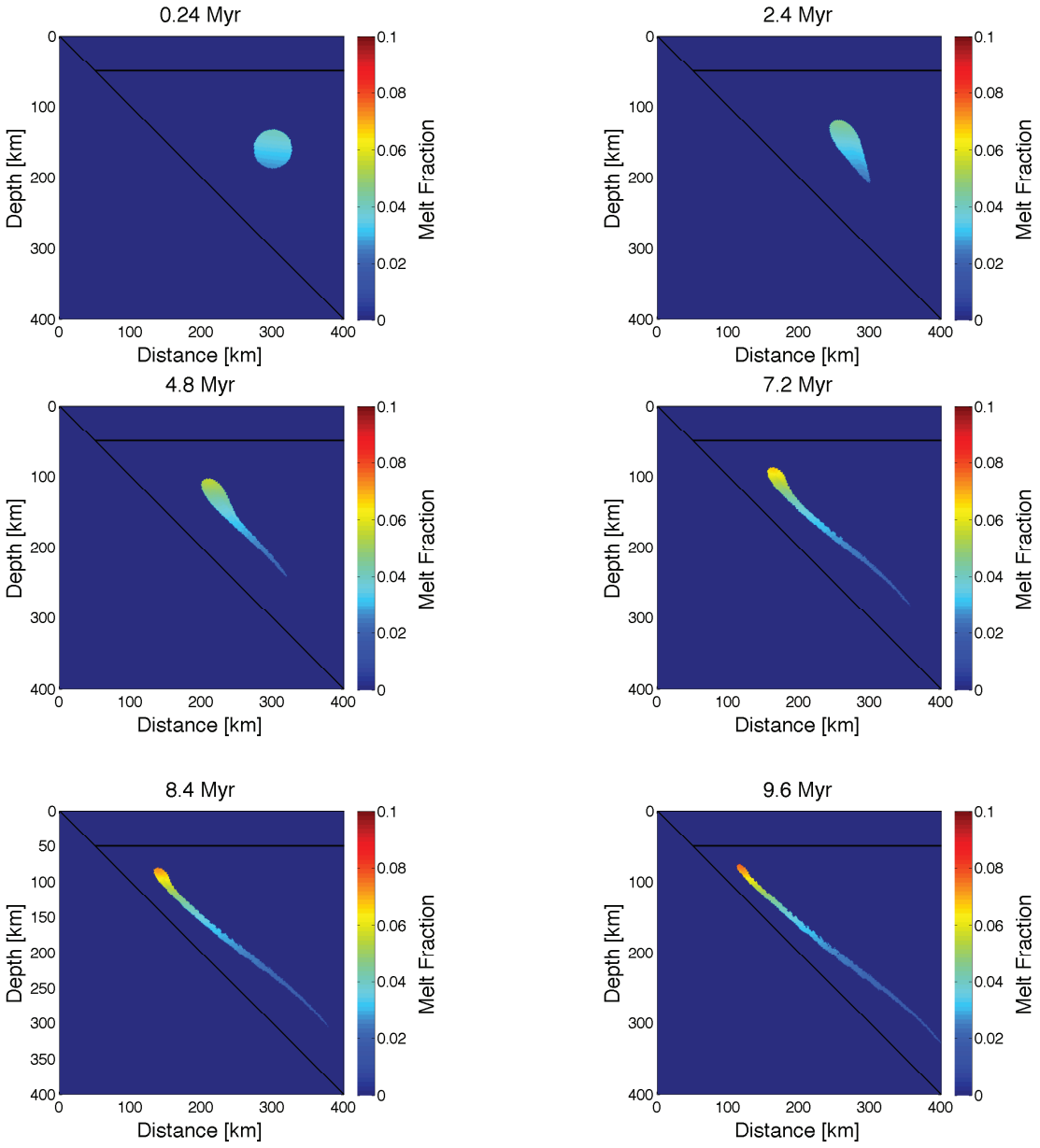

Fig. 6.17 Melt distribution over time for melting with a bulk water content of 0.763 wt%. The fracture endpoint is located at (300,160) km where the water content is added to a 27 km surrounding radius. The top left image is the initial flash melting then the following 5 images are how the partially molten region moves over time throught the wedge region. A large tail is formed with the lower part being dragged sdown by the solid flow.

6.6 Results

Figure 6.17 shows the partially molten region rising over time at six different time steps. The bulk water content was 0.763 wt% and the end point was located at coordinates (300,160) km. The bulk water content was added to a radius of 27 km around the end point. The top left image is the initial flash melt and subsequent images show the increase in melt fraction as adiabatic decompression melting takes place, as the partially molten region rises. The majority of the partial melt rises and increases in melt fraction, however a large tail to the plume is formed which gets dragged down by the solid flow. To try and reduce the size of the tail I am going to shift the fracture end point upwards to 130 km depth.

Figure 6.18 and 6.19 shows the results for a bulk water content of 0.763 wt% and a fracture endpoint of (300,130) km. The bulk water content is added to a radius of 27 km around the endpoint. The top left image in Figure 6.18 is the initial flash melting event and the melt fractions are ~ 0.04. The following five images are the results taken at 2.4, 3.6, 4.8, 6, and 7.2 Myr respectively. The partially molten region rises over time and also increases in melt fraction. The plume does not rise vertically but moves diagonally upwards, towards the wedge corner. In later time steps the melt fraction varies within the plume region. The upper part of the plume region has a higher melt fraction than the lower half. There is a slight tail to the plume but is much smaller than the tail in Figure 6.17. The plume region starts as a circular region, but as it rises it flattens into a plume shape. Figure 6.19 is the final time step at 8.4 Myr. The plume is pointing at the wedge corner and the plume head has the highest melt fractions of ~ 0.085. Towards the lower edges of the plume head the melt fraction decreases to ~ 0.05.

Figures 6.20 and 6.21 show the results for the case with a fracture endpoint of (300,130) km and a bulk water content of 2.996 wt%, added to a 27 km radius around the endpoint. The top left image in Figure 6.20 is the initial flash melting event with melt fraction of

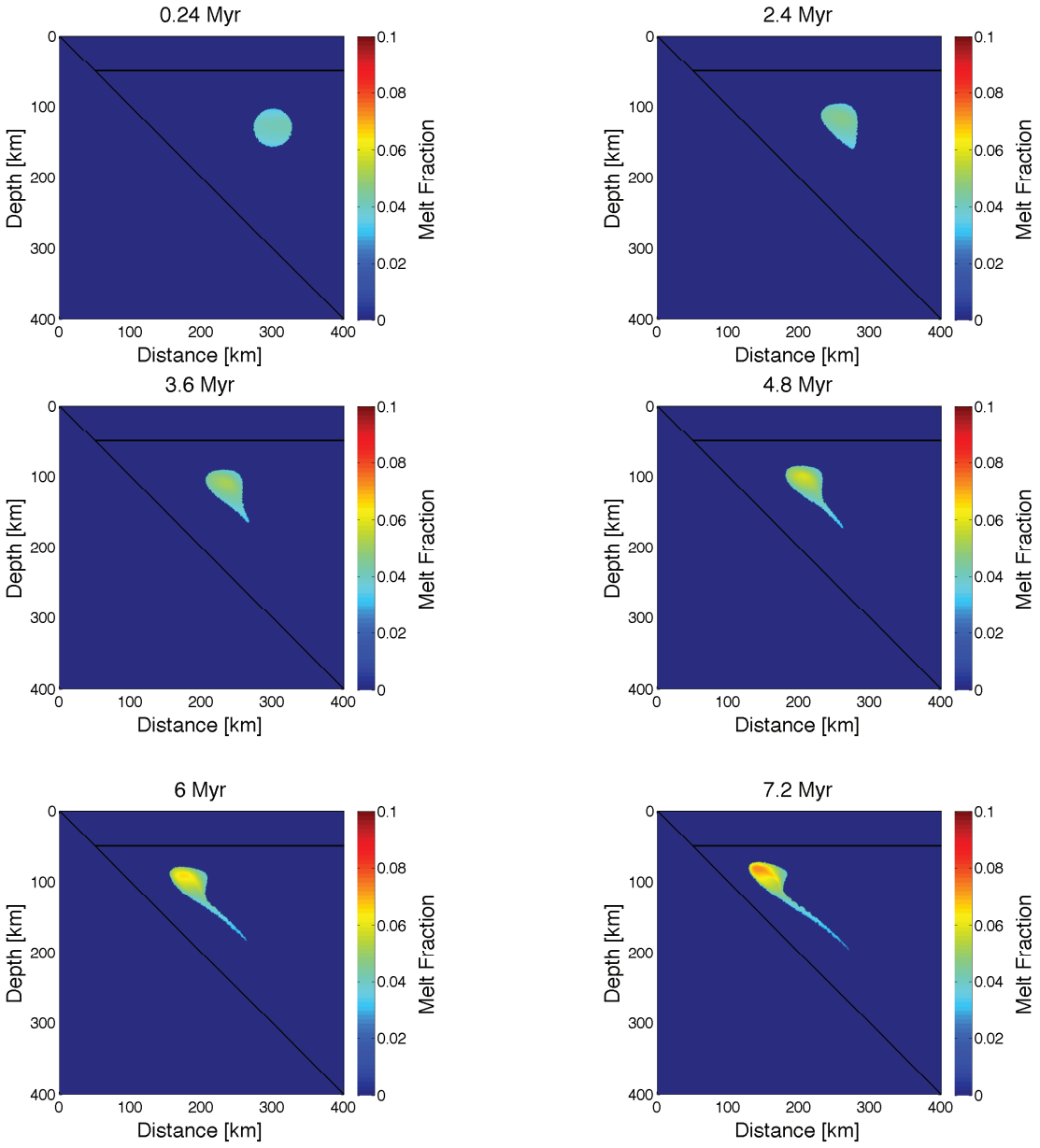

Fig. 6.18 Melt distribution over time for melting with a bulk water content of 0.763 wt%. The fracture endpoint is located at (300,130) km where the water content is added to a 27 km surrounding radius. The top left image is the initial flash melting then the following 5 images are how the partial melt increases and moves over time through the wedge region. By moving the fracture endpoint higher in the wedge a smaller tail to the plume is formed.

~ 0.15. The subsequent five images are the results at time steps of 2.4, 3.6 4.8, 6 and 7.2 Myr respectively. As the plume region rises the melt fraction increases due to the adiabatic

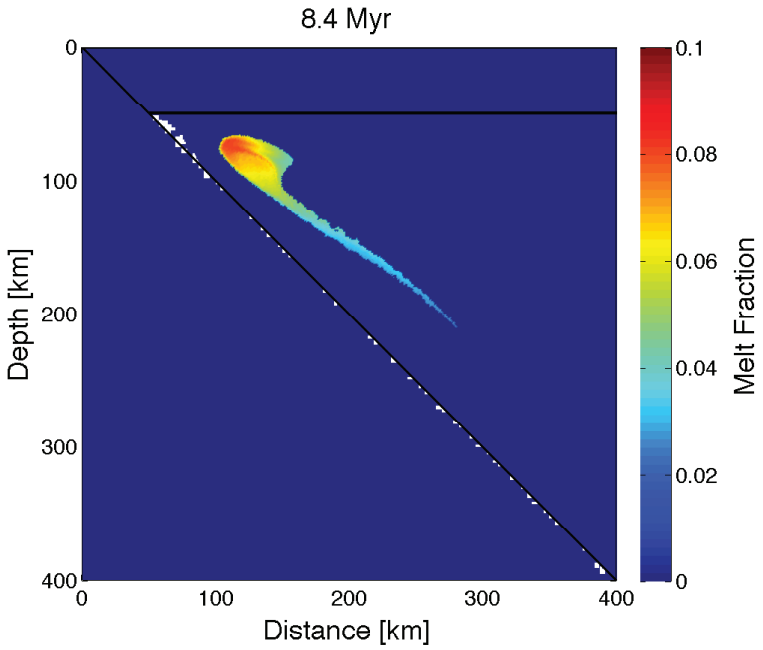

Fig. 6.19 Partial melt distribution for the final timestep for melting with a $X_{H_2O}^{bulk}$ of 0.763 wt%.The melt fraction values vary within the plume head region between ~ 0.05 and ~ 0.085 with the tail having values lower than 0.05.. The plume has reached the wedge corner.

decompression melting. The plume does not rise vertically but is deflected towards the wedge corner. The plume region starts as a circular region but flattens into a plume shape as it rises. The flattening is greater compared to Figure 6.18. The top region of the plume has the highest melt fractions and the melt fraction decreases towards the lower part of the plume. Figure 6.21 is the result from the final time step at 8.4 Myr. The plume is pointed at the wedge corner and the left half has already started to be deflected down by the corner flow. The centre and right parts of the plume that have not been deflected downwards have larger melt fractions, compared to the left part.

6.6.1 Melt Fraction

Figure 6.22 plots the melt fraction against time for the 0.763 wt% bulk water content case. The blue solid line represents the maximum melt fraction and the dashed blue line is the average melt fraction. For both lines the melt fraction increases with time to ~ 0.085 for the

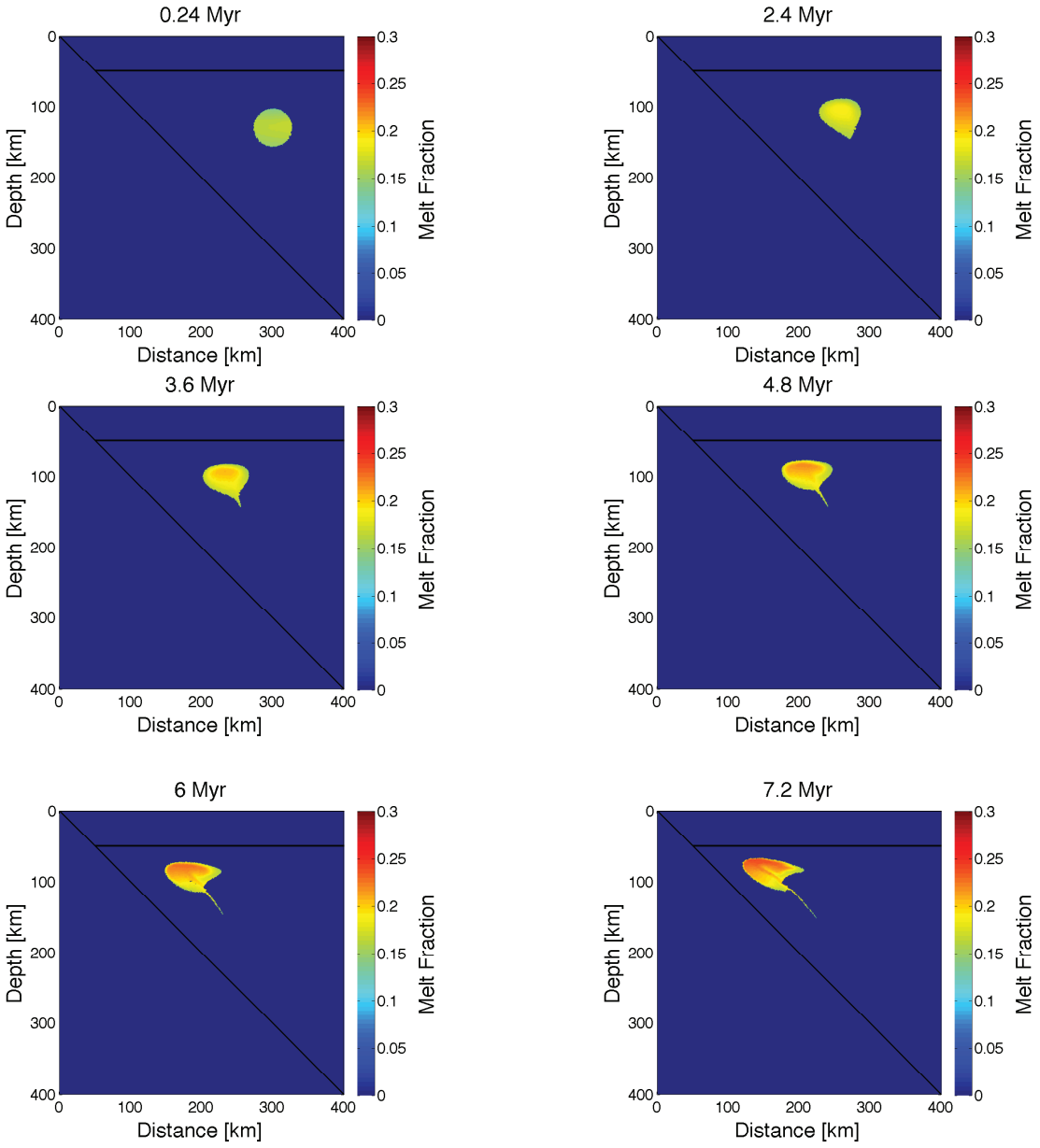

Fig. 6.20 Partial melt distribution over time for melting with a $X_{H_2O}^{bulk}$ of 2.996 wt%. The fracture endpoint is located at (300,130) km where the water content is added to a 27 km surrounding radius. The top left image is the initial flash melting then the following 5 images are how the partial melt increases and moves over time through the wedge region.

maximum melt fraction and to ~ 0.05 for the average melt fraction. As time progresses the difference between the maximum and average values increases showing there is a greater spread in melt fraction values as time increases, which is shown in Figure 6.18. The mean

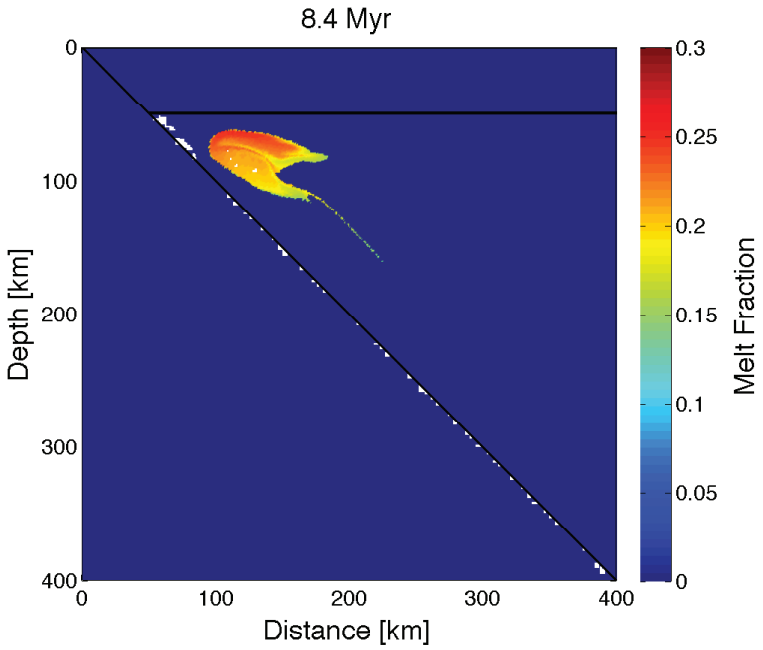

Fig. 6.21 Partial melt distribution for the final timestep for melting with a $X_{H_2O}^{bulk}$ of 2.996 wt%.The melt fraction values vary within the plume region between ~ 0.2 and ~ 0.25. The plume has reached the wedge corner and has started to deflect downwards on the left.

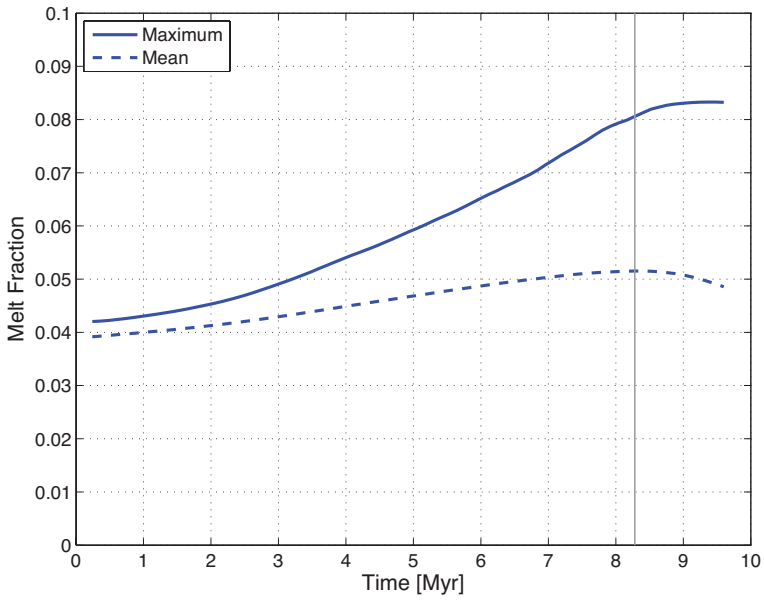

Fig. 6.22 Plot of melt fraction against time for the 0.763 wt% bulk water case. The solid blue line is the maximum melt fraction and the dashed blue line is the average melt fraction.

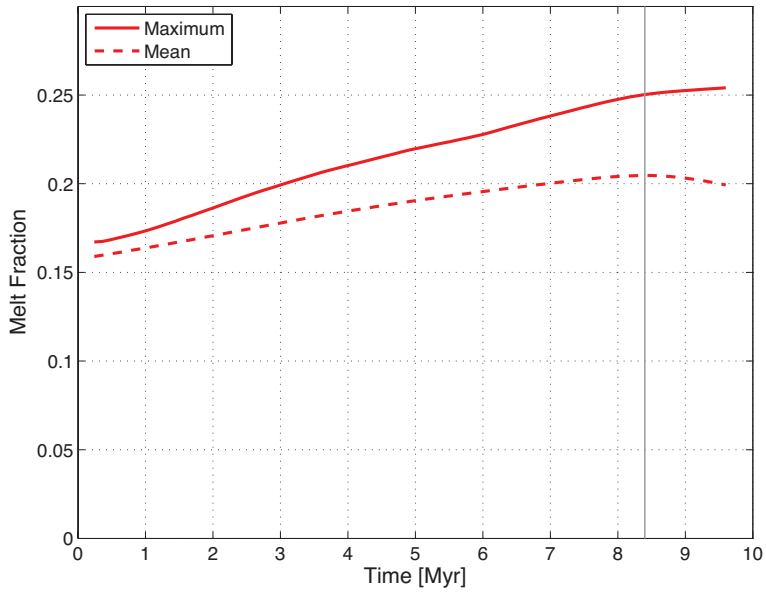

Fig. 6.23 Plot of melt fraction against time for the 2.996 wt% bulk water case. The solid red line is the maximum melt fraction and the dashed red line is the average melt fraction.

melt fraction start to decrease towards the end, even though the maximum melt fraction continues to increase. This could be due to the partially molten region reaching the wedge corner and starting to be deflected downwards, so some melt fraction values will start to decrease. The grey line in Figure 6.22 marks the time at which the average melt fraction is at a maximum which is ∼8.4 Myr. Figure 6.19 is taken at 8.4 Myr and shows that the plume has reached the wedge corner by this point.

Figure 6.23 plots the melt fraction against time for the 2.996 wt% bulk water constant model result. The maximum melt fraction is shown by the red line and the average melt fraction is shown by the dashed red line. The maximum melt fraction increases with time to ~ 0.25 and the average increase to ~ 0.20. As time progresses the difference between the maximum and average increases, again showing that the range in melt fraction within the partially molten region increases over time. As with Figure 6.22 the mean starts to decrease at the end but the maximum values continues to increase, suggesting some melt fractions are decreasing within the melt region at the end. The grey line in Figure 6.23 marks the time

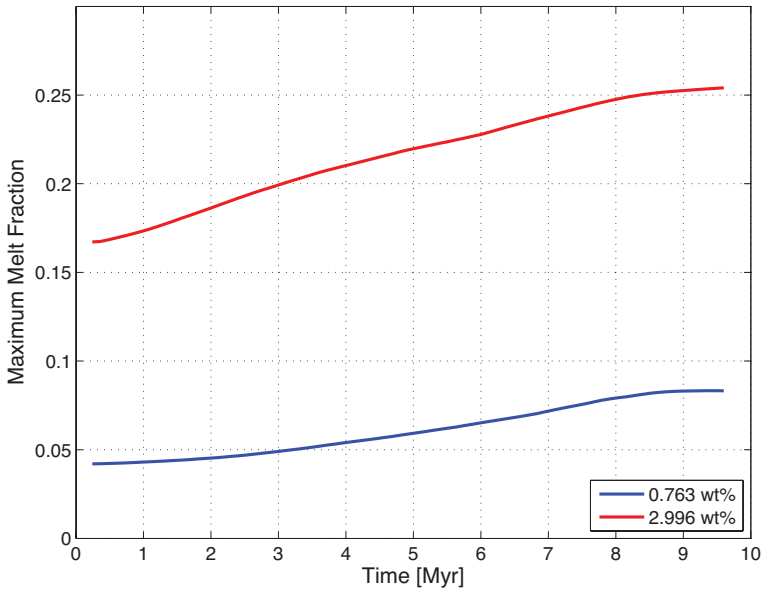

Fig. 6.24 Plot of maximum melt fraction against time. The blue line is the maximum melt fraction for the 0.763 wt% case and the red line is the maximum melt fraction for the 2.996 wt% case.

at which the average melt fraction is at a maximum which is ∼8.4 Myr. Figure 6.21 shows the plume has started to be deflected round by the cornerflow, and on the left side the melt fractions are lower than the rest of the plume head region.

Figure 6.24 plots the maximum melt fraction against time for a bulk water constant of 0.763 wt% shown by the blue line and a bulk water constant of 2.996 wt% shown by the red line. Both maximum melt fractions increase over time but the 2.996 wt% line has steeper increase compared to the 0.763 wt% line. For both lines the rate of increase in melt fraction decreases after 8.4 Myr, which is the point where the plume starts to be deflected downwards by the wedge corner.

6.6.2 Water Content in the Melt

Figure 6.25 plots the water content in the melt against time for the case using 0.763 wt% bulk water content. The solid blue line is the minimum water content and the dashed blue

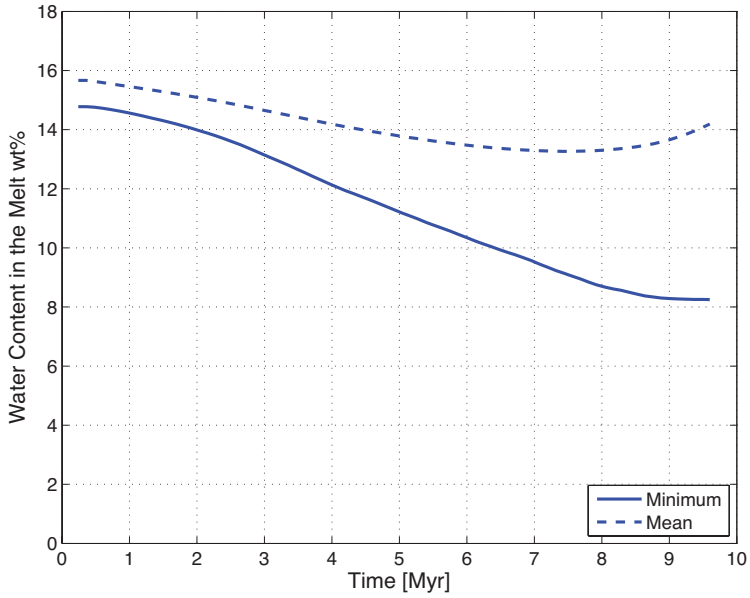

Fig. 6.25 Plot of water content in the melt against time for the 0.763 wt% bulk water case. The solid blue line is the minimum water content and the dashed blue line is the average water content.

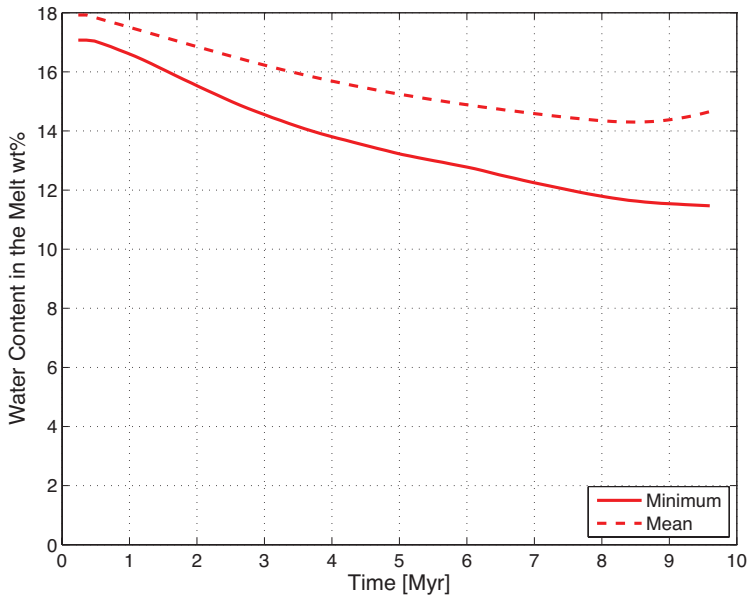

Fig. 6.26 Plot of water content in the melt against time for the 2.996 wt% bulk water case. The solid red line is the minimum water content and the dashed red line is the average water content.

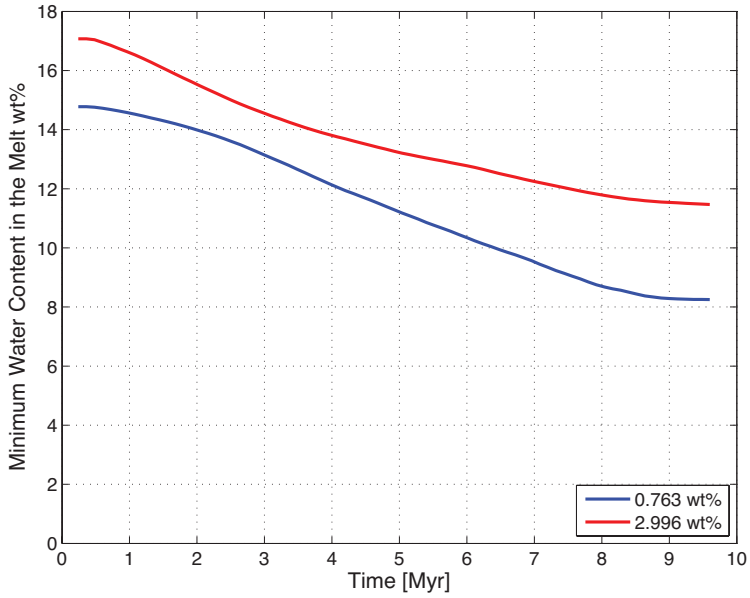

Fig. 6.27 Plot of water content in the melt against time. The blue line is the minimum water content for the 0.763 wt% case and the red line is the minimum water content for the 2.996 wt% case.

line is the average water content. Both water contents decreases with time to $\sim$ 13 wt% for the mean water content and to $\sim$ 8 wt% for the minimum water content. As the water content in the melt is directly related to the melt fraction, the same trend is shown in Figure 6.25 as Figure 6.22 that the difference between the two lines increases with time. This also means that after a certain time the average water content starts to increase as the corresponding average melt fractions are decreasing.

Figure 6.26 shows the water content in the melt against time for the model result using a bulk water content of 2.996 wt% The minimum water content in the melt over time is plotted as a solid red line and the dashed red line represents the average water content. Both decrease with time with the minimum water content decreasing to $\sim$ 11.5 wt% and the average water content decreasing to $\sim$ 14.5 wt%.

Figure 6.27 plots the minimum water content in the melt against time for the 0.763 wt% bulk water content in blue and the 2.996 wt% bulk water content in red. Both decrease in

water content over time, but the 0.763 wt% case has a greater decrease from $\sim$ 15 wt% to $\sim$ 8 wt% compared to the 2.996 wt% case, with a decrease from $\sim$ 17 wt% to $\sim$ 11.5 wt%. Both have a slow initial decrease, then decrease more rapidly before the rate starts to slow towards the end. The rate slows more for the 2.996 wt% case compared to 0.763 wt%.

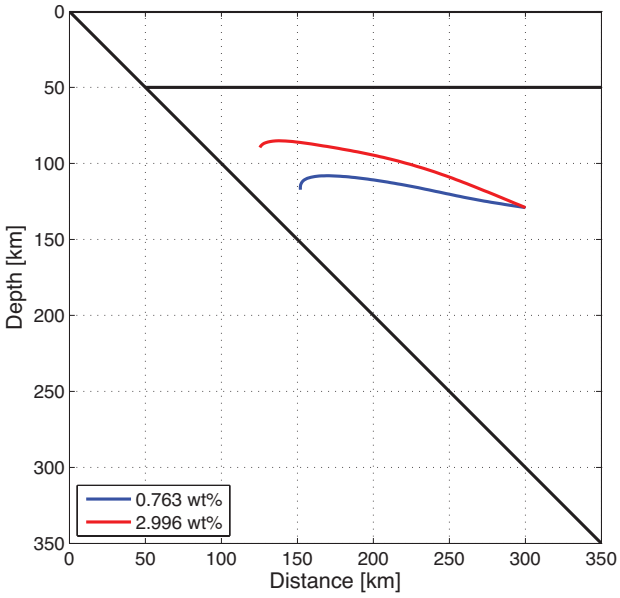

Fig. 6.28 Plot of mean position of the partially molten region for each time step. The blue line is mean position for the 0.763 wt% case and the red line is the mean position for the 2.996 wt% case. The red line plots a higher trajectory compared to the blue.

6.7 Discussion

I will compare the results from this chapter to the previous chapter but there are limitations due to the difference in radii between the two chapters. I also will discuss the movement of the plume region throught the wedge and also limitations of this model.

6.7.1 Trajectory of the Partially Molten Region

Figure 6.28 plots the mean x coordinate against the mean y coordinate for the plume region for each time step. The blue line plots the average trajectory for the 0.763 wt% case and the red line plots the trajectory for the 2.996 wt% case. The red line plots a higher trajectory compared to the blue line. This shows that the higher bulk water content and therefore the higher initial and subsequent melting had more buoyancy so the plume region rose higher. Figure 6.29 plots the trajectory of the position of the maximum melt fraction for each time

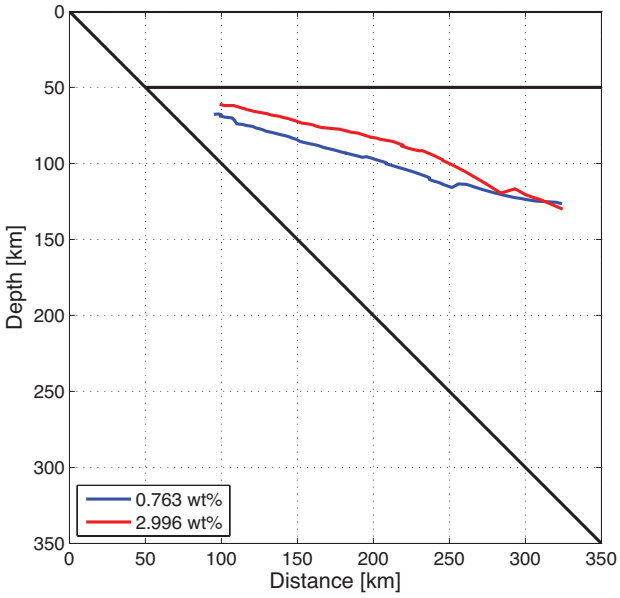

Fig. 6.29 Plot of average depth of the partially molten region over time. The blue line is average depth for the 0.763 wt% case and the red line is the aveage depth for the 2.996 wt% case. The red line has greater decrease over time compared to the blue.

step. The blue line plots the maximum melt trajectory for the 0.763 wt% case and the red line plots the trajectory for the 2.996 wt% case. These lines plot a closer trajectory to each other compared to Figure 6.28, but the red line still has a higher trajectory. Their final position is higher and closer to the wedge corner compared to the final average positions in Figure 6.28. This is because the average positions are lower in the plume region due to the spread in melt fractions and low melt fraction tail, and in the final timesteps the plume head starts to be deflected downwards by the wedge corner which is shown in Figure 6.28.

6.7.2 Comparison with previous chapter

I can compare the maxium melt fraction for both the bulk water content XH_2O_{bulk} of 0.763 wt% and the 2.996 wt%, with the corresponding maximum melt fractions F_{max} from the flash-ad case, from the previous chapter calculated using the thermal model temperature as shown in Table 6.1. For both bulk water contents the maximum melt fraction was higher

Velocity Regime	XH_2O_{bulk} wt%	F_{max}	XH_2O_{min} wt%
Cornerflow	0.763	0.14	5.07
Stokes flow	0.763	0.09	7.64
Cornerflow	2.996	0.32	9.11
Stokes flow	2.996	0.25	11.75

Table 6.1 Comparion of maximum melt fraction F_{max} and minimum water content in the melt XH_2O_{min} between this chapter and the previous chapter for two different bulk water contents XH_2O_{bulk} .

for the flash-ad case from the previous chapter. As discussed in Section 3 the temperature field for the Stokes flow thermal model is cooler than the corner flow thermal model. A cooler temperature will causes a lower initial flash melt so this may account for why the melt fractions are lower. Also in the previous chapter the maximum melt fraction was taken at the base of the overriding plate at 50 km depth. In the melting model from this chapter the partially molten region does not rise all the way to the overriding plate but to $\sim$ 75 km depth, so the adiabatic decompression melting from the previous chapter should be greater as it has risen to the overrriding plate. I also compare the minimum water content in the melt XH_2O_{min} to the previous chapters results in Table 6.1 . The minimum water contents are higher for the Stokes flow thermal model than the corner flow thermal model, but this is to be expected as the melt fractions for the Stokes flow thermal model are lower than the corner flow thermal model. Whilst the minimum water contents in the melt are higher compared to the previous chapter, they still fit with estimates of water contents in literature (Grove et al., 2003). However they are outside the estimated range from Plank et al. (2013).

6.7.3 Model Limitations

The original intention was to add water to radii that were the same size as previous chapters (0.5, 1 and 1.5 km) and use their corresponding bulk water content values. However as shown in Section 4, a 1 km radius region with water added will not rise after partially melting, but is

moved downwards by the velocity field. The analysis of viscosity showed that depending on location, a background viscosity of $\sim 1.7 \times 10^{20}$ Pa s or lower would be required for a 1km radius region with melt to rise. As shown in section 2, a viscosity of 10^{20} Pa s does not produce a feasible velocity field as a convection cell is formed. This is a big limitation as this meant I had to use a higher background viscosity and consequently use a larger radius for the water to be added to than the original 1 km radius. Analysis of the minimum radius against viscosity found that for a background viscosity of 10^{21} a radius of 12 km was needed for initial rise at (300,160) km. However when the vertical velocity over 20 timesteps was calculated a 12 km radius had a velocity of ~ 0 cm yr^{-1}, so an even larger radius was required for the region with melt to rise. The radius that was used for a background viscosity of 10^{21} Pa s at (300,160) km was 27 km, which much larger than the initial 1km region. Having to use a much larger region creates problems when comparing to the results from previous chapters. A larger region with partial melt will have a greater difference between the maximum melt fraction and the average melt fraction, compared to a 1 km region as is shown in the results in Section 6. This means comparing average melt fractions will be unrealistic, as the average melt fraction of the larger 27 km region with partial melt will be affected by the lower melt fractions at the edges of the plume and the plume tail. Also as it was not possible to model a small radius with partial melt, we can only assume that it would move in the same way as the larger region. Analysis of the rise velocities showed a smaller region would rise faster, but we have no way of determining if the trajectory of the region with partial melt would be the same as the larger region with the same bulk water content. It has been shown that the trajectory of the larger region with partial melt is affected by the melt fraction, with the higher melt fraction region having a higher trajectory. We can only assume this would be the case for a smaller partial melt region and it actually may have a higher trajectory, as the melt fractions within will vary less than the larger region. Therefore

whilst I have compared the results from this chapter to the previous chapter, there are too many limitations to be able to draw conclusions from the comparison.

6.8 Summary

This chapter added buoyancy into the thermal model. To do this the velocity field had to be solved using Stokes flow. After trying different velocity boundary conditions for the right hand side, a prescribed boundary condition was chosen. The new velocity field was incorporated into the exisitng thermal model, which was run until it reached a steady state temperature. Melting was incorporated into the thermal model, first by adding in flash melting, followed by the adiabatic melting that occurs as the partially molten region rises. The melting caused a decreases in density for the melt region which gave the region buoyancy. The first run of the melting model used a partial melt radius of 1 km and a background viscosity of 10^{21} Pa s, however the partially molten region did not rise but was carried downwards by the solid flow. Investigations of background viscosity and density showed that the minimum radius for partial melt to rise for a background viscosity of 10^{21} Pa s, a minimum partial melt radius of 27 km was required. For a partial melt radius of 1 km to rise the background velocity would need to be $\sim 10^{20}$ Pa s or lower, however at that viscosity, the velocity field is not stable and creates a convection cell. Using the partial melt radius of 27 km and a background viscosity two melting models were run; the first with a bulk water content of 0.763 wt% and the second with 2.996 wt%. For both cases the partial molten region rises and is deflected by the solid flow towards the wedge corner. The trajectory of the partially molten region is affected by the amount of melting, with higher melt fractions having more buoyancy, so the trajectory is higher. Comparison with the previous chapter shows the maximum melt fraction for both cases are lower than the corresponding values from the previous chapter, and the minimum water content in the melt values are higher. As the steady state temperature field for this chapter is lower than the cornerflow steady state

temperature field, this could be an explanation for the lower melt fractions. Discussion of the model limitations leading to a larger region with partial melt being used than previous chapter, led to the decision that conclusions cannot be drawn from the comparison of this chapter to the previous chapter. The next chapter will compare all the melting scenarios covered in this thesis to each other and to literature.

CHAPTER 7

DISCUSSION

7.1 Introduction

In this thesis I have examined five different melting cases. I now need to compare them to each other and also to observations from volcanic arcs, to determine which melting case is the best. All the melting cases use the assumption that water is added to the mantle wedge via a hydraulic fracture. This addition of water will cause instantaneous melting or 'flash melting'. This is the first melting case of just flash melting (flash). The second melting case is flash melting followed by hydrous flux melting (flash-flux). The third case introduces hydrous decompression melting after flash melting (flash-ad). The fourth case combines the three melting mechanisms, so is flash melting, then hydrous flux melting followed by decompression melting (flash-flux-ad). The last case is the flash ad case but with the addition of buoyancy (flash-ad-buoy). I will compare the maximum and average melt fractions, the average and minimum X_{H_2O} and the locations of the final partial melt events for all five cases. I will also compare the melt production rate for the first four cases. The flash-ad-buoy case only produced results for two $X_{H_2O}^{bulk}$ values and for one fracture event, so the melt production rate will not be comparable to the other cases. All the results figures will have the flash values plotted as red circles, the flash-flux values plotted as blue squares, flash-ad values

will be plotted as green triangles, flash-flux-ad will be plotted as light blue diamonds and the flash-ad-buoy values will be plotted as pink downwards pointing triangles.

7.2 Comparisons between Melting Models

7.2.1 Melt Fraction

Figure 7.1 plots $X_{H_2O}^{bulk}$ against the average melt fraction for each of the melting cases. The flash values show a linear positive relationship with $X_{H_2O}^{bulk}$ values. Flash-flux, flash-ad and flash-flux-ad all plot along curves of best fit. All cases show the general trend of increasing melt fraction with increasing $X_{H_2O}^{bulk}$ values. The flash values are lowest for corresponding $X_{H_2O}^{bulk}$ values, followed by flash-flux, then flash-ad-buoy, then flash-ad and flash-flux-ad have the largest average melt fractions. Figure 7.2 plots $X_{H_2O}^{bulk}$ against the maximum melt fraction for each of the melting cases. The flash, flash-flux and flash-ad all fit curves of best fit but the flash-flux-ad case does not. Apart from the flash-flux-ad case, all the melting cases show the trend of increasing maximum melt fraction with $X_{H_2O}^{bulk}$ value. The flash-flux-ad case initially has a decrease in maximum melt fractions with increasing $X_{H_2O}^{bulk}$ followed by an increase in maximum melt fraction. The flash case has the lowest maximum melt fractions closely followed by flash-flux. Then the flash-ad-buoy has the next lowest maximum melt fractions followed by flash-ad then flash-flux-ad has the highest maximum melt fractions. Generally there is little difference between the flash and flash-flux values.

I compared the melt fraction values to two studies. Kelley et al. (2010) estimated melt fractions from samples taken from the Mariana Arc region shown in Figure 7.3 and Portnyagin et al. (2007) estimated melt fractions for the Kamchatka arc as shown in Figure 7.4. Comparing Figure 7.1 to Figure 7.3, what is clear is only the flash-flux-ad case has melt fractions comparable to the results shown Figure 7.3. In Figure 7.2 the flash-ad maximum melt fractions fit the lower melt fractions estimates from Figure 7.3 and the flash-flux-ad

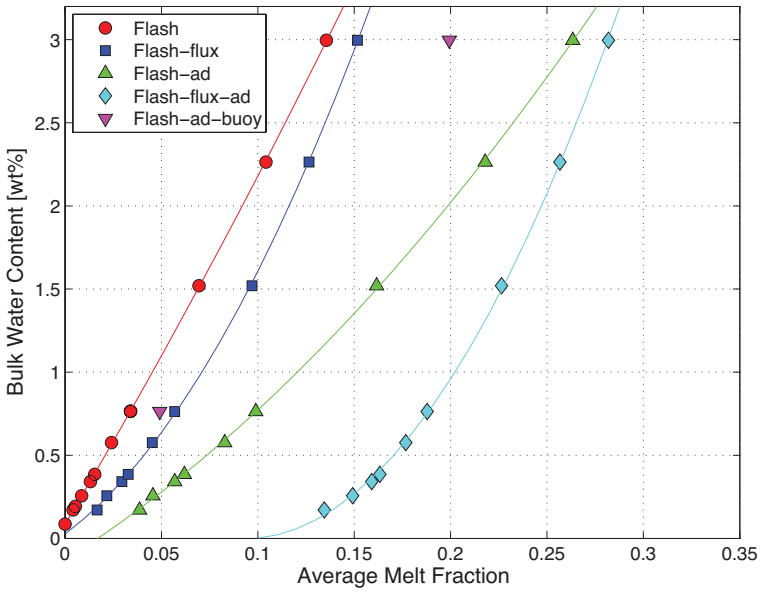

Fig. 7.1 $X_{H_2O}^{bulk}$ against average melt fraction for each melting case

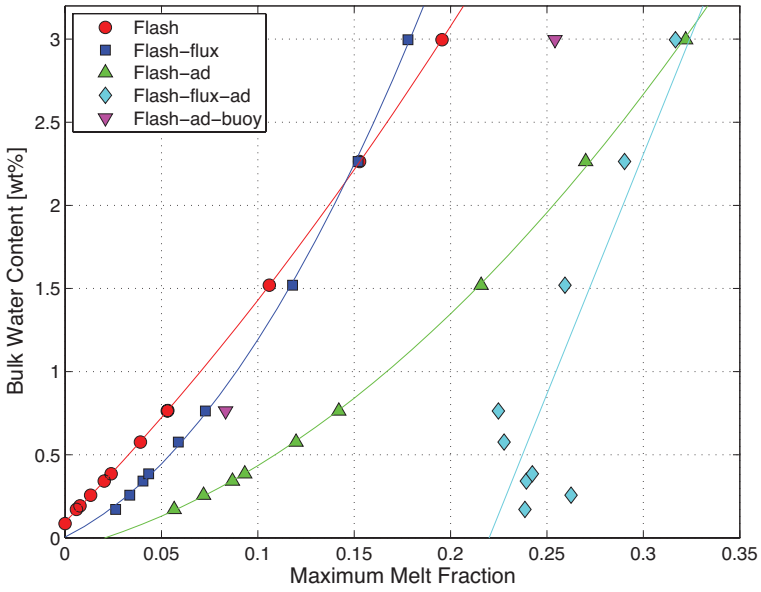

Fig. 7.2 $X_{H_2O}^{bulk}$ against maximum melt fraction for each melting case

maximum melt fractions fit the upper melt estimates. Figure 7.4 plots the degree of melting against water in the source ($X_{H_2O}^{bulk}$). The grey region marked 'CAVA' is the arc melt fraction

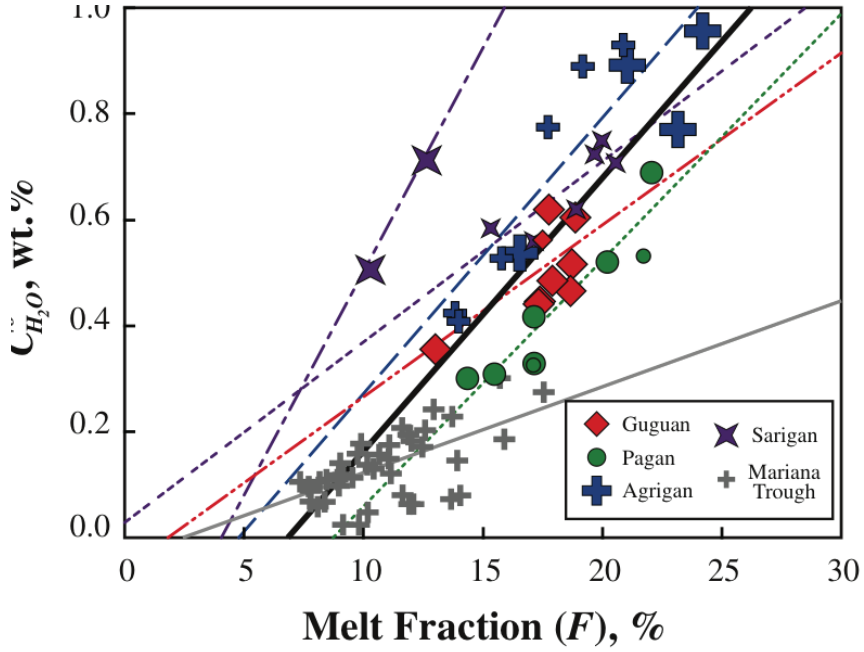

Fig. 7.3 Figure from Kelley et al. (2010) of plot of melt fraction against original water content $C^O_{H_2O}$ for the Mariana arc and trough modelled data. The lines shown are least-sqaures linear regressions for the back arc basin, whole arc and each island. The grey line is the Mariana Trough, the bold black line is all the Mariana arc data, the dotted line is Pagan Island, the double dot-dash line is Guguan Island, the long dash line is Agrigan Island, the dot-dash is sample S93 and triple dot line is Sarigan Island.

estimates. For the average melt fractions in Figure 7.1, the only melting case to fall in the estimated range is the flash-flux-ad case. For the maximum values in Figure 7.2 the estimated melt fractions from Figure 7.4 fall between the flash-ad and flash-flux-ad values.

From this the conclusion would be the flash-flux-ad melting case is the only case that produces melt fractions that are comparable to observations.

7.2.2 Water Content in the Melt X_{H_2O}

Figure 7.5 plots the average X_{H_2O} values against $X^{bulk}_{H_2O}$ for each of the melting cases. The flash-flux and the flash-flux-ad values mostly fit a line of best fit, showing a linear relationship increasing $X^{bulk}_{H_2O}$ values. The flash and flash-ad cases both look as if they would fit a curve rather than a line of best fit. For both of these cases the average X_{H_2O} increases rapidly with

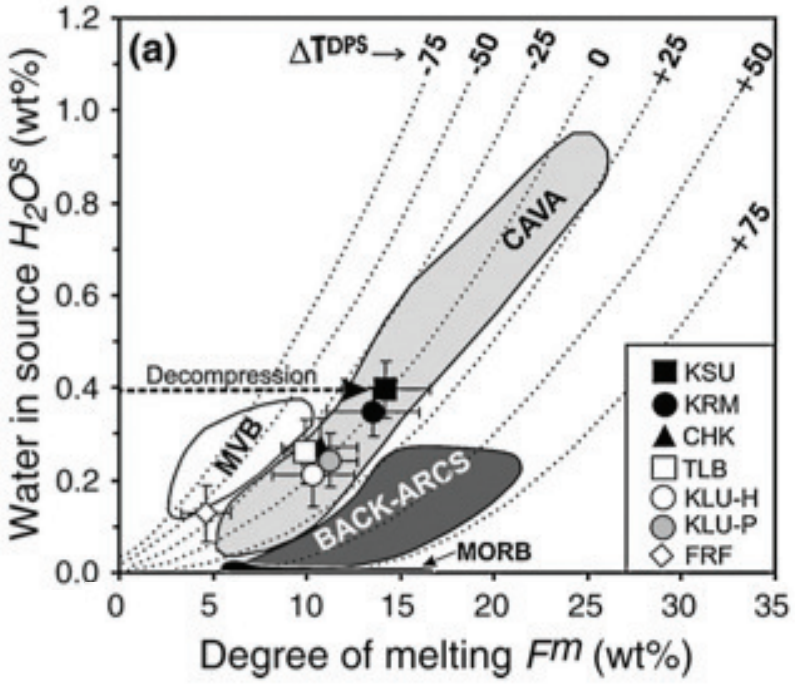

Fig. 7.4 $X_{H_2O}^{bulk}$ against degree of melting for each melting case for the Kamchatka region taken from Portnyagin et al. (2007). The grey CAVA region is the arc melt fraction estimates.

$X_{H_2O}^{bulk}$ then becomes steady. All cases show the general trend of average X_{H_2O} increasing with $X_{H_2O}^{bulk}$ values. The flash values are the highest, followed by flash-flux then flash-ad-buoy, flash-ad and flash-flux-ad have the lowest X_{H_2O} values. Figure 7.6 plots the X_{H_2O} values for the maximum melt fraction against $X_{H_2O}^{bulk}$ for each melting case. The cases all plot along lines of best fit showing they all have a linear relationship of X_{H_2O} increasing with $X_{H_2O}^{bulk}$ values. The flash and flash-flux values intersect, with the flash X_{H_2O} values being higher at low $X_{H_2O}^{bulk}$ values and the flash-flux X_{H_2O} values are higher at higher $X_{H_2O}^{bulk}$ values. The next lowest values are flash-ad buoy, then flash-ad and then flash-flux-ad have the lowest values.

Several studies discuss the X_{H_2O} value of arc magmas. Plank et al. (2013) estimated X_{H_2O} with a global average of $\sim$ 4 wt% and a range of 1-7 wt%. Other studies have suggested higher X_{H_2O} estimates with Grove et al. (2003) and Krawczynski et al. (2012) estimating a range of $\sim$ 10-14 wt% for the Mount Shasta region. For the upper limit of 14 wt% all the flash-ad and flash-flux-ad average X_{H_2O} values from Figure 7.5 fall below this value. For the

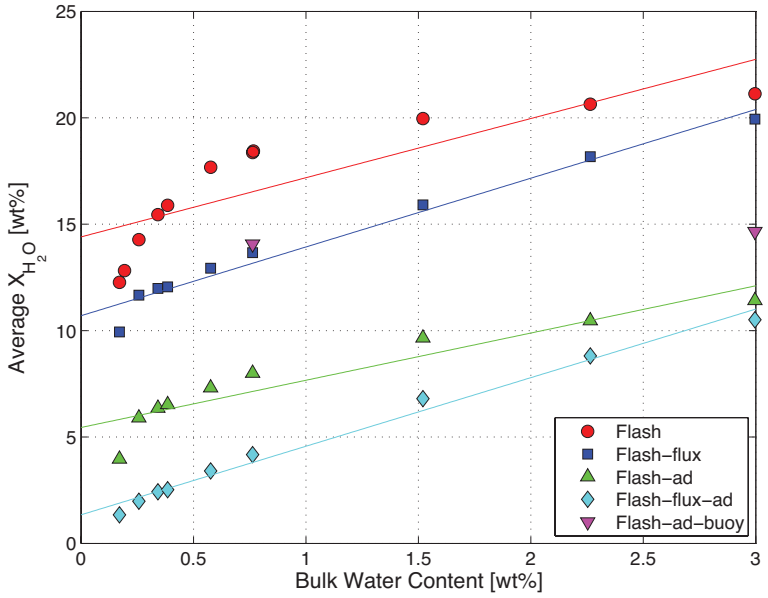

Fig. 7.5 Average X_{H_2O} against $X_{H_2O}^{bulk}$ for each melting case

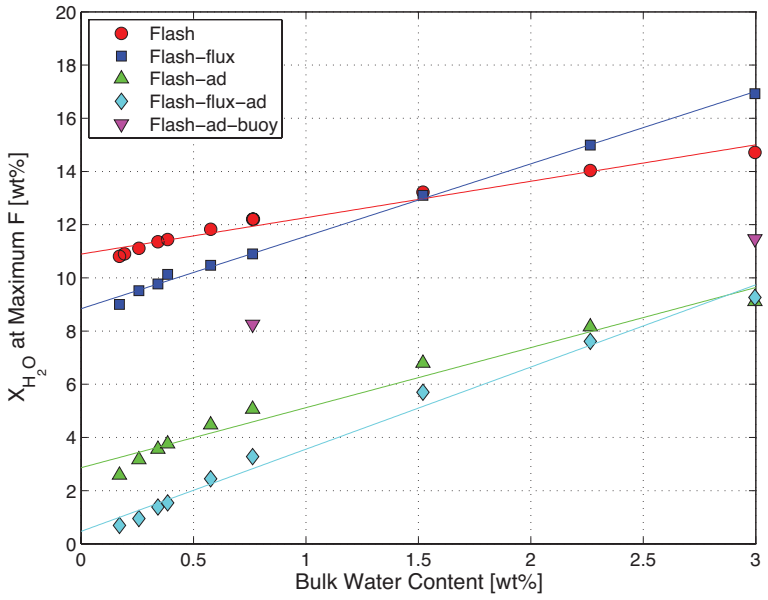

Fig. 7.6 The X_{H_2O} values at the maximum F value against $X_{H_2O}^{bulk}$ for each melting case

flash-flux case only $X_{H_2O}^{bulk}$ values under 1 wt% fall below 14 wt% and for the flash case only the three lowest $X_{H_2O}^{bulk}$ values have X_{H_2O} values under 14 wt%. For the range suggested by

Plank et al. (2013) of 1-7 wt%, flash, flash-flux and flash-ad-buoy have no X_{H_2O} values in this range. For flash-ad and flash-flux-ad, the $X^{bulk}_{H_2O}$ values under 1 wt% have X_{H_2O} values under 7 wt%. In Figure 7.6 all the flash-ad and flash-flux-ad X_{H_2O} values are lower than 14 wt%. Only the two highest $X^{bulk}_{H_2O}$ values have X_{H_2O} values higher than 14 wt% for the flash-flux case, and only the highest $X^{bulk}_{H_2O}$ value has a X_{H_2O} values higher than 14 wt% for the flash case. Again none of the flash, flash-flux or flash-ad-buoy cases have X_{H_2O} values under 7 wt%. All the X_{H_2O} values apart from the two highest $X^{bulk}_{H_2O}$ values are under 7 wt% for the flash-ad and the flash-flux-ad cases. For $X^{bulk}_{H_2O}$ values under 1 wt%, the flash-ad X_{H_2O} values are $\sim$ 4 wt% similar to the global average estimated by Plank et al. (2013). The flash-flux-ad X_{H_2O} values for $X^{bulk}_{H_2O}$ values under 1 wt% are lower, $\sim$ 2 wt%. The conclusion would be that the flash-ad and flash-flux-ad cases produce X_{H_2O} values that fit in the range suggested by Plank et al. (2013). All the melting cases have X_{H_2O} values that fit in the range suggested by Grove et al. (2003) and Krawczynski et al. (2012).

7.2.3 Melt Temperature

In the literature there are varying estimates for the temperature of magma formed at subduction zones. Kelley et al. (2010) and Kohut et al. (2006) both estimated high magmatic temperatures for the Mariana Arc at $>$ 1300°C. As 1300 ° C is the maximum temperature of the thermal model, the melt temperatures from the model were never going to match these estimates. However the Mariana Arc is unusual in subduction zone terms as it is an oceanic-oceanic subduction zone. It has a thin overriding plate, this also explains the low pressure values that Kelley et al. (2010) and Kohut et al. (2006) also estimated for the melting of $1.0 - 2.4 \pm 0.2$ GPa. This means the hottest part of the mantle wedge can be located at shallower depths, than my model with an overriding plate depth of 50 km. Other studies have found lower temperature ranges, Krawczynski et al. (2012) estimated magmatic temperatures between 900 - 1050 °C and Sisson and Grove (1993) estimated

magma temperatures between 950-1250 °C. The flash and flash-flux temperatures fall in the ranges suggested by Krawczynski et al. (2012) and Sisson and Grove (1993), but both the decompression melting cases have lower temperatures between 750-800 °C. It is clear that the melt temperature varies between melting cases, so I will now plot the melt temperature against X_{H_2O} to see if there is any relationship. These are shown in Figure 7.7, all are for the final X_{H_2O} and magma temperature values for a $X_{H_2O}^{bulk}$ of 0.763 wt%. Figure 7.7 is made up of four plots. Plot 1 is the flash case shown by red circles, plot 2 is the flash-flux case shown by blue squares, plot 3 is the flash-ad case shown by green triangles and plot 4 is the flash-flux-ad case shown by light blue diamonds. In plot 2, the wet melt temperature T_w is used rather than the thermal model temperature as the flux melting parameterisation by Davies and Bickle (1991) can calculate this value. In plot 1 the points cover a wide area but there is an overall trend of X_{H_2O} decreasing as the melt temperature increases. In plot 2 the points are distributed in two distinct regions A and B. As discussed in chapter 4, region A corresponds to the diagonal line of final melt events and Region B is the horizontal line of final melt events, as shown in Figure 7.10(top right). Region A is characterised by a decrease in X_{H_2O} as T_w increases. Region B shows a large increase in X_{H_2O} with a small increase in T_w . Plots 3 and 4 have similar trends of a rapid decrease in X_{H_2O} as temperature increases then X_{H_2O} becomes constant as temperature increases. The difference between plots 3 and 4 is Plot 3 has a larger spread in the data points distribution and the X_{H_2O} values in plot 4 are lower.

I can compare these plots to Figure 7.8 taken from Grove et al. (2012). The blue squares are experimentally studied primitive arc rocks from different regions, most are in the 1-7 wt% range suggested by Plank et al. (2013). The grey and white circles are values from Sisson and Grove (1993) from the Greater South Cascades. These values also fall within the range suggested by Plank et al. (2013) and the melt temperatures range between 950-1250 °C. The final set of values are estimates from the Mount Shasta region from Krawczynski et al. (2012),

shown by the yellow diamonds. These have increasing X_{H_2O} values with increasing melt temperature. The X_{H_2O} values are higher ranging from 3 wt% to 14 wt%, but the temperatures are lower from 900 - 1050 °C. Comparing Figure 7.8 with Figure 7.7, only plots 1 and 2 have similar temperature values to Figure 7.8, but only plots 3 and 4 have similar X_{H_2O} values. However if we look compare trends then it is clear that region A in plot 2 of Figure 7.7 is very similar to the Sisson and Grove (1993) trend in Figure 7.8. They both have a similar temperature range but the Sisson and Grove (1993) X_{H_2O} values are lower. Region B in plot 2 is a similar trend to the trend in the Krawczynski et al. (2012) values, in that they both have a rapid increase in X_{H_2O} as temperature increases, but the temperatures in region B are a lot higher and the trend is steeper. The Sisson and Grove (1993) values were estimated to be from melts at 0.4 GPa in comparison the average pressure of the final melt events in the flash-flux case is ~ 4 GPa. If the flash-flux case was to occur at lower pressures, but the same temperature, then the melt fraction could increase and X_{H_2O} decrease. Changing the height of the overriding plate from 50 km to a lower values would allow hotter temperatures at lower pressures.

7.2.4 Melt Production Rate

In Figure 7.9 the top left, top right and lower left figures are plots of melt production rate for each melting case for a fracture length of 4 km , 6 km and 8 km respectively. Over the three figures the flash values have linear increase of melt production rate with increasing $X_{H_2O}^{bulk}$ values. The other three cases have a steep increase in melt production rate between the first two $X_{H_2O}^{bulk}$ values, then the increase in melt production rate between the second and third $X_{H_2O}^{bulk}$ values have a much lower increase. The flash-ad values for the largest $X_{H_2O}^{bulk}$ for each each fracture length produce the highest melt production rates. In Figure 7.9, the lower right figure plots all the melt production rate values against $X_{H_2O}^{bulk}$ for each melting case. For $X_{H_2O}^{bulk}$ values under 1 wt% the flash values are the lowest, followed by flash-flux, then flash-ad

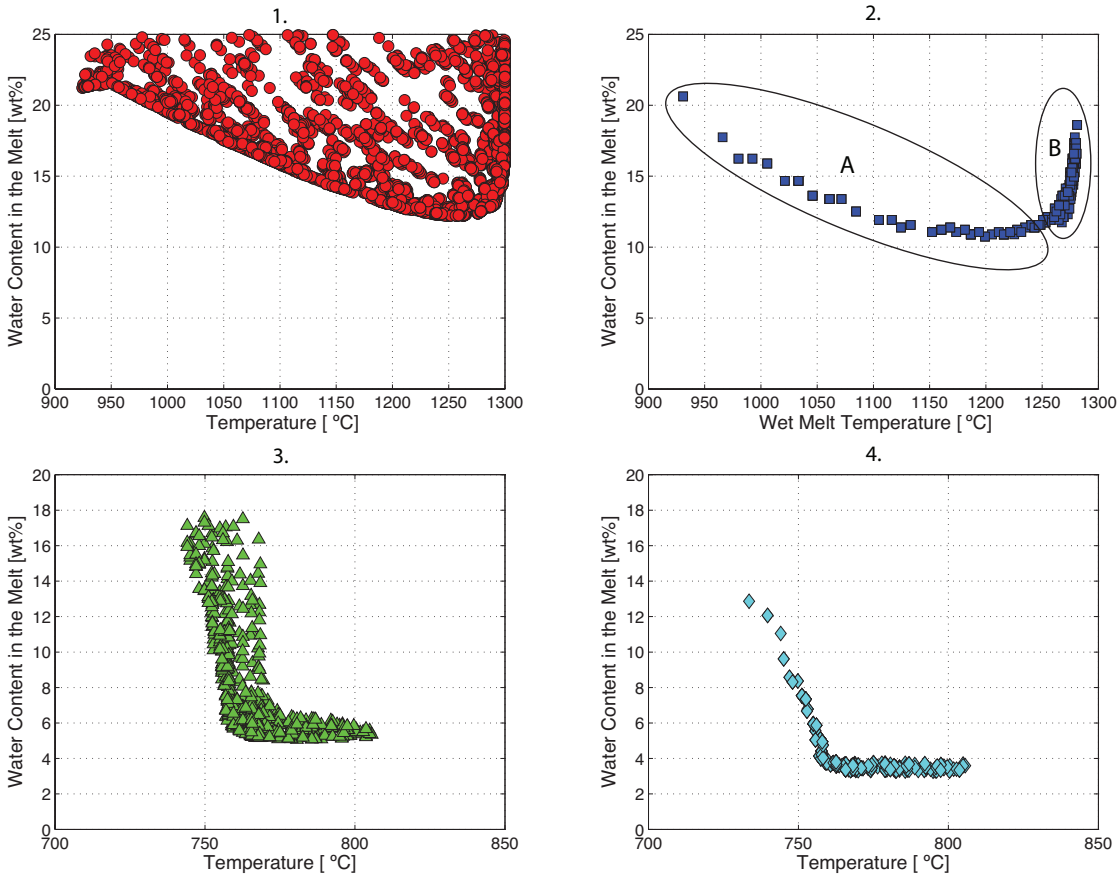

Fig. 7.7 1. Melt temperature against X_{H_2O} for the flash case. 2. Wet melt temperature against X_{H_2O} for the flash-flux case. 3. Melt temperature against X_{H_2O} for the flash-ad case and 4. Melt temperature against X_{H_2O} for the flash-flux-ad case. All plots are for the final melt events for the 0.763 wt% $X_{H_2O}^{bulk}$ for each melting case.

and finally flash-flux-ad. For $X_{H_2O}^{bulk}$ values above 1 wt% the flash-flux values are lowest, then flash, followed by flash-flux-ad and flash-ad are the highest melt production rate values.

Wada and Wang (2009) used the volcanic output rate to estimate melt production rate fo 17 subduction zones. They found the melt production rate varied from 24 km^3 Myr^{-1} up to 11000 ± 1000 km^3 Myr^{-1}. However Wada and Wang (2009) do not take into account the arc length of subduction zones, so the actual values that can be compared to my results will be lower, if we assume arc lengths between 500 -1000 km. The melt production rate values from Figure 7.9 would fit in this range in this case. Holbrook et al. (1999) and Lizarralde

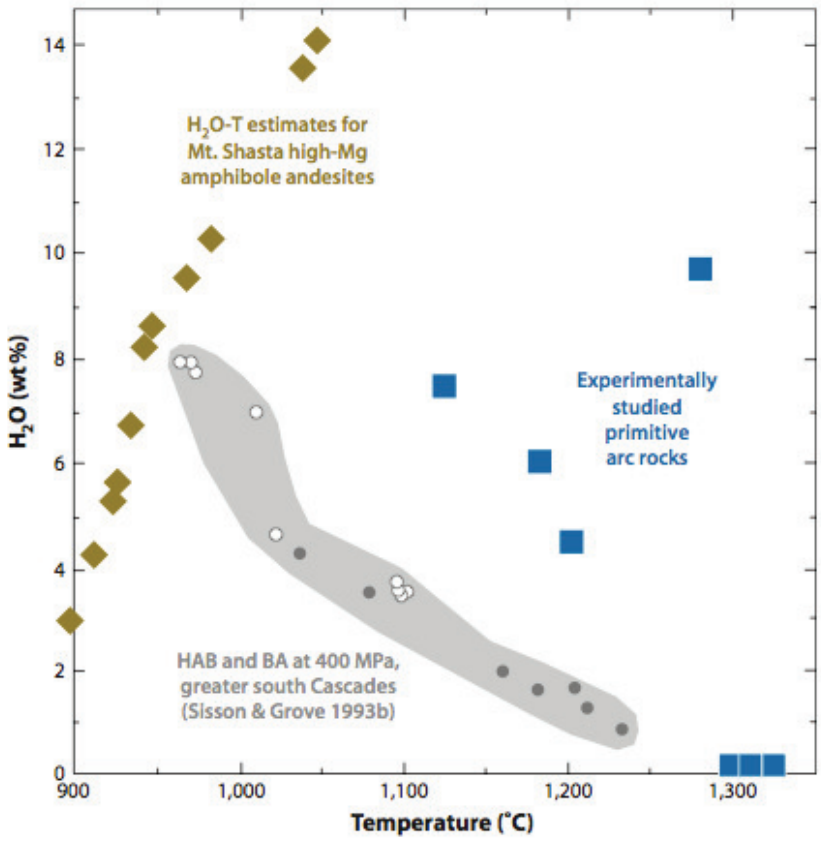

Fig. 7.8 Temperature against X_{H_2O} taken from Grove et al. (2012). The blue square are primitive arc rocks from Grove et al. (2012), the grey and white squares are results from Sisson and Grove (1993) and the yellow diamonds are results from Krawczynski et al. (2012).

et al. (2002) do take into account arc length, they estimated the melt production rate at the Eastern Aleutian to be $\sim$67 km^3 km^{-1} Myr^{-1}, which is higher than the values in Figure 7.9. The difference in values could be due to the large fracture size. Decreasing the fracture size would cause the time for 1000 fracture events to decrease, leading to a possible increase in the productivity rate.

7.2.5 Melt Focussing

Figure 7.10 plots the final partial melt locations for each of the melting cases. The top left is the flash melt locations, these occur over a wide area. The flash-flux locations are shown in

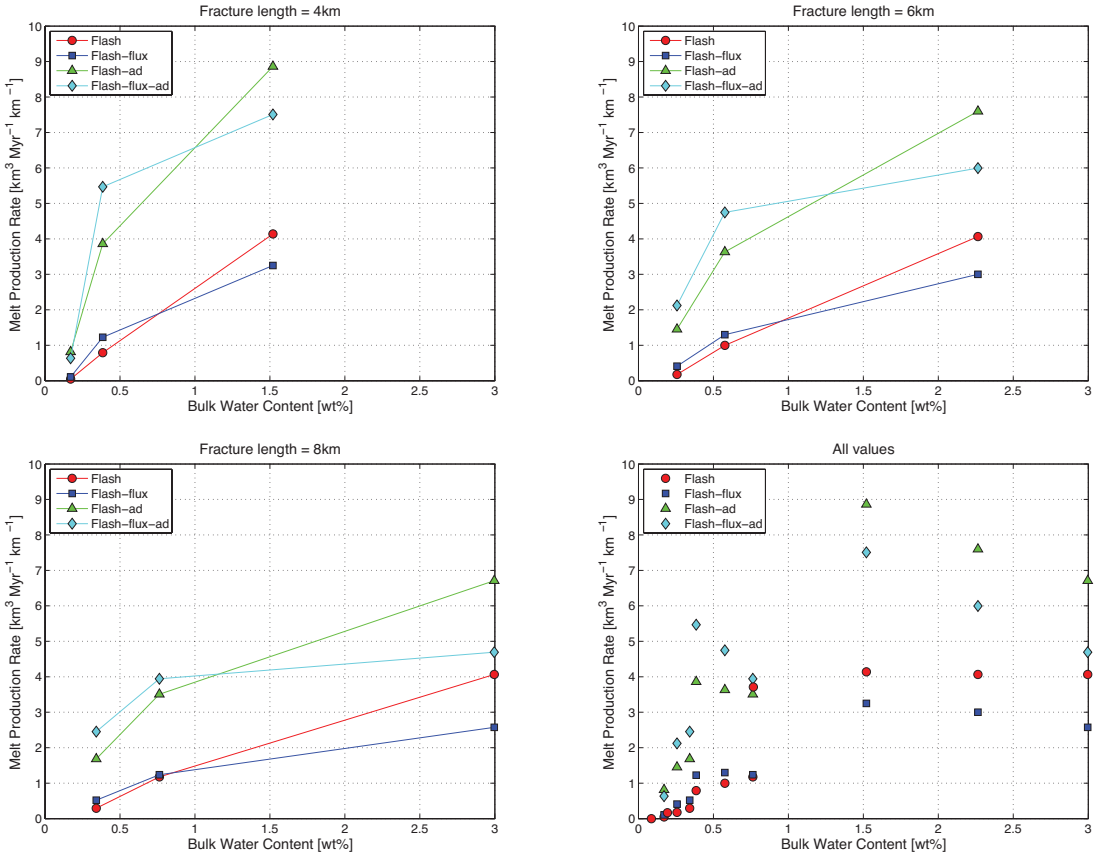

Fig. 7.9 Top left is the melt production rates for the 4 km length fracture events, top right is the melt production rates for the 6 km length fracture events, bottom left is the melt production rates for the 8 km length fracture events and the bottom right is all the melt production values from each melting case

the top right figure, they are more focussed but still occur over a wide range of depths. The bottom left is the two decompression melting cases and their final locations are the lower edge of the overriding plate. They are focussed to a certain depth but have a wide range of distances. The lower right figure is the flash-ad-buoy case, these values are more focussed. Apart from flash-ad-buoy, none of the melting cases have a mechanism of melt focussing that would explain the localization of volcanic arc fronts. This would indicate the melt focussing occurs during the migration of the partial melt to the surface, rather than during the melting process itself. A potential focussing mechanism suggested by Cagnioncle et al. (2007) and

England and Katz (2010b) is a sloping decompaction channel. The solidus at the top of the wedge forms an impermeable boundary and the decompaction channel will occur beneath the boundary (Cagnioncle et al., 2007). Sufficient crystallisation is required to seal the pore space against vertically rising magma (Spiegelman, 1993). At temperatures above the anhydrous solidus, isobaric productivity is high and a small decrease in temperature will result in significant crystallisation, which meets the conditions required to form an impermeable boundary. Below the anhydrous solidus the isobaric productivity is low, so will not produce sufficient crystallisation (Katz et al., 2003). England and Katz (2010b) therefore propose that the 'nose' of the anhydrous solidus is where the high-porosity channel will terminate. At the 'nose' the magma will rise and cause thermal erosion, establishing a pathway for the magma to reach the surface. This propsed mechanism is depicted schematically in Figure 7.11. The flash and flash-flux cases could have this focussing mechanism occur to them after the final melt events, however both the flash-ad and flash-flux-ad have final melt events occur at the overriding plate boundary, so the focussing mechanism could not occur afterwards. For these two cases the thing to consider is whether the decompression melting would occur up to the overriding plate, if the decompaction channel was to occur the decompression melting would occur up that location. The flash-ad-buoy case seems to have melt focussing in a similar manner to the mechanism suggested by Cagnioncle et al. (2007) and England and Katz (2010b), however as this case was only run for two $X^{bulk}_{H_2O}$ cases, more runs would be needed to see if this was the case.

7.3 Model Limitations

I used two thermal models in this thesis, both of which have limitations that need considering. The cornerflow thermal model (Chapter 2) did not fit the benchmark values from Van Keken et al. (2008). The difference in temperature between the benchmark and the thermal model was low enough however to justify using the thermal model for calculating melting. The

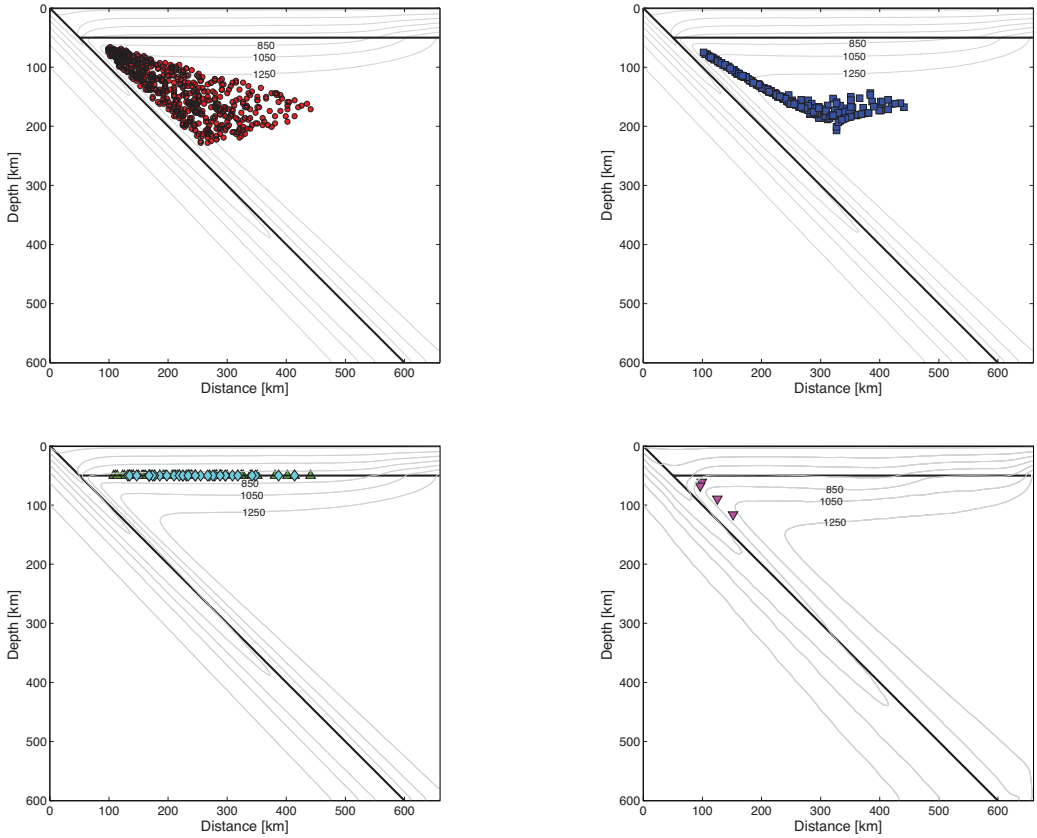

Fig. 7.10 Top left is the final partial melt locations for the flash case, top right is the final partial melt locations for the flash-flux case, bottom left is the final partial melt locations for the flash-ad and flash-flux-ad cases and the bottom right is the final partial melt locations for the flash-ad-buoy case

lowest grid resolution used in calculating the benchmark results was 0.5 km (Van Keken et al., 2008). I found that grid resolutions below 3 km would be too computationally expensive when running the thermal model, so this could account for the temperature difference. The other thermal model used a velocity field calculated using Stokes Flow. Due to the extra computation required to solve the velocity field, the lowest grid resolution used was 6 km, a 3 km grid resolution was computationally expensive. This led to the Stokes Flow thermal model having a cooler wedge region than the cornerflow thermal model, this could account for the flash-ad-buoy melt fractions being lower than the corresponding flash-ad values.

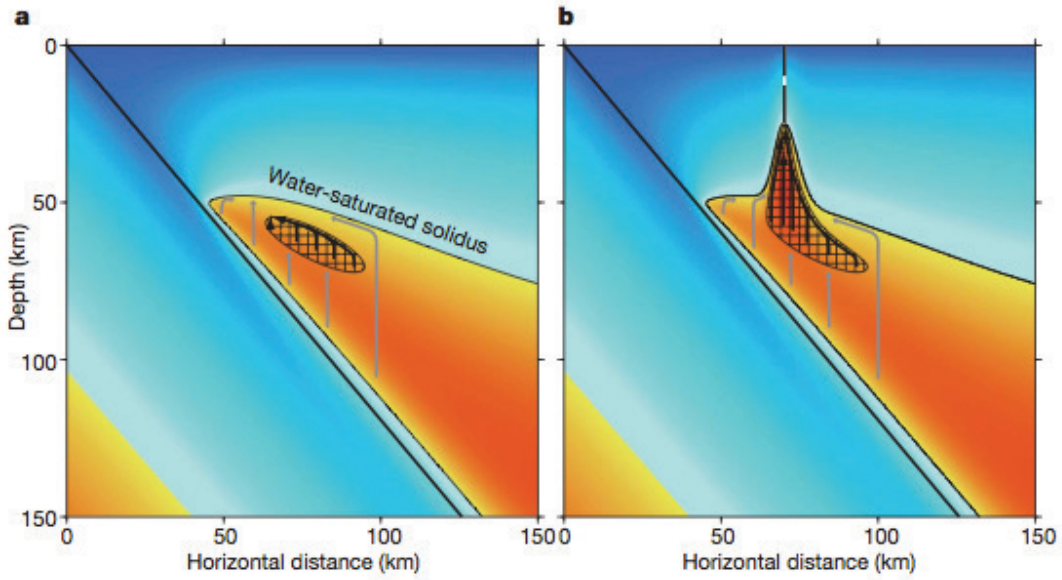

Fig. 7.11 The black diagonal line is the top of the slab. The black line separating the blue and yellow regions is the water saturated solidus and the the cross hatched region is above the anhydrous solidus of the ambient mantle. (a) the distibution of melting and temperature without heat transport by the migrating melt. The grey and black arrows show melt forming, rising, then travelling vai high-porosity channels to the 'nose' of the solidi. (b) Magma rising upwards from the 'nose' of the dry solidus heats the region above. Figure from England and Katz (2010b).

The melt temperatures calculated were limited by the maximum temperature of the thermal model. In both of the thermal models this was 1300 °C. The thermal models did not take into account an adiabatic gradient, if this was included it could be added a posteriori. This was the method used by Syracuse et al. (2010) who added an adiabatic gradient of 0.5 K km^{-1}. Syracuse et al. (2010) also started their thermal models with a mantle potential temperature of 1421.5 °C, which is based on Stein and Stein (1992). This is over 100 °C hotter than the background temperature of the thermal models used in this thesis. If a hotter background temperature of $\sim$ 1400°C was used or an adiabatic gradient was added both would increase the overall temperature of the steady state temperature field. This would lead to an increase in partial melting and lower X_{H_2O} values.

All the thermal and melting models have the same simplified geometry in my thesis. This is a slab dip of 45°, a fixed overriding plate depth of 50 km and a slab velocity of 5 cm yr^{-1}. Using the same geometry and plate velocities allowed me to directly compare my different melting models, where the only input variables changing were the fracture size and source region radius. In reality, subudction zones have a range of geometries with varying dips, slab velocities and overriding plate depths, which would lead to different temperature fields for each subduction zone as shown by Syracuse et al. (2010).

In the thermal and melting models a constant viscosity was assumed. In reality the viscosity in subduction zones is probably temperature dependent and would also be affected by different stresses; dislocation, diffusion and peierls creep and yield stress. More complex dynamical subduction models such as Garel et al. (2014) take into account these effects on viscosity..

7.4 Conclusions

From examining the melt fractions and X_{H_2O} values, the flash-ad and flash-flux-ad melting cases match observations from arcs. However the melt temperature is lower than temperature estimates from geothermometers. Also the final melt events occur at the overriding plate which would not allow any melt focussing to occur. However if the final melt events were to occur at a lower depth, either stopping at the maximum temperature in the wedge or at the solidus at the top of the wedge, this would increase the melt temperatures but the melt fractions would be lower and the X_{H_2O} values would be higher. Note that if the decompression melting stopped at the maximum temperature in the wedge the flash-flux-ad case would not occur, as the decompression melting portion will start at the point of maximum temperature. Increasing the maximum background temperature would increase the melt fractions produced. In the hydrous wet melting parameterisation by Katz et al. (2003), a $X^{bulk}_{H_2O}$ of 0.1 wt% would have a melt fraction $\sim$ 0.1 higher at 1350 °C, compared to 1300 °C at the same pressure. If

the background temperature was increased the melt fractions and X_{H_2O} values from the flash and flash-flux cases may then fit estimates from volcanic arcs.

CHAPTER 8

SUMMARY

8.1 Thesis Summary

The work completed for this thesis relates to subduction zone magmatism and the results are split into five major numerical modelling results chapters, covering two thermal models and four melting models. A brief summary of each of the chapters results and conclusions are summarised below.

Chapter 2 - covers the method used in constructing a thermal model for a subduction zone, with the wedge flow solved analytically. A marker-in-cell, finite difference method was used to allow subsequent tracking of water and partial melt. The thermal model was compared to a subduction zone thermal model benchmark. Comparison with the three benchmark temperature values showed the thermal model was cooler in the wedge than the benchmark, in the region next to the slab and under the overriding plate. However, by calculating the temperature difference between the two models, it was shown that the core of the mantle wedge, where the melting is most likely to occur, had a low temperature difference with the benchmark model. Based on this I concluded that the thermal model was suitable to be used

in the melting models.

Chapter 3 - tested the hypothesis that water being added to the mantle wedge via a large hydraulic fracture would cause melting. This water was assumed to cause instantaneous melting or 'flash melting'. The flash melting model used the temperature field taken from the thermal model and a range of initial bulk water contents $X_{H_2O}^{bulk}$ values, that were calculated from varying fracture sizes and search radii. Overall as the fracture size increased and the search radius decreased; melt fractions, melt volumes and water content in the melt X_{H_2O} all increased, this also corresponded to higher $X_{H_2O}^{bulk}$ values. It was shown that 50-70% of the fracture events produced melting. This proved the hypothesis that a large hydraulic fracture would cause melting in subduction zones. However whether the melting produced is sufficient compared to observations from arcs is another question. Comparisons of the melt fraction, melt production rate and X_{H_2O} with observations showed that the amount of melting produced was too low. This suggests more melting needs to occur at the same $X_{H_2O}^{bulk}$, which would increase the melt fraction and production rate and lower the X_{H_2O} wt% accordingly. Therefore other melting processes need to be considered to supplement the flash melting.

Chapter 4 - examined whether hydrous flux melting occuring after flash melting (flash-flux) would produce sufficient melting compared to observations. Overall as $X_{H_2O}^{bulk}$ increased the melt fraction increased. The results showed the final melt events occured in two distinct regions, both with differing melt fraction, X_{H_2O} and wet melt temperature T_w trends. Comparisons of the melt fraction, melt production rate and X_{H_2O} with observations showed that the amount of melting produced was too low. Therefore for thermal model conditions, flash melting followed by flux melting does not produce sufficient melting compared to volcanic arc observations.

Chapter 5 - examined hydrous decompression melting. It looked at two melting cases; the first was flash melting followed by hydrous decompression melting (flash-ad) and the second was flash melting, then flux melting, followed by hydrous decompression melting (flash-flux-ad). The flash-flux-ad case produced higher melt fractions and lower water content in the melt values than the flash-ad case. Both the flash-ad and flash-flux-ad melting cases produced melt fractions and X_{H_2O} values that fitted with observations from arcs. This suggests that hydrous decompression melting is a feasible melting mechanism for subduction zones. The final melt locations were all located at the base of the overriding plate over a wide region. Therefore hydrous decompression melting occuring vertically does not produce localised melting that is required to explain the sharpness of the volcanic front.

Chapter 6 - looked at adding buoyancy into the thermal model, to allow the partial melt region to migrate buoyantly. A new thermal model was built where the velocity field was solved numerically using Stokes flow. Investigations of background viscosity and density showed that for partial melt to rise for a background viscosity of 10^{21} Pa s, a minimum partial melt radius of 27 km was required. The melting case used was the flash melting, followed by hydrous decompression melting. Two $X^{bulk}_{H_2O}$ cases were run and for both, the partial molten region rises and is deflected by the solid flow towards the wedge corner. The trajectory of the partially molten region is affected by the amount of melting, with higher melt fractions having more buoyancy so the trajectory is higher. This suggests this melting mechanism could provide the melt focussing required for a volcanic front. Due to the difference in source region radius between this melting case and the other melting cases, it was not possible to compare the results directly between melting cases.

By comparing the melting cases to each other and observations from arcs the two decompression melting cases, flash-ad and flash-flux-ad, produce sufficient melting compared to observations from arcs. However these two melting cases had no mechanism for melt

focussing, adding in buoyancy provided a focussing mechanism. Unfortunately the buoyancy melting model (flash-ad-buoy), only worked for large partial melt regions, so we were unable to examine the results for a flash-ad-buoy for the same fracture size and source region radii as the other melting cases. Another limitation was the maximum background temperature was low compared to geothermometer estimates. Increasing the background temperature would increase the melt fractions and lower X_{H_2O} values, which may mean the flash and flash-flux cases then fit observations from arcs. The final conclusion drawn from melting models using the thermal model is that whilst large hydraulic fractures do produce melting via flash melting, it does not produce sufficient melting. For sufficient melting to occur, either hydrous decompression melting, or flux melting follwed by decompression melting needs to occur, after the initial flash melting.

8.2 Future Work

Future work for this study should focus on three main areas; varying the boundary conditions of the current thermal model, improving the buoyancy model and predicting melt compositions.

The boundary conditions used in the thermal model with the velocity field solved analytically, were the same as the benchmark model boundary conditions, as this allowed comparison to the benchmark model to see if the thermal model was suitable. However subudction zones have a wide range of geometries and temperature fields (Syracuse et al., 2010), so future work could investigate varying the slab dip, overriding plate depth, background temperature and slab velocity. Changing these variables would affect the thermal model, so the results produced from the melting models should change. Investigation into whether certain melting cases will produce results matching observations from volcanic arcs by changing these variables could take place.

More work could be done on the buoyancy model such as adding in temperature dependent viscosity to see if it is possible for smaller partial melt regions to rise buoyantly. If it was possible to have smaller partial melt regions rising buoyantly, the results could then be compared to the other melting models. Only the flash-ad case was tried in the buoyancy model so going forwards the flash-flux-ad case could also be incorporated.

Currently from the melting models, melt fraction, X_{H_2O} value, melt production rate and melt temperature and pressure can be calculated. Moving forward it would also be interesting to use these results to predict melt compositions. If the melt compositions could be predicted then they could be compared to magma compositions from volcanic arcs, which would further help to test the melting models.

BIBLIOGRAPHY

Asimow , P. D. and Langmuir , C. The importance of water to oceanic mantle melting regimes. *Nature*, 421(6925):815–820, 2003.

Asimow , P. D., Hirschmann , M., and Stolper , E. An analysis of variations in isentropic melt productivity. *Philos. T. Roy. Soc. A*, 355(1723):255–281, 1997.

Batchelor , G. K. *An Introduction to Fluid Mechanics*. Cambridge University Press, 1967.

Bebout , G. E. The impact of subduction-zone metamorphism on mantle-ocean chemical cycling. *Chem. Geol*, 126(2):191–218, 1995.

Behn , M., Kelemen , P., Hirth , G., Hacker , B., and Massonne , H. Diapirs as the source of the sediment signature in arc lavas. *Nat. Geosci*, 4(9):641–646, 2011.

Bourdon , B., Turner , S., and Dosseto , A. Dehydration and partial melting in subduction zones: Constraints from u-series disequilibria. *J. Geophys. Res-Sol. Ea*, 108(B6), 2003.

Cagnioncle , A., Parmentier , E., and Elkins-Tanton , L. Effect of solid flow above a subducting slab on water distribution and melting at convergent plate boundaries. *J. Geophys. Res*, 112(10.1029), 2007.

Carmichael , I. S. The andesite aqueduct: perspectives on the evolution of intermediate magmatism in west-central (105–99 w) Mexico. *Contrib. Mineral. Petr*, 143(6):641–663, 2002.

Caulfield , J., Turner , S., Arculus , R., Dale , C., Jenner , F., Pearce , J., Macpherson , C., and Handley , H. Mantle flow, volatiles, slab-surface temperatures and melting dynamics in the north Tonga arc–lau back-arc basin. *J. Geophys. Res-Sol. Ea*, 117(B11), 2012.

Dahm , T. Numerical simulations of the propagation path and the arrest of fluid-filled fractures in the earth. *Geophys. J. Int*, 141(3):623–638, 2000.

Davies , J. The role of hydraulic fractures and intermediate-depth earthquakes in generating subduction-zone magmatism. *Nature*, 398(6723):142–145, 1999.

Davies , J. and Bickle , M. A physical model for the volume and composition of melt produced by hydrous fluxing above subduction zones. *Philos. T. Roy. Soc. A*, 335(1638): 355–364, 1991.

Davies , J. and Stevenson , D. Physical model of source region of subduction zone volcanics. *J. Geophys. Res*, 97(B2):2037–2070, 1992.

Dimalanta , C., Taira , A., Yumul , G., Tokuyama , H., and Mochizuki , K. New rates of western Pacific island arc magmatism from seismic and gravity data. *Earth. Planet. Sc. Lett*, 202(1):105–115, 2002.

Elliott , T., Plank , T., Zindler , A., White , W., and Bourdon , B. Element transport from slab to volcanic front at the Mariana arc. *J. Geophys. Res*, 102(B7):14991–15, 1997.

Engdahl , E. R., van der Hilst , R., and Buland , R. Global teleseismic earthquake relocation with improved travel times and procedures for depth determination. *B. Seismol. Soc. Am*, 88(3):722–743, 1998.

England , P., Engdahl , R., and Thatcher , W. Systematic variation in the depths of slabs beneath arc volcanoes. *Geophys. J. Int*, 156(2):377–408, 2004.

England , P. and Katz , R. Melting above the anhydrous solidus controls the location of volcanic arcs. *Nature*, 467(7316):700–703, 2010a.

England , P. C. and Katz , R. F. Global systematics of arc volcano position. *Nature*, 468 (7325):E6–E7, 2010b.

Frohlich , C. The nature of deep-focus earthquakes. *Annu. Rev. Earth. Pl. Sc*, 17:227, 1989.

Garel , F., Goes , S., Davies , D., Davies , J. H., Kramer , S., and Wilson , C. Interaction of subducted slabs with the mantle transition-zone: A regime diagram from 2-d thermo-mechanical models with a mobile trench and an overriding plate. *Geochem. Geophys. Geosy*, 15(5):1739–1765, 2014.

Gerya , T. *Introduction to Numerical Geodynamic Modelling*. Cambridge, 2010.

Gerya , T. Future directions in subduction modeling. *J. Geodyn*, 52(5):344–378, 2011.

Gerya , T. and Yuen , D. Rayleigh-taylor instabilities from hydration and melting propel cold plumes' at subduction zones. *Earth. Planet. Sc. Lett*, 212(1-2):47–62, 2003.

Gill , J. *Orogenic Andesites and Plate Tectonics*. Springer, 1981.

Green , D. Contrasted melting relations in a pyrolite upper mantle under mid-oceanic ridge, stable crust and island arc environments. *Tectonophysics*, 17(3):285–297, 1973.

Green , H. W. and Houston , H. The mechanics of deep earthquakes. *Annu. Rev. Earth. Pl. Sc*, 23:169–214, 1995.

Grove , T., Parman , S., Bowring , S., Price , R., and Baker , M. The role of an H_2O-rich fluid component in the generation of primitive basaltic andesites and andesites from the mt. shasta region, n california. *Contrib. Mineral. Petr*, 142(4):375–396, 2002.

Grove , T. L., Elkins-Tanton , L. T., Parman , S. W., Chatterjee , N., Müntener , O., and Gaetani , G. A. Fractional crystallization and mantle-melting controls on calc-alkaline differentiation trends. *Contrib. Mineral. Petr*, 145(5):515–533, 2003.

Grove , T. L., Chatterjee , N., Parman , S. W., and Médard , E. The influence of H_2O on mantle wedge melting. *Earth. Planet. Sc. Lett*, 249(1):74–89, 2006.

Grove , T. L., Till , C. B., and Krawczynski , M. J. The role of H_2O in subduction zone magmatism. *Annu. Rev. Earth. Pl. Sc*, 40:413–439, 2012.

Grove , T., Till , C., Lev , E., Chatterjee , N., and Médard , E. Kinematic variables and water transport control the formation and location of arc volcanoes. *Nature*, 459(7247):694–697, 2009.

Hacker , B. R. H_2O subduction beyond arcs. *Geochem. Geophys. Geosy*, 9(3), 2008.

Hall , P. and Kincaid , C. Diapiric flow at subduction zones: A recipe for rapid transport. *Science*, 292(5526):2472, 2001.

Hasegawa , A., Nakajima , J., Umino , N., and Miura , S. Deep structure of the northeastern Japan arc and its implications for crustal deformation and shallow seismic activity. *Tectonophysics*, 403(1):59–75, 2005.

Hawkesworth , C., Turner , S., McDermott , F., Peate , D., and Van Calsteren , P. U-Th isotopes in arc magmas: Implications for element transfer from the subducted crust. *Science*, 276(5312):551–555, 1997.

Hirose , K. Melting experiments on lherzolite KLB-1 under hydrous conditions and generation of high-magnesian andesitic melts. *Geology*, 25(1):42, 1997.

Hirschmann , M. M. Mantle solidus: Experimental constraints and the effects of peridotite composition. *Geochem. Geophy. Geosy*, 1(10), 2000.

Hirschmann , M., Asimow , P. D., Ghiorso , M., and Stolper , E. Calculation of peridotite partial melting from thermodynamic models of minerals and melts. III. controls on isobaric melt production and the effect of water on melt production. *J. Petrol*, 40(5):831–851, 1999.

Hochstein , M. Crustal heat transfer in the Taupo Volcanic Zone (New Zealand): comparison with other volcanic arcs and explanatory heat source models. *J. Volcanol. Geoth. Res*, 68 (1):117–151, 1995.

Holbrook , W. S., Lizarralde , D., McGeary , S., Bangs , N., and Diebold , J. Structure and composition of the Aleutian island arc and implications for continental crustal growth. *Geology*, 27(1):31–34, 1999.

Iwamori , H. Transportation of H_2O and melting in subduction zones. *Earth. Planet. Sc. Lett*, 160(1-2):65–80, 1998.

Jagoutz , O., Müntener , O., Schmidt , M. W., and Burg , J.-P. The roles of flux-and decompression melting and their respective fractionation lines for continental crust formation: evidence from the kohistan arc. *Earth. Planet. Sc. Lett*, 303(1):25–36, 2011.

Jarrard , R. D. Relations among subduction parameters. *Rev. Geophys*, 24(2):217–284, 1986.

Jarrard , R. D. Subduction fluxes of water, carbon dioxide, chlorine, and potassium. *Geochem. Geophy. Geosy*, 4(5), 2003.

John , T., Gussone , N., Podladchikov , Y. Y., Bebout , G. E., Dohmen , R., Halama , R., Klemd , R., Magna , T., and Seitz , H.-M. Volcanic arcs fed by rapid pulsed fluid flow through subducting slabs. *Nat. Geosci*, 5(7):489–492, 2012.

Johnson , E. R., Wallace , P. J., Cashman , K. V., and Granados , H. D. Degassing of volatiles (H_2O, CO_2, S, Cl) during ascent, crystallization, and eruption at mafic monogenetic volcanoes in central Mexico. *J. Volcanol. Geoth. Res*, 197(1):225–238, 2010.

Jordan , T. H. Composition and development of the continental tectosphere. *Nature*, 274 (5671):544–548, 1978.

Katz , R. F., Spiegelman , M., and Langmuir , C. H. A new parameterization of hydrous mantle melting. *Geochem. Geophy. Geosy*, 4(9), 2003.

Kawamoto , T. and Holloway , J. R. Melting temperature and partial melt chemistry of H_2O-saturated mantle peridotite to 11 gigapascals. *Science*, 276(5310):240–243, 1997.

Kelley , K. A., Plank , T., Newman , S., Stolper , E. M., Grove , T. L., Parman , S., and Hauri , E. H. Mantle melting as a function of water content beneath the Mariana Arc. *J. Petrol*, page egq036, 2010.

Kelley , K. A., Plank , T., Grove , T. L., Stolper , E. M., Newman , S., and Hauri , E. Mantle melting as a function of water content beneath back-arc basins. *J. Geophys. Res-Sol. Ea*, 111(B9), 2006.

Keppler , H. Constraints from partitioning experiments on the composition of subduction-zone fluids. *Nature*, 1996.

Key , K., Constable , S., Matsuno , T., Evans , R. L., and Myer , D. Electromagnetic detection of plate hydration due to bending faults at the Middle America Trench. *Earth. Planet. Sc. Lett*, 351:45–53, 2012.

Kohut , E. J., Stern , R. J., Kent , A. J., Nielsen , R. L., Bloomer , S. H., and Leybourne , M. Evidence for adiabatic decompression melting in the Southern Mariana Arc from high-Mg lavas and melt inclusions. *Contrib. Mineral. Petr*, 152(2):201–221, 2006.

Krawczynski , M. J., Grove , T. L., and Behrens , H. Amphibole stability in primitive arc magmas: effects of temperature, H_2O content, and oxygen fugacity. *Contrib. Mineral. Petr*, 164(2):317–339, 2012.

Langmuir , C., Bezos , A., Escrig , S., and Parman , S. Chemical systematics and hydrous melting of the mantle in back-arc basins. *Geophys. Mono. A. G. U*, 166:87, 2006.

Langseth , M. G. and Silver , E. A. The Nicoya convergent margin—A region of exceptionally low heat flow. *Geophys. Res. Lett*, 23(8):891–894, 1996.

Lee , C.-T. A., Luffi , P., Plank , T., Dalton , H., and Leeman , W. P. Constraints on the depths and temperatures of basaltic magma generation on Earth and other terrestrial planets using new thermobarometers for mafic magmas. *Earth. Planet. Sc. Lett*, 279(1):20–33, 2009.

Lizarralde , D., Holbrook , W. S., McGeary , S., Bangs , N. L., and Diebold , J. B. Crustal construction of a volcanic arc, wide-angle seismic results from the western Alaska Peninsula. *J. Geophys. Res-Sol. Ea*, 107(B8):EPM–4, 2002.

Longhi , J. Some phase equilibrium systematics of lherzolite melting: I. *Geochem. Geophy. Geosy*, 3(3):1–33, 2002.

McKenzie , D. and Bickle , M. The volume and composition of melt generated by extension of the lithosphere. *J. Petrol*, 29(3):625–679, 1988.

McKenzie , D. The generation and compaction of partially molten rock. *J. Petrol*, 25(3):713, 1984.

McKenzie , D. P. Speculations on the consequences and causes of plate motions. *Geophys. J. Int*, 18(1):1–32, 1969.

Meade , C. and Jeanloz , R. Deep-focus earthquakes and recycling of water into the Earth's mantle. *Science*, 252(5002):68–72, 1991.

Minear , J. W. and Toksöz , M. N. Thermal regime of a downgoing slab and new global tectonics. *J. Geophys. Res*, 75(8):1397–1419, 1970.

Mysen , B. O. and Wheeler , K. Solubility behavior of water in haploandesitic melts at high pressure and high temperature. *Am. Mineral*, 85(9):1128–1142, 2000.

Peacock , S. A. Fluid processes in subduction zones. *Science*, 248(4953):329–337, 1990.

Peacock , S. M. Are the lower planes of double seismic zones caused by serpentine dehydration in subducting oceanic mantle? *Geology*, 29(4):299–302, 2001.

Pearce , J. and Peate , D. Tectonic implications of the composition of volcanic arc magmas. *Annu. Rev. Earth. Pl. Sc*, 23:251–286, 1995.

Pearce , J. A. and Parkinson , I. J. Trace element models for mantle melting: application to volcanic arc petrogenesis. *Geol. Soc., London, Special Publications*, 76(1):373–403, 1993.

Pearce , J. A., Baker , P. E., Harvey , P. K., and Luff , I. W. Geochemical evidence for subduction fluxes, mantle melting and fractional crystallization beneath the South Sandwich island arc. *J. Petrol*, 36(4):1073–1109, 1995.

Peate , D. W., Kokfelt , T. F., Hawkesworth , C. J., Van Calsteren , P. W., Hergt , J. M., and Pearce , J. A. U-series isotope data on Lau Basin glasses: The role of subduction-related fluids during melt generation in back-arc basins. *J. Petrol*, 42(8):1449–1470, 2001.

Pickering-Witter , J. and Johnston , A. D. The effects of variable bulk composition on the melting systematics of fertile peridotitic assemblages. *Contrib. Mineral. Petr*, 140(2): 190–211, 2000.

Plank , T., Kelley , K. A., Zimmer , M. M., Hauri , E. H., and Wallace , P. J. Why do mafic arc magmas contain 4wt% water on average? *Earth. Planet. Sc. Lett*, 364:168–179, 2013.

Portnyagin , M., Hoernle , K., Plechov , P., Mironov , N., and Khubunaya , S. Constraints on mantle melting and composition and nature of slab components in volcanic arcs from volatiles (H_2O, S, Cl, F) and trace elements in melt inclusions from the Kamchatka Arc. *Earth. Planet. Sc. Lett*, 255(1):53–69, 2007.

Press , W., Teukolsky , S., Vetterling , W., and Flannery , B. Numerical Recipes in Fortran 77: The Art of Scientific Computing, 933 pp, 1992.

Ranero , C. R., Morgan , J. P., McIntosh , K., and Reichert , C. Bending-related faulting and mantle serpentinization at the Middle America trench. *Nature*, 425(6956):367–373, 2003.

Roggensack , K., Hervig , R. L., McKnight , S. B., and Williams , S. N. Explosive basaltic volcanism from Cerro Negro volcano: influence of volatiles on eruptive style. *Science*, 277(5332):1639–1642, 1997.

Rüpke , L. H., Morgan , J. P., Hort , M., and Connolly , J. A. Serpentine and the subduction zone water cycle. *Earth. Planet. Sc. Lett*, 223(1):17–34, 2004.

Schmidt , M. and Poli , S. Experimentally based water budgets for dehydrating slabs and consequences for arc magma generation. *Earth. Planet. Sc. Lett*, 163(1-4):361–379, 1998.

Schmidt , M. and Poli , S. Generation of mobile components during subduction of oceanic crust. *Treatise on geochemistry*, 3:567–591, 2003.

Schutt , D. and Lesher , C. Effects of melt depletion on the density and seismic velocity of garnet and spinel lherzolite. *J. Geophys. Res-Sol. Ea*, 111(B5), 2006.

Silver , L. and Stolper , E. A thermodynamic model for hydrous silicate melts. *J. Geol*, pages 161–177, 1985.

Sisson , T. and Grove , T. Temperatures and H_2O contents of low-MgO high-alumina basalts. *Contrib. Mineral. Petr*, 113(2):167–184, 1993.

Sisson , T. and Layne , G. H_2O in basalt and basaltic andesite glass inclusions from four subduction-related volcanoes. *Earth. Planet. Sc. Lett*, 117(3):619–635, 1993.

Spiegelman , M. Physics of melt extraction: Theory, implications and applications. *Philos. T. Roy. Soc. A*, 342(1663):23–41, 1993.

Stein , C. A. and Stein , S. A model for the global variation in oceanic depth and heat flow with lithospheric age. *Nature*, 359(6391):123–129, 1992.

Stern , C. and Wyllie , P. Melting relations of basalt-andesile-rhyolite-H_2O and a pelagic red clay at 30 kb. *Contrib. Mineral. Petr*, 42(4):313–323, 1973.

Stern , R. J. Subduction zones. *Rev. Geophys*, 40(4):3–1, 2002.

Stolper , E. and Newman , S. The role of water in the petrogenesis of Mariana trough magmas. *Earth. Planet. Sc. Lett*, 121(3):293–325, 1994.

Syracuse , E. M. and Abers , G. A. Global compilation of variations in slab depth beneath arc volcanoes and implications. *Geochem. Geophy. Geosy*, 7(5), 2006.

Syracuse , E. M., van Keken , P. E., and Abers , G. A. The global range of subduction zone thermal models. *Phys. Earth. Planet. In*, 183(1):73–90, 2010.

Taira , A., Saito , S., Aoike , K., Morita , S., Totuyama , H., Suyheiro , K., Takahashi , N., Shinohara , M., Kiyokawa , S., Naka , J., and others . Nature and growth rate of the Northern Izu–Bonin (Ogasawara) arc crust and their implications for continental crust formation. *Isl. Arc*, 7(3):395–407, 1998.

Tatsumi , Y. and Eggins , S. *Subduction Zone Magmatism*. Cambridge, 1995.

Turner , S. and Hawkesworth , C. Constraints on flux rates and mantle dynamics beneath island arcs from Tonga–Kermadec lava geochemistry. *Nature*, 389(6651):568–573, 1997.

Twiss , R. J. and Moores , E. *Structural Geology*. WH Freeman, 1992.

Ulmer , P. and Trommsdorff , V. Serpentine stability to mantle depths and subduction-related magmatism. *Science*, 268(5212):858, 1995.

Van Keken , P., Currie , C., King , S., Behn , M., Cagnioncle , A., He , J., Katz , R., Lin , S., Parmentier , E., Spiegelman , M., and others . A community benchmark for subduction zone modeling. *Phys. Earth. Planet. In*, 171(1):187–197, 2008.

Van Keken , P. E. The structure and dynamics of the mantle wedge. *Earth. Planet. Sc. Lett*, 215(3):323–338, 2003.

van Keken , P. E., Hacker , B. R., Syracuse , E. M., and Abers , G. A. Subduction factory: 4. depth-dependent flux of H_2O from subducting slabs worldwide. *J. Geophys. Res-Sol. Ea*, 116(B1), 2011.

Wada , I. and Wang , K. Common depth of slab-mantle decoupling: Reconciling diversity and uniformity of subduction zones. *Geochem. Geophy. Geosy*, 10(10), 2009.

Walter , M. J. Melting of garnet peridotite and the origin of komatiite and depleted lithosphere. *J. Petrol*, 39(1):29–60, 1998.

White , S. M., Crisp , J. A., and Spera , F. J. Long-term volumetric eruption rates and magma budgets. *Geochem. Geophy. Geosy*, 7(3), 2006.

Wilson , C. R., Spiegelman , M., van Keken , P. E., and Hacker , B. R. Fluid flow in subduction zones: The role of solid rheology and compaction pressure. *Earth. Planet. Sc. Lett*, 401:261–274, 2014.

Zimmer , M. M., Plank , T., Hauri , E. H., Yogodzinski , G. M., Stelling , P., Larsen , J., Singer , B., Jicha , B., Mandeville , C., and Nye , C. J. The role of water in generating the calc-alkaline trend: new volatile data for Aleutian magmas and a new tholeiitic index. *J. Petrol*, 51(12):2411–2444, 2010.

APPENDIX A

SOLUTION FOR CORNER FLOW STREAM FUNCTION

WEDGE: Boundary conditions for the wedge side are:

$\mathbf{v} = 0$ for $\theta = 0$ and,

$\mathbf{v} = U\mathbf{a}_r$ for $\theta = \theta_d$

$$\Psi = r\Theta = r(A\sin\theta + B\cos\theta + C\theta\sin\theta + D\theta\cos\theta) \tag{A.1}$$

¥

$$v_r = \frac{\partial\Psi}{r\partial\theta} = \frac{\partial(r\Theta)}{r\partial\theta} = \frac{d\Theta}{d\theta}$$

$$v_r = \frac{d\Theta}{d\theta} = A\cos\theta - B\sin\theta + C\sin\theta + C\theta\cos\theta + D\cos\theta - D\theta\sin\theta \tag{A.2}$$

¥

$$v_\theta = -\frac{\partial\Psi}{\partial r} = -\frac{\partial(r\Theta)}{\partial r} = -\Theta(\theta)$$

$$v_\theta = -(A\sin\theta + B\cos\theta + C\theta\sin\theta + D\theta\cos\theta) \tag{A.3}$$

When $\theta = 0$, $v_r = v_\theta = 0$

By substituting these conditions into (A.2)

$$A = -D \tag{A.4}$$

By substituting the conditions into (A.3)

$$B = 0 \tag{A.5}$$

When $\theta = \theta_d$, $v_r = U$ and $v_\theta = 0$

C can be be found from substituting these conditions and equations (A.4) and (A.5) into equation (A.3)

$$C = \frac{D(\sin\theta_d - \theta_d \cos\theta_d)}{\theta_d \sin\theta_d} \tag{A.6}$$

Substitute the conditions and equations (A.4) and (A.5) into equation (A.2)

$$U = C(\sin\theta_d + \theta_d \cos\theta_d) - D\theta_d \sin\theta_d \tag{A.7}$$

Substituting equation (A.6) into equation (A.7) gives D

$$D = -\frac{U\theta_d \sin\theta_d}{\theta_d^2 - \sin^2\theta_d} \tag{A.8}$$

From equation (A.4) we get A

$$A = \frac{U\theta_d \sin\theta_d}{\theta_d^2 - \sin^2\theta_d} \tag{A.9}$$

And from equation (A.6) we get C

$$C = \frac{U(\theta_d \cos_d - \sin\theta_d)}{\theta_d^2 - \sin^2\theta_d} \tag{A.10}$$

Substituting equations (A.8) to (A.10) into equation (A.1) allows Ψ to be calculated

$$\Psi = \frac{Ur[(\theta_d - \theta)\sin\theta_d \sin\theta + \theta_d \theta \sin(\theta_d - \theta)}{\theta_d^2 - \sin^2\theta_d} \tag{A.11}$$